Implications of Regional Fault Distribution and Kinematics for the Uplift of Rift Flanks Around the Rwenzori Mountains, Southwestern Uganda

Dissertation
zur Erlangung des Grades „Doktor der Naturwissenchaften"
(Dr. rer. nat.)
im Promotionsfach Geologie/Paläontologie

am Fachbereich Chemie, Pharmazie und Geowissenschaften
der Johannes Gutenberg-Universität
in Mainz

Kevin (Frau) Aanyu
geboren in Uganda.

Mainz, den 29. September 2011,

Erklärung

Hiermit Versichere ich, die vorliegende Arbeit selbstständig und nur unter Verwendung der angegebenen Quellen und Hilfsmittel verfasst zu haben.

Mainz, den 29. September 2011.

Zusammenfassung

Die oberen 10-15 km der Erdkruste verhalten sich spröde, d.h. unter Spannung bilden sich natürliche Gleitflächen die als Störungen bezeichnet werden. Der Störungstyp - z.B. Ab- oder Aufschiebung, Blattverschiebung, Schrägabschiebung u.a. - ist charakteristisch für das verursachende Spannungsfeld. Auf diese Weise entwickeln sich zum Teil komplexe Störungssysteme. Geologische Spannungen sind stets kompressiv, variieren aber in verschiedenen Richtungen, so daß ein Spannungszustand durch die Orientiertung und Stärke der Hauptspannungen σ_1, σ_2 und σ_3 charakterisiert ist. Störungen sind Bewegungsflächen an denen gesteinsinterne Spannungen abgebaut werden können und die die Rotation oder Hebung von Blöcken oder Riftflanken ermöglichen. Höhere Riftflanken entwickeln sich dann, wenn sich der Versatz auf die Rift-Hauptstörungen konzentriert und nicht auf viele kleinere Störungen verteilt ist. Polyphase Störungssysteme können dazu verwendet werden Paläospannungen zu bestimmen, und in Riftsystemen können sie Veränderungen der Extensionsrichtung reflektieren. Mittels mikrotektonischer Untersuchungen können die Deformationsphasen im Dünnschliffe ermittelt werden. Mit Hilfe skalierter Analogmodelle kann die 3-D strukturelle Entwicklung eines tektonischen Modells untersucht werden. Außerdem können mit Hilfe solcher Modelle die physikalischen Rahmenbedingungen, wie das Spannungsfeld und die Wechselwirkung der physikalischen Eigenschaften des deformierten Materials mit dem Deformationprozess selbst, analysiert werden.

Das Ziel dieser Arbeit bestand in der Untersuchung der Störungsverteilung und der Störungskinematik im Zusammenhang mit der Hebung der Riftschultern des Rwenzori Gebirges. Das Rwenzori Gebirge befindet sich im NNE-SSW bis N-S verlaufenden Albertine Rift, des nördlichsten Segments des westlichen Armes des Ostafrikanischen Grabensystems. Das Albertine Rift besteht aus Becken unterschiedlicher Höhe, die den Lake Albert, Lake Edward, Lake George und Lake Kivu enthalten. Der Rwenzori horst trennt die Becken des Lake Albert und des Lake Edward. Es erstreckt sich 120km in N-S Richtung, sowie 40-50km in E-W Richtung, der höchste Punkt befindet sich 5111 ü. NN. Diese Studie untersucht einen Abschnitt des Rifts zwischen etwa 1°N und 0°30′S Breite sowie 29°30′ und 30°30′ östlicher Länge ersteckt. Auch die Feldarbeit konzentrierte sich auf dieses Gebiet.

Hauptzweck dieser Studie bestand darin, die folgende These auf ihre Richtigkeit zu überprüfen: 'Wenn es im Verlauf der Zeit tatsächlich zu wesentlichen Änderungen in der Störungskinematik kam, dann ist die starke Hebung der Riftflanken im Bereich der Rwenzoris nicht einfach durch Bewegung entlang der Graben-Hauptstörungen zu erklären. Vielmehr ist sie ein Resultat des Zusammenspiels mehrerer tektonische Prozesse, die das Spannungsfeld beeinflussen und dadurch Änderungen in der Kinematik hervorrufen.' Dadurch konzentrierte sich die Studie in erster Linie auf die Störungsanalyse.

Die Kenntnis regionaler Änderungen der Extensionsrichtung ist entscheidend für das Verständnis komplexer Riftsysteme wie dem Ostafrikanischen Graben. Daher bestand der Kern der Untersuchung in der Kartierung von Störungen und der Untersuchung der Störungskinematik. Die Aufnahme strukturgeologischer Daten konzentrierte sich auf die Ugandische Seite des Rifts, und Paläospannungen wurden mit Hilfe von Störungsdaten durch Spannungsinversion rekonstruiert.

Die unterschiedliche Orientierung spröder Strukturen im Gelände, die geometrische Analyse der geologischen Strukturen sowie die Ergebnisse von Mikrostrukturen im Dünnschliff (Kapitel 4) weisen auf verschiedene Spannungsfelder hin, die auf mögliche Änderungen der Extensionsrichtung hinweisen. Die Resultate der Spannungsinversion sprechen für Ab-, Über- und Blattverschiebungen sowie für Schrägüberschiebungen (Kapitel 5). Aus der Orientierung der Abschiebungen gehen zwei verschiedene Extensionsrichtungen hervor: im Wesentlichen NW-SE Extension in fast allen Gebieten, sowie NNE-SSW Extension im östlichen Zentralbereich.

Aus der Analyse von Blattverschiebungen ergaben sich drei unterschiedliche Spannungszustände. Zum Einen NNW-SSE bis N-S Kompression in Verbindung mit ENE-WSW bzw E-W Extension wurde für die nörlichen und die zentralen Ruwenzoris ausgemacht. Ein zweiter Spannungszustand mit WNW-ESE Kompression/NNE-SSW Extension betraf die Zentralen Rwenzoris. Ein dritter Spannungszustand mit NNW-SSE Extension betraf den östlichen Zentralteil der Rwenzoris. Schrägüberschiebungen sind durch dazu schräge Achsen charakterisiert, die für N-S bis NNW-SSE Kompression sprechen und ausschließlich im östlichen Zentralabschnitt auftreten. Überschiebungen, die hauptsächlich in den zentralen und den östlichen Rwenzoris auftreten, sprechen für NE-SW orientierten σ_2-Achsen und NW-SE Extension.

Es konnten drei unterschiedliche Spannungseinflüsse identifiziert werden: auf die kollisionsbedingte Bildung eines Überschiebungssystem folgte intra-kratonische Kompression und schließlich extensionskontrollierte Riftbildung. Der Übergang zwischen den beiden letztgenannten Spannungszuständen erfolgte Schrittweise und erzeugte vermutlich lokal begrenzte Transpression und Transtension. Gegenwärtig wird die Störungskinematik der Region durch ein tensiles Spannungsregime in NW-SE bis N-S Richtung bestimmt. Lokale Spannungsvariationen werden dabei hauptsächlich durch die Interferenz des regionalen Spannungsfeldes mit lokalen Hauptstörungen verursacht. Weitere Faktoren die zu lokalen Veränderungen des Spannungsfeldes führen können sind unterschiedliche Hebungsgeschwindigkeiten, Blockrotation oder die Interaktion von Riftsegmenten.

Um den Einfluß präexistenter Strukturen und anderer Bedingungen auf die Hebung der Rwenzoris zu ermitteln, wurde der Riftprozeß mit Hilfe eines analogen 'Sandbox'-Modells rekonstruiert (Kapitel 6). Da sich die Moho-Diskontinuität im Bereich des Arbeitsgebietes in einer Tiefe von 25 km befindet, aktive Störungen aber nur bis zu einer Tiefe von etwa 20 km beobachtet werden können (Koehn et al. 2008), wurden nur die oberen 25 km im Modell nachbebildet. Untersucht und mit Geländebeobachtungen verglichen wurden sowohl die Reihenfolge, in der Riftsegmente entstehen, als auch die Muster, die sich im Verlauf der Nukleierung und des Wachstums dieser Riftsegmente ausbilden. Das Hauptaugenmerk wurde auf die Entwicklung der beiden Subsegmente gelegt auf denen sich der Lake Albert bzw. der Lake Edward und der Lake George befinden, sowie auf das dazwischenliegende Rwenzori Gebirge. Das Ziel der Untersuchung bestand darin herauszufinden, in welcher Weise das südwärts propagierende Lake Albert-Subsegment mit dem sinistral versetzten nordwärts propagierenden Lake Edward/Lake George-Subsegment interagiert.

Von besonderem Interesse war es, in welcher Weise die Strukturen innerhalb und außerhalb der Rwenzoris durch die Interaktion dieser Riftsegmente beeinflußt wurden.

Drei verschiedene Versuchsreihen mit unterschiedlichen Randbedingungen wurden miteinander verglichen. Abhängig vom vorherrschenden Deformationstyp der Transferzone wurden die Reihen als 'Scherungs-dominiert', 'Extensions-dominiert' und als 'Rotations-dominiert' charakterisiert. Die Beobachtung der 3-dimensionalen strukturellen Entwicklung der Riftsegmente wurde durch die Kombination von Modell-Aufsichten mit Profilschnitten ermöglicht. Von den drei genannten Versuchsreihen entwickelte die 'Rotations-dominierten' Reihe einen rautenförmiger Block im Tranferbereich der beiden Riftsegmente, der sich um $5-20°$ im Uhrzeigersinn drehte. Dieser Winkel liegt im Bereich des vermuteten Rotationswinkel des Rwenzori-Blocks (5°). Zusammengefasst untersuchen die Sandbox-Versuche den Einfluss präexistenter Strukturen und der Überlappung bzw. Überschneidung zweier interagierender Riftsegmente auf die Entwicklung des Riftsystems. Sie befassen sich darüber hinaus mit der Frage, welchen Einfluss Blockbildung und -rotation auf das lokale Stressfeld haben.

Abstract

The topmost 10-15km of the earth's crust deforms by fracture when stresses build up. Normal, strike-slip, reverse or oblique faults are generally characteristic of stress fields in which they form, sometimes showing complex patterns. In geological situations, stresses are always compressive but vary in different directions. Hence a state of stress is evaluated in terms of orientation and magnitudes of the principle stresses σ_1, σ_2 and σ_3. Fault movements relieve the rocks of stress build-up and aid the tilting and uplift of blocks and rift-flanks. Displacements along major rift faults tend to produce higher flanks than distributed displacement on many faults. Different fault generations may be studied to unravel secular changes of stress fields and they may reflect change of extension directions in extensional rift settings. Tectonic evolution can be unravelled from microtectonic study of rocks. By running scale physical models of tectonic events, one can also study 3-D structural evolution of a specific model and how physical conditions like stress fields, boundary conditions or physical properties of the deforming material relate to deformation.

This study was geared at defining the implications of fault distribution and kinematics for the rift-flank uplift around Rwenzori mountains that lie in the Albertine Rift, which is the northern most segment of the western branch of the East African Rift System. The NNE-SSW to N-S striking Albertine Rift consists of basins that lie at different elevations and host the lakes Albert, Edward-George and Kivu. The Rwenzori horst separates the Albert from the Edward lake basin. It extends 120km in the N-S direction and 40-50km in W-E direction, reaching a height of 5111m a.m.s.l at its highest peak. The study targeted a section of the rift approximately within latitudes $1°0'$N and $0°30'$S and longitudes $29°30'$E and $30°30'$E, which also delimit the zone where field surveys were carried out.

The Primary aim for the study was to test the hypothesis that '*If indeed there is a major change in fault kinematics with time, then the high rift-flank uplift around the Rwenzoris is not simply controlled by movements along the major boundary faults but is a result of interplay of several tectonic processes that alter the stress field regimes to effect kinematic changes.*' As such, the study was mostly focused on faults. Assessment of regional variations in the local extension directions is vital in evaluation of rifting processes for rift systems with complex architecture such as the East African Rift. Thus the key objective was to map out faults and study their kinematics, so as to workout the stress field regimes responsible for their development. Structural measurements were taken mainly on the Ugandan side of the rift and paleostresses were reconstructed by inversion of fault-slip data using the *Stress inversion via simulation* method.

From field observations, geometric structure analysis and microstructural study (chap. 4), different causative stresses were envisaged with possible temporal change of extension directions. Results from inversion indicated normal, thrust, strike-slip and oblique-thrust faulting (chap. 5). Normal faults exhibited two modes of extension, characterised by

NW-SE trending σ_3-axes (main rift extension direction) observed in nearly all areas and NNE-SSW extension observed in the east central part.
Strike-slip faults exhibited three modes. One characterised by NNW-SSE to N-S compression and ENE-WSW to W-E extension was observed in the northern and central Rwenzoris. The second mode showed WNW-ESE compression and NNE-SSW extension, observed mainly in the central Rwenzoris whereas the other with oblique mode of slip and approximately NNW-SSE extension, was observed only in the east central part.
Oblique thrust faulting was characterised by tilted axes portraying approximately N-S to NNW-SSE compression, observed only in the east central part.
Finally, pure-thrusting exhibited mainly in the central and east central Rwenzoris, was characterised by NE-SW-trending σ_2-axes and NW-SE extension.

Three stress regimes were identified. An early *collisional thrusting* regime, followed by a *compressive intra-cratonic* regime and then an *extensional rifting* one. The transition of the latter two was gradual, probably involving localised transpression and transtension in certain areas. At present, the fault kinematics of this region are controlled by an extensional stress regime showing NW-SE to WNW-ESE and locally N-S directed extension. Local variation of stress fields reflected mixed effects of temporal fluctuation or rotation and reversal of axes-orientations and interference of regional stresses by stress fields around master faults. Differences in local state of gravitational potential energy, block rotation and/or uplift and stress field perturbation due to interaction of rift segments, are also potential contributing factors.

To investigate the influence of pre-existing crustal structures and constrain conditions under which the Rwenzoris formed, the rifting process was replicated using scale sandbox models (chap. 6). Since the Moho-discontinuity in the target region lies at average depth of 25km and active faulting can be traced down to 20km depth (Koehn et al. 2008), only the upper 25km was modelled. The order of development of fault segments was observed and growth patterns studied right from the point of nucleation, through the process of propagation and were compared with the field scenario. Focus was set upon development of the L. Albert and L. Edward-George sub-segments and between them the high uplifted Rwenzori block. The aim was to study how the southward propagating Lake Albert subsegment to the north interacts with the sinistrally offset, northward propagating Lake Edward-Lake George sub-segment. The objective was to explain how this interaction accounts for the structures and geometry observed within and around the Rwenzoris.

Three different sets of boundary conditions selected gave three experimental series, which were compared. Depending on the dominant type of deformational characteristics prevalent in the transfer zone, the series were respectively described as 'shear-dominated', 'extension-dominated' and 'rotation-dominated'. The experiments enabled 3-D structural evolution of rift segments to be studied by combining observations of model plan-view with those of section cuts. From plan-view and sections of developing fault and rift segments, kinematics resulting from a given set of boundary conditions were studied and results compared with the natural scenario. Of the three, the 'rotation-dominated' model created a 'pass' during segment interaction and captured a lozenge-shaped block that rotated through angles in the range 5-20° clockwise, qualifying it to be the closest approximation to the prototype. In brief, the models broadly addressed the role of pre-existing structures and relative sizes of overlap and/or overstep between two interacting rift segments, during development and evolution of the rift. They also addressed effects of interaction and block capture or rotation on local stress fields.

Contents

List of Figures

List of Tables

Symbol/Abbrev.	Description
ρ	Density
$\mathbf{g}$	Gravitational acceleration
K	Fault combination factor
e	Enhance factor
L_R	Model length ratio
ϕ	Angle of (internal) friction in intact rock
ϕ_r	Angle of sliding friction
ϕ_s	Angle of static friction
ρ_R	Model density ratio
R	Stress ratio
σ_n	Normal stress
τ	Shear stress
σ_v	Vertical stress
σ_1-axis	Maximum principle stress axis
σ_2-axis	Intermediate principle stress axis
σ_3-axis	Minimum principle stress axis
β	Misfit (°) between theoretical and measured slip direction
T_R	Model time ratio
V_R	Model velocity ratio
z	Depth from earth's surface
f_{max}	Maximum frictional resistance to slip
μ_o	Coefficient of internal friction of intact rock (tan ϕ)
μ_s	Coefficient of (static) friction (tan ϕ_s)
μ_w	Coefficient of internal friction along a plane of weakness (tan ϕ_r)
C_o	Cohesion or inherent shear strength of intact rock
S_w	Inherent shear strength of a plane of weakness
σ_1, σ_2, σ_3	Maximum, intermediate and minimum principle stresses
β_o	Angle between σ_1 and the normal to a failure plane formed in intact rock
β_w	Angle between σ_1 and the normal to a pre-existing plane of weakness, at which failure will occur along the plane
$\overline{D}$ [or D(mean)]	Mean stress difference
$\overline{\Phi}$ [or Φ(mean)]	Mean angular stress distance
$\supset$	here applied to indicate syn-tectonic growth of porphyroblasts

Abbreviation	Description
B-axis	Neutral strain axis
P-axis	Contractional strain axis
T-axis	Extensional strain axis
C-RWZ	Central Rwenzoris tectonic unit
KK	Kigolo-Kabakoru tectonic unit
KNG	Kilembe-Nyabirongo-Lake George flank tectonic unit

Symbol/Abbrev.	**Description**
SK	Sempaya-Kazingo tectonic unit
FFP	Freshfield Pass
D1, D2, D3, D4	Phases of deformation
P_C	Porphyroblasts of Cordierite
P_G	Porphyroblasts of Garnet
P_S	Porphyroblasts of Sillimanite
S1, S2, S3, S4	Foliations resulting from different phases of deformation
S_e	External foliation existing outside porphyroblasts as observed in thin-section
$S_{(Hmax)}$	Maximum horizontal principle stress
$S_{(Hmin)}$	Minimum horizontal principle stress
S_i	Internal foliation overgrown/included by porphyroblasts as observed in thin-section
MIM	Multiple inverse method
NF	Normal faulting
SS	Strike-slip faulting
TF	Thrust faulting
TS	Oblique thrust faulting
KK-12; KK-3	Fault subsets of Kigolo-Kabakoru tectonic unit
KK-12^1; KK-3^1	Preliminary stress states obtained for Kigolo-Kabakoru tectonic unit
KK-12^2; KK-3^2	Optimal solutions obtained for Kigolo-Kabakoru tectonic unit
KNG-1; KNG-2	Fault subsets of Kilembe-Nyabirongo-L. George flanks tectonic unit
KNG-1^1; KNG-2^1	Preliminary stress states determined for Kilembe-Nyabirongo-Lake George flanks tectonic unit
KNG-1^2; KNG-2^2	Optimal solutions obtained for Kilembe-Nyabirongo-L. George flanks tectonic unit
RA; RB; RC; RD	Fault subsets of the central-Rwenzoris tectonic unit
RA^1; RB^1; RC^1; RD^1	Preliminary stress states determined for the central-Rwenzoris tectonic unit
RA^2; RB^2; RC^2; RD^2	Optimal solutions obtained for the central-Rwenzoris tectonic unit
SK-1; SK-2	Fault subsets of Sempaya-Kazingo tectonic unit
SK-1^1; SK-2^1	Preliminary stress states obtained for Sempaya-Kazingo tectonic unit
SK-1^2; SK-2^2	Optimal solutions obtained for Sempaya-Kazingo unit
L	Overlap
S	Overstep
VD	Velocity discontinuity

Chapter 1

Introduction

1.1 Motivation

In the last two decades, much has been published on various aspects of the East African Rift System (EARS). Renewed research interests focus on the hydrocarbon potential of the rift but also on the fact that the EARS offers a great opportunity to study and understand the rifting process throughout its various stages of evolution. Additionally, understanding the behaviour of faults or fault systems is vital for the mining industry where tunnels and shafts are useful and for constructions such as dams or bridges. In aquifers and hydrocarbon reservoirs, faults can be potential conduits or on the contrary blockage to flow, depending on the sense of movement and porosity of material within fault cores. In developing intra-continental rifts, location and magnitude of faulting are controlled by thickness and character of the affected crust and by the presence of favourably oriented pre-existing weakness lines that can be exploited by new faults (Frostick 2005). However, fracture systems of intense magnitude cannot be simply due to pre-existing structures in the basement but must form in response to definite stress patterns (Le Bas 1971). Such stresses can for instance result from uplift that imparts excess potential energy to the elevated region or from disturbance of the isostatic equilibrium by changes in thickness of the crust and mantle lithosphere (Allen and Allen 1990).

Extension directions of some continental rifts are reported to have changed during rift evolution (Illies and Greiner 1978; Strecker et al. 1990; Strecker and Bosworth 1991; Ring et al. 1992). The changes are said to result from rotation or permutations of principal kinematic axes (Ring et al. 1992) and reflect change in the stress field or change of the state of stress. Over the time, such changes may result in formation of multiple fault-sets that present heterogeneous fault-slip data. Thus heterogeneous data sets can come from an area that experienced successive ages with different states of stress responsible for the different homogeneous fault-sets (Yamaji et al. 2010). Multiple fault patterns and multiple slickenline sets can also form in a single phase of faulting as a consequence of the kinematics of interacting faults (Nieto-Samaniego and Alaniz-Alvarez 1997), hence multiple fault-sets do not necessarily imply multiple stress-states or multiple deformations (Oertel 1965; Malone et al. 1975; Aydin 1997). On local scale, heterogeneous fault-slip data can result from spatial and temporal change in slip-direction due to change of local shear stress across a fault plane (Guatteri and Spudich 1998). Therefore, to understand and appropriately evaluate rifting processes for rift systems with complex architecture, the assessment

of regional variations in the local extension directions is vital (Acocella and Korme 2002). Additionally, analysis of microstructural fabrics of deformed rocks gives insight into the deformational phases they have suffered. As such, thin-section studies can successfully be used to reconstruct the structural and metamorphic history of rocks and if carefully interpreted can provide a direct source of information useful to reconstruct tectonic evolution (Passchier and Trouw 2005).

Apart from the fast processes that relate for example to catastrophic landslides, meteoritic impacts and seismic faulting, most tectonic processes take millions of years to develop (Price and Cosgrove 1990). Hence their characteristics prevent attempts to monitor the phenomena directly, so that many scientific studies base on hypotheses that must be tested. When laboratory models are used to reproduce such processes, model structures can be directly observed as they develop and be studied to gain important insights (Pollard and Fletcher 2005). By running scale models of tectonic events, one can separate the physically possible from the physically impossible hypotheses and the former can be studied in detail to illustrate tectonic processes to an extent not otherwise achievable (Ramberg 1967*a*). Physical or analogue models can be used to investigate the influence of different parameters on geological processes (Schellart 2002). Thus through physical modelling we can obtain valuable knowledge of how physical conditions such as stress fields, boundary conditions, temperature or physical properties of the deforming material, relate to deformation. It offers the opportunity to study 3-D structural evolution of a specific model, thus supplying a clear coherent kinematic picture that can help with the interpretation of natural prototypes. Analogue modelling requires some pre-set boundary conditions to define the context of a problem and selection of general boundary conditions requires among others, an understanding of the field observations that serve to characterise the structures (Pollard and Fletcher 2005).

1.2 Overview of study area

The study covers the Rwenzori Mountains that lie within a section of the Albertine Rift, which is the northern most segment of the western branch of the East African Rift System (EARS). The branch is located within latitudes 3°N and 5°S (Fig. 1.1) and runs over a distance of 2100km from L. Albert in the north to L. Malawi in the south. Although rifts are known to develop in different deformational environments, the EARS was formed within an extensional environment and evolved through a number of rifting episodes, the earliest of which occurred about 30Ma ago. The Albertine rift segment consists of basins that turn progressively in trend from NNE-SSW to N-S and host the lakes Albert, Edward, George, Kivu and Tanganyika (Fig. 1.1). This segment forms a section of the rift approximately between latitudes $1°0'$N and $0°30'$S. The basins lie at different elevations i.e. L. Albert's rift floor lies at 618m with shoulder elevations of 2200m (west) and about 1300m (east), L. Edward at 200m with shoulder elevations at 2300m (west) and 1600m (east) and L. Kivu at 1420m with shoulder elevations at 3000m (Chorowicz 2005; Ebinger 1989*a*). The L. Albert rift lies parallel to the NNE-SSW striking basement complex, its northern continuation beyond the Albert basin having been deflected eastwards around the resistant West Nile Craton (part of Congo craton). Faulting further north of the L. Albert rift terminates at the NW-SE trending Aswa shear zone (Schlueter 1997).

Between the Albert and Edward-George lake basins lies the Rwenzori horst (Fig. 1.1). It is uplifted about 5111m a.s.l. at its highest peak (Schlueter 1997) and is surrounded by

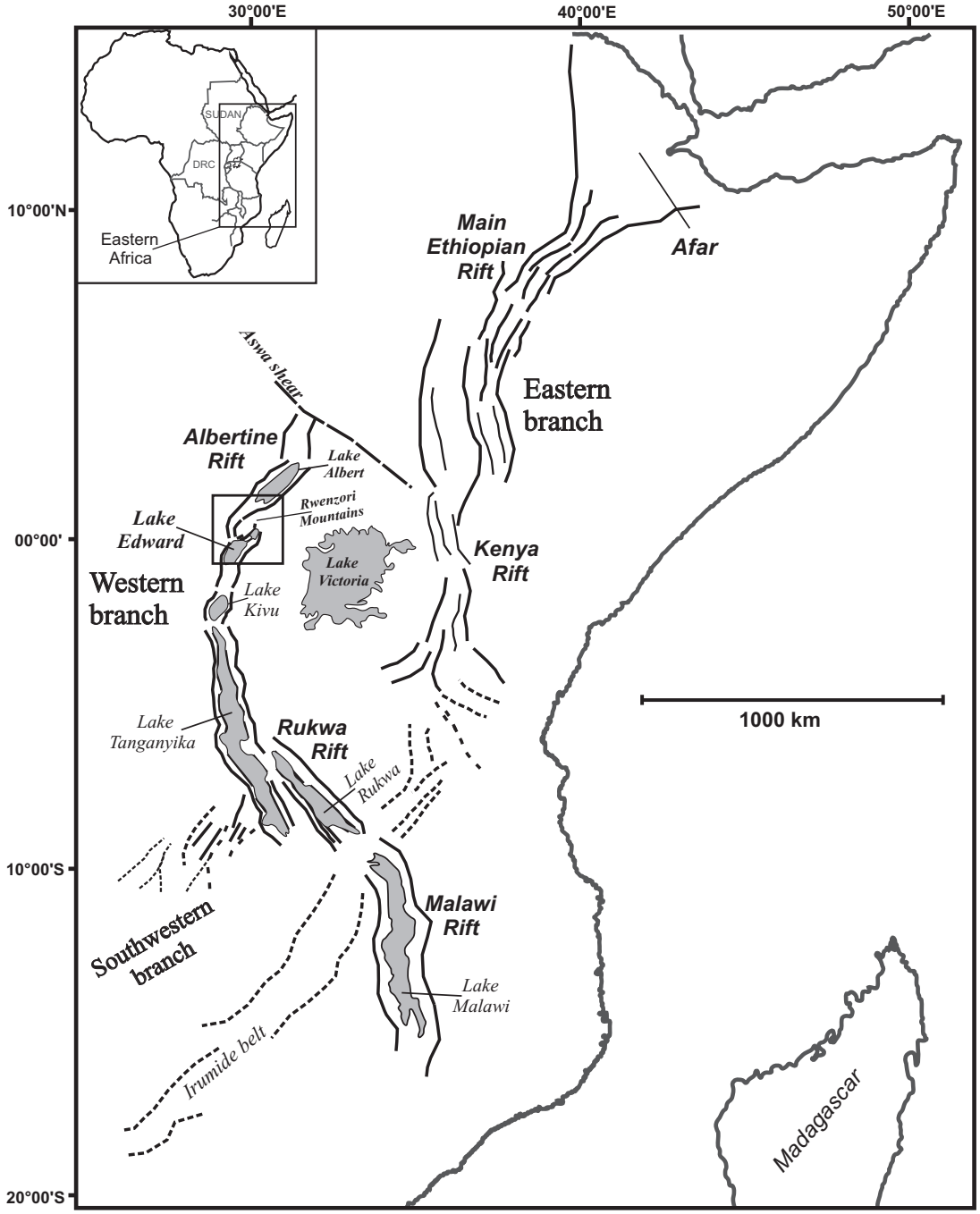

Fig. 1.1 General outline of the East African Rift System. The Rwenzori-horst lies in the western branch within a section (indicated by the square) of the Albertine Rift System, which terminates at the Aswa shear zone in the north. Note the change in trend of the rift from NE-SW around the L. Albert to nearly N-S around L. Edward.

the L. Albert-Semliki valley rift to the north and west. The Semliki basin is bounded by normal faults that dip N60°-80°W (Ebinger 1989*b*) along the western side of the Rwenzoris and by a faulted monocline at its northwestern margin. To the south and southeast, it is bounded by the L. Edward-George rift. Faults of the L. George basin with large throws and triangular scarps bound the eastern margin of the Rwenzoris. The Edward basin is itself bordered on the southeastern side by high-angle en-echelon normal faults with

minor throws (Ebinger 1989*b*). McConnell (1959) described the south and southeastern margins of this massif to be fading via a range of foothills into the down-thrown rifts of L. Edward and L. George. The Rwenzori horst is bordered by range-parallel NE-SW striking, rectilinear high angle normal faults (Fig. 1.2) namely: Ruimi-Wasa (RW), Bwamba (BW), Nyamwamba fault or ductile shear (Ny), Ibimbo Fault (IB), Kisomoro fault (KI) and the George fault (GF). The major border faults were reported to exhibit displacements greater than 6km (Ring 2008).

Smaller scale NE-SW striking faults were observed within the range together with transsection NW-SE to N-S striking faults. In places, ENE-WSW to SSE-WNW trends were also manifest. The minor faults were reported to exhibit smaller offsets of about 2km (Ring 2008). They have been observed from cross-cutting relationships (Koehn et al. 2010) and from analogue study, to be younger than the range-parallel faults. Lineations on such planes indicated normal, thrust and strike-slip displacements. Some exhibited oblique components suggesting rejuvenation of movement along pre-existing planes. The observed fault systems were comparable to the structural pattern in the Main Ethiopian Rift (MER), where a system of NE-SW striking border faults formed during the first rift-evolution phase and a later system of N-S to NNE-SSW striking sigmoidal overlapping, right-stepping en-echelon fault segments that accommodate about 80% of the present day strain (Corti 2008*b*,*a*). The lithologic units comprising Rwenzori rocks are mainly granitic and amphibolitic gneisses, schists and massive quartzites (McConnell 1959; Link et al. 2010; Nagudi et al. in preparation). Cenozoic detrital sediments that represent fluvio-glacial deposits are found in the valleys (Bauer et al. 2010).

1.3 Insights from previous work

The Western Rift like the rest of the EARS, is segmented along its axis into approximately 100km long asymmetric basins due to an interplay of at least three factors (McConnell 1972; Ebinger et al. 1993a; Shudofsky 1985; Ebinger 1989*b*). One factor is the response of old, cold continental lithosphere to the rifting process. Secondly, changing stress orientations during discrete rifting episodes. Third is the effect of along axis propagation of rifting, coupled with re-activation of pre-existing crustal shear zones. Transfer faults of the western rift accommodate large differences in elevation between adjoining basins and their uplifted flanks, as well as regional variations in relief related to the 1,300km-wide East African Plateau (Ebinger 1989*b*). Hence half-grabens are commonly separated along the length of the rift valley by horsts or sills. Ranalli (2000) demonstrated that crustal heterogeneities like pre-existing shear zones or faults present mechanical weaknesses in the crust. For instance, the deflection of the western rift from a N-S to a NW-SE orientation between lakes Tanganyika, Rukwa and Malawi (see Fig. 1.1) follows the Ubendian (2100-1800Ma) with about 140° striking ductile metamorphic fabric and domains of the Kibaran and post-Kibaran orogeny (1400-900Ma) that form N to NNE trending zones of ductile deformation (Morley 1995*a*). Several segments of the EARS also follow trends of Karoo basins, which most commonly trend NW-SE or NE-SW and less commonly N-S or W-E (Daly et al. 1989).

The Rwenzoris were generally built upon three major structural trends. The mainly folded Archean (older than 2500Ma) rocks form most of the Rwenzori block itself and the surroundings while the ENE-WSW to W-E trending rocks of the Paleoproterozoic Ubendian Belt mainly to the east, unconformably overlie the Archean rocks and transect the south-

ern part of the Rwenzori block. The NW-SE and NE-SW trending structural domains of the Mesoproterozoic Karagwe-Ankole Belt (KAB) on the other hand are found in the south. Rocks of both the Paleoproterozoic Ubendian and Mesoproterozoic Kibaran belts in this region are strongly deformed with polyphase faults and ductile shear zones. As such, they must have had a profound effect on the younger deformational episodes including rift formation and evolution, during which the Rwenzori massif developed. Pickford et al. (1993) reported that the emergence of this horst during a period of increased uplift in Late Pliocene-Pleistocene caused drainage reversals and ponding of small interrupted rivers into shallow lakes in the central uplifted plateau between the Western rift and the Kenya rift.

Range-parallel faults striking NE-SW to NNE-SSW are dominant from south to centre and in the northern part of the horst but towards the northern tip of L. George rift where a small valley with young rift sediments cuts into the range, steeply dipping NW-SE striking faults become dominant whereas range parallel faults lessen (Koehn et al. 2010). Johnson and McConnell (1951) suggested that steeply dipping faults in the northern ridge were caused by the necessity for relief from stresses due to differential uplift and cannot be regarded as primarily due to either compression or tension. However, evidence indicates that compression reigned during earlier stages and extension during the latest stages of movement. The high Rwenzoris within the basement show mainly steep NNW-SSE, NNE-SSW striking faults and a set of moderately southward-dipping W-E striking faults without range parallel ones. Together with variously trending late dyke networks cutting across the block, these trends correlate well with those of the surrounding mobile belts. Fault-slip data may indicate a change in the extension direction from ENE or East to SE, the latter direction being in accord with earthquake focal data and borehole break-outs (Ring 2008). However, block rotations and rift interactions in the Rwenzori area may also produce local stress fields that change in orientation through time (Koehn et al. 2008).

From kinematics, Chorowicz (2005) suggested that the EARS formed due to southeastward relative divergent drifting of the not yet well individualised Somalian plate. Chorowicz argued that this caused splitting of the continent along lines of pre-existing lithospheric weaknesses marked by ancient tectonic patterns that focused the extensional strain. Formal inversion of focal mechanism data of the entire EARS (Delvaux and Barth 2010) revealed a general W-E extension direction all over East Africa, with two dominant extensional stress regimes. One regime with a WNW-ESE oriented minimum horizontal principle stress $S_{(Hmin)}$ characterises the northeast segments (Main Ethiopian-, Albertine- and Kivu rifts) and the southwestern high plateau region (Luangwa, Mweru and Upemba grabens). The other with ENE-WSW $S_{(Hmin)}$-direction dominates the southernmost rift segment (Malawi and Central Mozambique rifts), the continental margin (Indian coast, Mozambique channel and Madagascar) and the central part of the Western Rift (South Tanganyika and Rukwa).

Basement control has been observed at different parts of the East African rift and it is interpreted as following pre-existing boundaries (Tiercelin et al. 1988; Chorowicz 1989, 1992; Lenoir et al. 1994; Theunissen et al. 1996; Ring et al. 2002). Around the Albertine Rift for instance, the Rwenzori block lies in the transition from the Rwenzori fold belt to the Karagwe-Ankole belt. It is also a structural node where the rift changes trend from a NNE-SSW strike of the L. Kivu-L. Edward stretch to the more NE-SW strike of L. Albert rift (McConnell 1959) and where the W-E striking Buganda-Toro system meets the western rift. The westward deflection of the rift valley around this node is said to be due to failure of the L. George rift to breach the Buganda-Toro units (Schlueter 1997). The Wasa fault that defines the eastern side of the northern Rwenzoris, stops at the Rwenzori

fold belt and reappears at the southern end of the Rwenzoris in the (Nyamwamba) ductile transcurrent dextral shear zone (Schlueter 1997), or in the Ibimbo fault (Koehn et al. 2010).

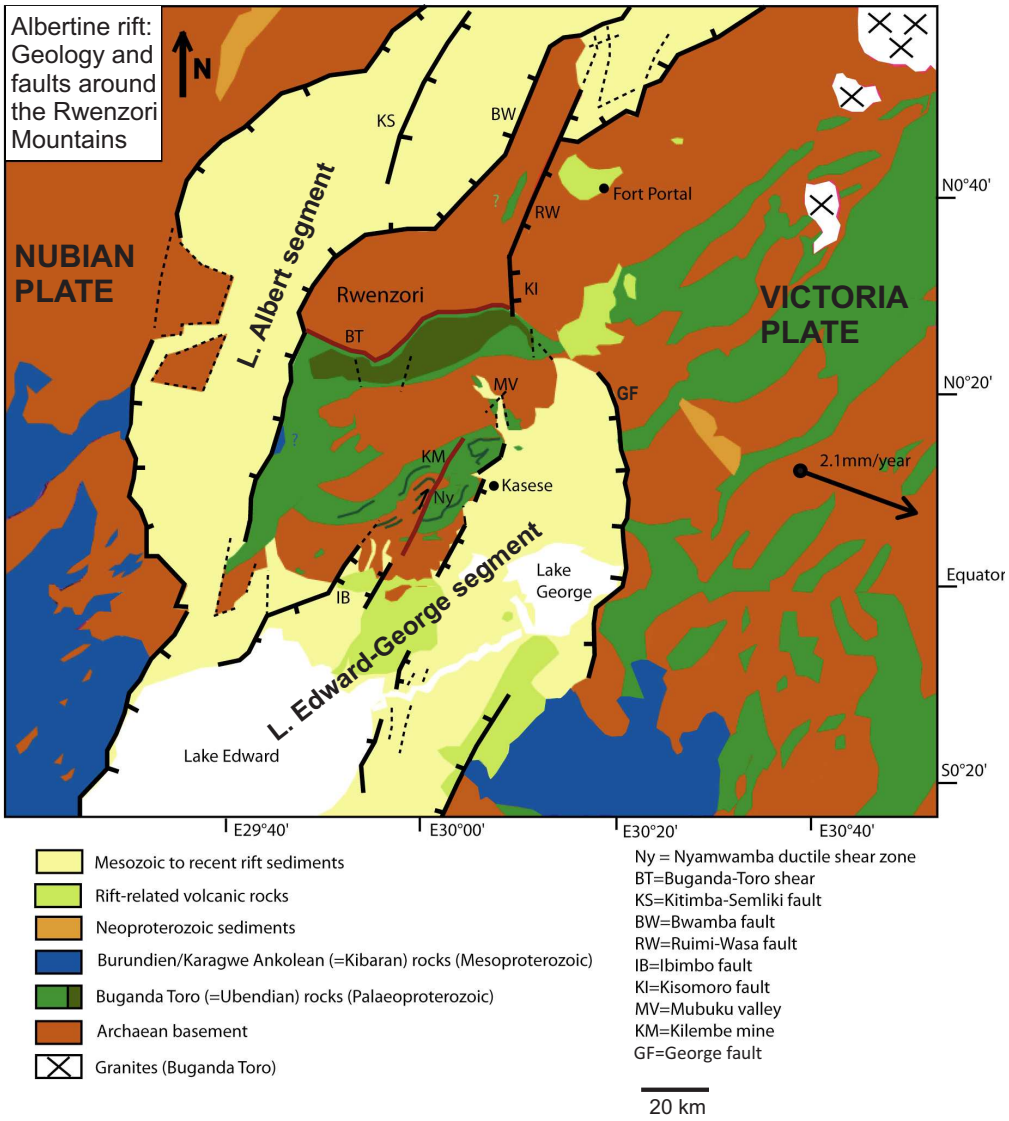

Fig. 1.2 Location of the study area within a section of the Albertine Rift separating the Victoria microplate from the Nubian plate. The map shows basement geology, the Rwenzori horst between the Albert and Edward-George segments and major faults that delimit the rift and bound the horst. Modified after Koehn et al. (2010).

Lenoir et al. (1994) observed that re-activation of the Tanzanian Ubendian belt during the Neoproterozoic Pan-African event (about 750Ma) produced sinistral brittle-ductile shear zones. The zones later became the preferential locus for the brittle rift faults during development of the western branch of the EAR. However, Ebinger (1989*b*) observed that along-axis segmentation is generally not inherited but rather a result of north- and southward along-axis propagation of rift border-fault segments, thereby linking originally isolated basins. Ebinger also noticed places in the western rift where border faults did not seem to cut cratonic basement, so that border and transfer faults were often poorly correlated with pre-rift structures. For instance, in the Kivu-Rusizi rift south of L. Ed-

ward, the orientations of Miocene-Recent dip-slip and oblique-slip faults showed little correlation with Precambrian shear zones or foliations in metamorphic basement (Ebinger 1989*a*). Basement blocks that are present within the Buganda-Toro mobile belt and some syn- to late-orogenic granites that crop-out towards the northeast (Nagudi et al. 2003) may suggest that this mobile belt represents the suture between the Congo and Tanzania cratons (Koehn et al. 2010).

1.4 Overview of this work

This study was geared at finding out the implications of fault distribution and kinematics for the rift-flank uplift around the Rwenzori mountains. As such, the study targeted the area around the L. Albert and L. Edward-George subsegments. The field study area and subject of discussion are delimited by latitudes $1°0'$N and $0°30'$S and longitudes $29°30'$E and $30°30'$E. Structural measurements were taken mainly on the Ugandan side of the rift. Hence the rift continuation northward beyond the L. Albert rift and southward beyond the L. Edward rift is outside the scope of this report.

The work was done in connection with project B1 of research unit *"Rift dynamics, uplift and climate change in equatorial Africa: Interdisciplinary research linking Asthenosphere, Lithosphere, Biosphere and Atmosphere"* (*www.riftlink.de*). The aim for this research unit was to address the underlying cause(s) of rift-flank uplift in the EAR since late Miocene, its impact on climate change in Equatorial Africa and the possible consequences for the evolution of Hominids. The immediate objective was to gain a process understanding of rift-flank uplift by investigating the origin of the more than 5000m high Rwenzori mountains. The various themes covered studies on seismicity, petrology, low-temperature thermo-chronology, structural geology, geomorphology, sedimentology, palaeontology, climatology and numerical modelling. Project B1 *"Structural expression of extreme rift-flank uplift"* under whose auspices this study was carried out, involved interpretation of satellite images, numerical modelling of fault patterns and fault growth, kinematic analysis of faults and dating of clay-rich fault gauge.

In order to determine the stress field regimes responsible for development of the faults, attitudes of faults and lineations were measured and sense of slip was inferred from striations. The stress inversion via simulation approach (Sippel et al. 2009) was used to estimate paleostresses from smaller-scale faults. Such faults are said to be of detailed scale with spatial wavelength of 1-100 km. They are believed to express 3^{rd}-order stress patterns that result from local density and strength contrasts, basin geometry, basal detachment, topography or active faulting (Heidbach et al. 2010). Observed cross-cutting relationships in the field suggested that the faults formed in response to more than one stress-state. Thus our data did comply with the requirement that fault orientations vary, although they may not reflect the exact fault distribution in the right proportions as they exist in the field, due to inevitable sampling bias. Inverse methods incorporate a number of assumptions (e.g. coaxial deformation, homogeneous stresses, fault-slip unaccompanied by plastic deformation) most of which are violated in the natural realm. However, it has been demonstrated and proven that they estimate quite reliable paleostress tensors at least on local scale (Xu 2004; Townend 2006; Sippel et al. 2009; Delvaux and Barth 2010). The data were analysed in four "tectonic units" namely:

(1) Sempaya-Kazingo (SK) covering the northern part,

(2) Central-Rwenzoris (RWZ) covering the peaks,

(3) Kigolo-Kabakoru (KK) in the east central part, and

(4) Kilembe-Nyabirongo-L.George flank (KNG) covering the south and southeastern parts.

Outcrops constituting the different units were thought to have sustained comparable local disturbances on stress fields, arising from the large-scale fault zones in their immediate vicinity. Therefore, they suffered relatively similar conditions of deformation (Sperner and Zweigel 2010). Where the geometry and number of complete data sets allowed, analyses were carried out for individual outcrops too. For purposes of clarity in the discussion, each stress field specified by any one of the fault-subsets in a tectonic unit, was referred to as a 'stress-state'. However, stress-states that showed similar attributes but were specified by fault-subsets from different tectonic units, were considered to represent a more regional stress field, referred to in the discussion as a 'stress regime'.

Sandbox analogue models were used in an attempt to constrain the conditions under which the Rwenzoris were formed by replicating the rifting process. It has been demonstrated that faults change orientation due to a deflection of the local stress field as a result of rigid body rotation (Brun 1999). Although rotation of the Rwenzori block has not yet been formally demonstrated, numerical models (Koehn et al. 2010) suggest a clockwise rotation as a captured micro-plate between two approaching oppositely propagating rift segments. Thus the sandbox analogue experiments were designed to model an expected clockwise rotation during extension. The models took into account the relative vertical and horizontal components of deformation along faults but they were not intended to reproduce the anomalously high uplift of the Rwenzori block.
By integrating results generated from the various objectives of this study, we attempted to relate how an interplay of local fault kinematics, effects of block rotation on the local stress fields and effects of temporally changing far-field stresses on fault orientation, could have resulted in development of complex stress fields that played a vital role in rift-flank or block uplift. Inferences were also made for other tectonic processes that could have contributed to the latter.

1.5 Aim and objectives

The primary aim for this study was to test the hypothesis that *'If indeed there is a major change in fault kinematics with time, then the extreme rift flank uplift around the Rwenzoris is not simply controlled by movements along the major boundary faults but is a result of interplay of several tectonic processes that alter the stress field regimes to effect kinematic changes'.* To reach our aim, the study was carried out in line with the following specific objectives:

(1) Mapping out the different fault patterns in the field and studying their kinematics so as to workout and understand the stress field regimes responsible for their development.

(2) Attempting to incorporate other processes that could have participated in enhancing the high rift-flank uplift.

(3) Carrying out microstructural thin-section study on some rock samples, so as to gain insight into the deformational phases recorded in the rocks.

(4) Simulating the rifting process using sandbox analogue experiments in order to replicate the faults and constrain the conditions under which the Rwenzoris developed.

(5) Studying fault development and growth during the simulation process; right from nucleation through the processes involved in propagation, so as to understand the role of the faults in the uplift process.

In line with the first objective, dynamic and kinematic analyses of the field data were carried out. We observed the argument that younger slip-fibres that form during later slip increments may erase older lineations so that slickensides on faults with single lineations only record movement direction for the last deformational increment in which that fault was active (Wojtal and Pershing 1991; Fossen 2010). It was thus anticipated that analysis of fault-slip data would provide among others, the presently active stresses in the Rwenzori region especially where reactivation obtains. Therefore all paleostress tensors of stress-states responsible for slip observed on the measured faults in the specified section of the rift were determined. Since local tectonic stress may be quite variable with respect to orientation (Zoback 1992a; Fossen 2010), this analytical study was intended to answer some related questions raised with regard to the state of stresses in the area. The target was to find out:

(a) If, and how local stresses in the study area varied.

(b) The most likely causes of local stress variation (if any).

(c) Whether or not, the entire study area was deformed in similar fashion under the same stress regimes.

(d) What stresses are presently active in the area and how they compare with the regional tectonic stresses.

(e) How the local stresses compare with those reported for other segments of the rift.

In the physical models, basal sheet geometry below the sand-pack was intended to mimic pre-existing heterogeneities in the crust. We modelled an expected clockwise rotation proposed by numerical models (Koehn et al. 2010), taking into account relative vertical and horizontal components of deformation along faults. However, the high uplift of the Rwenzoris was not simulated. Growth and development of rifts and fault patterns were studied as a function of the geometry, orientation and location of zones of weakness and was compared with that of the natural prototype. The analogues were intended to test the following:

(a) Whether or not fault patterns were controlled entirely by mechanical strength anisotropy of a pre-structured crust during extension.

(b) If change in fault orientation and kinematics caused block rotation or vice versa.

(c) If the extent of rift overstep played a decisive role in determining whether or not a horst block was captured or a transition zone developed between rift segments.

1.6 Structure of the thesis

The contents of this thesis are organised in the proceeding chapters as follows: The regional geology, tectonics and history of evolution of the East African Rift System are reviewed in chapter 2. The first part of chapter 3 contains a general review of the basic concepts and theories that explain faulting and rifting mechanisms, including those invoked by the techniques used in fault-slip analysis or referred to in the interpretation and discussion of ensuing results. The second part explains the methods employed at the different stages of this study and some illustrations of certain concepts involved. Results and discussion of the field study, geometrical data analysis and microtectonic thin-section study are presented in different sections of chapter 4, but the raw field data are presented in Appendix B. Graphical results and discussion of kinematic and dynamic analysis of faults are presented in chapter 5, however, numerical results calculated by each of the two methods are respectively presented in Appendices C and D. The results and discussion ensuing from sandbox analogue modelling on the other hand, are presented in chapter 6. Lastly, the final discussion and conclusions, including remarks on shortcomings of the methods employed in this study are presented in chapter 7.

Note that parts of chapter 2, chapter 3 and the bigger part of chapter 6 are published (Aanyu and Koehn 2011) in the Journal of African Earth Sciences 59 (2011) 168-184, under the title 'Influence of pre-existing fabrics on fault kinematics and rift geometry of interacting segments: Analogue models based on the Albertine Rift (Uganda), Western Branch-East African Rift System' (DOI:10.1016/j.jafrearsci.2010.10.003).

Chapter 2

Regional Geology and Tectonics

In this chapter the tectonic framework, regional geology of the study area and a time-constrained summary of the evolutionary history of the East African Rift System are reviewed.

2.1 Regional geology: a review

The study area is located in a region that, prior to rifting, was affected by at least four orogenic events described below. Signatures of the events are expressed by belts of rock with characteristics typical for the deformation style of the respective orogeny. The local geology of the study area can be seen in Fig. 1.2 on page 6, whereas the general geology of Uganda is shown in Fig. 2.1. Note the concentration of mountain peaks that define the Rwenzori horst and the Tertiary and Pleistocene volcanics located near the eastern and southern rims of the horst in Fig. 2.1. The old cratons and orogenic belts of the East African region are shown in Fig. 2.2.

Archean events

The Archean basement that is composed mainly of granitised formations, suffered a protracted period of tectonic activity superposed on old cratonic blocks and spanning the period 3000Ma to 2500Ma. In the study area, these rocks form the Archean gneissic granulitic complex (Fig. 2.1) constituting the oldest rock formations that stratigraphically underlie younger cover formations. From the work of Hepworth and MacDonald (1966), these rocks have been divided into four groups. Each group represents a different tectonic phase namely in sequence from the oldest to the youngest;

(i) Watian event dated about 2900Ma by Leggo (1974) and is characterised by retrogressive granulite-facies metamorphism, relatively simple folding upon W-E trending axes and presence of dykes that mark the time break between itself and the younger Aruan event,

(ii) Aruan event dated at 2600Ma by Leggo (1974), and characterised by folds plunging gently to the NNE with steep axial planes,

(iii) Mirian event, undated but observed in the northern and western parts of west Nile to post-date the Aruan event. It is characterised by approximately NE-trending recumbent isoclinal folds that are overturned northwest-ward,

(iv) Chuan or Aswa - the latest event characterised by a NW axial-fold trend that passes locally into mylonitic zones.

The rocks of the Nyanzian-Kavirondian system affiliated to the Nyanzian type-area in Kenya also date between 3000 and 2400Ma. They record an early N-S compressional phase that caused folding along W-E trending axes gently plunging about 30° east-ward, which may be related to the pattern of thrust faulting. Subsequent folding along NE and SE trending axes is related to far-field effects of the Pan-African event. In Uganda these rocks occur in the southeastern part at the edge of Lake Victoria and cover only about $1000km^2$. They are comprised of dominantly volcanic rocks of basic composition and poorly sorted sediments that form greenstone belts.

The Ubendian orogeny

The Paleoproterozoic Ubendian orogeny occurred between 2100 and 1800Ma. This produced high-grade metamorphic lithologies during its two deformational phases. The early (more regional) deformational phase marked by a W-E to WNW-ESE foliation and granulite facies metamorphism, is isotopically dated at 2100-2025Ma. It is interpreted as a product of collisional orogeny along the southwestern margin of the Tanzania and Congo cratons. The younger deformational phase was dated at 1950-1850Ma in the Ubende belt of western Tanzania (Theunissen et al. 1996). It was characterised by large NW-SE trending dextral shear zones and was restricted to the Ubendian belt. This resulted from a northward compressional stress regime. This regime caused north-ward directed thrusting of rocks of the Usagaran belt (Lenoir et al. 1994) immediately south of Tanzania Craton and intrusion of late- to post-kinematic calc-alkaline granitic batholiths dated about 1860Ma. Hence the upper time limit for the second event is placed at about 1860Ma, although a phase of tectonic reactivation occurred locally at about 1725Ma (Lenoir et al. 1994).

In Uganda, rocks of Ubendian age form the most extensive of the cover formations. They are predominantly argillaceous with some gneisses but with quartzites at or near the base of the system (basal quartzites), which are thickest around the Rwenzoris and thin towards the east. They are represented by the Buganda-Toro system which includes the Buganda-Toro supergroups and their equivalent on the Rwenzori mountains is the Rwenzori fold belt. The Buganda-Toro system has a simple structure to the east, which becomes more complex towards the west (Kilembe) in the Rwenzori fold belt. The latter commonly exhibits isoclinal folding on steeply plunging axial planes and its north-ward thrusted rocks transect the Rwenzoris. Metamorphism is also seen to increase in the same direction. Structures in the Rwenzori fold belt and elsewhere in the Buganda-Toro system persistently trend W-E to NE-SW. This, coupled with the presence of Ubendian age rocks that are thrusted north-ward against a resistant Speak gneiss on the Rwenzori mountains, are evidence that the rocks of Ubendian age in Uganda can be associated with effects of both the first and second phases of this orogeny.

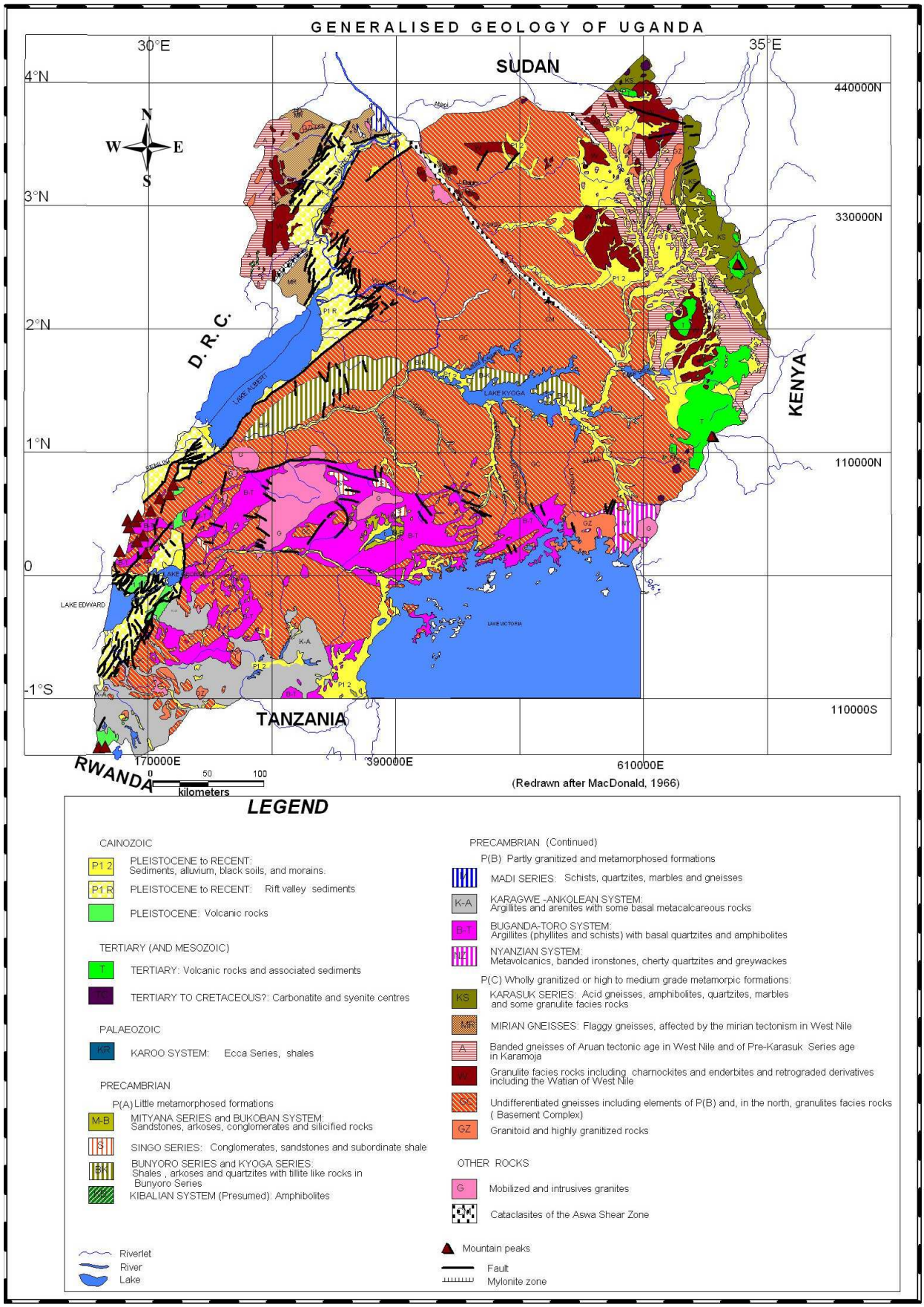

Fig. 2.1 Geology of Uganda. (Map source: Department of Geological Survey and Mines (DGSM), Entebbe-Uganda.)

The Kibaran orogeny

The Mesoproterozoic Kibaran orogeny, was a short-lived but prominent tectono-magmatic event dated about 1375Ma. Its rocks form two belts namely (1) the Karagwe-Ankole belt (KAB) northeast of the Ubende belt-Rusizian basement extension and east of the western rift, and (2) the Kibara belt (KIB) which is the domain occurring southwest of the Ubende belt-Rusizian basement extension (Tack et al. 2010). It is indicative of intracratonic regional-scale emplacement under an extensional stress regime. The mantle-derived magmas penetrated a zone of weakness at the rheological boundary between the domain of the Archean Tanzania Craton and that of the adjacent Paleoproterozoic basement (2100Ma mobile belt) to the left. Both domains were overlain by Mesoproterozoic (meta)sedimentary rocks. The rocks of these belts are mostly meta-sedimentary with minor meta-volcanics, intruded by voluminous S-type granitoids and subordinate mafic bodies of Mesoproterozoic age. The KAB has a northeasterly trend similar to that of the KIB but it swings to a NW trend near Lake Kivu. The belt is characterised by intrusion of syn-deformational S-type granitoids at different times (Klerkx et al. 1987). Tack et al. (1994) defined two contrasting domains of the KAB, the Western Domain (WD) and the Eastern Domain (ED). The ED is devoid of S-type granitoid rocks and of Sn-Nb-Ta-W and Au mineralisation.

In Uganda, the KAB unconformably overlies the Paleoproterozoic rocks of Buganda-Toro system in the Southwest. The KAB is characterised by predominantly Regional folds with NW-SE trending fold axes and Cross folds whose axes trend NE-SW. The latter are observed in certain places to predate the former. In some places however, the two trends appear to be contemporaneous and generally the major folds form syclinoria and anticlinoria. Typical of the eastern domain of the KAB which Tack et al. (1994) described as being characterised by the fading away towards the east of both deformation and metamorphism, structural complexity and metamorphic grade of the Karagwe-Ankole rocks gradually increases westward. The rocks are generally intruded by S-type granites of different ages named from oldest to youngest as G1, G2, G3 and G4. The G1 and G2 granites are constrained to this event by their ages. The G1 granites (e.g. Ntungamo, Kamwezi, and Lugalama) are early-orogenic, pre-D1 and show ages around 1330Ma. The G2 granites (e.g. Masha and Akabeeba) on the other hand are syn-orogenic, syn- D1, formed under tensional stress and show ages between 1280-1260Ma. Tack et al. (2010) argue that based on the intra-cratonic (intra-plate) nature of the KAB and KIB, compressional deformation post-dating the Kibaran event, including folding and thrusting within both belts must reflect far field effects of global orogenic events. Thus the younger granites are assigned to the post-Kibaran event.

The post-Kibaran orogeny

A post-Kibaran event was characterised by intrusion of later S-type granites, and A-type granitoid rocks emplaced very locally in the western domain of the KAB at about 1205Ma, followed by tin granites (e.g. at about 986Ma) which gave rise to the Sn-metallogenic province overprinting large areas of both the KAB and KIB (Tack et al. 2010). This time of occurrence of compressional deformation reflecting far-field effects of global orogenic events external to the craton, is also consistent with the proposed time-frame for Rodinia amalgamation at about 1000Ma. They also stated that the G3 granites were S-type, syn-orogenic, syn-D2, formed under compressional stress and showed ages around 1180Ma

whereas G4 granites are A-type, syn-orogenic, syn-D2, but formed under transpression. According to Klerkx et al. (1987) G4 granites give whole-rock Rb-Sr ages of 1125 ± 25Ma (Bukirasazi granite).

In Uganda, some major and minor NW-SE and NE-SW striking faults hosted by the KAB rocks appear to post-date the Kibaran orogeny and may thus belong to this later phase. The G3 granites in western Uganda (e.g. Rubanda, Kamwenge, and Chitwe) show ages around 1180Ma, Chitwe granite in particular dating 1198 ± 47Ma. The G4 granites (e.g. Dwata, Ibanda, and Rwabaramira) show ages around 976 ± 13Ma and are characteristically peraluminous tin granites invaded by pegmatitic and quartz veins that host Tn, W and Nb/Ta mineralisation (Schlueter (1997) and references therein). It is therefore clear that both the WD and ED of the KAB are present in western Uganda.

The Pan-African orogeny

A Neoproterozoic Pan-African orogeny occurred approximately between 725 and 500Ma and comprised of two phases. The early Pan-African phase dated about 725Ma was characterised by W-E compression. The second phase was correlated with the thermal effect dated about 500Ma by Rb-Sr and K-Ar analyses on minerals. This phase corresponds to the late effects of the nearby Pan-African belts including the Mozambiquian belt, Lufilian arc and Zambezi belt (Lenoir et al. 1994). Indeed rocks of the Nyanzian-Kavirondian system that were initially folded along W-E trending axes, are said to have been re-folded along SE- and NE- trending axes due to W-E compression of the Mozambiquian orogeny. The NW-trending Aswa shear or fault zone which is composed of a pattern of en-echelon faults and at which the Albertine segment of the western branch of the East African Rift terminates in the north, is thought to have been important during the Mozambiquian orogeny. The Aswa possibly corresponds to a lateral thrust ramp of this age, accommodating left-lateral transpressional deformation and later reworked by transtensional movements (Chorowicz 1989).

2.2 Rift evolution: a review

The timing of inception and subsequent evolution of segments of the EARS have been constrained in the work of various researchers. Ages have been determined by examining tectonic relationships between the various fault systems and their host volcanic and/or sedimentary units, which have consequently been petrologically and radiometrically analysed.

Rifting Phase-I

The first manifestation of open fractures in the Afar and Ethiopian plateau was placed around 30Ma (Hoffman et al. 1997; Mège and Korme 2004). Chorowicz et al. (1998) noted that during the same time, three convergent graben structures nucleated at Lake Tana, forming a triple junction. Between 29.9 and 28.7Ma, rifting initiated in the Gulf of Aden and in the southernmost part of the Red Sea between 27.5 and 23.0Ma (Hughes et al. 1991). The Afar depression probably formed later in the Miocene (Chorowicz 2005).

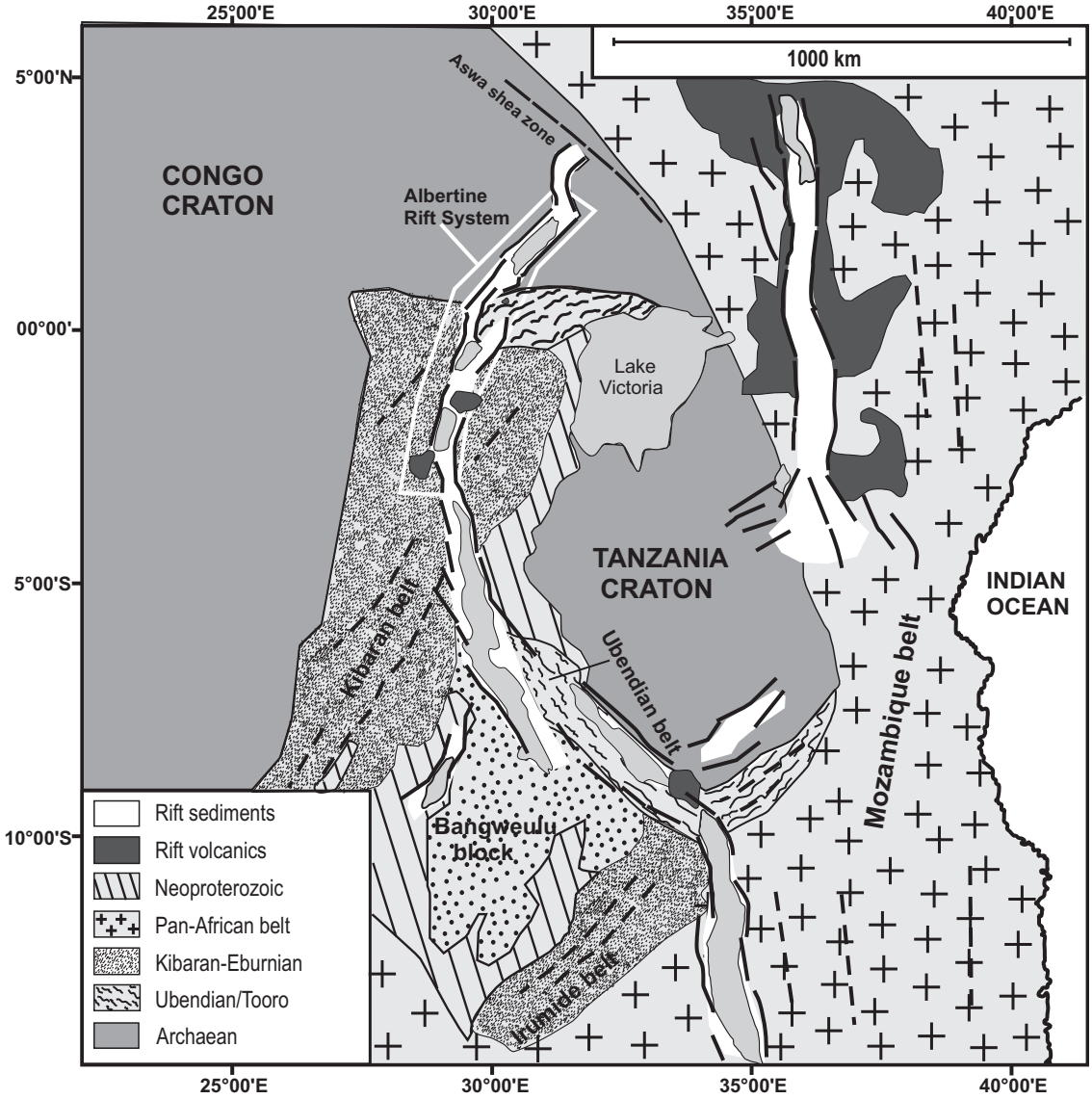

Fig. 2.2 Relative location of Archaean cratons and mobile belts constituting the basement structure of East Africa prior to rift development. The white rectangular box encloses the Albertine Rift System. The Cenozoic rift is outlined by black lines at the borders of white areas that are marked as containing rift sediments. Modified after Link et al. (2010).

Shackleton (1978) postulated that prior to rifting in the now Gregory rift, there was uplift in central Kenya and corresponding subsidence in the now Turkana basin in late Cretaceous. This resulted in development of a monocline flexure to the west now represented by the Uganda escarpment and the Turkwell fault (Baker and Wohlenberg 1971). This was followed in Oligocene around 33–29Ma by extensive basalt eruptions in the Turkana basin constituting the earliest volcanic activity and nephelinitic volcanism along the up-warped Uganda escarpment in mid-Tertiary around Miocene (Bellieni et al. 1981). Volcanism appeared further south at the now triple junction between the northern Kenyan, Central Kenyan and Nyanza rifts at about 20Ma (Pickford 1982; Fitch et al. 1985) concurrently as in the Lotikipi Plain further North (Morley et al. 1992). Major faults developed and propagated between 16 and 14Ma to connect the central and northern parts of the Gregory rift (Kampunzu and Mohr 1991; Smith and Mosley 1993).

Rifting Phase-II

The second major phase of faulting occurred in late Miocene-Pliocene at about 7-4Ma (Kampunzu and Mohr 1991; Strecker et al. 1990), including development of the west-dipping Sattima fault which produced the Aberdare Range of the Kenya rift. The Elgeyo escarpment initiated between 14 and 6.2Ma (Baker and Wohlenberg 1971) and the Nguruman fault being active at 12-7Ma (Bosworth et al. 1992). The third phase in Late Pliocene-Pleistocene initiated intense rifting on the floor of the already distinct inner rift and continued uplift on rift shoulders to produce the graben structures present today (Schlueter 1997). Meanwhile faulting in the Main Ethiopian Rift (MER) connecting the nucleated northernmost Afar domain to the Turkana basin which forms the northern limit of the Gregory Rift in northern Kenya, commenced after 11Ma (Wolfenden et al. 2004). Faulting in this part commenced later than the basaltic volcanic eruptions around the Turkana basin which occurred till early Miocene (Bellieni et al. 1981).

Prior to development of the western arm of the EARS, western Uganda lay at an altitude of about 500m above sea level (Schlueter 1997). However, in Mid-Miocene around 12Ma ago, a shallow down-warp initiated a basin that filled up with fluviatile and evaporite deposits named the Kisegi formation (Pickford et al. 1993). The northern part of this basin covered the now Lake Albert basin and was probably contributed to by the westward slanting of the eastern Uganda border, which was up-warped in the same period due to preceding volcanism and incipient rifting around Turkana basin. At about 12.6Ma the first lavas in the western rift erupted in the Virunga volcanic field (Bellon and Pouclet 1980), but it is unclear whether or not faulting occurred at this time. The timing for the first rifting phase in Uganda is constrained by the initial lacustrine conditions (Pickford et al. 1993), which began about 11–10Ma ago with formation of Lake Obweruka, a 550km long basin that filled the valley formed by this rifting phase. Lake Obweruka became permanent when the rate of downthrow exceeded sedimentation rates about 8 to 7Ma ago, which was when the first major rifting episode occurred. However, the rift shoulders became climatically significant at a much later time around 4Ma ago (Pickford et al. 1993).

The oldest volcanic sediments from south Kivu dated 10-8Ma and were related to a major tectonic phase (Ebinger 1989*a*). Ebinger cited an age of 5Ma for fauna in the sediments of Rusizi basin, which overlie basalts that dated about 6.5-5.0Ma. Ebinger also observed that volcanic centres dated at 7.2Ma had been subsequently displaced by border faults suggesting that the latter are even younger. In Lake Tanganyika, the central and northern basins started to subside in Middle to late Miocene respectively around 12–9Ma and 8–7Ma and the southern basin in Pliocene at about 2–4Ma (Cohen et al. 1993). In the Rungwe volcanic field further south, volcanism began at about 8.6Ma while the Malawi Rift began to subside approximately 9–8Ma ago (Ebinger 1989*a*; Ebinger et al. 1993a). Major rifting occurred in the north of Lake Malawi between 6 and 4Ma and the rift increased in length southwards (Flannery and Rosendahl 1990).

Rifting Phase-III

The period Late Pliocene-Pleistocene is proposed to have been a time of renewed uplift (Schlueter 1997) during which the Albertine rift became more compartmentalised due to the emergence of the Rwenzoris. It resulted in division of Lake Obweruka into smaller lakes around 2.6Ma ago (Pickford et al. 1993). Terraces formed by Pliocene-Pleistocene lacustrine sediments for instance in the eastern Kivu and Rusizi basins also indicate that

during this time rift basins became narrower due to increased uplift (Ebinger 1989*a*). Therefore a third phase of rift development was proposed by Pickford et al. (1993) at 14-12Ka. During this time the Beni Gap that drained the Lake Albert into the Zaire Basin was tilted north-ward and raised by 300m, thereby diverting the Albert flow north-ward into the Nile Basin. Back-tilting of the rift walls may have produced about 1000m rise in the Rwenzoris, caused drainage reversals in western Uganda and led to the formation of Lake Victoria (Schlueter (1997) and references therein). This phase initiated intense rifting on the floor of the already distinct sections of the inner rift and continued uplift on rift shoulders to produce the graben structures present today (Schlueter 1997).

Thus on local basis, rift fracturing and subsidence nucleated at different locations during the late Miocene, first in the Afar and Kenya Rift, then the Virunga and central Tanzania in late Miocene (Chorowicz 2005). From each of these places it propagated along axis to the north and south to link originally isolated basins (Ebinger 1989*b*; Chorowicz 1992). However in general, the EARS propagated southward and is still propagating in similar manner at present in areas that present zones of weakness in the lithosphere (Kebede and Kulhanek 1992). The further southward defined lines of propagation e.g. along the Limpopo suture, Lake Kariba and near Lake Mweru (Brandl 1986), are at various early stages of evolution. Hence based on precise criteria defined by Chorowicz et al. (1987), Mondeguer et al. (1989) and Hayward and Ebinger (1996), the maturity of rift segments reduces southward from *Oceanic rift stage* at the Afar, through *Advanced rift stage* in the Main Ethiopian Rift, to a *Typical rift stage* in the northern Tanganyika Rift, an *Initial rift stage* in the Malawi Rift, and a *Pre-rift stage* for example in the Limpopo area. Different extension rates were earlier suggested e.g. mean rates of 2.5cm/year (Oxburgh and Turcott 1974) and 5cm/year (Kampunzu and Mohr 1991; Kampunzu et al. 1998). However, extension rates an order of magnitude lower, have more recently been constrained from geodetic data analyses. The latter have indicated that extension rates generally decrease from 6-7mm/year in the Main Ethiopian Rift, $3 - 4mm/year$ in the Central EAR, to less than 1mm/year south of Mozambique; and that extension is directed approximately W-E (Calais et al. 2006; Stamps et al. 2008).

Chapter 3

Basic Concepts and Methods

In the first part of this chapter, the origin of intra-continental rifts is summarised, with brief mention of the models that have been used to explain their mechanisms of formation (mathematical relations excluded). It includes a simple review of theory and basic concepts of faulting and the basic theories and underlying assumptions and/or hypotheses invoked by the techniques employed in fault data analysis. Certain criteria referred to in the discussion and interpretation of results, including basics on usage and scaling of analogue experiments in modelling lithospheric extension, are also explained.

The activities involved in the study included a detailed field study of structures especially faults and taking oriented rock samples for thin-section production. Fault-slip data were measured so as to determine stress tensors of paleostresses responsible for the faults. Focal plane solutions from seismic data of the Rwenzori region were inverted to determine the the current extension directions in that region. Sandbox analogue modelling was carried out to simulate the rifting process. As indicated by Pollard and Fletcher (2005) analogue modelling requires some pre-set boundary conditions to define the context of a problem but selection of general boundary conditions requires among others, an understanding of the field observations that serve to characterise the structures. The second part of this chapter contains a brief account of the field- and microtectonic study as methodological tools, followed by a detailed description and illustration of the methods that were used in analysis of fault-slip data. Analogue modelling was a core objective for replicating faults to constrain the conditions for development of the Rwenzoris. A detailed description and illustration of the setup and scaling of the sandbox analogue experiments is presented at the end of the chapter.

3.1 Basic concepts: A review

3.1.1 Origin of intra-continental rifts

Rifting occurs when the earth's crust is stretched by plate-tectonic movements, causing faults to develop. Thus the morphology of rifts is that of a central depression (valley) flanked by two uplifted shoulders that are cut by a series of faults, which step down towards the valley. Rift basins can also form under regional compression (e.g. the Baikal rift) or tearing (e.g. the Dead Sea rift) but the main rift basins of Africa were formed in a predominantly extensional plate-tectonic setting particularly during the Tertiary-

Quarternary periods, in which time the East African Rift was formed (Frostick 2005). Seismological studies have indicated that many rifts are structurally asymmetric, with one margin higher than the other and a tilted floor that contains sediments which mask the underlying geology. The higher margin is cut by the largest faults (main border faults) while the lower one consists of a series of smaller synthetic[1] and antithetic[2] faults that fragment the geology into a series of small horst blocks with intervening valleys (Frostick 2005). Intra-continental rifts occur in ancient cratonised platforms and have a remarkably uniform width of about 50km (McConnell 1972).

The rifting process may be active or passive. In active rifting, impingement of a thermal plume or sheet on the base of the lithosphere causes convective thinning, domal uplift and crustal extension. In passive rifting tensional forces in the continental lithosphere cause thinning and passive up-welling of hot asthenosphere (Allen and Allen 1990). The heating effect of the hot mantle plume reaches the overlying lithosphere mainly by convection (conduction and magma generation and migration are also possible but unimportant). The location and magnitude of faulting is controlled by the thickness and character of the affected crust and by the presence of favourably oriented pre-existing weakness lines exploitable by new faults (Frostick 2005). However, fracture systems of such magnitude as the EAR cannot be simply due to pre-existing structures in the basement, but must have formed in response to a definite stress pattern (McConnell 1972). Such stresses result for instance from uplift that imparts excess potential energy to the elevated region or from disturbance of the isostatic equilibrium by changes in thickness of the crust and mantle lithosphere (Allen and Allen 1990).

3.1.2 Rifting mechanism

According to McConnell (1972), the fundamental mechanism for intra-continental rifting is dependent on high heat flow causing expansion, upward arching and extension. The consequent lowering of density enables the cold central strip of the arch to sink into the hotter underlying migmatitic crust e.g. in the Rhine graben. In the East African Rift for example, volcanism has been suggested to result from up-welling of mantle material along narrow dyke-like channels (Harris 1969; Jakovlev et al. 2008). The heat is derived from radioactive decay in the mantle and in a manner that is comparable to penetrative convection (Elder 1966; McConnell 1972). However, Mckenzie (1978) observed from a number of continental wells that radioactive elements involved were strongly concentrated towards the surface and that their influence on temperature distribution throughout most of the continental lithosphere was small. As already stated, two end-member mechanisms are generally agreed to generate extensional basins. In active rifting, the ascent of the asthenosphere causes convective thinning, domal uplift and lithospheric extension (Fig. 3.1a). In this mode, volcanism and doming precede rifting but the crust and mantle do not necessarily thin in a homogeneous way. Passive rifting involves horizontal tectonic stresses that produce lithospheric thinning and passive mantle up-welling (Fig. 3.1b). In this mode the crust and mantle may thin homogeneously, however, volcanism and doming are expected to post-date rifting. Hence the resulting basin geometry, rates of subsidence or uplift, sedimentation and erosion, magmatism, etc. are surface expressions of processes operating at crustal and mantle levels. Such processes are directly related to

[1] Smaller faults similar in attitude to a larger fault to which they are associated.

[2] Smaller faults with similar trend but dip to opposite direction as that of a larger fault to which they are associated.

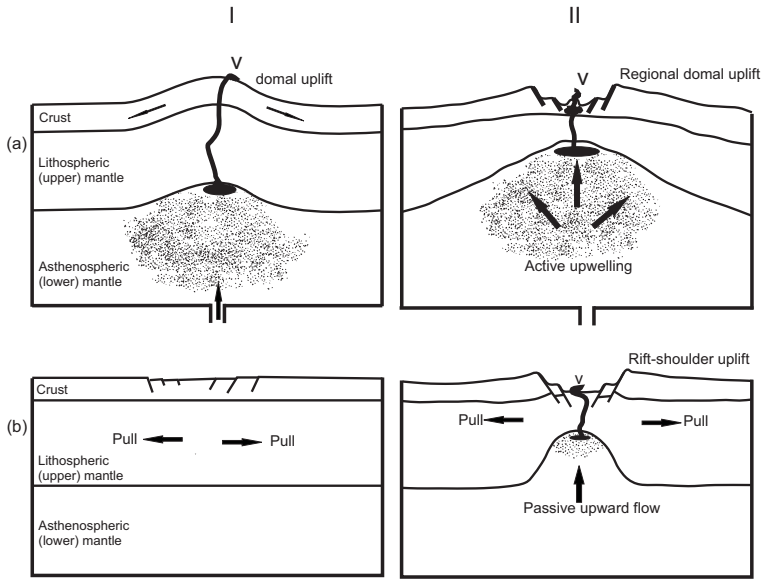

Fig. 3.1 Modes of rifting. (I) Early stage (II) Subsequent stage. (a) Active mode: lithospheric tension results from local extensional stresses caused by hot spots or mantle plume impingement on the base of the lithosphere. (b) Passive mode: lithospheric tension results from far-field extensional stresses. Stippling indicates hot, low density regions of the sub-lithospheric upper mantle. V=volcanism. Modified after M.H.P. Bott 1995.

the deformational pattern of the lithosphere when subjected to deviatoric tensile stresses and consequently to its rheological behaviour (Fernàndes and Ranalli 1997). The two mechanisms are, however, complementary since most rifts show both active and passive signatures. Although there is no control over the compatibility between the imposed deformation mode in kinematic models and the actual mechanical behaviour in rocks, predefining the velocity field allows for a variety of deformation modes (Fernàndes and Ranalli 1997).

(a) The McKenzie (or Pure shear) model

According to the Mckenzie (1978) model for rifting crustal thinning and increase in geothermal gradient are ascribed to mechanical lithospheric stretching, as a consequence of which a net syn-rift subsidence occurs. As such the resultant upper crustal subsidence is attributed to crustal thinning buffered by uplift due to an increase in the geothermal gradient. After rifting the geothermal gradient re-equilibrates with time and the lithosphere cools, leading to post-rift subsidence. Thus the model attributes basin subsidence to syn-rift and post-rift components (Kusznir and Ziegler 1992). It however, assumes that lithospheric stretching is uniform with depth and that the lithosphere behaves plastically with local Airy[3] isostasy. In this case the familiar block rotation tectonics of rifted basins cannot occur and neglects the role of basement faults.

(b) The Wernicke (or Simple shear) model

The Wernicke (1985) model assumes that extension of continental lithosphere is accommodated along a shallow dipping shear zone which cuts from the surface down through the entire crust and lithospheric mantle to the asthenosphere. However, no major dip-slip fault or

[3]From Airy's model stating that isostatic equilibrium is attained because mountains have a crustal root that compensates for the relief i.e. tallest mountains have the deepest roots; in contrast to Pratt's model that explains isostatic equilibrium to results from lateral density variations i.e. mountain root reaches same level (compensation depth) so that the less dense part reaches the higher height.

shear zone passing continuously from the surface down into the upper mantle, as suggested by Wernicke's model, has been observed on any deep seismic section (Kusznir and Ziegler 1992). According to Kusznir and Ziegler (1992), major basement faults are restricted to the brittle upper crustal seismogenic layer (topmost 10-15km), where extension is achieved by simple shear (planar faulting). In the lower crust and upper mantle rocks deform plastically rather than in a brittle manner (Kusznir and Park 1987) and lithospheric extension is achieved by pure shear i.e. distributed stretching (Mckenzie 1978). It is thus agreed that continental lithosphere deforms by a combination of simple and pure shear (Kusznir et al. 1987) and that the Mckenzie (1978) and Wernicke (1985) models represent end-members of a coupled simple shear-pure shear model. The deformational framework of such a coupled model results in three distinct but related responses (Kusznir and Ziegler 1992) namely:

(i) *Crustal thinning*, due to both faulting (simple shear) of the upper crust and plastic distributed stretching (pure shear) of the lower crust.

(ii) *Perturbation of the lithosphere temperature field*, by both simple shear and pure shear stretching and its subsequent thermal re-equilibration

(iii) *Isostatic response of the lithosphere to loads* during both syn- and post-rift stages of basin formation associated with crustal thinning, thermal perturbation and re-equilibration, sedimentary loading and erosion.

In some cases these responses may be supplemented by the generation of melt during continental lithosphere extension due to decompression and partial melting of the lower lithosphere and upper lithosphere (McKenzie and Bickle 1988; White and McKenzie 1989).

(c) The flexural cantilever model

This model of continental extension and sedimentary basin formation is a mathematical model of the geometric, thermal and flexural isostatic response of the lithosphere to extension by faulting (simple shear) in the upper crust and plastic distributed deformation (pure shear) in the lower crust and lithospheric mantle (Kusznir and Ziegler 1992). It considers the long term ($> 10^6$ years) isostatic balance of the lithosphere in response to crustal thinning, thermal and sedimentary loads. However it does not address processes at the co-seismic time-scale. Since the model does not address fault growth (Kusznir and Ziegler 1992) which is the central subject for this study, this brief mention of it suffices.

3.1.3 Faulting and fault analysis

Various concepts and theories, hypotheses or assumptions are taken into consideration when studying fault patterns. Below are some employed by the fault data analysis techniques, including criteria invoked in the discussion and interpretation of the results.

(a) Andersonian stress

Anderson's concept of the *standard state* of stress in the earth's crust (similar to hydrostatic state) holds that *horizontal pressure increases in step with the vertical pressure.* As such, the magnitude of horizontal stresses at any specific depth in the crust is equal to that of the vertical *geostatic stress* induced at that depth by gravitational loading (Price and Cosgrove (1990), p.127). Based on the assumption that *no shear stress exists at the earth's surface*[4] anderson pointed out that deviations from the standard state

[4]That is, shear stress cannot occur at the interface between atmospheric air and the ground, thus one of the principal stresses has to be vertical and the other two horizontal.

(which if sufficient could cause faulting) would occur if there is:
(i) unequal decrease in magnitude of both horizontal principal stresses,
(ii) unequal increase in magnitude of both horizontal principal stresses and
(iii) an increase in magnitude of one horizontal stress coupled with a decrease in magnitude of the other horizontal principal stress.
Thus depending on which of the three principal stresses lies in the vertical, Anderson (1951) defined three tectonic stress regimes as follows: *Normal-fault regime* where the maximum principal stress σ_1 is vertical, *Thrust-fault regime* where the minimum principal stress σ_3 is vertical and *Strike-slip fault regime* where the intermediate principal stress σ_2 is vertical. This classification is however, strictly valid only in coaxial deformational regimes where principal strain axes do not rotate but remain parallel to the principal stress axes. The deforming rock must also be isotropic so that the vertical stress σ_v can be related to the weight and density of the overlying rock column (in a manner similar to hydrostatic stress experienced by a fluid at rest) according to the equation (3.1) below, where ρ is rock density, **g** is gravitational acceleration and z is depth from earth's surface;

$$\sigma_v = \rho g z. \tag{3.1}$$

(b) Navier-Coulomb failure criterion

The Navier-Coulomb criterion of shear failure is based on Amontons' Law of frictional sliding which states that *the force of friction is directly proportional to the applied load* and can be represented diagrammatically as shown in Fig. 3.2.

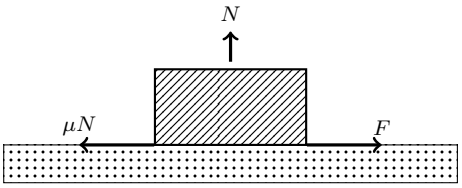

Fig. 3.2 Amonton's law of sliding friction where the coefficient of friction $\mu = 0.75$ at the point of frictional sliding along a surface. Modified after Ragan (2009).

The law can be expressed mathematically as:

$$f_{max} = \mu_s N, \tag{3.2}$$

where f is a frictional resistive force equivalent to the force applied, N is a normal force acting on the object and equivalent to its weight and the constant of proportionality μ_s is the coefficient of static friction (Ragan (2009), p.241). Equation (3.2) holds just before the object starts sliding or when it slides with no acceleration. Applying the idea of a triangle of forces (Fig.3.3a), the angle that the resultant vector R makes with N is called the angle of static friction ϕ_s; so that from equation (3.2),

$$\frac{f_{max}}{N} = \mu_s = \tan\phi_s, \tag{3.3}$$

For a block of weight W, on a plane inclined at an angle α (Fig. 3.3b and c), equation (3.3) yields

$$\frac{f_{max}}{N} = \frac{W\sin\alpha}{W\cos\alpha},$$

and

$$\mu_s = \tan \alpha.$$

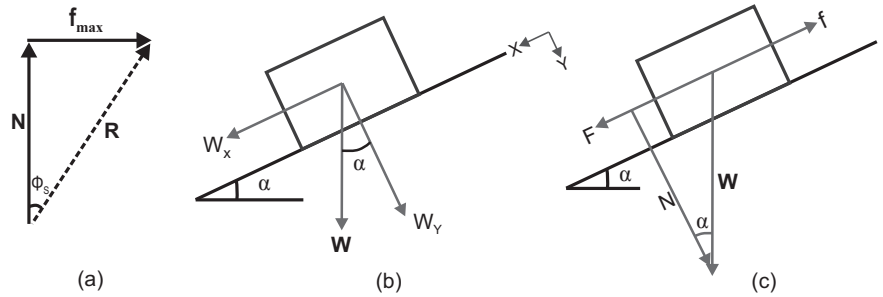

Fig. 3.3 Resolution of forces. (a) Resultant for a block sliding along a flat surface indicated in Fig. 3.2; ϕ_s=angle of static friction. b-c: Friction for a block on an inclined plane. (b) Components of weight **W**; the components W_X and W_Y are resolved along X and Y directions, respectively. (c) Forces at equilibrium. Adopted from Ragan (2009).

Expressed in terms of the normal and shearing components of the traction acting on the plane of sliding - by dividing both sides of equation (3.2) by the nominal surface area of contact - Amontons' law can be expressed as:

$$\tau = \mu_s \sigma_n, \tag{3.4}$$

where τ and σ_n are the shear and normal stresses, respectively acting on the potential fracture plane (Price and Cosgrove (1990), p.66). If the outward normal vector of the potential fracture plane is oriented at an angle ϵ to the direction of maximum principle stress σ_1, then the normal and shear stresses are given by

$$\sigma_n = \frac{1}{2}(\sigma_1 + \sigma_3) + \frac{1}{2}(\sigma_1 - \sigma_3)\cos 2\epsilon, \tag{3.5}$$

$$\tau = -\frac{1}{2}(\sigma_1 - \sigma_3)\sin 2\epsilon; \tag{3.6}$$

and

$$\mu_s = \tan \phi_r. \tag{3.7}$$

where ϕ_r is the angle of sliding friction on that plane (Jaeger et al. (2007), p.23).

But cohesion C_o of the rock must be overcome before fracture occurs (Price and Cosgrove (1990), p.27), therefore the complete shear criterion is expressed as

$$\tau = C_o + \mu_s \sigma_n; \tag{3.8}$$

which produces a Mohr diagram with a straight-line failure envelop (Fig. 3.4). Conversely, failure will not occur on any plane for which

$$\tau < C_o + \mu_s \sigma_n. \tag{3.9}$$

(c) Mohr's hypothesis

From the shear criterion in equation (3.8), Coulomb's theory predicts that the compressive stress σ_1 required to cause failure will increase linearly with the confining stress σ_3. But

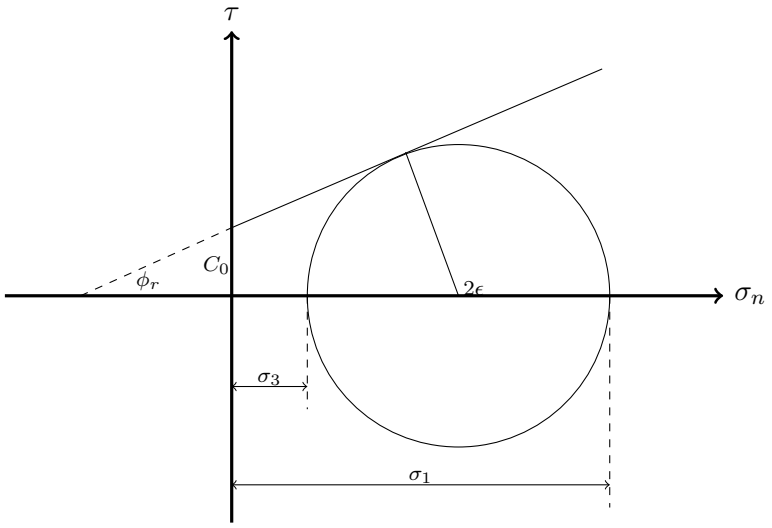

Fig. 3.4 Mohr's stress circle with a straight-line failure envelope. Adopted from Jaeger et al. (2007).

experiments typically show that σ_1 at failure increases at a less-than-linear rate with σ_3 (Jaeger et al. 2007). To correct for this deficiency, Mohr replaced Coulomb's equation by a relation of the form

$$|\tau| = f(\sigma_n), \tag{3.10}$$

which produces a non-linear curve (Fig. 3.5) so that failure should occur if one of the Mohr's circles touches the curve defined by this equation. This will necessarily occur for the circle defined by σ_1 and σ_3 and so the value of σ_2 is not expected to affect the onset of failure (Jaeger et al. 2007). The state of stress at the point of contact of the Mohr's

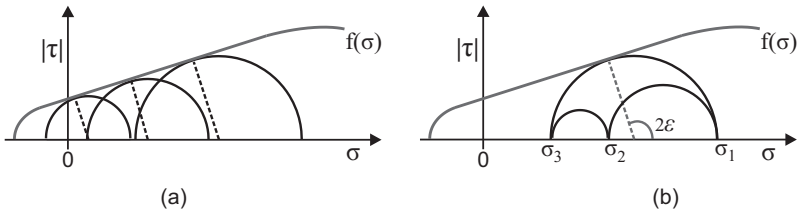

Fig. 3.5 (a) Mohr's non-linear failure curve defined as the envelop of all Mohr circles that cause failure. (b) Construction showing that according to the Mohr hypothesis, the intermediate principle stress does not influence the onset of failure. ϵ= the angular difference between the direction of maximum principal stress axis σ_1 and that of the normal to the failure plane. Modified after Jaeger et al. (2007)

circles and the failure curve represents the forces acting on the plane. Thus similar to the Coulomb theory, Mohr's theory predicts that the failure plane passes through the direction of the intermediate stress and its normal vector makes an angle ϵ with the direction of maximum principal stress σ_1.

Conjugate fault-sets

A conjugate fault system has two sets of oppositely dipping faults where the lineations are perpendicular to the line of fault intersection. They express the simplest case of plane strain[5]. The sense of slip is complementary on the two sets and the angle between them should be constant and consistent with the mechanical properties of the rock (and

[5]Strain under a state of stress in which one normal stress is zero - zero strain in one normal direction.

pore fluid pressure) at the time of deformation (Price and Cosgrove (1990), p.192). Since conjugate sets develop symmetrically about the principal stresses for the three standard categories, slip direction or lineation would be in the dip direction for reverse and normal faults and in the strike direction for strike-slip faults according to Andersonian theory. Hence revealing the orientations of the principal stresses.

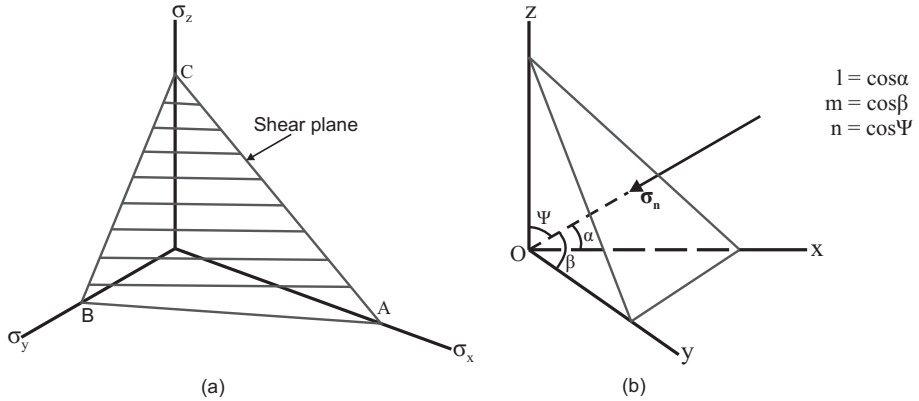

Fig. 3.6 (a) A shear plane that is oblique to all axes of principle stress. (b) Cosine directions for a plane oblique to three orthogonal axes. Modified after Price and Cosgrove (1990).

Oblique-slip faults

These may develop in a stress field in which the principal stress axes are inclined to the vertical or horizontal. Since pure dip-slip and pure strike-slip can only occur along strength anisotropies which contain the σ_1 or σ_2 axis when Andersonian stresses prevail in rocks containing strength anisotropies, oblique-slip can occur along anisotropies if they are favourably oriented (Yin and Ranalli 1992) i.e. when such a plane is oblique to all the three principal stress axes (Fig. 3.6a) or by a regeneration of movement along a pre-existing fault plane. The latter implies that dip- or strike-slip faults can be transformed into oblique faults if, subsequent to faulting, the region in which the structures developed underwent tilting (Price and Cosgrove 1990). However, tilting is found to result in only minor deviations from the vertical or horizontal directions.

The direction of maximum shearing stress τ_{max} on a plane that is inclined to all the three principal stress axes (Fig. 3.6b), depends on the magnitude of all three principal stresses. The pitch γ of the direction of action of τ_{max} in the plane is given by:

$$\tan\gamma = \frac{n}{l \cdot m}\left[m^2 - (1 - n^2) \cdot R\right], \tag{3.11}$$

where R is the stress ratio expressed as

$$R = \frac{\sigma_{yy} - \sigma_{zz}}{\sigma_{xx} - \sigma_{zz}}, \tag{3.12}$$

l, m, n are the direction cosines of the pole of the plane relative to principal stress directions; and σ_{xx}, σ_{yy} and σ_{zz} are principal stresses in the x, y and z directions, respectively (Jaeger and Cook 1979). If an assumption is made that σ_1, σ_2 and σ_3 respectively coincide with the x, y and z axes, then equation (3.11) can be re-written as

$$\tan\gamma = \frac{n}{l \cdot m}\left[m^2 - (1 - n^2) \cdot \frac{\sigma_2 - \sigma_3}{\sigma_1 - \sigma_3}\right] \tag{3.13}$$

In an analysis where l, m, n, σ_1, σ_2 and σ_3 are all known, one can determine the values of σ_n, τ_{max} and γ. Using the relationships $\tau_{max} = \mu_s\sigma_n$ or $\tau_{max} = C_o + \mu_s\sigma_n$ it can be ascertained whether slip can take place and if so, in which direction the slip will occur. Thus depending on orientation of a plane and the relative sizes of the stresses at the point of slippage, a plane may undergo normal-, reverse- or strike-slip displacement with either oblique dextral- or oblique sinistral-slip components (Jaeger et al. (2007), p.422-423). Hence deviation of principal stress axes from the vertical or horizontal directions predicted by Anderson may indicate that the area has been tilted since the time of deformation or that the stress field was rotated or refracted through this volume of rock. Fossen (2010) noted that such deviations can occur near large and weak faults or joint zones.

Effect of anisotropy on strength

Given equations (3.5), (3.6) and (3.7) it follows that, if C_w is the inherent shear strength of the planes of weakness and μ_w is the coefficient of internal friction along the same planes, then the condition for sliding along these planes (equation 3.8) can be written as

$$\sigma_1 = \sigma_3 + \frac{2(C_w + \mu_w\sigma_3)}{(1 - \mu_w \cot\epsilon)\sin 2\epsilon}, \tag{3.14}$$

where ϵ is the angle between σ_1 and the normal to the planes of weakness (Jaeger et al. (2007), p.104).

The value of σ_1 required to cause failure, as given by the above equation, tends to infinity as $\epsilon \to \pi/2$ or $\epsilon \to \tan^{-1}\mu_w = \phi_w$ such that for angles between these two values, failure will occur at a finite value of σ_1 that varies with ϵ (Jaeger et al. 2007). The minimum such value of σ_1 is given by:

$$\sigma_1^{min} = \sigma_3 + 2(C_w + \mu_w\sigma_3)[(1 + \mu_w^2)^{\frac{1}{2}} + \mu_w], \tag{3.15}$$

which occurs at a specific angle ϵ_w that is given by:

$$\tan 2\epsilon_w = \frac{-1}{\mu_w}. \tag{3.16}$$

Hence if a plane of weakness is oriented from σ_1 by some angle other than ϵ_w, failure can still occur but only at a value of σ_1 as given by the previous equation, that is greater than σ_1^{min}. For values of $\epsilon < \phi_w$, failure along the plane of weakness is not possible, for any value of σ_1.

If we define the inherent shear strength of the intact rock (its cohesion) as C_o and its coefficient of internal friction as μ_o, then because planes of weakness are by definition weaker than the intact rock, we assume that $\mu_w < \mu_o$ and $C_w < C_o$ (Jaeger et al. 2007). Thus if the Coulomb failure criterion is satisfied, failure can occur on a plane other than the pre-existing planes of weakness if σ_1 reaches the value

$$\sigma_1 = 2C_o \tan\epsilon_o + \sigma_3 \tan^2\epsilon_o, \tag{3.17}$$

where ϵ_o is the angle for a new fracture formed in intact rock and according to the relation $2\epsilon = \phi_r + 90^\circ$, the value of ϵ_o is given by,

$$\tan 2\epsilon_o = \tan(\phi_o + 90^o) = \frac{-1}{\tan\phi_o} = \frac{-1}{\mu_o}. \tag{3.18}$$

Hence for a fixed value of σ_3, the value of σ_1 required to cause failure somewhere within the rock will be equal to the smaller of the two values given by equations (3.14) and (3.17). This means that failure will occur along a plane of weakness if its σ_1 value is lower than that for intact rock, but if that value is greater then failure occurs along a 'fresh' plane within the intact rock (Jaeger et al. 2007).

Conditions for fault reactivation

Pollard and Fletcher (2005) have demonstrated that in a zone where faults already exist, the fractures induce heterogeneous stress fields, therefore re-activation of pre-existing planes does not follow the *Navier-Coulomb fracture criterion*. This implies that the angle between the maximum principal stress axis and fault plane is not fixed and oblique-slip is a common feature (Sperner and Zweigel 2010). The maximum principal stress axis could hence lie anywhere in the compression quadrant limited by the fault plane and the plane perpendicular to the slip direction (Angelier and Mechler 1977; Sperner and Zweigel 2010).

Slip along an existing plane that contains the σ_2-axis will result when

$$\frac{\sigma_1}{\sigma_3} = \frac{1+d}{1-d}, \tag{3.19}$$

where

$$d = \frac{sin2\omega + cos2\omega \cdot tan\phi_s}{tan\phi_s}; \tag{3.20}$$

and where ω is the dip of the fault plane (Price and Cosgrove (1990), p.204-5). If $\phi_s = 30°$, ideal Andersonian faults will dip at 60°. If a stress-state that would potentially reactivate such faults has a horizontal σ_1-axis, then the angle $\omega = 60°$; in which case according to equations (3.19) and (3.20), the ratio σ_1/σ_3 tends to infinity (Jaeger et al. (2007) p.74). Consequently, thrusts of dip = 30° would develop before σ_1 attains a value high enough to permit rejuvenation and reverse shear of the pre-existing normal faults. Price and Cosgrove (1990) have demonstrated (p.205) that such reverse re-shear on ideal Andersonian planes could only take place if the angle of sliding friction ϕ_r were considerably lower than the angle of friction ϕ of the solid intact rock (as would occur if the fault planes contained clay fault-gouge) and/or the σ_1-axis was inclined to the horizontal (e.g. due to differential uplift and denudation). If the latter alternative obtains, the inclined principle stress will greatly enhance the probability of reverse re-shear on one set of normal faults. The normal stress on the latter fractures will also attain a high value which will completely inhibit re-activation on the second set of planes, because σ_1 acts at a high angle to the conjugate set of normal faults.

Nieto-Samaniego and Alaniz-Alvarez (1995) observed that when σ_3 is positive (compressive) and σ_1 is vertical, pre-existing fractures that strike sub-parallel to σ_3 direction are not suitable to slip but when principal stresses are inclined (non-Andersonian stresses) slip may occur along these planes instead of rock fracturing. Pre-existing fractures that strike sub-parallel to σ_2 direction and dip $> 23°$ will also readily slip. Thus if a pre-existing normal fault lies in an optimum orientation with respect to an active stress-state, only a modest reduction in the horizontal (σ_3) stress is required for renewed slip (Ragan (2009), p.257). For pre-existing thrust faults a considerable increase in the horizontal (σ_1) stress component is required for renewed slip, whereas for wrench faults all that is required is the condition $\sigma_1 \geq \sigma_2 \geq \sigma_3$, hence a range of possibilities. Therefore, resistance to slip is least for normal fault and greatest for thrust faults. This is also portrayed by the ratios

of differential stresses required for frictional sliding on normal, strike-slip or wrench and thrust faults, respectively expressed as (j-1)/j : 2(j-1)/(j+1) : (j-1), where j is a constant (Price and Cosgrove (1990), p.27). The value of j is given by

$$j = \frac{1 + \sin \phi_r}{1 - \sin \phi_r},$$

where ϕ_r is the angle of sliding friction on the respective plane. When j=4.0 (a value that obtains if the coefficient of friction μ=0.75), the ratio of the magnitude of the differential stresses necessary for sliding to occur on the three types of faults are respectively 1:1.6:4 (Price and Cosgrove (1990), p.128).

(d) The Wallace-Bott hypothesis

The Wallace-Bott hypothesis consists in the gross assumption that slip on a planar fracture surface will occur in the direction of maximum resolved shear stress; so that a stress denoted by the tensor σ results in the traction $\mathbf{t}= \sigma\mathbf{U}$ on a fault plane that has a unit vector $\mathbf{U}$ perpendicular to the plane. The normal stress σ_n applied to such a plane is given by:

$$\sigma_n = \mathbf{t} \cdot \mathbf{U}, \tag{3.21}$$

and the magnitude of the shear stress τ is given by:

$$\tau = |\mathbf{t} - \sigma_n \mathbf{U}|, \tag{3.22}$$

whereby the magnitude and direction of the shear stress are together denoted by the vector:

$$\tau = \mathbf{t} - \sigma_n \mathbf{U}, \tag{3.23}$$

But since faulting occurs to relieve this stress, fault movement is indicated by $-\tau$ rather than τ (Yamaji et al. 2010).

Hence the Wallace-Bott hypothesis dictates that strike-slip faults result from a horizontal maximum shear stress, normal or reverse faults result if the largest shear stress is in the dip direction and oblique-slip faults result from any other case. This hypothesis implies that faults are planar, fault blocks are rigid, block rotations are negligible and faults were activated during a single phase of deformation under a uniform stress field (Fossen (2010), p.194) such that no stress perturbations occur. Although these simplifications disagree with field observations such as geometrical complexity of fault surfaces (Wallace and Morris 1986; Pascal 2002) and block rotations along fault surfaces (Twiss and Geffel 1990; Twiss et al. 1991; Pascal 2002) and although local perturbations on a stress field may occur, empirical observations and numerical modelling (Dupin et al. 1993; Pollard et al. 1993; Maerten 2000; Pascal 2002) have demonstrated that the Wallace-Bott hypothesis is reasonable, save for small deviations. Hence stress inversion techniques that are build on these assumptions can calculate reliably the orientation and relative size of the stress axes responsible for formation of faults whose plane-orientation, lineation-orientation and sense-of-slip are known.

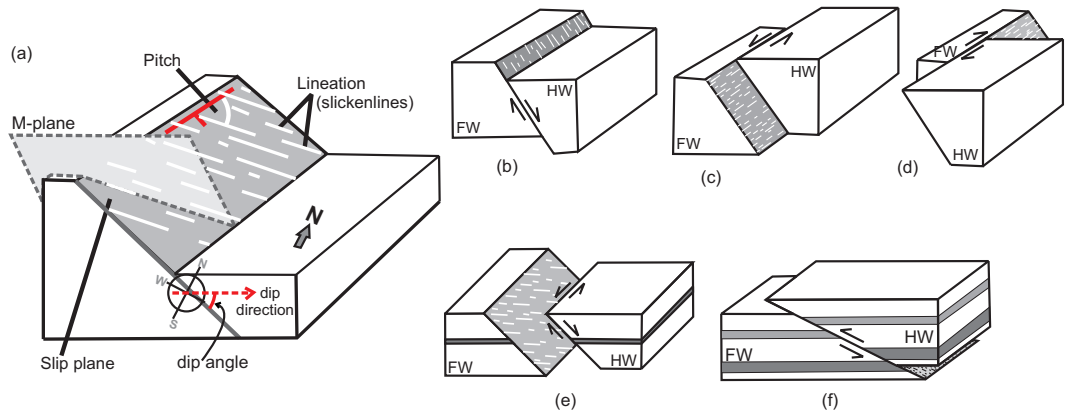

Fig. 3.7 Block diagrams demonstrating fault-slip sense and measurement of fault-slip data. (a) Measurement of fault orientation and pitch. b–f: Relative sense of slip; FW=footwall block, HW=hanging wall block, half-arrows indicate directions of relative movement. (b) Normal or pure dip-slip (c) Sinistral strike-slip (d) Dextral strike-slip (e) Oblique dip-slip (f) Reverse-slip. (Partly modified after Fossen (2010); p.156, 195)

(e) Requirements for inversion of data

In forward problems the direction of shear-sliding on a plane is determined from known magnitudes and orientation of principle stresses relative to the plane (Price and Cosgrove 1990). On the contrary, paleostress determination is a reverse problem where the orientation and relative magnitudes of the principle stresses (hence the shape of the stress ellipsoid) are reconstructed by inversion of fault-slip data. In the last few decades, several numerical inversion techniques (Turner 1953; Etchecopar et al. 1981; Reches 1987; Angelier et al. 1982; Sperner et al. 1993; Nemcok and Lisle 1995; Yamaji 2000; Xu 2004; Otsubo et al. 2006) have been developed and applied to fault-slip analysis with a common aim - to characterise the average reduced stress tensor that explains slip directions observed on faults in a tectonic site (Dupin et al. 1993). However, to solve this inverse problem using any of the available inverse techniques, the following conditions need to be met:
(a) The stress tensor is symmetric and deformation is coaxial (pure shear),
(b) The regional stress tensor is spatially and temporally homogeneous,
(c) Faults develop in accordance with the Mohr-Coulomb fracture criterion and the slip direction is parallel to the maximum resolved shear stress acting upon the fault surfaces,
(d) Faults preserve their geometry throughout history and
(e) Faults and lineations in a population have a variety of attitudes and therefore clearly constrain paleostresses (Wojtal and Pershing 1991; Pollard et al. 1993).

To determine paleostress tensors by inversion, orientations of faults and pitches of corresponding lineations are required. Slip on a fault plane is inferred from fibrous lineations or striae called slickenlines, observed on a fault plane (Fleuty 1974). The long axis of the fibres is interpreted to be parallel to the slip-direction and the sense of imbrication to correspond to the sense of motion on the fault (Marshak and Mitra 1988). The slickenlines are generally assumed to record the direction of the last increment of slip on a fault surface (Pollard et al. 1993; Fossen 2010), where earlier slip events might have been obscured or totally obliterated. A complete fault slip datum usable for stress reconstruction comprises the fault-plane orientation recorded as dip-direction and dip-amount plus the orientation of the striae (Pitch or Rake) recorded as azimuth and plunge of lineations; and the slip-sense - whether normal, reverse, dextral or sinistral (Fig. 3.7). Data of unknown

sense of slip can be incorporated when using some methods but some assumptions have to be made and the quality of the result is compromised. Depending on the choice of method, some parts of the analysis require the quality of the sense-indicator to be stated as a parameter (Sperner and Zweigel 2010). With at least 9-10 complete fault-slip data sets that fulfil the above stated criteria, reliable paleostresses can be constrained.

(f) Basis for fault-slip inversion

When paleostresses are determined by inversion of fault-slip data, it is not possible to obtain absolute values of the principle stresses. Instead, the relative magnitudes are estimated using the stress ratio R (expressed as ϕ and defined as (1-R) in some texts) which is given by

$$R = \frac{(\sigma_2 - \sigma_3)}{(\sigma_1 - \sigma_3)}. \tag{3.24}$$

The value of R determines the shape of the stress ellipsoid (Fig.3.8). The value of R=1 implies that $\sigma_1 = \sigma_2$ (uniaxial tension) and the stress ellipsoid is oblate in shape; with axial symmetry about its σ_3-axis. A value R=0 on the other hand implies that $\sigma_2 = \sigma_3$ (uniaxial compression) resulting in a prolate-shaped stress ellipsoid (Fossen (2010), p.194), which has axial symmetry about its σ_1-axis (Yamaji et al. 2010). Since stresses are generally

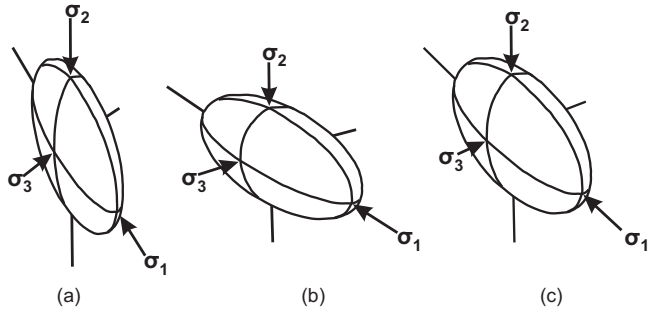

Fig. 3.8 Shapes of stress ellipsoids. (a) Oblate ellipsoid; R=1, $\sigma_1 = \sigma_2$, a state of uniaxial tension. (b) Prolate shape; R=0, $\sigma_2 = \sigma_3$, a state of uniaxial compression. (c) Regular shape; where $0 < R < 1$, $\sigma_1 > \sigma_2 > \sigma_3$, a state of plane stress. Modified after Fossen (2010); p.196.

represented as 3x3 symmetric matrices, the ratio R is used to express the stress tensor, which in the coordinate system defined by the principle stresses, is written as

$$\begin{pmatrix} \sigma_1 & 0 & 0 \\ 0 & \sigma_2 & 0 \\ 0 & 0 & \sigma_3 \end{pmatrix}.$$

An isotropic stress can be added to the stress tensor expressed in the matrix above (in a way similar to adding a constant) without changing orientations of axes and the components can be multiplied by a constant thereby contracting or inflating the stress ellipsoid but its shape is maintained (Fossen 2010). Therefore the tensor can be expressed in terms of two constants a and b as shown in equation (3.25), where $a = b/(\sigma_1 - \sigma_3)$ and $b = -\sigma_3$.

$$\begin{pmatrix} \sigma_1 + b & 0 & 0 \\ 0 & \sigma_2 + b & 0 \\ 0 & 0 & \sigma_3 + b \end{pmatrix} \begin{pmatrix} a & 0 & 0 \\ 0 & a & 0 \\ 0 & 0 & a \end{pmatrix} = \begin{pmatrix} 1 & 0 & 0 \\ 0 & R & 0 \\ 0 & 0 & 0 \end{pmatrix} \tag{3.25}$$

Consequently, a reduced stress tensor represents the stress tensors that have common

principle orientations and a common R-value (Yamaji et al. 2010), thereby giving both the orientation and shape of the stress ellipsoid. As such, a reduced stress tensor contains only four unknowns (instead of six contained in the full stress tensor) represented by R and the orientations of the three principle stresses (Fossen 2010). Hence the need for at least four different fault-slip data sets. The more reliable results though are obtainable for inversion of at least 10 data sets, which when applied to a stress inversion program, give many more equations than unknowns - as for instance demonstrated (in equation 3.32 on page 41) for the multiple inverse method.

WSM[6] Stress regime assignment (after Zoback, 1992)

The WSM employs the standard geologic or geophysical notation to define stress magnitudes. Thus compressive stress is positive and the principal compressive stresses are related in such a way that $\sigma_1 > \sigma_2 > \sigma_3$; σ_1 being the maximum and σ_3 the minimum. Using the plunge of the three principal axes and the azimuth of the maximum horizontal compressive stress $S_{(Hmax)}$, three standard categories of tectonic stress regimes are defined, i.e. Normal faulting (NF), Strike-slip faulting (SS) and Thrust faulting (TF). Two other stress-states are defined from combination of a strike-slip regime with either normal- or thrust faulting regime, respectively denoted as NS and TS. Category NS represents a case where the maximum stress or P-axis is the steeper plunging of the P- and B-axes and is described as a stress-state of predominantly normal faulting with strike-slip component. TS represents data where the minimum stress or T-axis is the steeper plunging of the B- and T-axes, described as predominantly thrust faulting with strike-slip component. The criteria are summarised in table 3.1.

WSM quality ranking scheme for stress orientations (version 2008)
This scheme assigns each stress data record a quality between A and E. The highest quality is A and E the lowest. A-quality means that the orientation of the maximum horizontal compressional stress $S_{(Hmax)}$ is accurate to within $\pm 15°$. B-quality to within $\pm 20°$, C-quality to within $\pm 25°$ and D-quality to within $\pm 40°$. For most methods, these quality classes are defined through the standard deviation of $S_{(Hmax)}$ and since E-quality data have standard deviation greater than 40°, they are not useful. Stress indicators of quality A to C are considered reliable for analysing stress patterns and interpretation of geodynamic processes (Heidbach et al. 2008).

Table 3.1 Plunge (Plg) of PBT-axes as used in stress regime assignment

P/σ_1-axis	B/σ_2-axis	T/σ_3-axis	Regime	$S_{(Hmax)}$-azimuth
$Plg > 52°$		$Plg < 35°$	NF	azim. of B-axis
$40° < Plg > 52°$		$Plg < 20°$	NS	azim. of T-axis+90°
$Plg < 40°$	$Plg > 45°$	$Plg < 20°$	SS	azim. of T-axis+90°
$Plg < 20°$	$Plg > 45°$	$Plg < 40°$	SS	azim. of P-axis
$Plg < 20°$		$40 < Plg < 52°$	TS	azim. of P-axis
$Plg < 35°$		$Plg > 52°$	TF	azim. of P-axis

[6] World Stress Map Project

3.1.4 Analogue modelling

Analogy is both the cognitive process of transferring information about a particular subject (the analogue or source) to another particular subject (the target) and a linguistic expression corresponding to such a process (source: Wikipedia, the free encyclopedia). As such, analogical models (also called dynamical analogies) are defined as a method of representing a phenomenon of the world (the target system) by another more understandable or analysable system, which is smaller and/or faster than the target system but exhibits similar properties of dynamical behaviour.

(a) Types and usage of models
According to Fernàndes and Ranalli (1997), the mode of lithospheric extension can be prescribed in modelling either implicitly by imposing a deformation pattern which the lithosphere is assumed able to sustain (kinematic models) or explicitly by specifying equations governing the rheological behaviour (dynamic models). Kinematic models have been used in passive rifts to account for observations such as rates of subsidence or uplift of the basement, volcanism and differential stretching (Mckenzie 1978; Buck et al. 1988; Cloetingh et al. 1993, 1995). Dynamic models have been applied to passive and active rifting mechanisms and to lithosphere-asthenosphere interaction (Braun and Beaumont 1987; Bassi et al. 1993; Keen 1985). Fernàndes and Ranalli (1997) also noted that some models use a mixed approach where the mode of lithospheric deformation is imposed kinematically, while the deformation of the underlying substratum is treated dynamically (Keen et al. 1987). Rheological controls based on the depth variation of brittle and ductile strength and the effects of gravitational buoyancy forces arising from lateral thickness variations, have been used to externally constrain the mode of deformation imposed in kinematic models (Kusznir and Park 1987; Buck 1991; Negredo et al. 1995).

Analogue models can be used to investigate the influence of different parameters on geological processes. They offer the opportunity to study the 3-D structural evolution of a specific model, thus supplying a clear coherent kinematic picture, which can help with the interpretation of natural prototypes (Schellart 2002). They have been used to simulate deformation processes that produce structures such as faults, folds, rifts etc. either under atmospheric gravitation or in a centrifuge that presents an artificial gravitational field due to a centripetal force developed as it spins round. The former technique is cheaper but the construction of models may be more difficult and it should be made of extremely weak materials that can be properly scaled for gravity. The evolution of an experiment can also be continuously recorded, unlike the centrifuge which has to be switched off in order to take record. The latter technique is expensive but has the advantage that its analogue materials have a relatively high strength and are therefore relatively easy to work with during construction and analysis of the model (Schellart 2002).

Some modelling approaches make use of plastic materials (e.g. Tapponnier et al. (1982); Chemenda et al. (1995, 1996, 2000)) or viscous rheologies (e.g. Funiciello et al. (2000); Faccenna et al. (2001)). Others use materials with different rheologies (brittle and viscous), to incorporate the different behaviour of rocks at different depths in the crust and mantle, which are mainly related to the rheological approximation of the lithosphere and sub-lithospheric mantle (e.g. Davy and Cobbold (1991, 1988); Ratschbacher et al. (1991); Brun et al. (1994); Brun (1999); Schellart et al. (2002); Burg et al. (2002)). It has been demonstrated that dry cohesionless quartz sand can reasonably approximate the mechanical properties of the upper crust. Thus in sandbox modelling, sand is used as the analogue material, because pure sand is rheologically brittle (does not flow but develops faults) as

most of the rocks at the earth's surface. It is also rate-independent i.e. no matter how fast it is deformed, the result will not be altered. Unlike plaster which must be mixed and allowed to set under certain controlled conditions in order for faults to develop, sand does not require particular pre-conditioning before the experiment (Davy and Cobbold 1988). In a sandbox, however, the boundary conditions (e.g. displacement distribution at the base of a model, specified fault shape) define the initial state of the modelling materials during the experiment, hence the results depend on them (Pollard and Fletcher 2005).

General boundary conditions define the context of a problem so that appropriate theoretical principles, fundamental laws and governing equations (and computational tools in the case of numerical models) can be used to find a solution (Pollard and Fletcher 2005). But since tectonic processes are multifaceted, it is difficult to obtain a single set of boundary conditions to address all facets. As such, the selection of general boundary conditions is influenced by practical necessity and models are simplified by eliminating variables whose effects are negligible. However, selection of general boundary conditions requires an understanding of both the field observations that serve to characterise the structures and the physical principles and scaling relationships that underlie possible models for these structures. In sandbox modelling, the chosen boundary conditions and modelling materials determine the extent of the lateral edge effects on a model. The materials are considered to be isotropic and homogeneous so that there are no spatial and temporal variations in material properties (Pollard and Fletcher 2005). The geometry of pre-cut rigid plates and edge effects that occur adjacent to walls of a model especially due to friction between the walls and analogue material, affect the results (Morley 1995*b*). Thus it is important to recognise their extent and magnitude before analysing deformation patterns. As such a model is better if it is made large enough so that the deformation zone of interest is distant from the walls.

(b) Scaling of models

Unlike numerical models which obey the fundamental laws of mechanics by design, analogue models do so by virtue of the fact that they are part of the natural world from which these laws are derived (Pollard and Fletcher 2005). Thus the same dimensionless groups of physical quantities that appear in the governing equations for a particular process in the earth are used to scale the physical models of this process. According to the scale model theory of Hubbert (1937), a model is properly scaled to its natural prototype if it is geometrically, kinematically and dynamically similar. Geometrical similarity between an analogue model and a natural prototype implies that all corresponding lengths are proportional and all corresponding angles within the bodies are equal such that the model ratio for length L_R is given as;

$$L_R = \frac{L_m}{L_p} \tag{3.26}$$

Where L_m = model length and L_p = length of the rock being simulated (prototype)

For kinematic similarity, the geometrically similar model and prototype have to undergo similar changes of shape and/or position, where the time required for any change in the model is proportional to that required for the corresponding change in the prototype (Ramberg 1967*b*). This establishes a model ratio T_R given as;

$$T_R = \frac{t_m}{t_p} \tag{3.27}$$

Where t_m and t_p represent the time required for a similar change to occur in the model

and prototype, respectively.

For dynamical similarity between a geometrically and kinematically similar model and prototype, the two bodies need to have similar ratios and distributions of different kinds of driving and resistive forces (gravitational, frictional and viscous) acting on the different particles of the body (Schellart 2002). Thus because the two bodies are kinematically similar, it follows that the velocities **V** and accelerations **A** of corresponding points are proportional (Price and Cosgrove 1990), so that:

$$V_R = \frac{V_m}{V_p} = \frac{L_R}{T_R}, \tag{3.28}$$

and

$$A_R = \frac{A_m}{A_p} = \frac{L_R}{{T_R}^2}. \tag{3.29}$$

Unless the experiment is performed in a centrifuge where the centripetal force developed as the latter spins round is much stronger than the natural force of gravity, the gravitational acceleration **g** in both the model and rock prototype is the same (Price and Cosgrove 1990) - that is, $A_R = 1$. It therefore follows from equation (3.29) that:

$$A_R = \frac{L_R}{{T_R}^2} = 1. \tag{3.30}$$

The mass ratio M_R between the two is given by

$$M_R = \frac{M_m}{M_p} = \rho_R \cdot L_R^3 = L_R^3 \cdot \frac{\rho_m}{\rho_p}. \tag{3.31}$$

3.2 Methods

3.2.1 Field study

Field observations of deformed rocks and their structures represent the most direct and important source of information on how rocks deform (Fossen 2010). Physical models provide valuable knowledge of how various physical conditions (including stress field, boundary conditions, temperature or physical properties of the deforming material) relate to deformation. Numerical simulations on the other hand allow us to control the various parameters and properties that influence deformation. Additionally, both physical models and numerical simulations also provide information on how deformation structures evolve, thereby providing insights into deformation processes involved. However, both are only aiding tools used to help complete the picture of deformation history that is only partly obtainable directly from the rocks. Therefore, they are both built basing on information gathered during field surveys and thus require objective and accurate field observations. As such, the dips and dip-directions were taken for fault planes, joints, foliations, dykes and shear planes, whereas plunge and plunge-direction were taken for lineations pitch, stretching lineations and fold-axes. These were used in geometric, dynamic and kinematic analyses of the structures.

3.2.2 Microtectonic study

Analysis of microstructural fabric of deformed rocks gives insight into the deformational phases they have suffered. Phases of deformation are determined for individual thin-sections and schemes of regional deformation phases are evaluated from schemes of individual thin-sections combined with field observations (Passchier and Trouw (2005); p.196). As such, thin-section studies can be used successfully in reconstruction of structural and metamorphic history of rocks and if carefully interpreted can provide a direct source of information useful to reconstruct tectonic evolution (Passchier and Trouw 2005). Metamorphic mineral growths may contain textures and structures reflecting kinematics and deformation history (Fossen (2010); p.300). For instance, sheet silicates (e.g. biotite, muscovite) and elongate minerals that (re-)crystallise or grow in a differential stress field, orient their sheets or direction of elongation parallel to σ_2 or σ_3 and perpendicular to σ_1 (Nelson 2010). Hence rock deformation in a compressional stress field results in development of fold axes and foliation perpendicular to the direction of maximum compressional stress. Thus the sometimes identifiably varying deformation styles, structural geometry and even mineral assemblages exhibited, offer direct evidence for the different episodes and/or types of deformation.

In order to obtain an overview of the deformational phases suffered by rocks of this study area, analyses were done on some oriented thin-sections cut from samples of mica-schists. Being the 'softer' rock type, the different deformation phases and/or metamorphic events represented by the structural features that were imprinted on these rocks may be identifiable. Therefore, their porphyroblast-matrix[7] relations were studied. When a porphyroblast grows at low- to medium-grade metamorphic conditions, minerals adjacent to the growing grain that do not participate in the reaction (e.g. opaque minerals and quartz)

[7] A porphyroblast is a single crystal of diameter that exceeds the surrounding and inferred to have grown in a solidified rock in response to changes in metamorphic conditions. Matrix refers to the fine-grained ground mass in a rock (Passchier and Trouw (2005); p.314-315).

are not removed completely (Passchier and Trouw 2005). They are instead overgrown and enclosed by the former as passive inclusions. Such inclusion structures mimic the rock structure at the time of their growth and allow a reconstruction of the relative timing of mineral growth, reflecting metamorphic conditions and deformation (Passchier and Trouw (2005); p.191). Since the thin-sections were oriented, the deformational trends inferred from microstructural study were correlated with those obtained from analyses of fault-slip data and from field observations.

3.2.3 Stress reconstruction

As already stated, two methods were applied in combination to constitute the *Stress inversion Via Simulation* method (Sippel et al. 2009). The *kinematic method* (Turner 1953) treats strain and strain-rate and consists of plotting the fault planes and corresponding lineations on a stereoplot, resulting in mutually orthogonal symmetry axes (P and T) of the *contractional-* and *extensional-quadrants*, respectively . The other, the *paleostress method* (Yamaji 2000) based on fault-slip inversion, relates stress and slip through the Wallace-Bott hypothesis[8], resulting in a *reduced stress tensor* which gives the orientation and shape of the stress ellipsoid. A complete fault slip datum usable for stress reconstruction comprises the fault-plane orientation (dip direction and dip amount), orientation of the striae (azimuth and plunge) and the slip-sense (normal, reverse, dextral or sinistral). For manipulation using the PBT-axes method, quality of the sense-indicator for each datum was specified by a number 0–3 where 0=not recorded, 1=excellent, 2=good and 3=poor (Sperner et al. 1993). Applicability and reliability of results obtained using the kinematic method is dependent on a uniform strain field and on a correct grouping of slip information generated during different deformational phases, whereas that for the fault slip inversion approach relies on assumptions underlying the Wallace-Bott hypothesis (Fossen 2010).

Before analysis, the data were divided into four groups loosely described as "tectonic units" (Fig. 3.9. The grouping was based on their location relative to the large-scale ('master') faults. The units included: *Sempaya-Kazingo*, SK - at the tip of the northern ridge of the massif, *Central-Rwenzoris*, C-RWZ - including all the high peaks between Nyamwamba (Ny) and Bwamba (BW) faults, *Kigolo-Kabakoru*, KK - including all foothills around the NW-SE striking Mubuku valley and northeast of it; located south to southwest of Kisomoro (KI) fault and northeast of the Nyamwamba (Ny) fault or actually cut by it and *Kilembe-Nyabirongo-George flank*, KNG - located between Nyamwamba and Ibimbo (IB) faults to the west and the George fault (GF) to the east. These 'tectonic units' were thought to have sustained comparable disturbances of the stress field arising from the large-scale fault zones in their immediate vicinity and the effect of interacting rift segments, so that deformation conditions would be relatively similar (Sperner and Zweigel 2010). Thus results are discussed under these unit however, where the geometry and number of complete data sets allowed, analyses were also carried out for individual outcrops.

[8]That is, slip on a planar fracture surface will occur in the direction of maximum resolved shear stress. Hence strike-slip faults result from horizontal maximum shear stress, normal or reverse faults result if the largest shear stress is in the dip direction and oblique-slip faults result from any other case (Sec. 3.1.3).

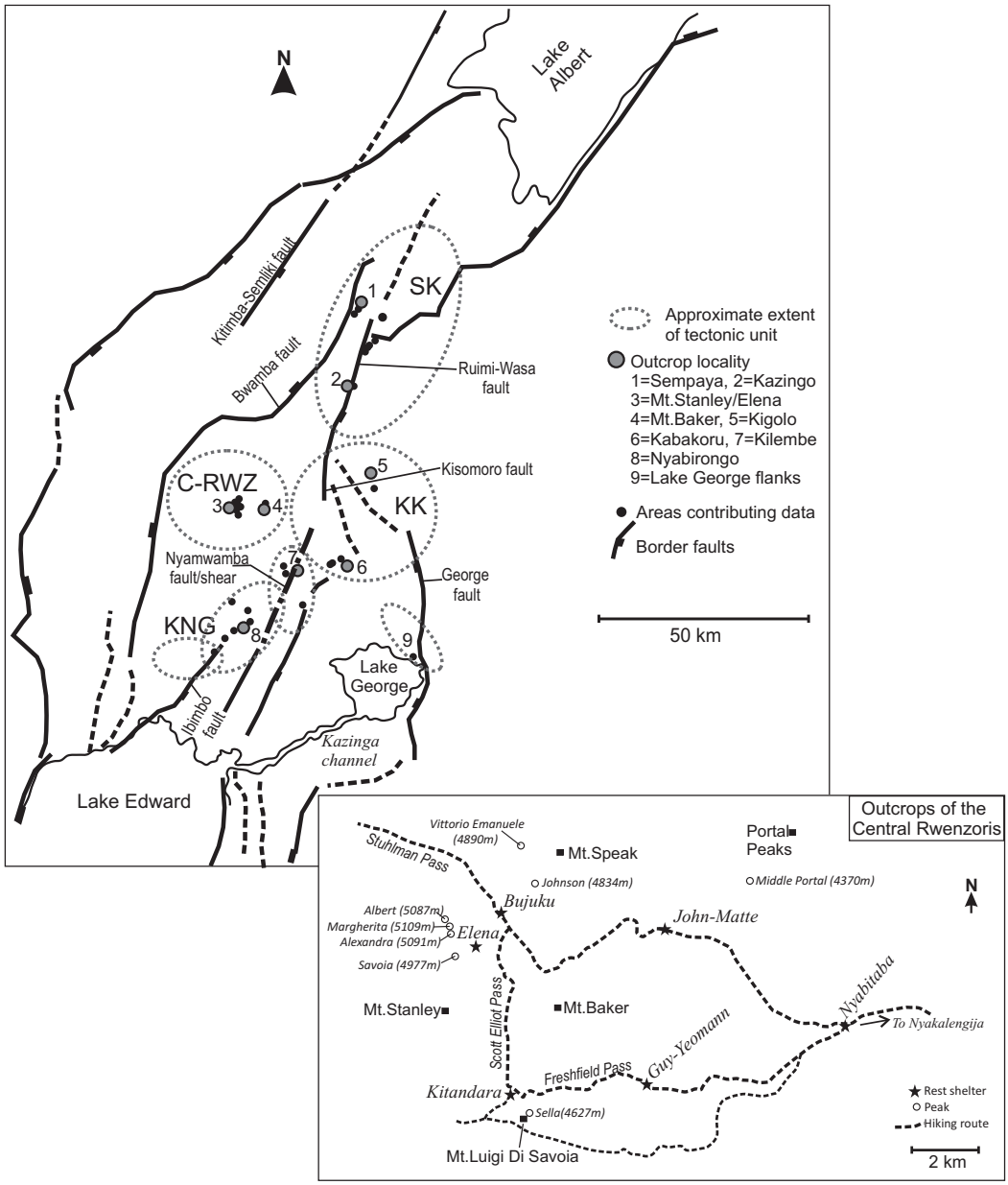

Fig. 3.9 Top: Sketch of Rwenzori block showing distribution of tectonic units relative to major border faults. SK=Sempaya-Kazingo, C-RWZ=Central-Rwenzoris, KK=Kigolo-Kabakoru and KNG=Kilembe-Nyabirongo-George flank. Outcrop localities are shown in the legend. Bottom: Magnification of Central Rwenzoris unit, showing the hiking route and relative reference positions of outcrop localities.

Kinematic approach: PBT-axes method

The Kinematic approach gives the orientation of the paleo-strain axes, but the magnitudes of responsible stresses can only be obtained by adding information about displacement and area of each fault included in the analysis (Fossen (2010), p.197); a detail that is beyond scope of the data collected. The software package TectonicsFP 1.7.01 (Reiter and Acs 1996–2009) invokes the PBT-axes method (Sperner et al. 1993) to graphically construct three theoretical strain axes (P, B and T) for each fault-slip datum, which respectively approximate to the principal stress axes σ_1, σ_2 and σ_3 (Ortner et al. 2002). Since lineations

that do not exactly lie on the fault plane (as is the case for most field measurements) cause errors in calculation, data is first corrected by this program to bring all lineations onto the fault planes. Data is visualised using: (i) Angelier-plots (Fig. 3.10a) which display fault planes as great circles in the lower hemisphere projection (Angelier 1979; Sperner and Zweigel 2010). The accompanying arrow corresponds to the slip-direction and indicates the sense of movement of the hanging-wall block. (ii) Hoeppener (tangent-lineations) plot (Fig. 3.10b) which displays poles to fault planes in the lower hemisphere projection (Hoeppener 1955). Corresponding lineations are drawn in the pole points as tangents to the common great circle of the fault plane pole and the lineation and an arrow indicates the sense of movement of the hanging-wall block. (iii) Pt-axes plot (Fig. 3.10c-left) which displays calculated P-, B- and T-axes of fault planes in the lower hemisphere projection. The P-axis is constructed in the direction of contraction and is assumed to be coincident with the axis of maximum stress σ_1. The neutral B-axis constructed parallel to the fault plane is assumed to coincide with the axis of intermediate stress σ_2, while the T-axis constructed in the direction of extension coincides with the axis of minimum stress σ_3.

The assumption that slip occurs in the direction of maximum resolved shear stress, coupled with an arbitrary unit shear stress τ=1 on each fault plane, enables the Numeric Dynamic Analysis (NDA) to calculate a *reduced stress tensor* for a set of fault-slip data (Spang 1972; Sperner et al. 1993). However, for this operation to yield reasonable results, at least four independent faults - that are oriented differently and with different slip directions - are required (Sperner and Zweigel 2010). Both PBT and NDA regard all faults as neoformed[9] and assume the orientation of the fault planes to be dependent on the acting stress field (Sippel et al. 2009). Thus the P-axis is constructed with a defined uniform angular distance θ[10] from the respective fault plane (3.10c-right). The value $\theta = 30°$ was used since it corresponds to laboratory studies on brittle deformation (Byerlee 1968; Verhoogen et al. 1970; Jaeger and Cook 1979). The value is also associated with high shear-to-normal-stress ratios on fault planes according to the Mohr-Coulomb fracture criterion; and previous studies (Sperner 1996; Reicherter and Peters 2005) have already shown that it is appropriate for natural fault-slip data (Sippel et al. 2009).

The kinematic axes for a heterogeneous data set thus calculated and constructed, form clusters that aid the separation of such data into kinematically homogeneous subsets. For a defined *prediction-probability* (significance level), TectonicsFP 1.7.01 is able to calculate a mean vector and (aperture of) the associated *cone of confidence*[11] for the clusters, using either *Fisher statistics method* (Fisher 1953) or *R% and Center method* (Wallbrecher 1986). For Fisher statistics a *concentration parameter K* (precision, closeness) ranging between 2 (uniform distribution) and infinity (parallel fabrics) is calculated. For the *R*% and Center Method a *concentration parameter R* ("Prozentueller Regelungsgrad") ranging between 0% (uniform distribution) and 100% (parallel fabrics) and the spherical aperture of the confidence cone are calculated. Spherical aperture refers to the radius of the small circle of a spherical normal distribution with equal *R*%-value as the given data (Ortner et al. 2002).

Depending on the geometry of a data set, paleostress-tensors can be calculated using a number of methods (Ortner et al. 2002) e.g. Direct inversion (Angelier 1979), Numerical dynamic analysis (Spang 1972) and the right dihedra method (Angelier and Mechler 1977).

[9] That is, both fracture and slip on the plane are assumed to be caused by the same stress-state.

[10] θ is measured in the plane containing the fault-plane-normal and the slip line.

[11] A small circle within which the true mean of the sampled population of structures is expected to lie.

Since all the above mentioned methods are included in TectonicsFP1.7.01, three comparable kinds of paleostress-plots can be derived from the respective paleostress-tensors, that is,

i.) *Dihedra-* or "beachball" plot (Fig. 3.10d) to display the calculated orientations of the principal axes (σ_1, σ_2 and σ_3) of the paleostress tensor as compressive and distensive dihedra for a stress tensor in the lower hemisphere.

ii.) *Fluctuation-histogram* plot (Fig. 3.10e) to show the angular deviation of the calculated maximum shear stress in the fault plane from the measured striae (frequency (%) on the vertical and sine of deviation angle on the abscissa); and to check the quality of the calculation.

iii.) A dimensionless *Mohr-circles* plot is drawn in the σ_1-σ_3 plane to visualise the normal- (abscissa) and shear-stress (ordinate) introduced by the stress tensor for each fault plane (Fig. 3.10f). The Mohr plots are said to be dimensionless because only stress ratio R is known but the absolute values of σ_1, σ_2, σ_3 are not known; the distance of σ_1 and σ_3 from the origin is unknown and arbitrary in the diagram and the position between σ_1 and σ_3, where the two circles meet, is defined by the stress ratio R (Reiter and Acs 1996–2009). The shear conditions for each fault plane are calculated after a graphical solution of Wallace (1951).

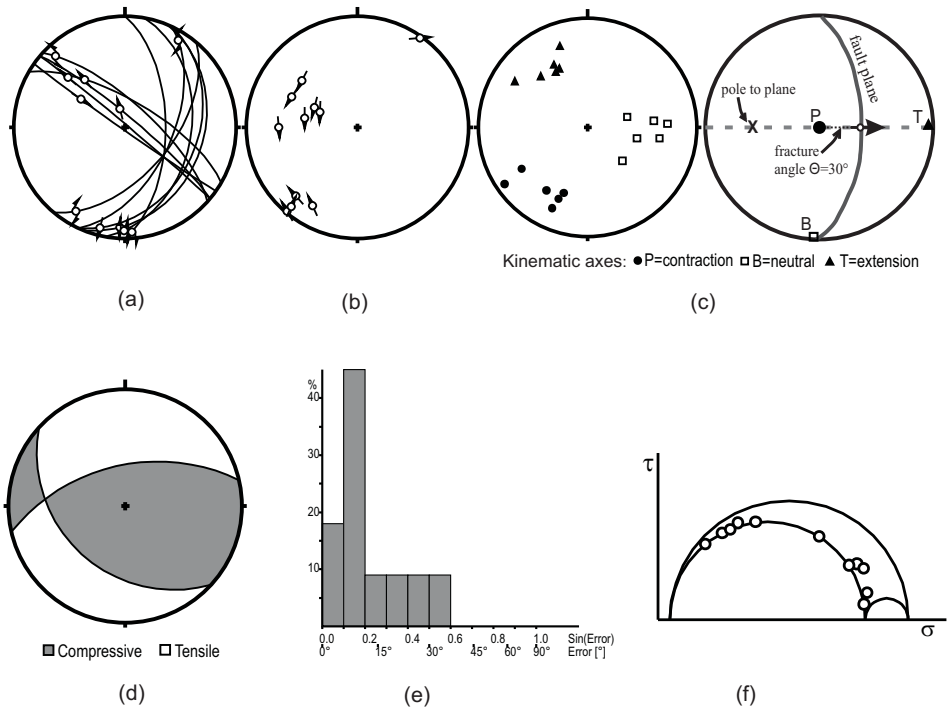

Fig. 3.10 Data visualisation using TectonicsFP1.7.01 program software. (a) Angelier diagram. (b) Hoeppener diagram. (c) left: Pt-axes plot; right: construction of P-axes. [d-f]: Paleostress plots (d) Dihedra. (e) fluctuation histogram: abscissa=sine of deviation angle (Error[°]) between measured direction of striae and calculated maximum shear stress direction; ordinate=frequency (%) of stress-states whose angles of deviation fall within a particular bin-width. (f) dimensionless Mohr diagram: τ=shear stress, σ=normal stress.

Paleostress approach: Multiple inverse method

The multiple inverse method (MIM) is a numerical technique used to separate stresses from heterogeneous fault-slip data so as to understand secular changes in crustal stress, with the assumption that stresses with common principal orientations and common stress ratio represent a state of stress (Yamaji et al. 2010). Similar to the PBT-axes method, a minimum of four independent faults is required for a meaningful calculation that eliminates under-determined problems[12] during inversion. This is because a state of stress has four degrees of freedom[13]. Thus with sufficient data sets, it is possible to calculate orientations of the three mutually orthogonal principal stress axes σ_1, σ_2 and σ_3 (where $\sigma_1 \geq \sigma_2 \geq \sigma_3$) and the ratio of principal stress differences $R = (\sigma_2 - \sigma_3)/(\sigma_1 - \sigma_3)$; which together constitute the corresponding *Reduced Stress Tensor*. The *misfit-angle* β[14] is used as a measure for the fit between a certain stress-state and observed fault kinematics. The reduced stress tensor is then estimated as the one that is associated with the least sum of all misfit angles (Yamaji et al. 2010).

The main processor (version 6.02) of MIM calculates stresses that are consistent with the data. For an input of N fault-slip data and a fault-combination-factor k ($3 \leq k \leq 8$), the main processor calculates the number of fault-subsets equal to the binomial coefficient

$$ {}_N C_k = \frac{N!}{k!(N-k)!} \tag{3.32}$$

where $N!$ stands for the factorial of N,

$$ N! = N \cdot (N-1) \cdot \ldots \cdot 2 \cdot 1 \tag{3.33}$$

The post processor (version 4.16) enables visualisation of stresses on a pair of σ_1 and σ_3 stereograms (Fig. 3.11a) as *tadpole symbols* whose colours denote the stress ratio R and provides functions to analyse the data and stresses. The position of the head of a tadpole symbol on the σ_1 (σ_3)-stereogram indicates the σ_1 (σ_3) orientation, while its tail designates the azimuth and plunge of the σ_3 (σ_1) orientation. Lengths of tails of tadpole symbols indicated above the colour bar denote plunge of stress axes drawn proportional to the difference between 90° and the plunge of the σ_3-axis for the stereogram on the left or plunge of σ_1-axis for a stereogram on the right i.e. 0° (longest tail) to 90° (no tail). For a given set of data, clusters of tadpole symbols with similar colours and similar attitudes represent significant stresses, each of whose representative reduced stress tensors should be determined (Otsubo et al. 2006). Erroneous solutions (noise) appearing in a different colour can be thinned out and the correct solutions enhanced by imposing a high *enhance factor* e, to a data set. In general the value e=8 was applied in the analysis. From the same window, values of standard deviation, mean angular stress distance[15] $\overline{\Phi}$ (expressed as Φ(mean) in the discussion) and mean stress difference[16] $\overline{D}$ (expressed as D(mean) in the discussion) can be read for a data set under a specified state of stress. Values of $\overline{\Phi}$ range between $0 - 90°$, where $\overline{\Phi} = 0°$ corresponds to identical stress-states while $\overline{\Phi} = 90°$

[12]Problems in which the number of unknown parameters i.e. 4, is greater than the number of data.

[13]Three degrees of freedom for the attitude of the stress ellipsoid σ_1, σ_2, σ_3 and a fourth one for the stress ratio R.

[14]Angular difference between the theoretically calculated maximum shear stress (τ_{max}) direction and the observed slip direction along a fault plane.

[15]Mean distance between stress-states expressed as angles.

[16]Mean distance between stress-states expressed as values ranging between 0 and 1.

corresponds to stress-states that are uniformly distributed. The stress difference has a one-to-one correspondence to the angular stress distance in a way that

$$\frac{D}{2} = \sin\frac{\Phi}{2}.$$

Combined approach: Stress inversion via simulation

The data were separated into kinematically homogeneous subsets using the software program TectonicsFP 1.7.01 (Reiter and Acs 1996–2009). This program plots **Angelier** diagrams (Angelier 1979), **tangent-lineation** diagrams (Hoeppener 1955) and **PBT-axes plots** (Sperner et al. 1993) for the data. The *R% and Center Method* (Wallbrecher 1986) was applied to calculate mean vectors and to accentuate clusters of stress axes by plotting the associated cone of confidence at 95% significance level. The direct inversion method minimises the angles β between the calculated directions of maximum shear stress acting along fault planes thereby limiting its applicability to data sets where the fault planes are distributed homogeneously in space (Ortner et al. 2002). Because of scattered fault orientations and high percentage of oblique-slip data (both likely caused by the re-activation of faults with varying orientations), the Direct Inverse Method has advantage over the Numerical Dynamic Analysis which considers all faults as neoformed in accordance with the Mohr-Coulomb criterion (Sperner and Zweigel 2010). Fluctuation histograms derived from direct inversion show lower fluctuations hence a better result is anticipated. Thus the fluctuation-histograms and Mohr plots were derived from the respective paleostress-tensors calculated by direct inversion (Angelier 1979) on the homogeneous PBT-derived subsets. The dihedra (beachballs) were obtained directly from the calculated stress tensor orientation determined by the right dihedra method (Angelier and Mechler 1977). Data which could not be assigned to any consistent subset were plotted on separate PBT-axes plots as 'remnants' (for cases where they constituted $\geq$ 20% of the data subset), while data with unknown sense-of-slip were left for later consideration.

Data comprising the kinematically homogeneous subsets separated out in the PBT-axes method were imported into MIM and simulations run under a specified fault *combination factor* K. Yamaji (2000) cautioned that smaller values of K may yield erroneous and unstable solutions and Yamaji et al. (2010) recommended K=5 for better convergence of clusters. However, to accommodate the low fault count on some data subsets in the studied area, we used the value K=4. The first simulation run under MIM was intended to find preliminary stress-states by testing the data against the σ_1 and σ_3 axes directly obtained from mean vectors of the PBT-axes. In the second simulation run, the preliminary stress-states were improved as they were tested against the entire fault population from the target area. In the case of inversion of focal-plane solutions, we used the value K=5.

Applying MIM to the PBT-derived subsets

MIM considers slip on both neoformed faults and along pre-existing (re-activated) faults hence its application here to compliment the PBT-method, which regards all faults as neoformed (Sperner and Zweigel 2010). MIM calculates σ_1, σ_2 and σ_3 vectors, generates a complete number of stress-states (all solutions that fulfil the low-misfit-angle criterion) for a given set of fault-slip data and plots them on paired stereograms (one perpendicular to σ_1-axis, the other perpendicular to σ_3-axis) of lower-hemisphere, equal-area projection (Fig. 3.11a). Each state of stress is completely depicted by a tadpole symbol on one of the paired stereograms. The result is a large number of diffuse clusters of corresponding

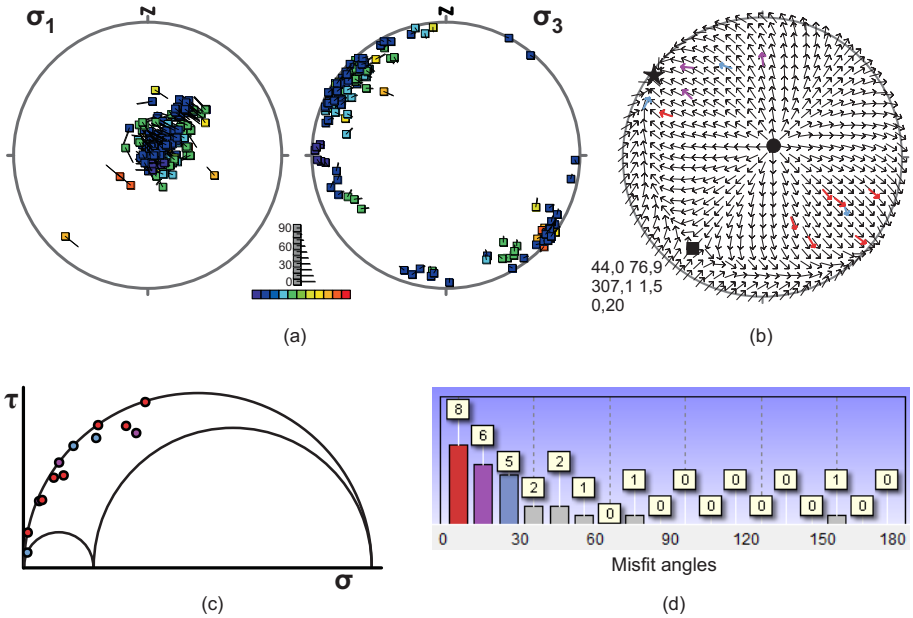

Fig. 3.11 Data visualisation using MIViewer (version 4.16) in MIM. (a) Paired σ_1, σ_3 stereograms. (b) Tangent lineations plot. (c) Mohr diagram: τ=shear stress; σ=normal stress. (d) Fluctuation histogram: abscissa=misfit angles (β°) between measured direction of striae and maximum resolved shear stress direction, bin-width=10°; ordinate=frequency of occurrence of faults whose angles of deviation fall within a particular bin-width.

σ_1- and σ_3-axes in the MIM plot, including but concealing the best-fitting stress-states for the fault population. Clusters of tadpole symbols with similar colours depicting a common stress ratio R and similar attitudes depicting similar σ_1 and σ_3 vectors represent significant stresses for a data set.

Simulation involves specifying a state of stress so that the post processor (*MIViewer 4.16*) calculates the theoretical slip-direction (direction of maximum shear stress, τ_{max}) on each fault, plots them on a stereonet and calculates the angular misfits between the theoretical and observed slip-directions. The resulting misfit-angles β are collectively visualised on a lower-hemisphere, equal-area projection tangent-lineation diagram while their frequencies plot on a fluctuation histogram with bin width of 10°. For subsets indicating more than one stress-state, the angular difference between the stress-states is calculated by MIViewer 4.16 as *Angular Stress Distance* Φ, ranging between 0° for identical stress-states and 90° for stresses that activate faults in opposite directions, when both stress-states are specified. A simulation run is thus completed in two steps. First, a state of stress is designated by specifying the azimuths and plunge of the principal stresses σ_1 and σ_3 and a value for R. The second step involves checking the associated misfit-angle distribution. When a simulation is complete the information is visualised, as illustrated in Fig. 3.11b to d, on tangent lineation plots, fluctuation histograms and Mohr circle diagrams. Shear and normal stresses on the Mohr diagrams are normalised by the differential stress so that τ-values range from 0–0.5 whereas σ-values range from 0–1.0.

The β-distribution serves as a measure for consistency between a stress-state and a data set since a β-value estimates the slip potential for a fault-slip datum under a given stress (Sippel et al. 2009). We use the threshold value $\beta = 30°$ proposed by Nemcok and Lisle (1995). As stated by Yamaji and Sato (2006), the threshold value $\beta = 30°$ corresponds to

the value of *"Stress Distance"* $D \leq 0.517$ of Orife and Lisle (2003). Since D values range from 0 for identical stress tensors to 2 for tensors activating a given fault in opposite directions, the faults separated out will be only those that perfectly or very closely fit to the stress-state in question. Hence, 'a fault-slip datum is said to fit a stress if the angular misfit of its observed and theoretical slip directions, the latter of which is obtained from the stress, is smaller than the threshold (Yamaji and Sato 2006). Therefore, a stress-state that exhibits greatest frequency of low-misfit-angles (fluctuation peaks reduce from origin towards the right) constitutes the most significant stress-state. The first series of simulations were intended to test stress-states only against the particular fault-slip data of a PBT-separated subset. The first stress-state to be tested was the one characterised by directions of σ_1, σ_2 and σ_3 derived from the mean vectors of the associated P, B and T axes, respectively and R-value derived from the corresponding MIM clusters. The solutions were improved by testing different R values indicated by the different colours of the respective MIM clusters.

In the second simulation series, each preliminary stress-state was tested against the entire fault population of the locality from which it was derived, to estimate its potential to be responsible for the activation of other fault-slip data, in particular the remnants (Sippel et al. 2009). Similar to the first simulation, a threshold value $\beta = 30°$ was used to decide whether or not a fault-slip datum fitted to a certain stress-state. Having identified all fault-slip data that could have been activated by a certain stress-state, the degree of misfits was further minimised by interactively checking and comparing the changes in misfit angles when the parameters of stress were slightly varied. Precaution was taken to ensure that such interactive search via successive simulations did not span beyond the space indicated by the previously obtained consistent solutions of PBT and MIM. Thus, only stress-states represented by MIM clusters falling within or in the immediate vicinity of the PBT-derived cones of confidence were tested (Sippel et al. 2009). Ultimately, the information was visualised by the same diagrams as shown in Fig. 3.11 (b to d). Fault data with unknown sense-of-slip were plotted together with the theoretical slip pattern of stress-states determined as optimal solutions. Data that were inconsistent with any of the separated subsets (final remnants) were presented in a separate tangent-lineations plot only in cases where they accounted for more than 20% of the whole data set (Sperner and Zweigel 2010).

3.2.4 Sandbox modelling

Several previous experiments have employed sand as analogue material (Davy and Cobbold 1991; McClay et al. 2002; Michon and Sokoutis 2005; Schreurs et al. 2006). Likewise in this study, dry quartz sand of 0.1–0.4mm size was used to model the brittle behaviour of the upper crust. Unlike brittle-ductile multilayer models that include one or more ductile layers below a brittle one and result in distributed faulting (Brun 1999; Corti 2004; Tirel et al. 2006), faulting in a single layer model is localised. Justification for using brittle crust only in these experiments is derived from experiments (Sokoutis et al. 2007) that have demonstrated that maximum thinning of experimental lithosphere and brittle crust generally occurs at the same spots, implying that although mantle weakness may localise deformation in the crust, it plays a minor role in determining the amount of deformation in the crust. It also has a far-field effect i.e. it does not localise but distributes deformation in the upper crust.

Model scaling

Scale models are required to fulfil the condition of geometric, kinematic and dynamic similarity with the prototype being modelled (Price and Cosgrove 1990) so that sets of model ratios can be established between corresponding parameters (e.g. length, density, time, viscosity etc). Although it is difficult to work with a time ratio that is consistent with ratios of viscosities of real and model materials, physical models done without a centrifuge can still produce fracture patterns similar to those that develop in nature.

The upper crust is brittle with cohesion $C_o = 10^7 Pa$, density $\rho = 2700 kgm^{-3}$, obeys the Mohr-Coulomb failure criteria and has an angle of friction $\phi = 30 - 32°$. Sand can approximate mechanical properties of the upper crust since it is rheologically brittle and cohesionless, has a density $\rho = 1600 kgm^{-3}$ and is a Mohr-Coulomb material with an angle of friction $\phi = 30°$. The height and length of the models were scaled in accordance with equation 3.26 on page 34. To ensure that the size of the model was of comparable order of magnitude to its prototype, a scale of approximately 1:357000 (model:nature) was used. The Moho-discontinuity within the rift being modelled lies at about 25km depth and active faulting can be traced down to 20km depth (Koehn et al. 2008). The model thickness was thus limited to 7cm in order to approximate the 25km thick crust, covering the 20km depth within which brittle deformation is expected. Hence a geometric similarity between the two, with a value of length ratio $L_R = 2.8 \times 10^{-6}$. Opening rates for the western rift are reported in the range 1-4mm/year, thus an average rate ∼2.5mm/year (7.93×10^{-8}mm/second) was considered. The sandbox models on the other hand were extended at rates of 2.8×10^{-2} to 3.35×10^{-2}mm/second. Considering the average opening rate for the natural counterpart and an average rate 3.35×10^{-2}mm/second for the models and applying the scaling equation (3.27) which states that

$$T_R = \frac{t_m}{t_p},$$

the ratio T_R between the time required for a similar change to occur in the model t_m and prototype t_p was of the order of magnitude 2.37×10^{-6}. Experiments were carried out under normal gravitational field so that from equations (3.29) and (3.30) the ratio of accelerations $A_R = 1$, hence dynamic similarity of the model and prototype.

Scope of experiments

Fault nucleation, propagation and evolution in the upper crust of a developing rift zone were simulated by deforming a pack of fine-grained, dry quartz sand in an extensional sandbox. Particularly interest lay in the order of development of fault segments, which were compared with the variously oriented faults observed in the Rwenzori region. The experiments were carried out in a simple sandbox of adjustable length of up to 70cm, maximal height of 22cm and fixed width of 40cm. According to the length scale, the box width represented more than 142km in nature and therefore covered the area of interest. One end-wall was fixed and the other movable by means of a worm-screw, whose one-round crank caused a displacement of 0.15cm on the mobile wall. The free-ends of basal sheets placed below the sand and attached to an extending wall on one end, presented segments of velocity discontinuity (VD) that focused deformation above them. In reality thermal events, thinning of the crust and mantle lithosphere and the elevation history of a surface are all related, although it is not easy to discriminate the driving mechanism from the resultant process. The models used in this study only took into account thinning of the brittle upper crust but elevation- and thermal-history were not modelled. Surface processes such as magmatism, erosion and sedimentation were also not incorporated.

Model setup

From sediment age, earthquake and geomorphological evidence, the rift youngs from L. Albert toward Semliki basin and it youngs also from L. Edward toward L. George basin (Nelson et al. 1992). Thus experiments generally modelled the sinistrally overstepping segments around the Rwenzori block, where the Albert segment propagated southeastward and then southward, while the Edward-George rift propagated northward and later northeastward (Fig. 3.12). The seismically active zone northeast of the block was supposed to be a northward continuation at the tip of the George rift, currently propagating to connect to the Albert segment. To constrain the physical boundary conditions necessary to develop particular end-member configurations of rift-segments, a sequence of experiments with different basal set-up were carried out in the initial modelling attempt. From the latter, some specific boundary conditions were determined and applied to later experiments. To compare different kinds of interaction between rift segments that propagate towards each other, the overstep and extension-orthogonal spacing between the VD segments were varied and the effects studied using three experimental series introduced below.

Series A: Constant extension-orthogonal spacing
In these experiments three VD segments (Fig. 3.13a) were set below the sandpack - two at the periphery and one in the centre. The central segment oversteps left-laterally with one adjoining segment and right-laterally with the other. The left-laterally overstepping segments mimicked the Albert and Edward-George rift-segment interaction while the other presented comparison. For experiments 1, 2, 3, 4 and 5 the VD segments were respectively offset by 6-, 8-, 10-, 12- and 15 cm. Extension-orthogonal spacing between basal sheets was kept constant at about 1.0cm.

Series B: Constant VD segment offset
In these series, both adjoining VD segments were offset by an optimal 10cm from the central VD segments (Fig. 3.13b). The extension-orthogonal spacing between adjacent basal sheets was however varied at 2.5-, 4.0- and 6.0 cm for experiments sb7, sb8 and sb9 respectively.

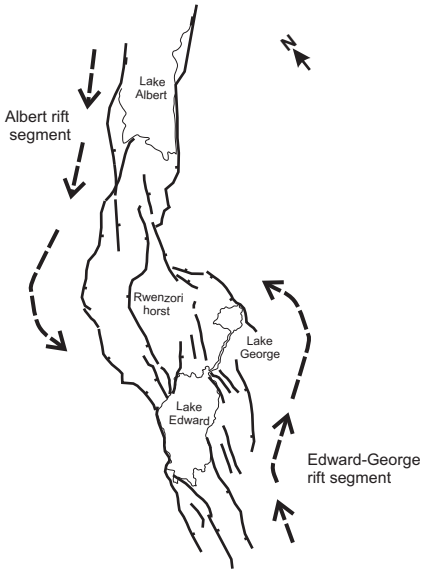

Fig. 3.12 Modelled geometry of the Rwenzori horst and surrounding rift. Broken-line arrows indicate propagation direction of the two rift segments to capture the horst.

Series R: Basal sheet attached to rubber strips

From numerical models (Koehn et al. 2008) clockwise rotation could be attained by mimicking left-lateral overstep of the rift segments that sandwich the Rwenzoris. Thus below the sand-pack we introduced left-laterally overstepping rubber strips at the centre of the model, so that two offset rift segments nucleate during deformation. Rubber strips of average width 5-8cm were attached to the basal sheet, which in turn was connected to the mobile wall. When the worm-screw was turned the pull exerted by the moving wall on the rubber strip in turn exerted traction below the sand pack thereby localising deformation above the rubber. At the region of offset, a "rigid-bridge" was placed between the rubber sheets and attached to each of them. The limits of the rubber strips were cut either orthogonal or oblique to extension vector (see Fig.3.13) and they presented velocity discontinuities (VDs) at the interface with the sand, thereby localising initial deformation above them and parallel to their lengths. The height of the sandpack was 7cm at the beginning of each experiment and the length varied between 29cm and 34cm. Three model settings with left-lateral VD overstep but different geometries of basal-sheet and rubber-strip configurations were used as described below.

i.) Experimental series 1 (SbR3), *shear-dominated transfer*: The model was made up of two rubber strips (7cm-wide, overlap=10cm, overstep=16cm) with straight boundaries that were oriented perpendicular to extension vector throughout the width of the model but parallel to boundaries of a "rigid-bridge" that connects the strips at the zone of overlap in the centre (Fig. 3.13c). The model was deformed by extension of about 3.2cm (11.43km).

ii.) Experimental series 2 (SbR4), *extension-dominated transfer*: The model was made up of 6cm-wide rubber strips (overlap=15cm; overstep=6cm) with straight boundaries that were oriented parallel to the boundaries of a "rigid-bridge" and orthogonal to extension vector throughout the width of the model (Fig. 3.13d). The "rigid-bridge" at the centre was surrounded by rubber sheets in contrast to series 1 (refer to Fig.3.13c). Three different runs of similar set-up were performed, varying the maximum extension from 1.5cm (5.36km) to 3cm (10.71km).

iii.) Experimental series 3 (SbR5), *rotation-dominated transfer*: The model was made up of approximately 7cm-wide rubber strips (overlap=10cm; overstep=5cm) with straight boundaries orthogonal to extension vector near the two "limiting walls" of the model, but oblique to boundaries of the "rigid-bridge" and consequently oblique (65–70°) to extension vector at the centre of the model (Fig. 3.13e). Three different runs of similar set-up were performed, varying the maximum extension from 1.5cm (5.36km) to 3cm (10.71km). A fourth run (SbR7; described below) was done with larger dimensions of the basal sheet, hence different spacing of VD segments.

Experiment SbR6 was set up similar to SbR3, where two rubber strips overstepped left-laterally and were separated at the centre by a "rigid-bridge". However, as shown in Fig. 3.13f, its rubber strips (10cm-width) and "rigid-bridge" (9cm-width) were wider than those for SbR3 and were oriented about 58° to extension vector. The "rigid-bridge" was placed sub-parallel to extension vector and it prevented lateral overlap between rubber strips i.e. actual overlap L = 0cm. The model was extended up to 5.8cm (20.71km).

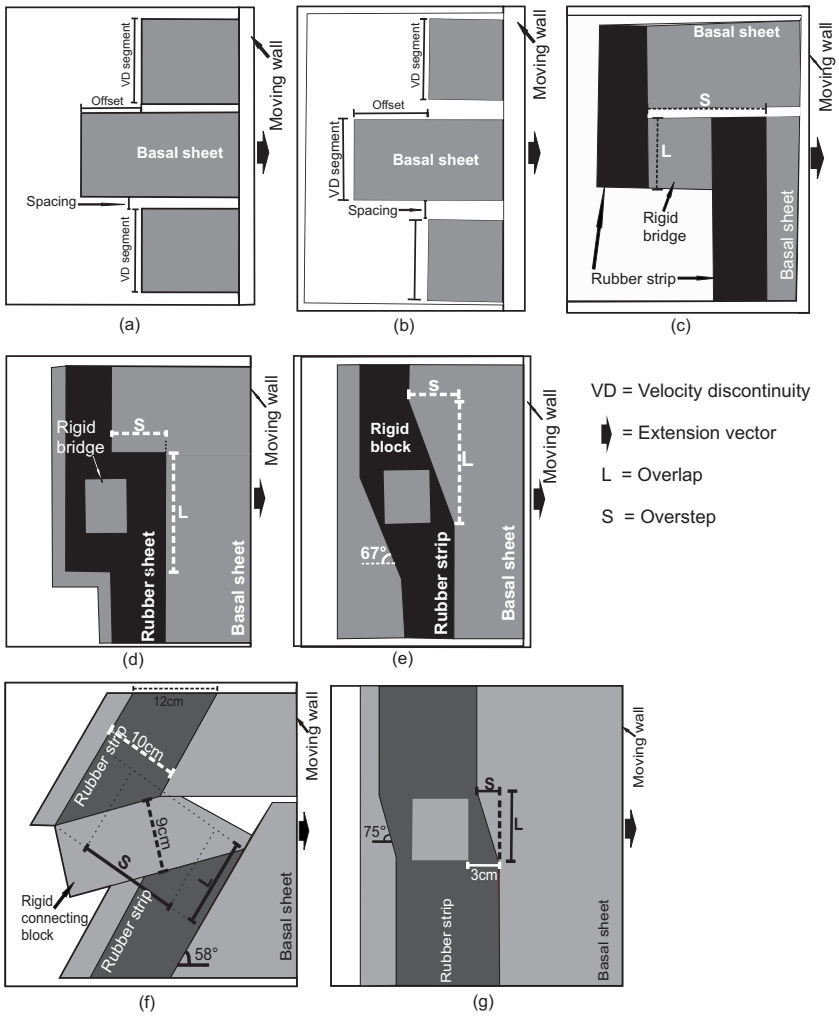

Fig. 3.13 Sketches of plan-view setup below the sandpack. (a) Series A. (b) Series B. [c-g]=Series R: (c) Series 1 (SbR3): VD segments orthogonal to extension vector; wide overstep. (d) Series 2 (SbR4): VD segments orthogonal to extension vector; small overstep and rubber surrounds rigid block. (e) Series 3 (SbR5): VD segment in the centre is oblique to extension vector. (f) Experiment SbR6: rubber strips non-orthogonal to extension vector (g) Experiment SbR7. L=overlap, S=overstep. Arrows indicate extension vector.

Experiment SbR7 was also set up similar to experimental series 3 (SbR5), but with a wider strip of rubber (10.5cm) and larger "rigid-bridge" in the centre (8.5cmx7.0cm) enclosed within the oblique section of the rubber strip, which was oriented 75° to extension vector (Fig. 3.13g). The oblique segment of length represented by L (=11cm) created a small left-lateral offset of about 4cm between the two orthogonal segments of the rubber strip. The model was extended to a maximum of 5.5cm (19.64km).

Varying the sizes of offset and extension-orthogonal spacing between VD segments resulted in different rift evolution patterns and geometries and variable behaviour of interacting fault and rift segments. The implications of the developed fault geometries, age relationships and model rift-segment interactions were discussed with reference to structures found in the Albertine Rift System.

Chapter 4

Field Study and Microtectonics

This chapter contains a short discussion of field observations and how the rock samples and structural data collected were put to use. Field observations and usage of data are presented first, followed by results of geometric structure analysis and finally results of microstructural study.

4.1 Field observations and data

During the field surveys several observations were made, oriented rock samples collected and structural measurements taken for various structure types. Apart from faults, the field study revealed several other structures - both brittle and ductile - that were correlated in trend. These included dykes, folds, foliation, joints, shear planes and stretching lineations. A photograph in Fig. 4.1a, taken along the northeastern nose of the mountains, shows part of the western border fault. The Rwenzoris are sliced by high angle normal faults, examples of which are shown in figures 4.1b and c. Surface expressions of faults at depth were also seen where there has been relative displacement of volcanic layers e.g. Fig. 4.1d or of detrital sediments e.g. Fig. 4.2a.

Crenulation and fold axial planes generally portrayed NE-SW and NW-SE trend with SE and SW dip respectively, as exemplified by figures A.1c and d. Plunge was generally steeper (50–75°) for the NE trending axes and the limbs were tighter than for the NW trending fold axes. The N-S trending foliation showed steep east-ward dip, while the majority of stretching lineations dipped SE-ward. However, foliation more commonly showed W-E to ENE-WSW strike and occasionally porphyroclasts were found to possess trails parallel to the foliation e.g. Fig. A.2a. The NE and NW oriented shear zones likewise showed SE- and SW-ward dips respectively, for example figures 4.2b, A.1a and A.1b. Most faults, joints and dykes also portrayed NE-SW and NW-SE strike with southeast- and southwest-ward dip, respectively. However, N-S strike was also observed on a minor scale.

From the observations above, some structural trends (e.g. NE-SW oriented fold axes) suggested local NW-SE compression and NE-SW extension, while others (e.g. NE-SW oriented ductile shear planes) suggested local NE-SW compression and NW-SE extension. The N-S striking joints and normal faults suggested W-E extension whereas similarly oriented strike-slip faults could suggest same extension direction but with approximately N-S compression. An example of an old fault plane with calcitic mineral growths forming

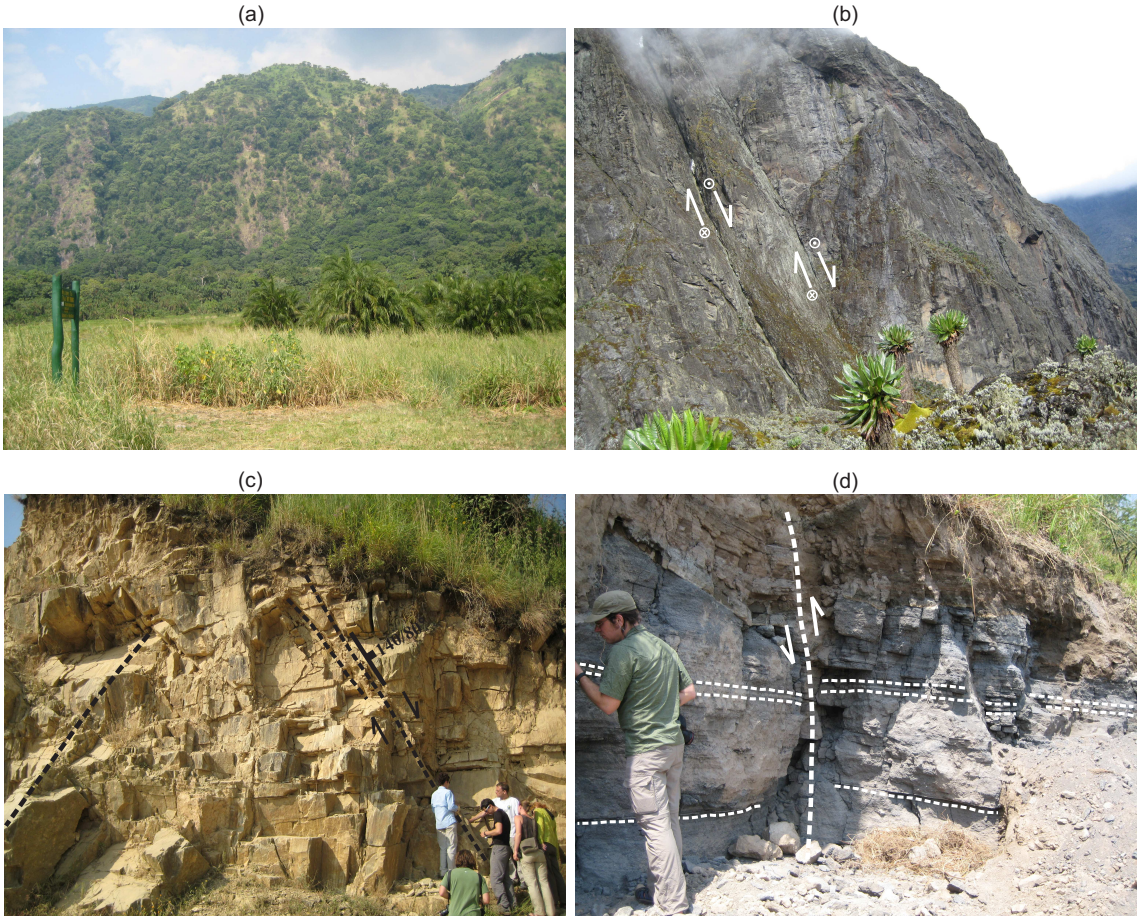

Fig. 4.1 (a) The face in a distance forms part of the western border fault (dip 270/50°) flanking the northeastern nose of the Rwenzori block. Photograph taken near Sempaya hotsprings. (b) Two brittle normal faults on an outcrop along the way from Elena towards Kitandara, on the left side. (c) Trace (right) of a normal fault dipping 80°SE; to the left is a trace of a conjugate fault dipping in the opposite direction. Photograph taken at elevation 1514m, facing SW. (d) NE-SW striking fault in volcanic layers at Bunyaruguru volcanic field; displacement of about 5cm was observed on the thin white layer highlighted in the centre of the photograph.

lineations indicative of slip direction is shown in Fig. A.2b. In some instances joints exhibited upward bending and change of dip from top to bottom. At Kanyampara river for example, dips of joints were observed to change from NW (310/75) to SE (130/75) whereas on a fault at Kajwenge the dip changed from NE at the top to SW at the bottom. Such bending of fractures with changing dip-directions, coupled with existence of lineations on the fault plane cutting across the same joints, suggested ductilely deformed rocks that were later reactivated in a brittle deformational phase.

The structural measurements presented in tables B.1 to B.5 were used for geometric data analysis (section 4.2) so as to show the spatial distribution and orientation of the various structures. Thin-sections were cut from oriented rock samples and used in microtectonic study of the rocks (section 4.3). Fault-slip data (table B.5) were also used in kinematic analysis so as to obtain kinematic axes and in dynamic analysis so as to determine paleostresses responsible for the faults and deduce the shape of the corresponding stress ellipsoid.

Fig. 4.2 (a) Down-dropped sediments (centre) that left a shoulder to the south, indicating a new normal fault or recent reactivation with normal displacement, of an old fault beneath the sediments. First sighted in 2009, the trend of the fault was sub-parallel to that of the Kazinga channel (ENE), south of which it was located. (b) Shear zone of dip 190/51° containing about 12cm-wide gouge and shear bands with top-to-north. It was found within N-ward-thrust mylonitic amphibolite rock at elevation 4308m, a few hundreds of meters from Kitandara hut towards Freshfield Pass.

4.2 Geometric analysis

Although limited measurements were taken for each of the encountered structure types, the data as shown in the respective Pi-plots[1] and corresponding Eigenvector-plot[2] and/or Rose-diagram[3], presented agreeably representative trends. Attitudes of fold axes and of dikes are useful stress indicators but in this case the data collected were too few to be plotted on a diagram. The plots in Fig. 4.3 show general spatial distribution of structures, where the total sum of measurements were plotted together for each structure type. Figure 4.3a shows the Pi-plot and Eigenvector-plot for foliation. It portrayed scattered poles in the northern hemisphere indicating various trends but general southward dip, with gentle to moderately steep angles. Likewise, the poles to shear planes concentrated in the central northern hemisphere (Fig. 4.3b) and the Rose diagram indicated mainly WNW-ESE strike with dips of 40-60°. Stretching-lineations indicated concentration in the southern hemisphere of the lineations-plot with azimuths ranging between 080 and 220 and plunge of 20-50° (Fig. 4.3c), which correlated well with the trends of shear planes. The joints on the other hand displayed general heterogeneous Pi-pole distribution with gentle to moderate plunge, representing steep to sub-vertical joints (Fig. 4.3d). The eigenvalues indicated highest pole concentrations to the east and west of the eigenvector diagram indicating predominantly N-S strike of joints.

In Fig. 4.3e, the total sum of fault planes are displayed on a Pi-plot. These too portrayed general heterogeneous Pi-pole distribution with gentle to steep plunge. Similar to joints, the eigenvalues for faults indicated highest pole concentrations to the east and west, followed by the north and then south of the eigenvector diagram. Although a whole range of strike azimuths was represented, the Rose-diagram showed predominant NNE-SSW to

[1]Lower hemisphere projection of poles to planes

[2]Equal area projection of eigenvectors with a best-fit great circle passing through eigenvectors with median, greatest and smallest eigenvalues as poles; after Bingham (1964). Note: for planes, TectonocsFP uses data of corresponding poles to planes for computation

[3]Directional histogram

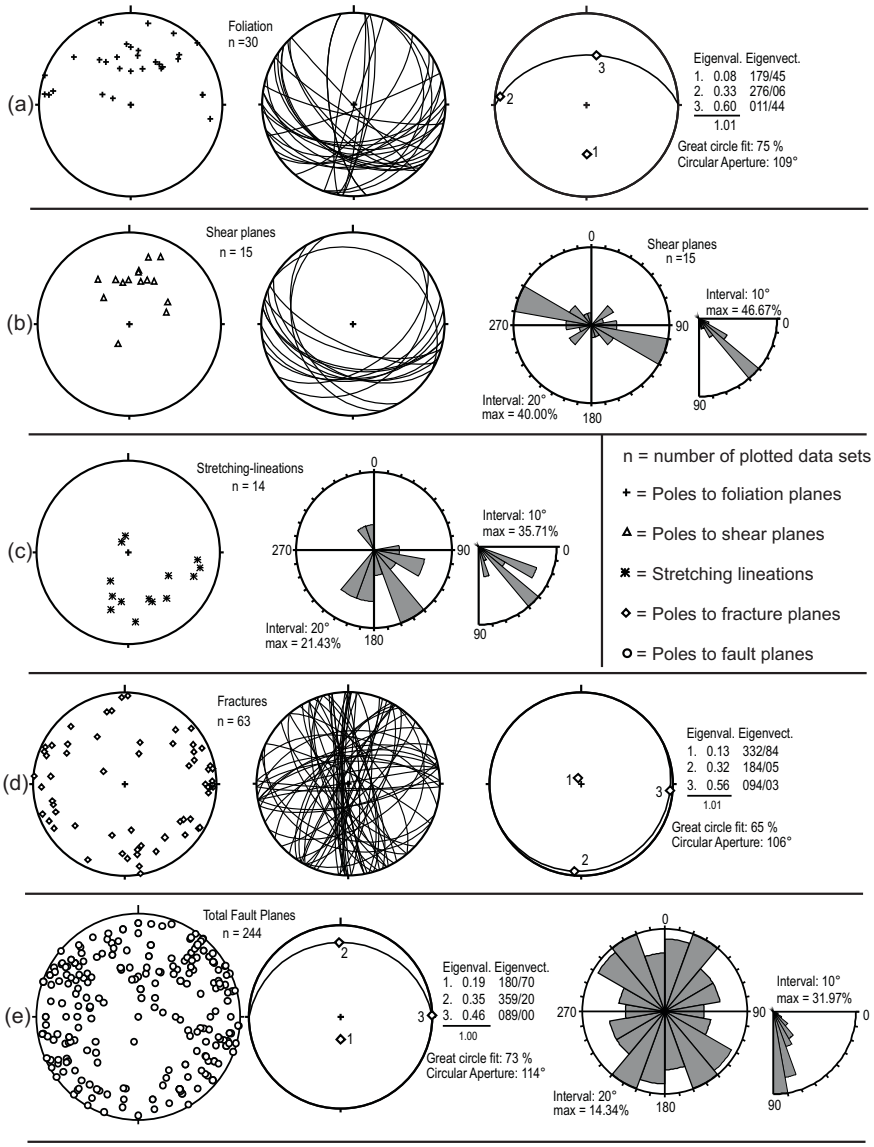

Fig. 4.3 Lower hemisphere projection diagrams showing general distribution of structures in the study area. (a) Pi-plot, planes and eigenvector diagram for foliation. (b) Pi-plot, planes and Rose diagram for shear planes. (c) Lineations-plot and Rose-diagram for stretching lineations. (d) Pi-plot, planes and eigenvector diagram for joints. (e) Pi-plot, planes, eigenvector diagram and Rose-diagram for faults.

NW-SE fault plane strike, with moderately-steep to vertical dips. Such heterogeneity was not only evident in the distribution for summed up data but was also portrayed on outcrop-scale.

Figure 4.4 shows geometric distribution of fault plane data on outcrop-scale, displayed on Pi-plots and corresponding Rose diagrams. Kigolo portrayed two dominant directions of strike in the NW-SE and NNE-SSW (Fig. 4.4b). Bujuku and Kilembe exhibited a whole range of azimuths dominated respectively by NNE-SSW (Fig. 4.4e) and NE-SW (Fig. 4.4i). Whereas most outcrops exhibited heterogeneous fault trends, some were dominated by one clear preferred strike direction e.g. Elena with approximately NW-SE to NNW-SSE (Fig. 4.4c), Kitandara with NNW-SSE (Fig. 4.4g) and Nyabitaba-John Matte with NE-SW (Fig. 4.4h) trend. From the overview of fault distribution presented above, it became

clear that the fault-slip data were of heterogeneous nature even on outcrop-scale. Hence the reason for the choice of method for further data analysis lay in the fact that both the BPT-axes method and the multiple inverse method that comprise the Stress Inversion Via Simulation (SVS) method, were capable of separating stresses from heterogeneous data, provided a data set consisted of at least four independent faults of known attitudes.

4.3 Microstructural study

Microstructural study was carried out on a few thin-sections cut from mica schists, with the aim to identify the different deformation phases and/or metamorphic events represented by micro-structural features. Rocks were composed mainly of muscovite, biotite, chlorite, quartz and feldspars. Porphyroblasts were mainly of cordierite, some of which were surrounded by sillimanite over-growing the muscovite around the blasts. A few euhedral-subhedral garnet blasts were seen to over-grow micas and feldspars. From the appearance in thin-section, older foliations may have been obliterated or their orientations disturbed during progressive or subsequent deformation but three to four deformational phases were identified.

Assuming that the cordierite porphyroblasts had not been significantly re-oriented during or after their growth, two to three deformational phases (D1, D2, D3) were respectively recorded by the straight, folded or bent and oblique inclusion line patterns in Fig. 4.5a. The porphyroblast includes two S_i[4] patterns namely:

(i) straight approximately W-E oriented inclusions S1 indicating that the blast grew after D1, which was probably a ductile deformation phase of relatively high-grade metamorphism during which the rocks developed straight W-E schistosity overgrown and preserved by the blast.

(ii) folded or bent inclusions S2 oriented at high angles to S1, indicating that blast growth continued inter-tectonically before and syn-tectonically through the next phase of deformation D2, which was probably a ductile deformation phase of medium-grade metamorphism that developed the bent foliation patterns. Hence, the relative growth range for this group of porphyroblasts was D1<P_C $\leq$D2, where P denotes the Porphyroblast.

The third and faint foliation pattern S3 (Fig. 4.5a) beyond the rims of the cordierite blast represented the S_e[5] foliation, developed oblique to S1 as a result of D3 deformation. Presence of crenulations and enormous cracks along rims of the blasts suggested that D3 was a brittle-ductile deformation phase of low-grade metamorphism, which occurred at very low temperatures. In Fig. 4.5b however, cordierite porphyroblast growth appeared to have ceased before development of the crenulation cleavage caused by D2 and which wraps around it. Hence the blast included only straight S1 patterns and the relative growth range for its group of porphyroblasts was D1<P_C <D2.

Figures 4.5c and d show cordierites that include curved and crenulated patterns that suggested post-D2 and syn-D3 growth, represented in D3$\supset$P growth range. Porphyroblasts that grew following folded mica-rich zones (e.g. Fig. 4.6a) suggested syn- and post-D3

[4]Surfaces of aligned elongate inclusions (internal foliation) within the porphyroblast.
[5]External foliation existing in the matrix (Passchier and Trouw 2005).

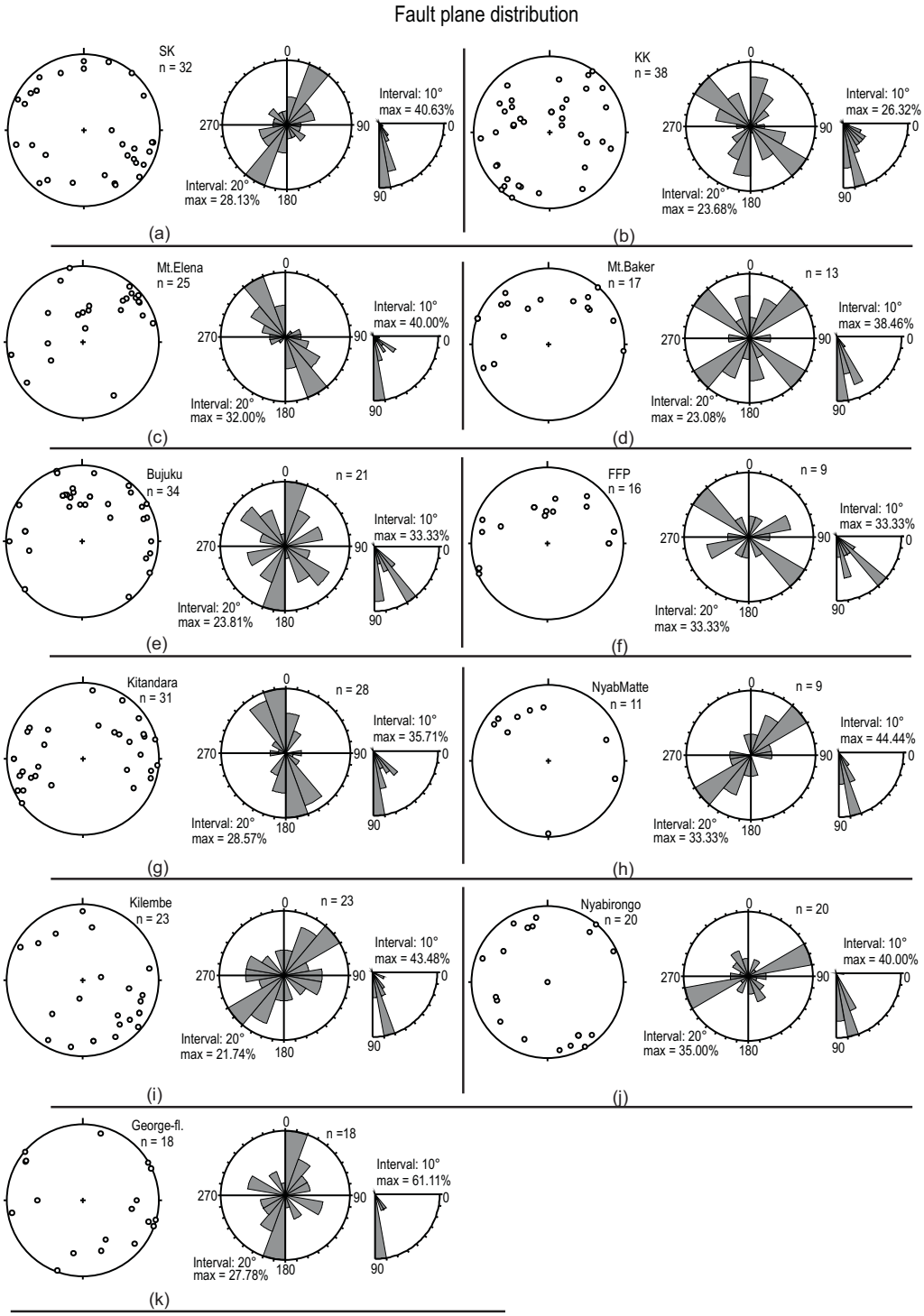

Fig. 4.4 Outcrop-scale distribution of faults. left: Pi-plot; right: Rose diagram (a) Sempaya-Kazingo (b) Kigolo-Kabakoru (c) Elena (d) Mt.Baker (e) Bujuku (f) Freshfield Pass (g) Kitandara (h) Nyabitaba-John Matte (i) Kilembe (j) Nyabirongo (k) Lake George-flanks.

growth, during which schistosity was refolded along S3 axes oblique to S1. Their relative growth range was D3$\supset$P$_C$ $\leq$D4. The latest and probably brittle phase of deformation D4 was of very low-grade metamorphic conditions as suggested by breakage of micas at the would-be fold-hinge zones and development of kinks (Fig. 4.6b). Such features

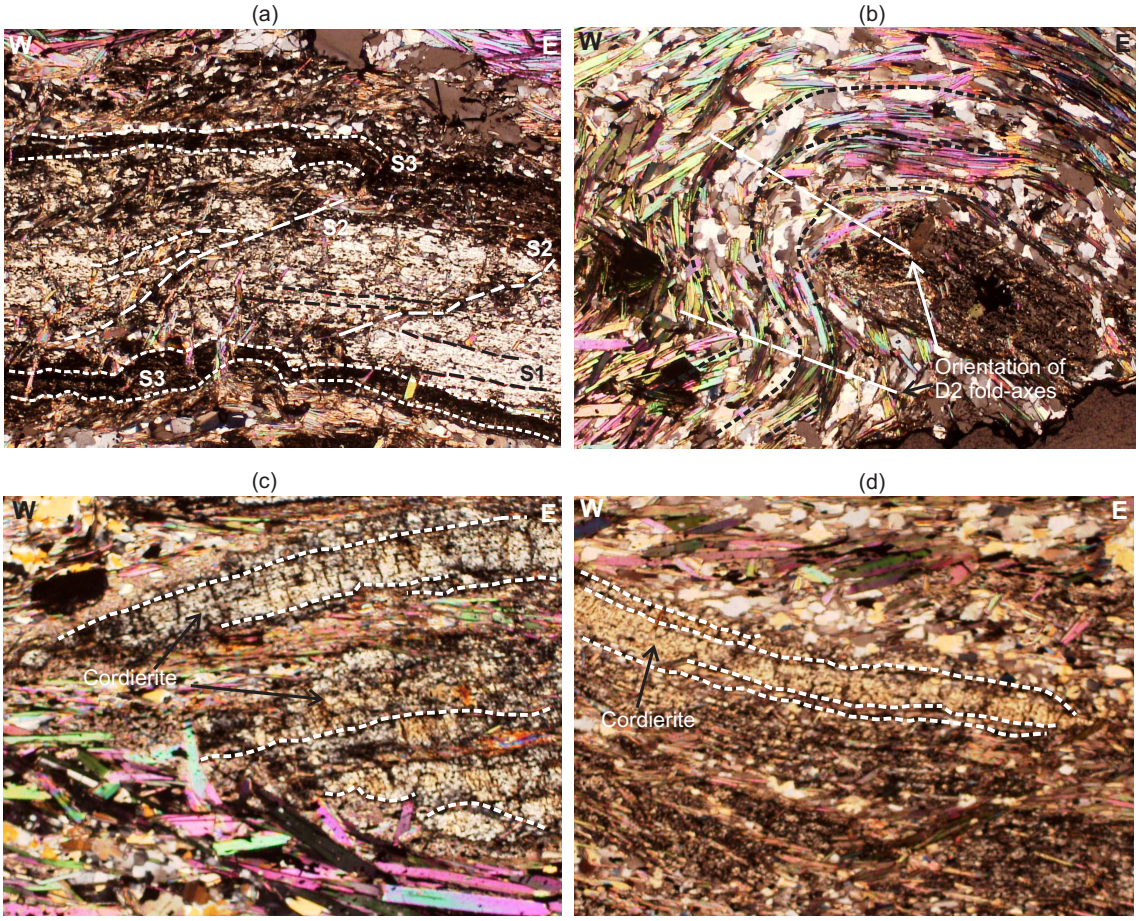

Fig. 4.5 Micrographs showing (a) D1, D2, D3 deformation fabrics. Two S_i foliations S1, S2 included by cordierite porphyroblast. Straight W-E trending inclusion patterns S1 highlighted by black broken lines represent D1. Bent N-S trending patterns S2 highlighted by white broken lines cutting across S1 patterns at high angles represent D2. Faint patterns S3 oblique to S1 and highlighted by white broken lines represent D3. Porphyroblast growth range D1<P≤D2. (b) D2-micas forming S2 crenulation cleavage folded around a cordierite blast that included straight S1 foliation; growth range D1<P<D2. (c-d) Cordierite blasts that over-grew bent or curved D2 inclusion fabric, which is oblique to the poorly developed younger foliation defined by recrystalised micas. Curved inclusion patterns suggested syn-tectonic blast growth, probably syn-D3; growth range D3⊃P. Elongate nature of blasts indicated growth along compositional layering.

are said to develop in micas when slip occurs on (100)[001] at low temperature and/or low strain rate (Passchier and Trouw (2005); p.61). Kink bands can also form in fine grained metamorphic rocks due to application of compressional stress, thus Fig. 4.6b may reflect D3 which was a brittle ductile deformation phase. Microboudinage in cordierite porphyroblasts for instance in figures 4.6c and d, also attested to similar deformation conditions.

On the whole, porphyroblasts were generally elongate indicating growth along compositional layering and the S_i surfaces were clearly defined suggesting low-temperature metamorphic conditions (Passchier and Trouw 2005). The presence of passive inclusions mainly of quartz and opaque minerals in cordierite porphyroblasts, indicated cordierite growth under low to medium grade metamorphic conditions. Evidence suggested that foliation in the schists has been re-oriented at least three times during the deformation phases D2, D3 and D4. The latest and poorly developed foliations resulting from D4 over-grew the

cordierites as seen in Fig. 4.6d. Although the micas that describe this late foliation were scattered and did not grow along fold hinges, which would otherwise describe the most recent foliation, their longer axes clearly traversed older foliations. The absence of broken or micro-faulted inclusions indicated that cordierite growth was complete by the time the brittle deformation phase D4 set in. Inclusions of quartz also showed strong andulose extinction and sub-grain development, attesting to dynamic recrystallisation due to recent strain effect.

Microboudinage was seen in some porphyroblasts having necks corresponding with crenulation fold axes and with quartz and mica recrystallising in the necks (see Fig.4.6c, d). The micro-boudins indicated breakage under brittle deformation and the recrystalised quartz and mica in the neck grew during and/or after deformation. As noted by Passchier and Trouw (2005) the mineral assemblage that grows in necks of micro-boudins is indicative of the metamorphic conditions during deformation. They also noted that at low temperatures, minerals are found to deform in brittle manner by a combination of a fast and slow process especially by fracturing accompanied by pressure solution or by kinking in combination with twinning. Although there was no evidence for twinning, fracturing, kinking and pressure solution leading to recrystallisation of quartz and mica presented good evidence that D4 was a brittle deformation phase that occurred at low temperature conditions.

The garnets were undeformed, small-sized and randomly oriented suggesting availability of many suitable nucleation sites, hence high nucleation rate relative to growth rate (Passchier and Trouw 2005). They contained inclusions of opaque minerals with both straight-line and random patterns. Although they did not exhibit any zonation, some parts of these blasts were inclusion free. Because of their undeformed nature and lack of zonation and the fact that for garnets multiple nuclei form simultaneously and grow amoeba-like with a constant growth rate to coalesce later to a single garnet (Passchier and Trouw (2005), p.190), it can be deduced that the garnets formed post-D4. As such their relative growth range would be D4<P_G. The observations and deformation history deduced from the different mineral relations were summarised in a relative age diagram in Fig. 4.7a.

The following inferences were made from deformational micro-structures, assuming that the cordierite porphyroblasts were not significantly re-oriented during or after growth:

(a) S1 was a W-E striking foliation indicating N-S compression during D1.

(b) S2 was a NNW-SSE striking foliation indicating ENE-WSW compression during D2.

(c) S3 was an ENE-WSW striking foliation indicating NNW-SSE compression during D3.

(d) The youngest and poorly developed foliation S4 with NE-SW strike indicated growth during a brittle regime D4, with approximately NW-SE compression direction.

(e) Foliations S3 and S4 were both oblique to S1 but S4 was steeper and deflected S3 where they intersected.

(f) Similar to rocks metamorphosed in a differential stress field, the ENE-WSW strike of S3 foliation and the NNW-SSE strike of S2 foliation in thin-section were respectively sub-parallel to the NE-SW and NW-SE orientations of crenulation and fold axes observed in the field. They also corresponded with those of other structures e.g. joints and faults as earlier seen in sections 4.1 and 4.2. Since under deformation the fracture or shear orientation and dip are strongly linked to pre-existing pervasive fabrics that

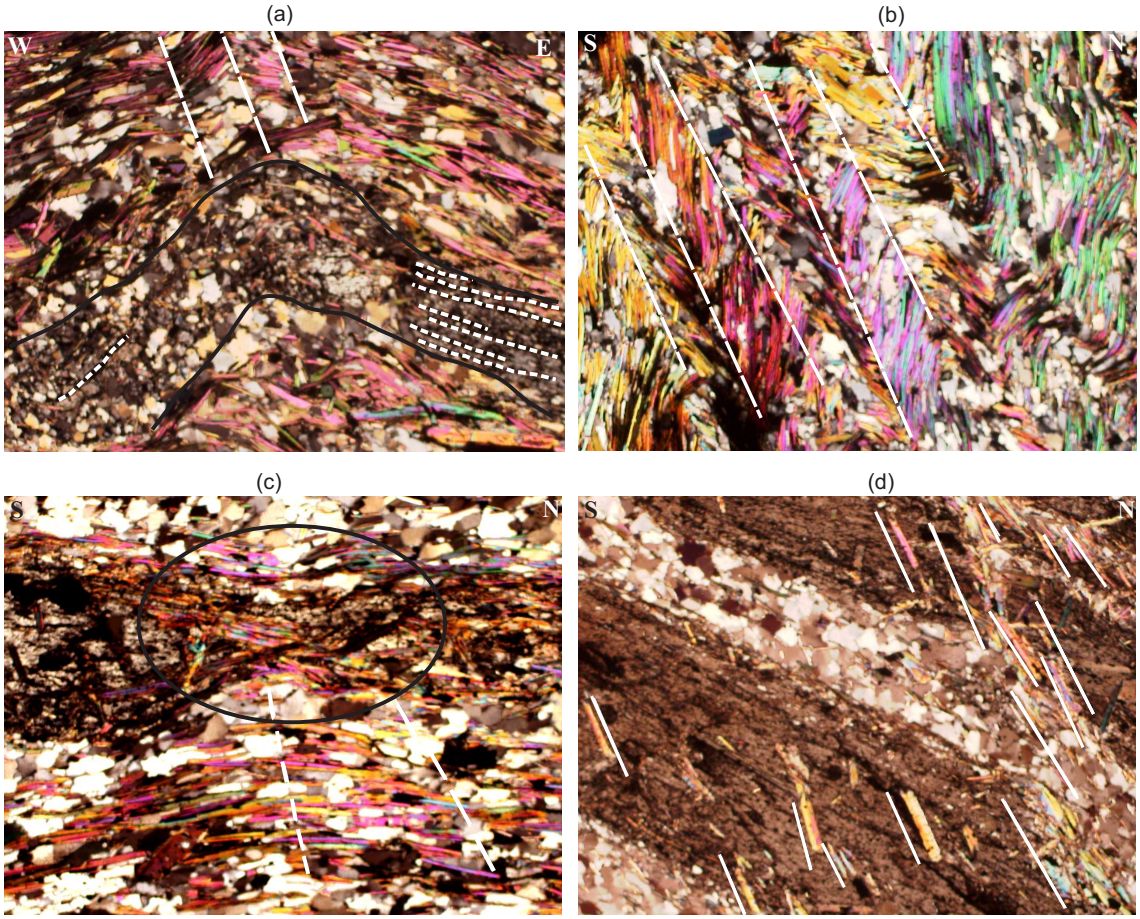

Fig. 4.6 Micrographs showing (a) Cordierite blasts that mimic D3 folded pattern in mica-rich zones. (b) D3 tight folds or kinks in mica. Relative growth range D3⊃P≤D4. The large blast in a is older, having grown after D1 (i.e. growth range D1<P) as suggested by the very straight inclusion patterns. [c-d]: Cordierite microboudinage from D4 (in c:centre - encircled; in d:upper-right) sub-parallel to axes of crenulation cleavage probably D3; indicates that porphyroblast growth was complete before D4. In c, post-D4 mica growth between microboudins (encircled) developed a new cleavage pattern oblique to the older one. In d, a new cleavage developed through the necks (highlighted by the white lines parallel to the micas), sub-parallel to the post-D4 mica crystals that over-grew cordierite blasts.

present anisotropic fracture strength, such sub-parallel relationships indicated that the faults and shear zones to some extent took advantage of pre-existing cleavage planes.

(g) The inferred compression directions suggested extension in the W-E, NNW-SSE, ENE-WSW and NE-SW directions respectively, during deformation phases D1, D2, D3 and D4. With the assumption that foliations S1, S2, S3, S4 developed in the same sequential order and that the direction of compression reflected by each of them corresponded to the direction $S_{(Hmax)}$[6] of the stress field prevalent at the time of its development, rotation of stress axes can be inferred. Hence it was generally deduced that axes of extension rotated in clockwise manner from the W-E through NNW-SSE, ENE-WSW and NE-SW directions as seen in Fig. 4.7b, similar to the clockwise rotation of extension directions demonstrated for different sections of the East African rift by workers such as Strecker et al. (1990); Strecker and Bosworth (1991) and Ring et al. (1992).

[6]The maximum horizontal principle stress direction.

However, according to these results, the final rotational increment from ENE-WSW to NE-SW direction was counterclockwise, implying non-uniform clockwise rotation of axes. It can thus be argued that the variation of horizontal extension directions during the different respective deformational phases reflected temporal rotation and/or deflection of stress axes.

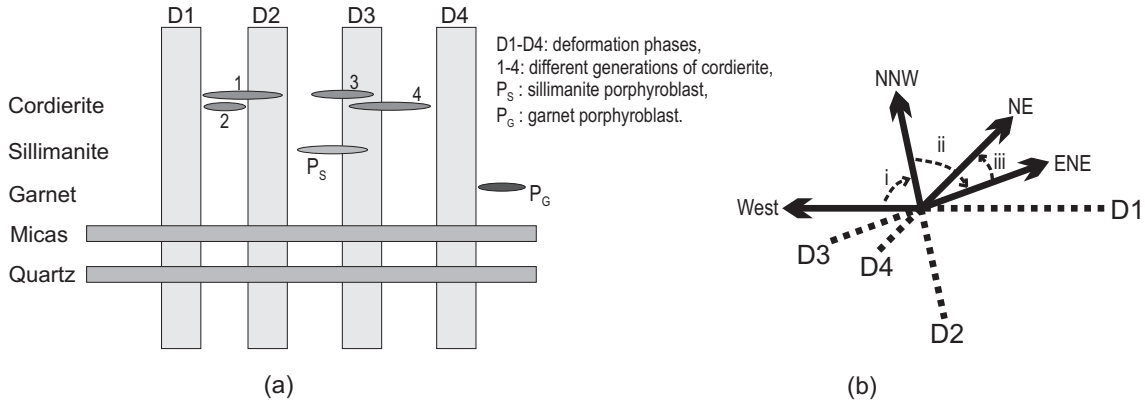

Fig. 4.7 (a) Relative age diagram summarising deformation history. Micas,quartz that form the foliation and matrix grew throughout the rock history, probably re-crystallising after each phase of deformation. Different generations of cordierite porphyroblasts reflected growth ranges D1<P_C ≤D2, D1<P_C <D2, D3⊃P_C, D3⊃P_C ≤D4 for the respective groups 1, 2, 3 and 4. Sillimanite grew around cordierites of post-D2 age, hence growth range D2<P_S ≤D3. Garnets were undeformed, post-D4 age, growth range D4<P_G. D1, D2, D3, D4=deformation phases. P=Porphyroblast; subscript C=Cordierite, S=Sillimanite, G=Garnet. (b) Vector diagram illustrates clockwise rotation of extension directions in the Rwenzori region as deduced from microtectonic study of rock thin-sections. Notice that rotation step iii was counter-clockwise.

Chapter 5

Results of Fault-Slip Analysis

This chapter contains results of fault-slip data analysis for the different tectonic units. For purposes of comparison, stress-states were also determined for single outcrops, for cases where at least 5 data sets showed misfits $\leq 30^{\circ}$ and the specified stresses differed from those obtained for the whole 'tectonic unit'. Although for most of such cases the number of data sets that satisfied a certain stress-state on a single outcrop (n^*) were in general less than 10, they portrayed differences in stress axes orientations that evidently suggest temporal and/or spatial variation of stresses. First, stress-states inferred from PBT-axes separation and solutions obtained by applying MIM[1] to the PBT-derived subsets are presented, followed by a treatment of fault data with unknown sense of slip. Numerical results calculated by the PBT-axes method are presented in Appendix C, whereas those from the MIM are presented in Appendix D. A discussion of the results with summation and proposed chronology of stresses, are presented at the end of the chapter.

5.1 Kinematic and dynamic analysis

Separation of clusters of P (σ_1), B (σ_2) and T (σ_3) axes yielded at least two kinematically homogeneous subsets for each tectonic unit. PBT-inferred stresses are presented on diagrams showing mean vectors of P-, B- and T-axes for each of the obtained subsets, where clusters of stress axes were accentuated by plotting their associated cones of confidence (95% significance). The respective dihedra were generated directly from the stress tensors calculated using the right dihedra method. MIM-generated stress-states on the other hand were portrayed on tangent-lineation plots that show relative positions of the stress axes.

5.1.1 Northern Rwenzoris

Separation of clusters of P, B and T-axes for Sempaya-Kazingo area yielded two kinematically homogeneous subsets SK-1 and SK-2, attesting to two states of stress with different modes of slip.

(a) Extension (main rift)
PBT-mean-vectors for subset SK-1 (Fig. 5.1a-left) indicated a steep ($> 70^{\circ}$) P-axis also supported by the dihedra-plot (SK-1; Fig. 5.2), sub-horizontal NE-SW trending B-axis

[1] Multiple Inverse Method

and horizontal NW-SE trending T-axis, representing a tensional stress-state with NW-SE directed extension. The directions of slip were reflected on Angelier- and Hoeppener plots in figure 5.1a-centre and right, respectively. The fluctuation-histogram bars show low dihedral-angles with good distribution (Fig. 5.3a-left). The Mohr plot indicated moderate (> 1.0) to high shear-to-normal-stress ratios, all data plotting near the outer envelope and R=0.24 (Fig. 5.3a-right). The same state of stress was reflected by the outcrop scale dihedra (Semp-1) in figure 5.4-top right. Visualised in MIM, tadpole symbols in paired-stereograms indicated steeply plunging to vertical σ_1-axes and horizontal to sub-horizontal σ_3-axes (Fig. 5.5a) and cluster locations were consistent with those of PBT-mean-vectors and their cones of confidence. The first and second series of simulation with MIM respectively yielded stress-states SK-1^1 (Fig. 5.6a-left) and SK-1^2 (Fig. 5.7a-left), which confirmed a tensional state with a sub-vertical σ_1-axis and NW-SE directed extension. All data plotted with misfit (β) angles $\leq 30^\circ$ on the fluctuation histogram (Fig. 5.7a-lower right).

(b) Strike-slip

For subset SK-2 (Fig. 5.1b), the plots indicated a steep B-axis and sub-horizontal P and T axes as shown also by the dihedra-plot (SK-2; Fig. 5.2). These represent a strike-slip stress-state with NNW-SSE directed compression and ENE-WSW extension and dominantly dextral displacements. Since none of the axes is perfectly vertical or horizontal ($< 10^\circ$ to the horizontal), we considered this stress field to have an oblique component. The fluctuation-histogram showed that all data possess dihedral-angles $< 15^\circ$ (Fig. 5.3b-left). The corresponding Mohr plot indicated moderate (> 1.0) to high shear-to-normal-stress ratios, with data plotting near the outer envelope and R=0.26 (Fig. 5.3b-right). The same state of stress was reflected by the outcrop scale dihedra (Semp-2) in figure 5.4-top right. Tadpole symbols in MIM paired-stereograms showed that both σ_1 and σ_3 axes were sub-horizontal (Fig. 5.5b) and cluster locations were consistent with those of PBT-mean-vectors and their cones of confidence. The first and second series of simulation with MIM respectively yielded solutions SK-2^1 (Fig. 5.6b-left) and SK-2^2 (Fig. 5.7b-left), which confirmed a strike-slip state of stress with sub-horizontal NNW-SSE compression and sub-horizontal ENE-WSW extension. All data plotted with $\beta < 10^\circ$ on the fluctuation histogram (Fig. 5.7b-lower right).

In both cases, majority of τ/σ_n-values plotted near the outer envelope of the Mohr-diagram with moderate to high ratios (Fig. 5.7a-upper right and Fig. 5.7b-upper right, respectively). This indicated that these stress-states would induce high shear-to-normal-stress ratios (τ/σ_n) on the respective faults. Such τ/σ_n-values that plot tangential to the outer envelope of the Mohr diagram approximate the Mohr-Coulomb fracture criterion, thus indicated high potential of slip along the respective faults. Since both criteria for faulting were fulfilled, SK-1^2 and SK-2^2 were considered as optimal solutions. For both stress-states $R = 0.2$, tending towards axial compression $\sigma_1 > \sigma_2 = \sigma_3$. The low R-value implied that σ_3-axes were more unstable than σ_1-axes, thus small changes in stress could cause σ_2- and σ_3-axes to flip positions. The tensional stress with NW-SE directed extension (SK-1^2) is typical for range-parallel faults, thereby attesting to rift-control. The pure dextral strike-slip state with nearly N-S compression and W-E extension (SK-2^2) can be a local variation of the stress field responsible for forming transsection faults. Johnson and McConnell (1951) noted that in the Sempaya gorge vertical shears striking N10-30°E contained mylonite or gouge and McConnell (1959) described them as older faults mostly dextrally deformed, only slightly revived by later mainly vertical movements. This agrees with our observation that SK-1^2 is the more recent stress, re-activating some of the faults that were

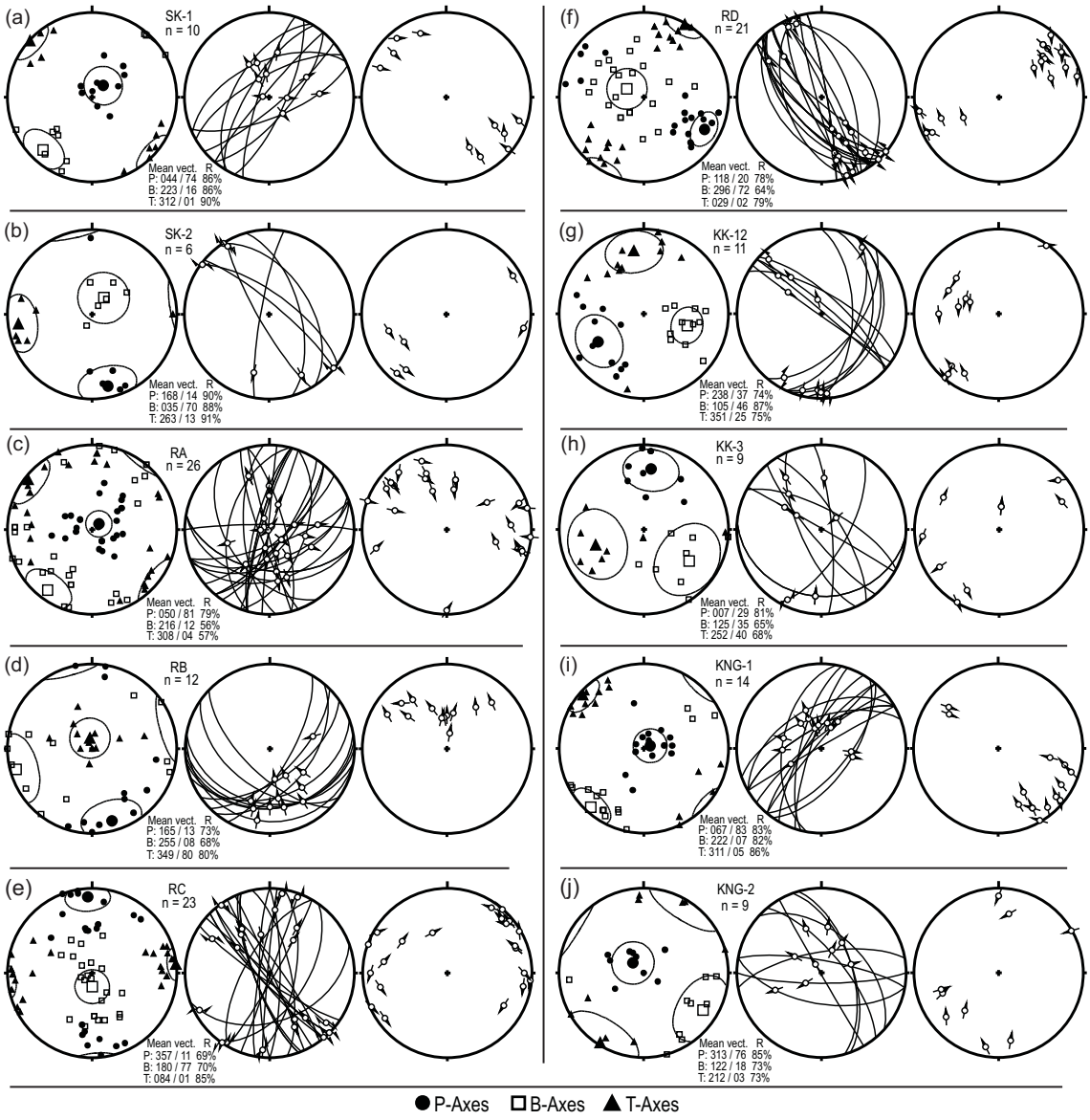

Fig. 5.1 PBT-derived plots showing data subsets. Left: PBT-axes plot with mean vectors; P=contraction-axis, B=neutral-axis, T=extension-axis. Centre: Angelier plot - great circles represent fault planes, arrows indicate slip-direction and sense of movement of the hanging-wall block. Right: Hoeppener plot - small circles represent poles to fault planes, corresponding lineations (tangent to pole points) and arrows indicate sense of movement of hanging-wall block. (a) SK-1 (b) SK-2 (c) RA (d) RB (e) RC (f) RD (g) KK-12 (h) KK-3 (i) KNG-1 (j) KNG-2.

earlier activated by SK-2^2. Hence the SS stress-state SK-2^2 with its steep faults and W-E directed extension represent intra-cratonic forces that acted on the Africa plate prior to rifting, whereas SK-1^2 was active through rift evolution. The two states of stress therefore represent two different stress regimes.

5.1.2 Central-Rwenzoris (around peaks)

Here P, B and T-axes cluster separation yielded four kinematically homogeneous subsets RA, RB, RC, RD that portrayed varying states of stress and three modes of slip.

(a) Extension (main rift)
PBT-mean-vectors and slip vectors for subset RA (Fig. 5.1c) portrayed a sub-vertical P-axis and sub-horizontal NE-SW trending B- and NW-SE trending T-axes, representing a tensional stress-state with NW-SE directed extension (like SK-1). The dihedra indicated a vertical compression axis (RA; Fig. 5.2left), more than 90% of the data exhibiting dihedral-angles $< 30°$ (Fig. 5.3c-left). The Mohr plot indicated that R=0.18 (Fig. 5.3c-right), with low τ/σ_n ratios and most of the data plotted near the inner envelop. On outcrop scale however, local variations in orientation of stress axes existed; for example between the subset dihedra Bujuku-A, FFPNyabMatte-A and Kitand-B of figure 5.4-bottom. Visualised in MIM, tadpole symbols in paired-stereograms indicated steeply plunging to vertical σ_1-axes and horizontal to sub-horizontal σ_3-axes (Fig. 5.5c) and cluster locations were consistent with those of the PBT-mean-vectors and their cones of confidence. The first and second series of simulation with MIM respectively yielded solutions RA^1 (Fig. 5.6c-left) and RA^2 (Fig. 5.7c-left), which confirmed a tensional state of stress with a sub-vertical σ_1-axis, a WNW-ESE directed σ_3-axis and $R = 0.1$ (Fig. 5.7c-upper right) tending to axial compression $\sigma_1 > \sigma_2 = \sigma_3$, in which case σ_3-axis is unstable. The low shear-to-normal-stress ratios for RA^2 suggested that σ_3-axis was probably sub-parallel to the fault planes, resulting in small shear stresses. Outcrop-scale simulations for subsets that portrayed this mode of slip yielded optimal solutions shown in diagrams e, f, h of figure 5.8 on page 73.

(b) Thrusting
For subset RB the PBT-diagrams showed horizontal NNW-SSE - and ENE-WSW - trending P and B axes respectively and a sub-vertical T-axis and indicated upward movement of the hanging wall block (Fig. 5.1d). They implied a compressional stress-state with NNW-SSE directed compression as expressed by the corresponding dihedra (RB; Fig. 5.2left). At least 80% of the data showed dihedral-angles $\leq 30°$ (Fig. 5.3d-left). The Mohr diagram (Fig. 5.3d-right) indicated low shear-to-normal-stress ratios, data plotting near the outer envelope and R=0.27. On outcrop scale, this mode of slip was observed mainly at Elena and between the Freshfield Pass and Nyabitaba and John-Matte huts, respectively shown by subset dihedra Elena-B and FFPNyabMatte-C (Fig. 5.4-bottom). Tadpole symbols in MIM paired-stereograms indicated horizontal σ_1-axes and vertical σ_3-axes (Fig. 5.5d) with cluster locations that coincided with those of the PBT-mean-vectors and their cones of confidence. The two series of simulation with MIM respectively yielded solutions RB^1 (Fig. 5.6d-left) and RB^2 (Fig. 5.7d-left), confirming a compressional stress-state with vertical σ_3-axis, sub-horizontal NNW-SSE directed σ_1-axis and sub-horizontal ENE-WSW directed σ_2-axis. Stress ratio R=0.7 suggested plane-deviatoric stress $\sigma_1 > \sigma_2 > \sigma_3$, under which the axes are equally stable. Outcrop-scale simulation for subsets that portrayed this mode of slip only yielded one optimal solution shown in figure 5.8b (each of the others generated a stress-state count too low for inversion).

(c) Strike-slip I
Subset RC indicated a steep B-axis, sub-horizontal N-S trending P-axis and horizontal ENE-WSW trending T-axis (Fig. 5.1e), implying a pure strike-slip state of stress with ENE-WSW directed extension (Fig. 5.2left; RC). This subset was characterised by conjugate fault sets, hence exhibiting both dextral and sinistral displacements. Although 90% of the data showed dihedral-angles $\leq 30°$ (Fig. 5.3e-left), the distribution of the frequency

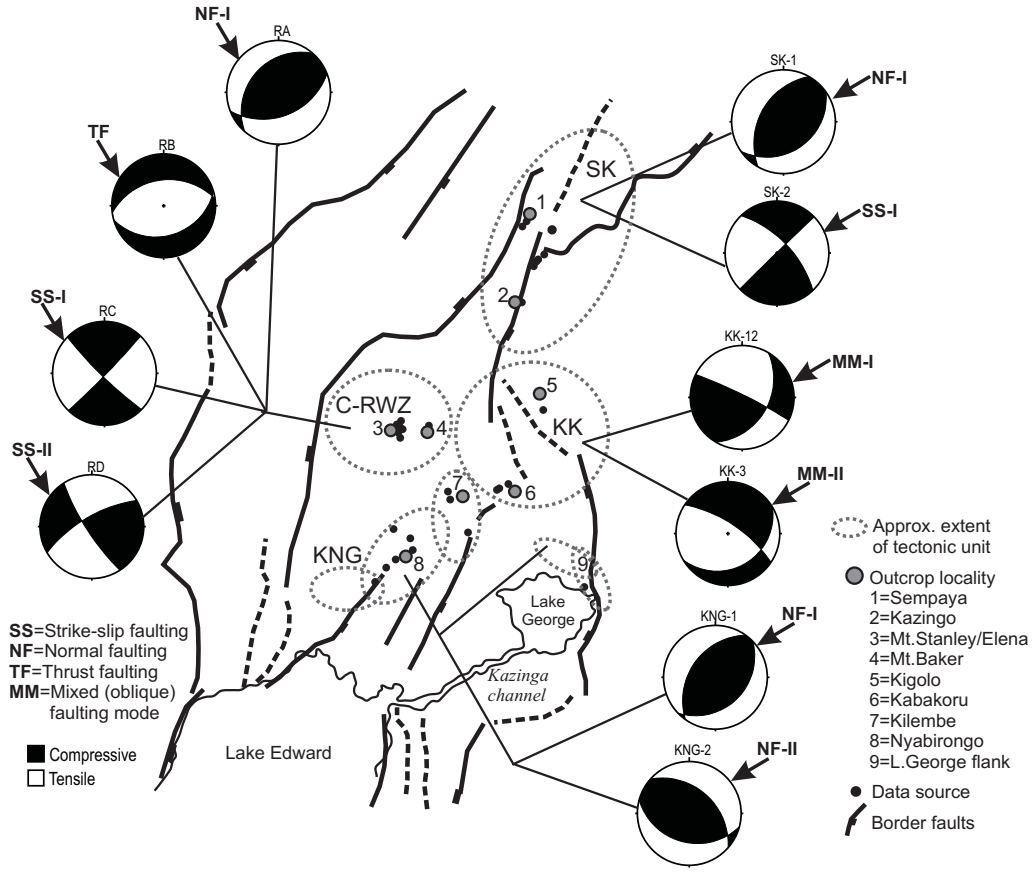

Fig. 5.2 Sketch of Rwenzori block showing approximate extents of 'tectonic units' SK, C-RWZ, KK, KNG and PBT-axes derived dihedra for stress-states represented by fault subsets SK-1, SK-2, RA, RB, RC, RD, KK-12, KK-3, KNG-1 and KNG-2. The inferred faulting modes (Roman numerals denote different modes of slip) are indicated by black arrows that point to the respective dihedra. (Note: the initials and/or Arabic numerals at the end of subset names simply denote different subsets - not necessarily different source locations). σ_1=compressive dihedra (black), σ_3=distensive or tensile dihedra (white) and σ_2=neutral and runs parallel to the intersection plane between the compressive and distensive dihedra.

bars with a maximum peak only at 30% and shifted to the right, was improper. The Mohr diagram (Fig. 5.3e-right) indicated moderate to high shear-to-normal-stress ratios, majority of data plotting near the outer envelope and R=0.82 (tending toward axial tension, $\sigma_1 = \sigma_2 > \sigma_3$). This mode of slip was observed mainly on outcrops around Bujuku (subset Bujuku-B; Fig. 5.4-bottom), which yielded an oblique state of stress shown in figure 5.8g. Tadpole symbols in MIM paired-stereograms (Fig. 5.5e) indicated variously inclined σ_1- and σ_3-axes, hence a girdle-like distribution. Simulation with MIM yielded stress-states RC^1 (Fig. 5.6e) and RC^2 (Fig. 5.7e) as preliminary and optimal solutions respectively, confirming a strike-slip state of stress with sub-vertical σ_2-axis, sub-horizontal N-S compression, horizontal W-E extension and R=0.7.

(d) Strike-slip II

For subset RD Angelier-, Hoeppener- and PBT-mean-vector plots (Fig. 5.1f) portrayed a moderately steep B-axis, sub-horizontal WNW-ESE trending P-axis and sub-horizontal NNE-SSW trending T-axis. These indicated strike-slip state of stress with WNW-ESE compression and NNE-SSW extension. Displacement sense was dominantly sinistral, although faults showed possible conjugates. Inclination of its P- and B-axes (Fig. 5.2)

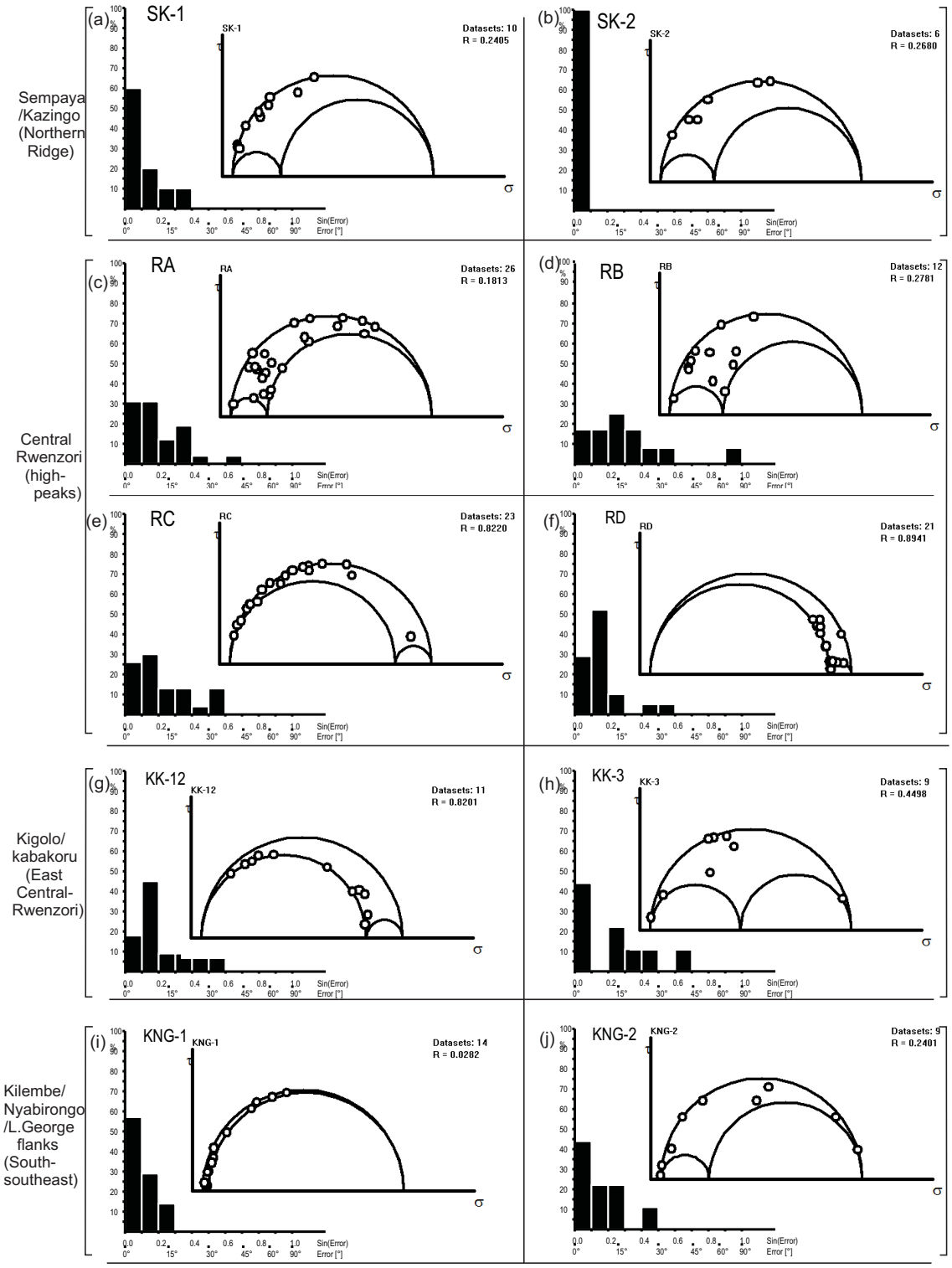

Fig. 5.3 Paleostress plots for stress-states specified by dihedra plotted in figure 5.2. Left: Fluctuation-histogram; abscissa=sine of angle of deviation of the calculated maximum shear stress in the fault plane from the measured striae, ordinate=frequency (%). Right: Dimensionless Mohr plot; abscissa=calculated normal stresses σ_n, ordinate=calculated shear stresses τ, R=stress ratio. (a) SK-1 (b) SK-2 (c) RA (d) RB (e) RC (f) RD (g) KK-12 (h) KK-3 (i) KNG-1 (j) KNG-2.

respectively to the vertical and horizontal, suggested a slight oblique-normal component. Up to 90% of the data showed dihedral-angles $\leq 20°$ (Fig. 5.3f-left), although the highest frequency bar was shifted to the right. The Mohr diagram (Fig. 5.3f-right) indicated very low τ/σ_n ratios, data plotting near the inner envelop and R=0.89 (axial tension $\sigma_1 = \sigma_2 > \sigma_3$). On outcrop scale however, there were local variations in orientation of stress axes. For example between subset dihedra Mt.Baker-A, FFPNyabMatte-B, Kitand-A and Elena-A (Fig. 5.4-bottom). Visualised in MIM paired-stereograms (Fig. 5.5f), the tadpole symbols exhibited a girdle-like distribution because σ_1- and σ_3-axes were variously inclined. MIM simulation yielded stress-states RD^1 (Fig. 5.6f) and RD^2 (Fig. 5.7f) as preliminary and optimal solutions respectively, confirming an oblique strike-slip state of stress with a vertically inclined σ_2-axis, a sub-horizontal WNW-ESE compression and horizontally inclined NNE-SSW extension. Its low R-value R=0.2 (Fig. 5.7f-upper right) pointed to axial compression $\sigma_1 > \sigma_2 = \sigma_3$, in which σ_3-axis is unstable and can flip between its position and that of σ_2-axis. Notice that the flipped configuration for stress-state RD^2 approximates that for stress-state RB^2 (see Fig. 5.7d-left).

The angular difference $\approx 55°$ of compression directions between strike-slip states RC^2 and RD^2 can be explained by temporal rotation or tilting of axes, suggesting two different stress regimes. The stress field represented by RD^2 with mainly dextral displacements appears to be the most prominent in the high peaks region and small outcrop-scale variations (e.g. compare a, c, d and g in 5.8) indicate slight spatial changes of stress axes orientations. Although it has been shown that multiple fault sets do not necessarily imply multiple deformation phases (Oertel 1965; Malone et al. 1975; Aydin 1997), it can be argued here that at least three or four different stress-states are responsible for activating faults within the high Rwenzoris.

5.1.3 East central part

Separation of PBT-axes clusters for Kigolo-Kabakoru area yielded two kinematically homogeneous subsets KK-12 and KK-3, indicating two different oblique modes of slip.

(a) Oblique mode I

PBT-mean-vectors and slip directions for subset KK-12 (Fig. 5.1g) portrayed NE-SW trending P- and NNW-SSE trending T-axis inclined to the horizontal and B-axis inclined nearly halfway between the vertical and horizontal. This corresponds to an oblique stress-state with a strong strike-slip component and inclined NE-SW compression and NNW-SSE extension (Fig. 5.2), characterised by mainly dextral-slip. The fluctuation-histogram (Fig. 5.3g-left) showed a maximum peak at 45% shifted away from the origin, making the distribution of the bars improper for a representative stress state. The Mohr plot (Fig. 5.3g-right) indicated very low to moderate τ/σ_n ratios, with data plotting near the outer envelope and stress ratio R=0.82. Small variations of axes for subsets that exhibited this mode of slip were indicated by the dihedra labelled KK-1, KK-2 and KK-rest-B (Fig. 5.4-top right). Tadpole symbols in MIM paired-stereograms (Fig. 5.5g) exhibited girdle-like distribution since at least two of their principal axes were neither vertical nor horizontal but rather variously inclined. Simulation with MIM yielded KK-12^1 (Fig. 5.6g) and KK-12^2 (Fig. 5.7g) as preliminary and optimal solutions respectively, attesting to an oblique strike-slip state of stress with ENE-WSW directed σ_1-axis, NNW-SSE directed σ_3-axis and R=0.8 (axial tension). Since this stress configuration was not observed elsewhere in the study area, KK-12^1 was considered to exert a very local stress field.

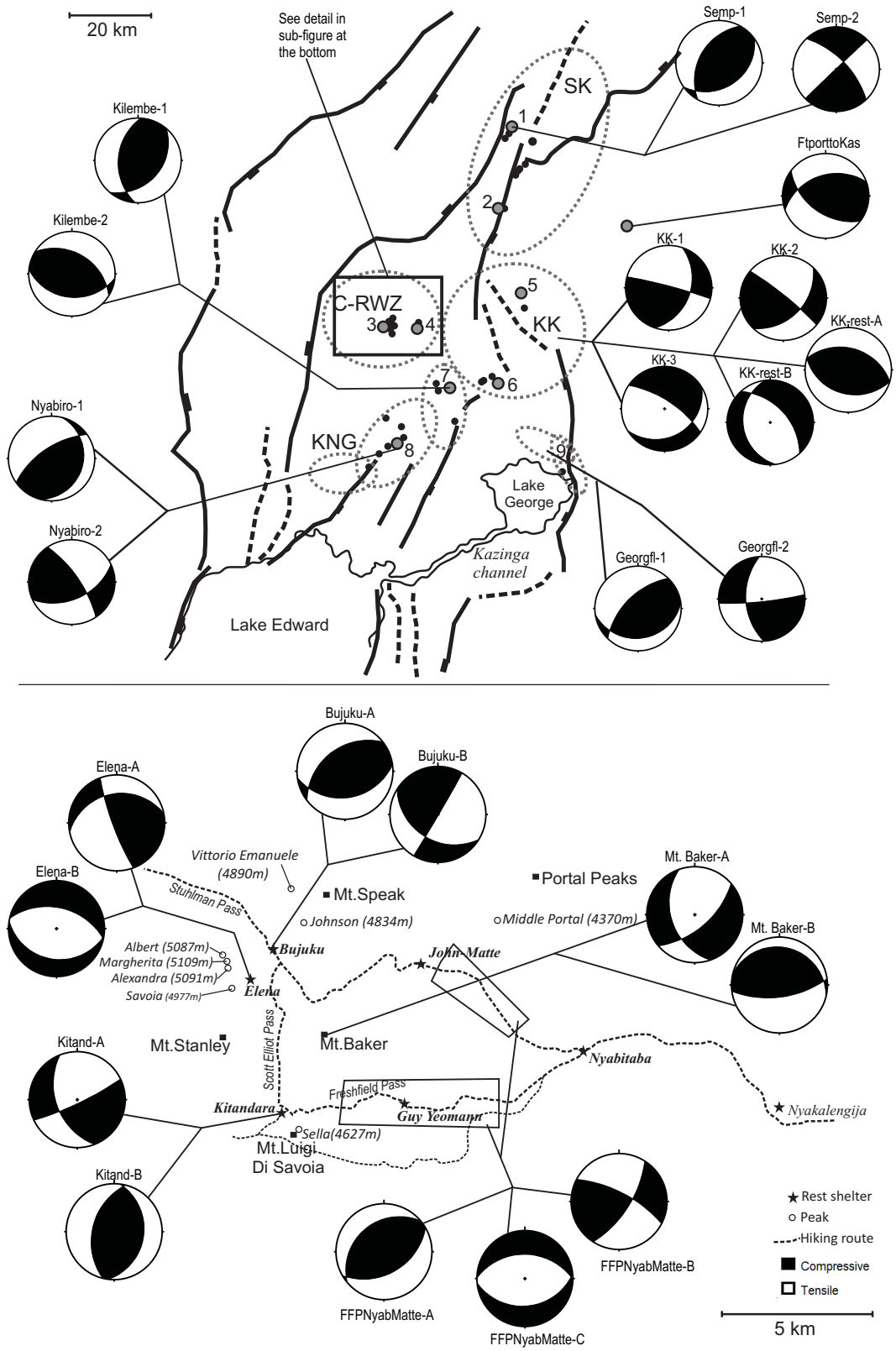

Fig. 5.4 Dihedra showing general outcrop-scale distribution and variation of stress states. σ_1=compressive dihedra (black), σ_3=distensive or tensile dihedra (white) and σ_2=neutral and runs parallel to the intersection plane between the compressive and distensive dihedra. Bottom: magnified view of outcrop locations within the central Rwenzoris area. Note: initials and/or numerals at the end of subset names simply denote different subsets - not necessarily different source locations.

(b) Oblique mode II

Subset KK-3 showed mean-vectors for which all axes P, B, T were inclined (Fig. 5.1h) suggesting obliquity of the stress state, expressed also by the dihedra-plot (Fig. 5.2). It portrayed inclined N-S directed compression and ENE-WSW extension. The fluctuation-histogram (Fig. 5.3h-left) showed maximum peak only at 44%, followed by a bin not represented by any data and a right-ward-shifted peak. The Mohr-plot (Fig. 5.3h-right) indicated moderate to low τ/σ_n ratios, most of the data plotting near the outer envelope and R=0.45. Tadpole symbols in MIM paired-stereograms showed that both σ_1 and σ_3 axes were sub-horizontal (Fig. 5.5h) and cluster locations were consistent with those of PBT-mean-vectors and cones of confidence. MIM simulation yielded KK-3^1 (Fig. 5.6h) and KK-3^2 (Fig. 5.7h) as preliminary and optimal solutions respectively, attesting to an oblique compressional state of stress with approximately NNW-SSE directed σ_1-axis, ENE-WSW directed σ_3-axis and R=0.3.

Both stress-states showed high τ/σ_n-ratios for data with β-values $\leq 30^\circ$ and data constituting the respective subsets plotted near the outer envelope of the Mohr diagram. We thus concluded that KK-12^2 and KK-3^2 were optimal solutions for the slip-data from this unit. However, they represent the same stress regime, the difference arising from flipping of axes. Since most faults attested to pure strike-slip with NE-SW compression, it can be argued that stress fields in this area were strongly perturbed locally and were probably controlled by kinematic partitioning. Nieto-Samaniego and Alaniz-Alvarez (1995) observed that when σ_3 is positive (compressive) and σ_1-axis is vertical, pre-existing fractures that strike sub-parallel to σ_3-direction are not suitable to slip but when principal stresses are inclined (non-Andersonian stresses) slip may occur along these planes instead of rock fracturing. Local variation of P and T axes (compare Fig. 5.1g and h, with Fig. 5.8i and j) and the high R-value for stress-state KK-12^2 suggested possibility of reversal between σ_1 and σ_3 axes. These differences can be best explained both by temporal variations and/or flipping of stress axes orientations and by local perturbations of the regional stress field. Alternatively, minor representation of normal faulting in this area, in spite of a large scale extensional regional stress field, suggested prevalence of a local axial compressional stress field that is strong enough to appreciably deflect axes of the regional stress field; but whose axes are unstable enough (very high R-value) to cause short term temporal reversals between its σ_1 and σ_3 axes. Since this area covers the part of the Rwenzoris where the block is still attached to the Tanzania craton, a complex stress field could have developed from concentration of stresses at the tip of the rift segment on the right side of the Rwenzori block, which is still propagating to detach the block from the Tanzania craton. A regional stress field imposed on effects of block rotation and uplift (greater gravitational potential energy) to the left, versus flatter cratonic ground under influence of mainly the regional stress field to the right, could also complicate the stresses.

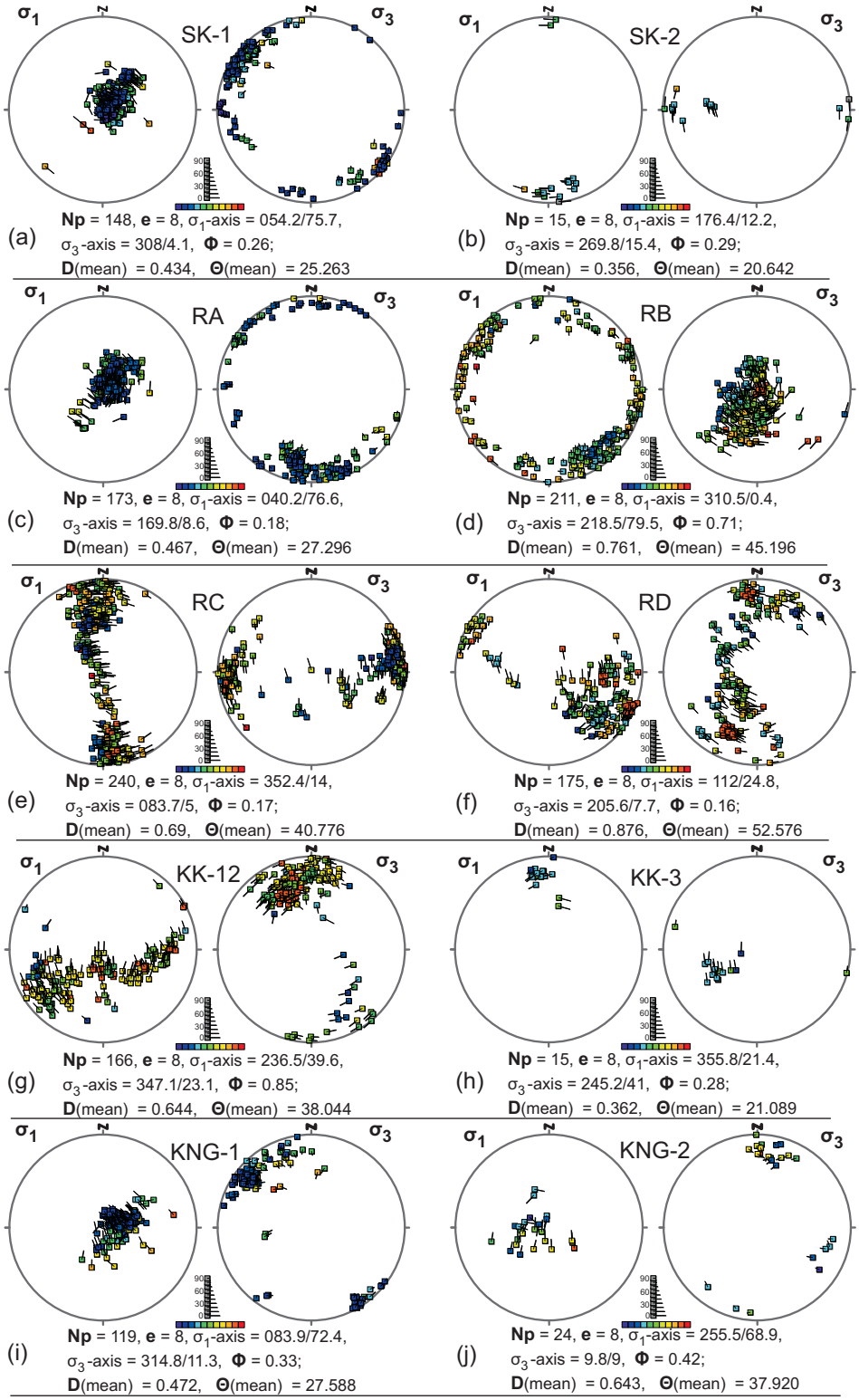

Fig. 5.5 Paired stereograms projected perpendicular to σ_1 and σ_3 axes, indicating subsets (a) SK-1 (b) SK-2 (c) RA (d) RB (e) RC (f) RD (g) KK-12 (h)) KK-3 (i) KNG-1 (j) KNG-2. **Np**=the number of stress-states plotted on each stereogram; **e**= enhance factor; Φ=stress ratio (elsewhere denoted as R); **D**(mean)=mean stress difference (range 0-1); Θ(mean)=mean angular stress distance (range 0°-90°.

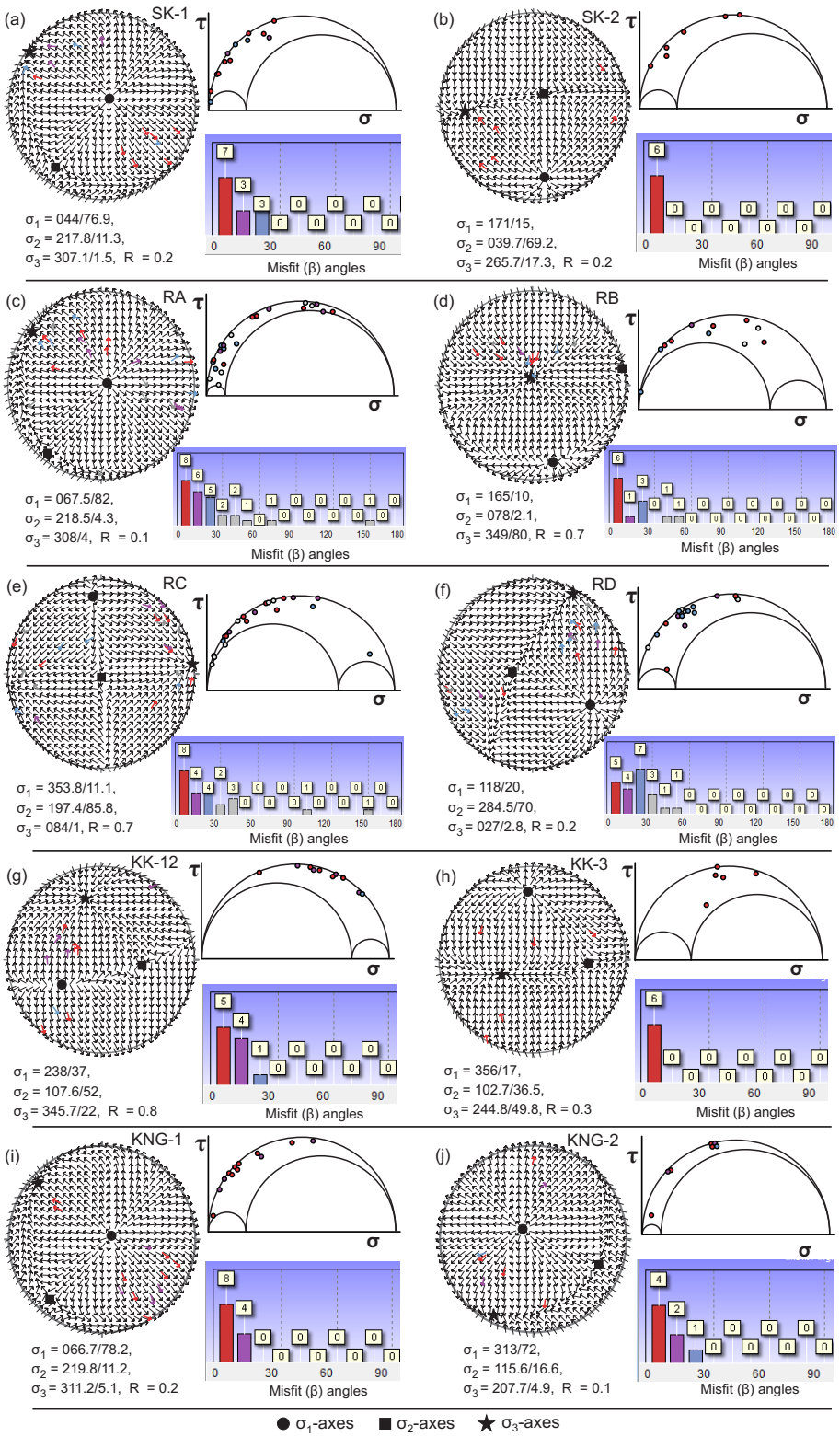

Fig. 5.6 MIM-generated preliminary stress states. (a) SK-1, (b) SK-2, (c) RA, (d) RB, (e) RC, (f) RD, (g) KK-12, (h) KK-3, (i) KNG-1, (j) KNG-2. Left: Tangent-lineations plot - fine gray arrows=theoretical slip directions for the specified stress-state whose parameters are listed below the diagram, R=stress ratio; thick (coloured) arrows=(observed) slip directions for measured fault data. Upper-right: Mohr diagram for specified stress state, τ=shear stress (value-range 0-0.5), σ=normal stress (value-range 0-1.0). Lower-right: Angular misfits β° between theoretical and observed slip directions. Threshold value of $\beta = 30^\circ$

5.1.4 South to southeastern part

For outcrops around Kilembe-Nyabirongo-George flanks that lie south to southeast of the Rwenzoris, separation of P-, B- and T-axes clusters yielded two kinematically homogeneous subsets KNG-1, KNG-2 that exhibited two different modes of extension.

(a) Extension I (main rift)
Subset KNG-1 represents a tensional stress-state with a vertical P-axis and horizontal NE-SW-trending B-axis and NW-SE-trending T-axis and directions of slip portrayed by its corresponding Angelier- and Hoeppener plots (Fig. 5.1i). High R[%] values ($> 80\%$) accompanying the mean vectors showed that the axes forming the P, B and T clusters respectively, were sub-parallel. The vectors indicated NW-SE extension (Fig. 5.1), typical for range-parallel faults. The fluctuation-histogram (Fig. 5.3i-left) showed well distributed peaks with more than 80% of data having dihedral-angles $< 15°$. The Mohr plot (Fig. 5.3i-right) indicated moderate to high τ/σ_n-ratios and R=0.03. As shown by the dihedra in figure 5.4 (subsets Kilembe-1, Nyabiro-1 and Georgfl-1), stress axes varied locally. Tadpole symbols in MIM paired-stereograms (Fig. 5.5i) indicated steeply plunging to vertical σ_1-axes and horizontal to sub-horizontal σ_3-axes and cluster locations consistent with locations of the PBT-mean-vectors and the corresponding cones of confidence. The resulting MIM-generated solutions KNG-1^1 (Fig. 5.6i) and KNG-1^2 (Fig. 5.7i) confirmed a tensional state of stress, whose extension axis trends NW-SE, the intermediate axis trends NE-SW and R=0.2. All data that constituted this subset plotted with misfits $\leq 20°$ and their τ/σ_n-values plotted near the outer envelop of the Mohr diagram with high shear-to-normal-stress ratios. This was the predominant stress-state exhibited in each of the three outcrop localities - Kilembe mines area, Nyabirongo and the lake George flanks. The variation of axes orientations in these localities by angles $\leq 20°$ can be due to local disturbances of the regional stress field.

(b) Extension II
The slip directions and mean vectors for subset KNG-2 indicated sub-vertical P-axis, sub-horizontal NW-SE-trending B-axis and horizontal NE-SW-trending T-axis (Fig. 5.1j). The relatively high R[%] values ($> 70\%$) indicated that the axes forming the P, B and T clusters respectively were sub-parallel. This corresponds to an oblique tensional state with NE-SW directed extension (Fig. 5.2), typical for transsection faults. Although the maximum peak of the fluctuation-histogram (Fig. 5.3j-left) was only up to 44%, it showed fair distribution of peaks with more than 80% of the data having dihedral-angles $< 20°$. The Mohr plot (Fig. 5.3j-right) indicated moderate shear-to-normal-stress ratios, with most of the data plotting near the outer envelope and R=0.24. As shown by the dihedra in figure 5.4 (subsets Kilembe-2, Nyabiro-2 and Georgfl-2), the σ_3-axes nearly coincided in trend but the σ_1- and σ_2-axes were variously inclined at different localities. Similar to KNG-1^2, the tadpole symbols in MIM paired-stereograms (Fig. 5.5j) portrayed steeply plunging to vertical σ_1-axes and horizontal to sub-horizontal σ_3-axes and cluster locations consistent with locations of the PBT-mean-vectors and the corresponding cones of confidence. MIM simulation yielded KNG-2^1 (Fig. 5.6j) and KNG-2^2 (Fig. 5.7j) as preliminary and optimal solutions respectively, confirming a tensional state of stress whose extension axis trends NNE-SSW, intermediate axis trends WNW-ESE and R=0.1. The data plotted near the outer envelop of the Mohr diagram with high τ/σ_n-ratios and with misfits $\leq 30°$. Over 70% of fault data that attested to this stress field were measured from around the Kilembe mines, implying greater gravitational potential energy and instability of axes than around the L. George flanks and Nyabirongo which are comparatively lower in altitude.

Both states of stress were considered to be optimal solutions but KNG-1^2 appears to be more regional so that its effect is superimposed on KNG-2^2, which exerts only a local influence. The trend of extension axes for the two differ by $\approx 76^\circ$ suggesting different causative forces, probably from axes reversals. On outcrop scale (compare Fig. 5.8k with Fig. 5.8l) variations in axes orientation attested to local changes of the regional stress field and reversals between σ_2 and σ_3 axes, given that R=0.1 for stress-state KNG-2^2 and the fact that axes of the regional stress field are expected to be stable. Although the regional tectonic stress field is stronger and its axes do not easily flip (Zoback 1992a; Fossen 2010), a flip between σ_3- and σ_2-axes of the local stress field would have a reinforcing effect with NW-SE directed extension. Hence the direction of subsequent slip will be determined by the regional stress field. This might explain the limited number of NW-SE striking fault planes in this area and high τ/σ_n-ratios under stress-state KNG-1^2 for faults that were explained by both stress-states but exhibited low τ/σ_n-ratios under stress-state KNG-2^2. Since the two rift segments are already joined at the southern end of the Rwenzori block, presence of mainly normal faults could imply dominance of tensional stresses in this part i.e. there is no more stress concentration therefore there is limited interference on the regional extensional stress field. Hence KNG-2^2 is regarded as a local deviation (of transient nature) of the regional stress field KNG-1^2 resulting from temporal axes reversals and the two are considered to belong to the same stress regime.

5.1.5 Data with unknown sense-of-slip

Fault data with unknown sense-of-slip were plotted together with the theoretical slip pattern of one of the stress-states determined for the respective tectonic unit. Although the results of this subsection were referred to in the discussion, they were not incorporated in the interpretation so as to avoid any form of bias on the reduced stress tensors for the paleostresses determined. Hence also presented here separately.

Sempaya-Kazingo area
Assigning the normal-slip pattern of stress SK-1^2 to the faults of unknown sense-of-slip from Sempaya-Kazingo area, the tadpole symbols of the paired MIM stereograms (Fig. 5.9a-left) formed clusters identical with those of subset SK-1 (see Fig. 5.1a-left), save for a thin cluster of axes inclined to σ_1. The thin cluster can be part of a girdle formed by all faults, suggesting oblique-slip on some planes. On plotting the faults against stress-state SK-1^2 (Fig. 5.9a-centre), at least 50% of data were explained with even better misfits obtained under lower stress ratio R=0.1 (Fig. 5.9a-upper right), although some showed low τ/σ_n-ratios. The lowest misfits were however obtained when an assumed flip-configuration of SK-1^2 in which σ_3-axis occupies the present σ_2-position (217.8/11.6), was imposed on the faults with R=0.1. On the contrary, imposing the strike-slip pattern of stress SK-2^2 to the same faults and plotting them against this stress showed that SK-2^2 accounted for none of them as all faults showed misfits $> 40^\circ$. Thus the plots were not shown. Since low R-values suggest prior occupancy of the present σ_2-axis position by σ_3-axis, the faults could have been older but re-activated by SK-1^2 as normal faults with low τ/σ_n-ratios.

Central-Rwenzoris
Faults of the Central-Rwenzoris were assigned a normal-slip pattern of stress-state RA^2. The resulting tadpole-symbol distribution and colours for the paired MIM stereograms (Fig. 5.9b-left) were similar to those of subset RA (see Fig. 5.1d-left). Indeed the corresponding tangent-lineations plot (Fig. 5.9b-centre) showed that more than 60% of the

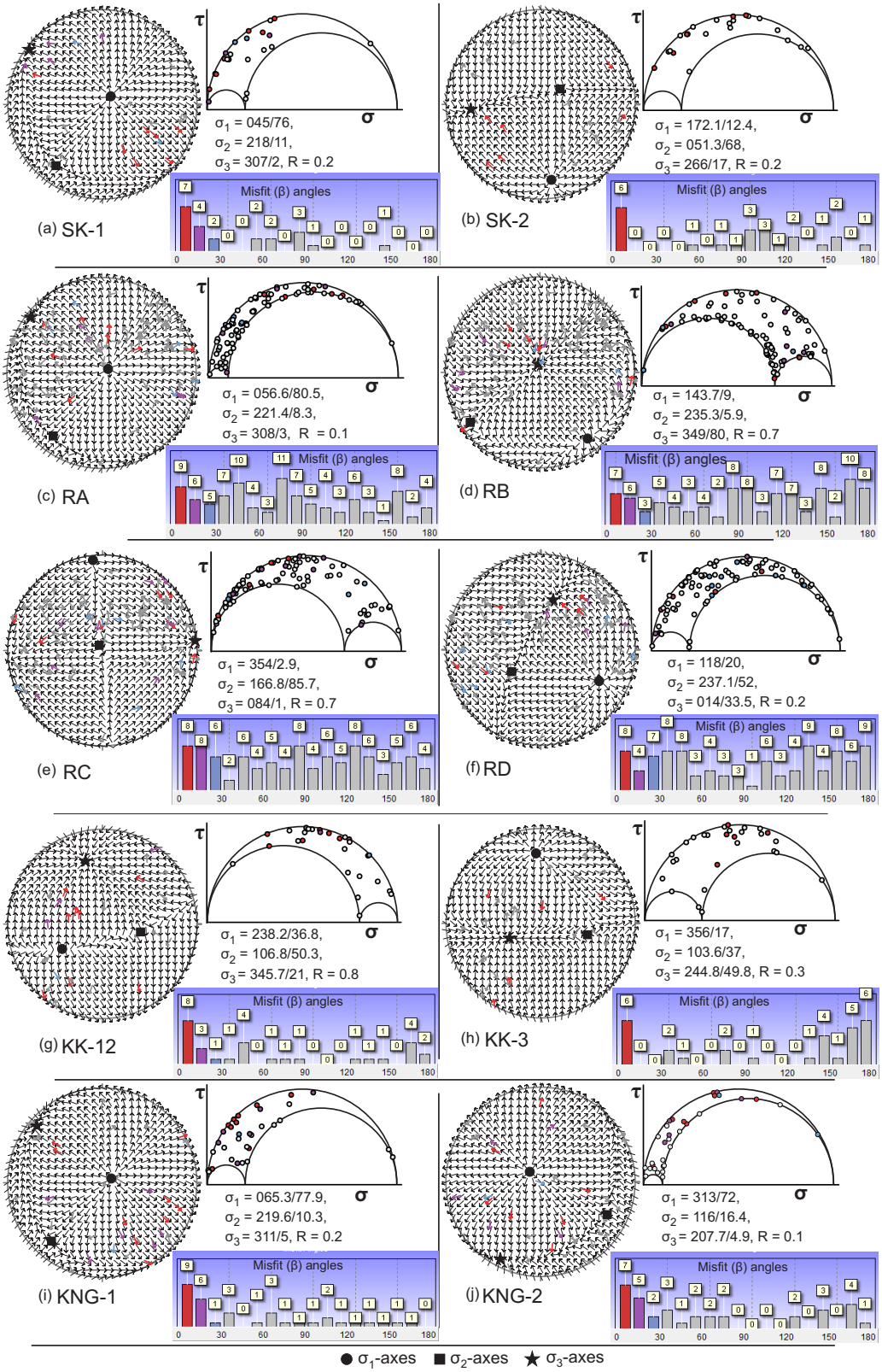

Fig. 5.7 MIM-generated optimal stress states. (a) SK-1 (b) SK-2 (c) RA (d) RB (e) RC (f) RD (g) KK-12 (h) KK-3 (i) KNG-1 (j) KNG-2. Left: Tangent-lineation diagram; fine gray arrows indicate theoretical slip directions for the specified stress-state whose parameters are listed below the diagram, R=stress ratio; thick (coloured) arrows denote (observed) slip directions for measured fault data. Upper-right: Mohr diagram for specified stress state; τ=shear stress, σ=normal stress. Lower-right: Angular misfits β° between theoretical and observed slip directions. Threshold value of $\beta = 30^\circ$.

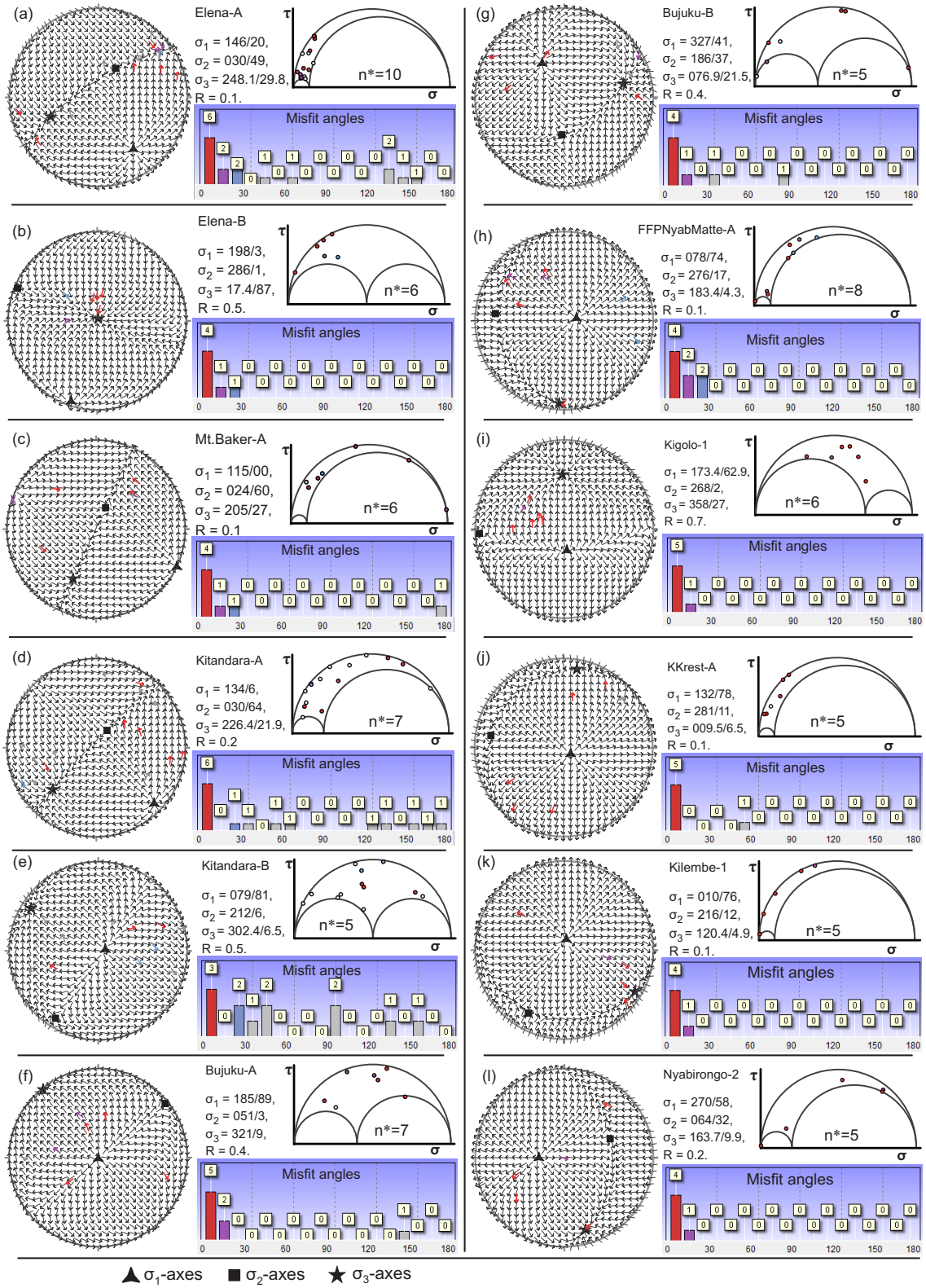

Fig. 5.8 MIM-generated outcrop-scale solutions. Left: Tangent-lineation plot; Upper-right: Mohr-diagram; Lower-right: Angular misfits $\beta°$. Threshold value $\beta = 30°$. (a,b) Elena (c) Mt.Baker (d) Kitandara (e) Kitandara (f,g) Bujuku (h) stretch from Nyabitaba to John-Matte hut and the Freshfield Pass (i,j) Kigolo (k) Kilembe (l) Nyabirongo. Note: the ending letters and/or numerals denote different subsets - not necessarily different source localities.

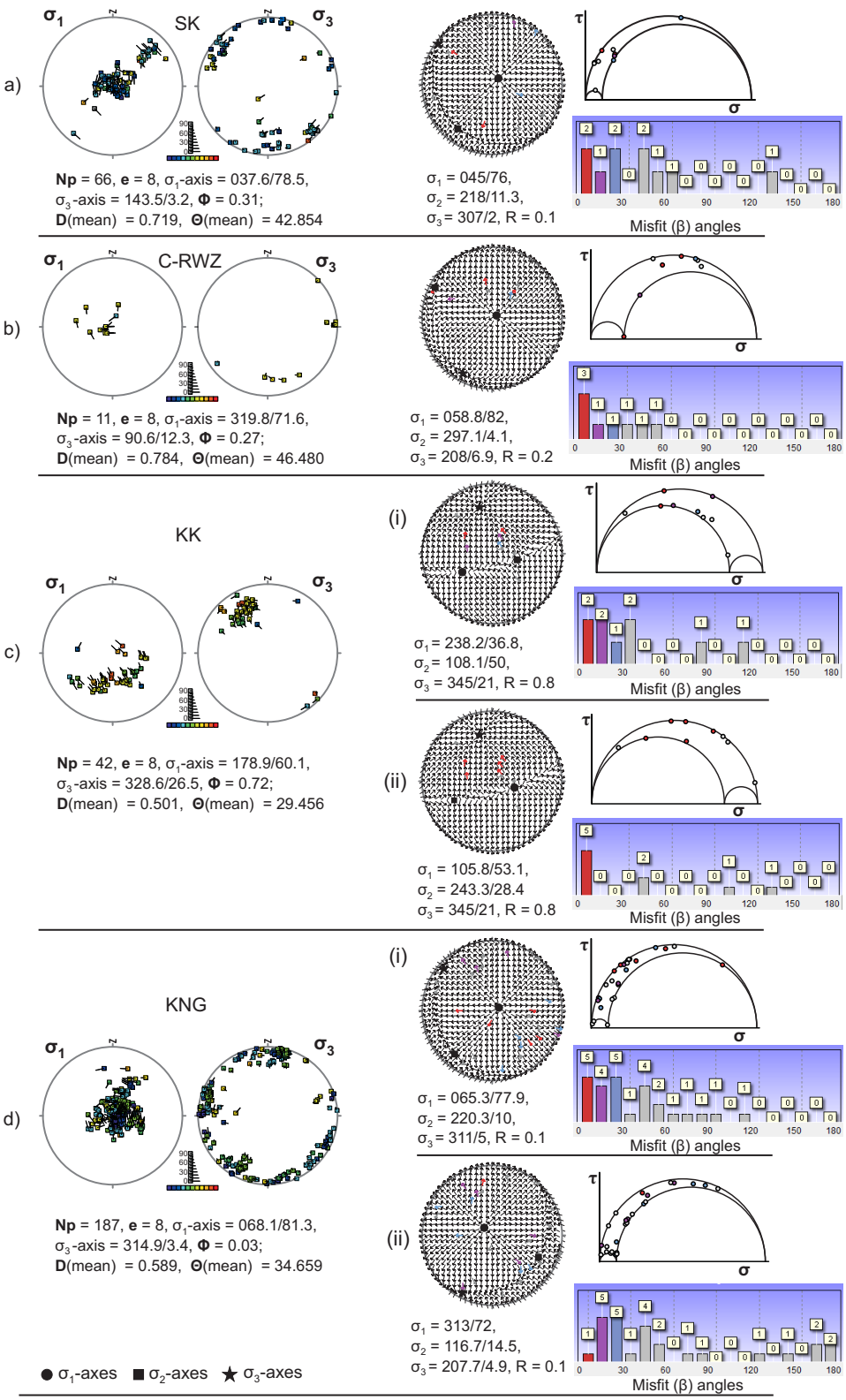

Fig. 5.9 Results from MIM-simulation on fault data with unknown sense-of-slip. left: paired stereograms. centre: tangent-lineations plot. upper right: Mohr plot. lower right: Angular misfits $\beta°$. (a) Data from Sempaya-Kazingo assigned to stress-state SK-1[2]. (b) Data from central Rwenzoris assigned to stress-state RA[2]. (c) Data from Kigolo-Kabakoru assigned to stress-state (i) KK-12[2]; (ii) an assumed flip-configuration of stress-state KK-12[2], in which the σ_1-axis occupies the present σ_2-position and vice versa. (d) Data from Kilembe-Nyabirongo-George flank assigned to stress-state (i) KNG-1[2]; (ii) KNG-2[2].

faults could be explained by a tensional stress-state with orientations of σ_1 = 058.8/82, σ_2 = 297.1/4.1, σ_3 = 208/6.9 and R=0.2. Under this stress the faults plotted close to the outer Mohr-circles envelop (Fig. 5.9b-upper right) with high τ/σ_n-ratios. Note that the listed parameters specifying the reduced stress tensor of the stress-state found to activate these faults were very similar to those of stress-state KNG-2^2 exhibited in the south-southeastern part. They also approximated the would-be flip-configuration for stress-state RA^2 in which the σ_2-axis would have occupied the present σ_3-axis position and vice versa.

Kigolo-Kabakoru area

Unlike the oblique compressional stress-state KK-3^2, assigning a normal-slip pattern of the tensional stress KK-12^2 to faults of unknown sense-of-slip from the east central part yielded paired MIM stereograms (Fig. 5.9c-left) whose tadpole-symbol distribution and colours were identical with those of subset KK-12 (see Fig. 5.1h-left). The colours depicted moderate stress ratios. The tensional stress KK-12^2 accounted for about 40% of the faults (Fig. 5.9c,i-left). Most plotted tangential to the outer Mohr-circle envelop (Fig. 5.9c,i-upper right) although most of them showed τ/σ_n-ratios < 1.2. The lowest misfits were, however, obtained under an assumed flip-configuration of stress-state KK-12^2 in which the present σ_2-position (105.8/53.1) was occupied by σ_1-axis and vice versa (Fig. 5.9c,ii). This may suggest that these faults were older and were active in the past but in its present configuration, stress-state KK-12^2 did not re-activated slip along their planes.

Kilembe-Nyabirongo-George flank area

Since both solutions obtained for the south-southeastern part portrayed tensional stress-states with sub-vertical compressional-axes, all fault-slip data with unknown sense-of-slip were arbitrarily assigned"normal-slip" vectors and tested against both solutions. The paired stereograms (Fig. 5.6d) showed tadpole-symbol distributions that mimicked partly that of subset KNG-1 (see Fig. 5.4j-left) and partly subset KNG-2 (see Fig. 5.4k-left). It was however, much closer to KNG-1, save for the very low ϕ value (0.03) depicting pure axial compression, $\sigma_1 > \sigma_2 = \sigma_3$. Stress-states KNG-$1^2$ and KNG-2^2 respectively, accounted for 50% and 20% of the data (Fig. 5.6d,i and ii, respectively). Most of the data showed moderate to high τ/σ_n-ratios, plotted near the outer Mohr-circle envelop and suggested that the faults were (re-)activated mainly by the regional stress field represented by KNG-1^2.

5.2 Discussion

Employing Zoback's classification criteria (Heidbach et al. 2008), results of the analyses summarised in figure 5.10 indicated normal faulting (NF), strike-slip faulting (SS), pure thrust faulting (TF) and oblique thrust faulting (TS). This implies existence of nearly all categories of faulting. Since fault re-activation (even thrusts reactivated as low-angle normal faults) becomes easier when stress trajectories markedly deviate from the vertical and horizontal (Sibson 1985; Nieto-Samaniego and Alaniz-Alvarez 1995), the expressed obliquity in the principal axes (non-Andersonian stress) for all the SS category of stresses here can be interpreted to represent extensive (re-)activation of faults in transtensional tectonics, which suggests a transition between strike-slip and normal faulting. The TS stress-state KK-3^2, however, indicated some local transpressional tectonics suggesting a transition between strike-slip and reverse faulting. All stresses in the NF category and the one TF category on the other hand showed sub-vertical and sub-horizontal principal axes that can pass for Andersonian stresses, although it was generally evident that stress-states with high R values exhibited a more oblique component. Tensional and strike-slip stress-states also exhibited large variation of axes directions within some tectonic units and these are referred to in our discussion as different modes.

5.2.1 Observed modes of faulting

(a) Extension mode I
This was characterised by sub-vertical to vertical σ_1-axes and horizontal to sub-horizontal NE-SW trending σ_2-axes and NW-SE extension axes, typical for the main rift extension direction. Stress-states SK-1^2 from northern-Rwenzoris, RA^2 from the central-Rwenzoris and KNG-1^2 from south-to-southeastern Rwenzoris, exhibited this direction of extension with minor differences of $\pm 4^\circ$ (see Fig. 5.10). Such coincidence of stress axes and similarity of values of stress ratio R (respectively, 0.2 vs. 0.1 vs. 0.2) indicated that the three represent the same (regional) stress regime.

(b) Extension mode II
This was characterised by sub-vertical to vertical σ_1-axes and horizontal to sub-horizontal WNW-ESE trending σ_2-axes and NNE-SSW extension axes. It was mainly observed around Kilembe (Fig. 5.8j) and Kabakoru areas (see Fig. 5.4; respectively, subsets KK-rest-A and Kilembe-2) in the east-central part of the Rwenzoris and is represented by stress-state KNG-2^2. The difference in trend of σ_3-axes between stress-state KNG-2^2 (027-207) exhibited at the southeastern to east-central part of the Rwenzori block and the strike-slip state RD^2 (014-194) exhibited within the central high peaks region, was only 13°. Hence the two represent the same stress field but probably due to local differences in gravitational potential energy, the stress field within the central-Rwenzoris was altered to generate strike-slip movements.

(c) Strike-slip mode I
This mode was characterised by sub-vertical to vertical σ_2-axes and horizontal NNW-SSE to N-S directed σ_1-axes and ENE-WSW to W-E directed extension. It was observed in the northern ridge and central Rwenzoris, represented by SK-2^2 and RC^2 respectively. In the central Rwenzoris it was observed in areas surrounding Bujuku hut, although the outcrop-scale dihedra indicated more tilted axes (see Fig. 5.8g and Fig. 5.4-subset Bujuku-B).

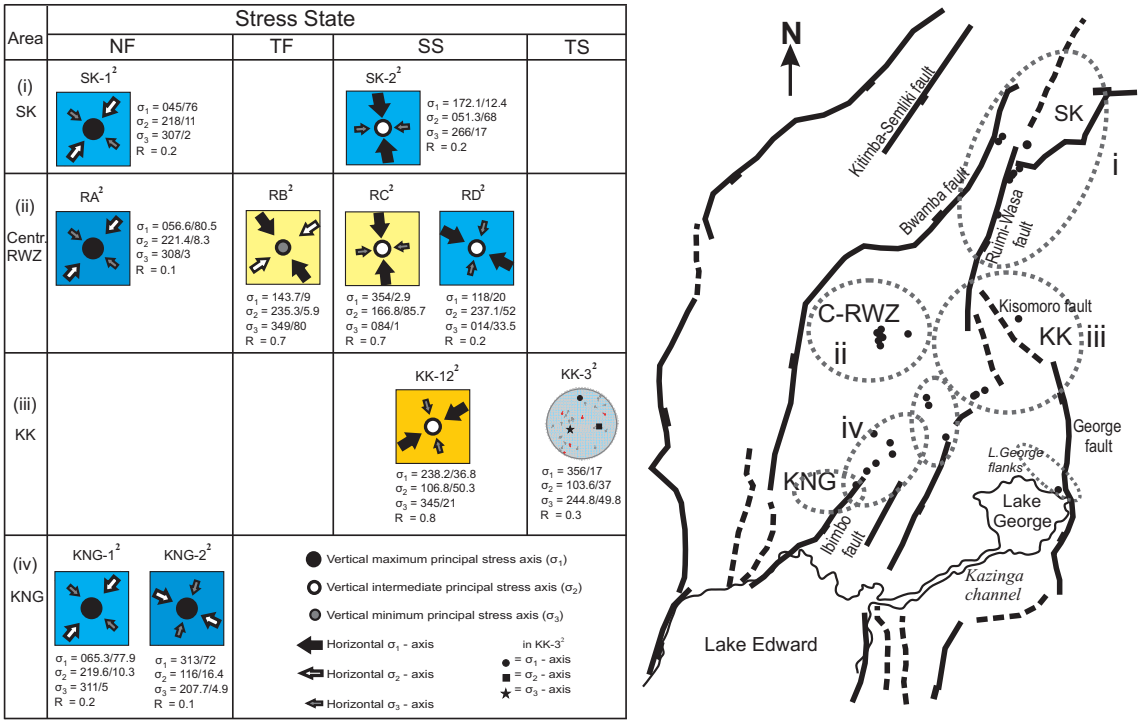

Fig. 5.10 Left:Summary of MIM-generated optimal stress states. Right:Relative location and approximate extents of 'tectonic units' where respective stress-states were obtained. (i) SK=Sempaya-Kazingo: stress-states SK-1^2 and SK-2^2. (ii) C-RWZ=central Rwenzoris: stress-states RA^2, RB^2, RC^2 and RD^2. (iii) KK=Kigolo-Kabakoru: stress-states KK-12^2 and KK-3^2. (iv) KNG=Kilembe-Nyabirongo-George flank: stress-states KNG-1^2 and KNG-2^2.

(d) Strike-slip mode II

This was also characterised by sub-vertical to vertical σ_2-axes but with sub-horizontal WNW-ESE directed compression axes and NNE-SSW extension axes, represented by the stress-state RD^2 from central Rwenzoris. On outcrop-scale however, the representative subsets exhibited dihedra with tilted axes (see Fig. 5.8a, c, d and Fig. 5.4-subsets Elena-A, Mt.Baker-A and Kitand-A).

(e) Strike-slip mode III (Oblique mode I)

This was observed in the east central part represented by stress-state KK-12^2. It was characterised by tilted axes showing ∼NNW-SSE extension. It exhibited mixed strike-slip and normal modes of slip in a manner that, ignoring the criteria of Zoback (1992a), was preferably referred to as *oblique mode-I*. The stress-state KK-12^2 is an average of subsets KK-1 and KK-2 (see Fig. 5.4) of the east-central Rwenzoris. This mode was also observed in a minor subset 'FFpNyabMatte-B' (Fig. 5.4) westward towards the high peaks.

(f) Oblique mode II

This was also observed in the east central part, represented by stress-state KK-3^2 and characterised by tilted axes with N-S to NNW-SSE compression. The trend of σ_1-axes was comparable to that for SK-2^2 of the northern part and that for RC^2 of central Rwenzoris, varying by angles $< 5°$. This suggested that the oblique stress-state KK-3^2 belonged to the same stress regime as the strike-slip states SK-2^2 and RC^2. This regime likely prevailed prior to rifting, when the Africa plate was in a state of compression under intra-cratonic forces created by the spreading zones that surround it.

(g) Thrusting

This mode of faulting was characterised by sub-vertical to vertical σ_3-axes and sub-horizontal NE-SW directed σ_2-axes and NW-SE compression. It was mainly observed in the central Rwenzoris represented by stress-state RB^2 and in particular from outcrops around Elena hut and Freshfield Pass (see Fig. 5.4-subsets Elena-B and FFPNyabMatte-C). The TF stress-state RB^2 of the central-Rwenzoris showed σ_1-axis trend ≈144-324 and TS stress-state KK-3^2 (*oblique mode II*) of Kigolo-Kabakoru showed σ_1-axis trend 356-176. The two showed a difference in trend of $\approx 32^\circ$ suggesting similar cause. Differences in axes orientations originated from local interference of stress fields around the "re-activated" Nyamwamba and Bwamba faults, resulting in slightly varying local stresses. Because the central-Rwenzoris are located between these two dextrally displacing shear/fault zones, stress axes around this zone could have rotated counter-clockwise. The Kigolo-Kabakoru area on the other hand, would be expected to experience a smaller counter-clockwise rotation and because its eastern end is relatively 'free' tilting occurred in the vertical (σ_3) axis. This introduced an oblique component of displacement, hence predominantly thrust faulting with a strike-slip component. We thus argue that RB^2 and KK-3^2 represent different stress-states that belonged to the same thrusting regime. The difference probably arises from short term fluctuations of the stress field and/or complication of the stress field around Kigolo-Kabakoru where the Rwenzori block is still connected to the Tanzania craton.

A comparable state of stress was also exhibited by dihedra from a minor subset (KK-rest-B; Fig. 5.4) of Kigolo-Kabakoru area, although its axes were tilted (σ_1 = 062/11, σ_2 = 328/17 and σ_3 = 183/69) and the σ_1-axis directed ∼NE-SW. The difference in σ_1-axes directions between RB^2 and the stress-state inferred from subset 'KK-rest-B' (see Fig. 5.4) was $\approx 74^\circ$. This difference can be explained by temporal rotation and/or tilting of axes. Hence we suggest that the latter was a state of stress transient between pure thrusting and strike-slip.

Average and spread of stress states

On the whole, stress-states suggested by the PBT-axes mean vectors exhibited very modest variations from MIM-generated parameters of reduced stress tensors characterising the optimal solutions (see Fig. 5.10). Clusters of tadpole symbols that represented stress-states in the paired stereograms generally exhibited values of *mean stress difference* [$\mathbf{D}$(mean) < 0.7, save for RB^2 and RD^2 whose values reached 0.76 and 0.87, respectively. As such they did not vary much from the value $D \leq 0.517$ which corresponds to the threshold value of $\beta = 30^\circ$ (Orife and Lisle 2003). Values of mean *angular stress distance* [Θ(mean)] ranged from $20 - 40^\circ$, save again for RB^2 and RD^2 whose values reached 45° and 52°, respectively. The moderate $\mathbf{D}$(mean) and Θ(mean) values suggested that the stress-states were nearly similar therefore they would have activated slip along planes in complimentary directions. Majority of the optimal stress-states showed very low R-values (≤ 0.3) hence approximated axial compression $\sigma_1 > \sigma_2 = \sigma_3$. Stress-states RB^2 and RC^2 with R = 0.7 tended toward pure-plane deviatoric stress $\sigma_1 >> \sigma_2 >> \sigma_3$, whereas KK-$12^2$ with R=0.8 approached a state of axial tension $\sigma_1 = \sigma_2 > \sigma_3$. Comparing the results obtained here with those obtained from recent studies for example by Delvaux and Barth (2010), it is evident that the analyses provided reliably consistent paleostress tensors despite the low fault-plane count for subsets representing some of the stress states.

5.2.2 Summation of stresses

(a) Tensional stress states
Although they were observed at different scales in the different tectonic units, the tensional and strike-slip stress-states that were exhibited by at least two of the four tectonic units, were summed up to represent the average stress fields in the study area.

Parameters specifying the stress tensor for the main tensional stress-state averaged to σ_1=066/78, σ_2=225/12, σ_3=315/4 and R=0.2 (Fig. 5.11a,iv). These showed axial tension with NE-SW directed $S_{(Hmax)}$-axes (σ_2) and NW-SE extension. Save for the opposing plunge directions, the parameters indicated a difference in orientation of the $S_{(Hmax)}$- and $S_{(Hmin)}$-axes from that determined by Delvaux and Barth (2010), of 12° and 13° respectively. The fault planes were preferably ENE-WSW to NNE-SSW striking, most of them dipping steeper than 70° whereas the lineations dominantly pitched perpendicular to them with plunge of $40 - 80°$ (Fig. 5.11a,ii).
Parameters for the minor tensional stress-state with NNE-SSW extension direction (Fig. 5.11b,iv) averaged to σ_1=279/80, σ_2=103/11, σ_3=015/1 and R=0.1 indicating axial tension. The fault planes were dominantly striking NW-SE with steep to vertical dips and some lineations pitched perpendicular and others parallel to them with moderate plunge (Fig. 5.11b,ii-iii).

(b) Strike-slip stress states
Parameters specifying the stress tensor for the strike-slip stress with W-E extension averaged to σ_1=357/8, σ_2=119/81, σ_3=265/10 and R=0.3 (Fig. 5.12a,iv). These suggested tendency towards axial tension with nearly N-S directed compression. The fault planes were most preferably striking NW-SE to NNE-SSW with very steep dips ($> 80°$) and lineations pitched in similar directions with horizontal to gentle plunge (Fig. 5.12a,ii).
A second strike-slip state (Fig. 5.12b,iv) with NNE-SSW extension showed stress tensor parameters averaging to σ_1=107/12, σ_2=258/74, σ_3=015/10 and R=0.4 indicating triaxial deviatoric stress. Lineations tended to parallel the strike of faults, which was dominanlty NW-SE and with very steep to vertical dips (Fig. 5.12b,ii).

5.2.3 Proposed relative chronology of stresses

Determination of paleostress field changes from fault-slip data alone is not easy. As such, inferences to the relative chronology of stresses were made with reference to earlier work carried out on other rift segments, in comparison with extension directions deduced from micro-structures. For example Strecker et al. (1990) studied changes of fault kinematics and reported clockwise rotation in extension direction of the central Kenya rift from approximately NE-SW through ENE-WSW, W-E to NW-SE direction. Bosworth and Strecker (1997) used inferences from fault kinematics, dyke orientations, alignment of volcanic centres and seismic data. They consequently reported changes in extension direction of the Kenya rift from NE-SW during initial rifting stages in late Miocene, through W-E extension in late Pliocene to Mid-Pleistocene, to between WNW-ESE and NW-SE. In the Gulf of Suez and northern Red Sea, Bosworth and Strecker (1997) reported change in extension direction from NE-SW (perpendicular to the rift) to N-S direction before 125Ka ago. Further south along the western branch of the rift, Ring et al. (1992) carried out kinematic analysis of Neogene and Quarternary faults of the N-S striking Malawi rift and reported rotation of extension direction from ENE-WSW to NW-SE.

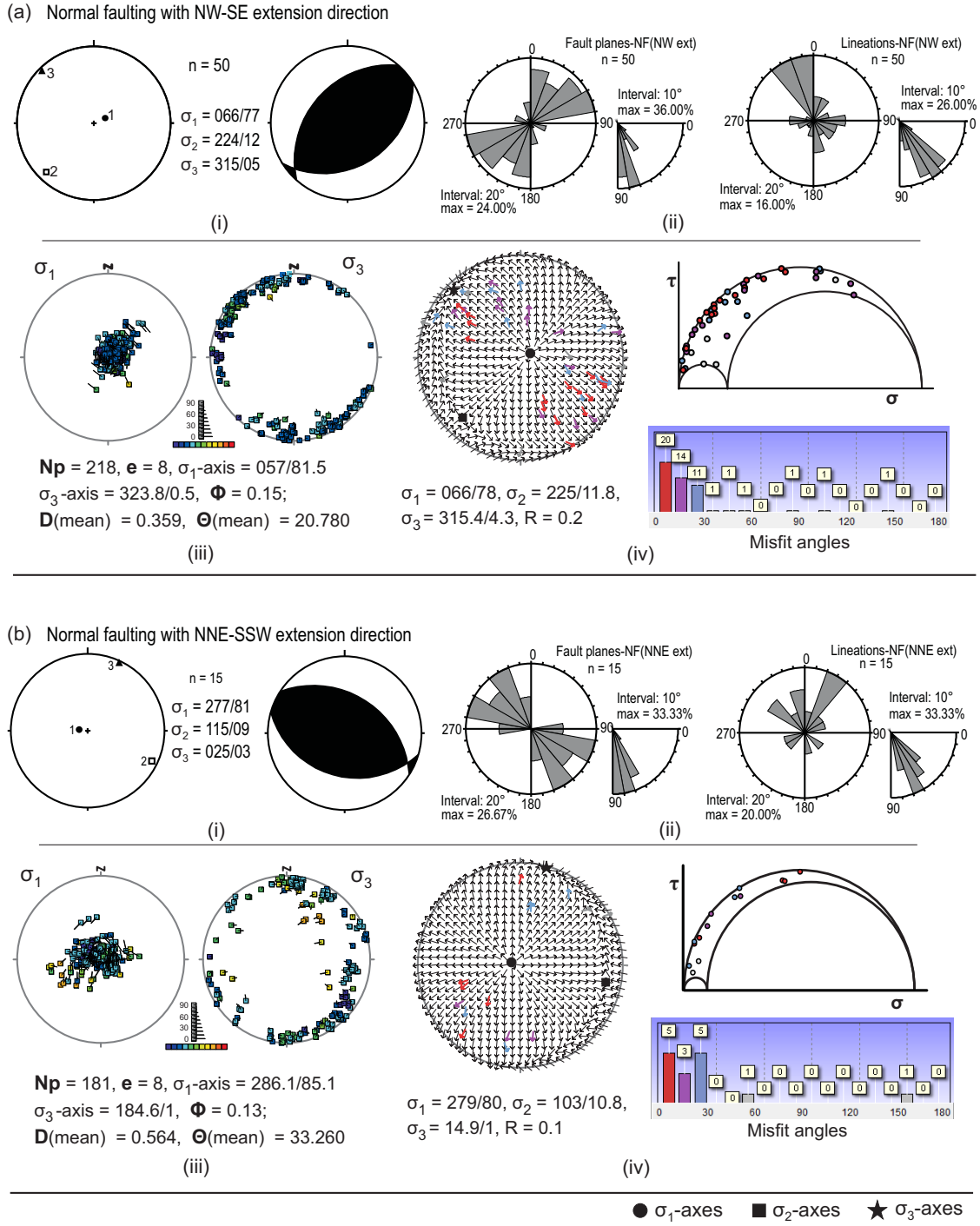

Fig. 5.11 Average stress tensor for summed-up tensional stress states. (a) NW-SE extension. (b) NNE-SSW extension. (i) PBT-generated stress tensor and corresponding dihedra. (ii) left: Rose diagram for fault planes, right: Rose diagram for lineations. (iii) Paired stereograms. (iv) left: Tangent-lineations plot. upper right: Mohr plot. lower-right: Angular misfits.

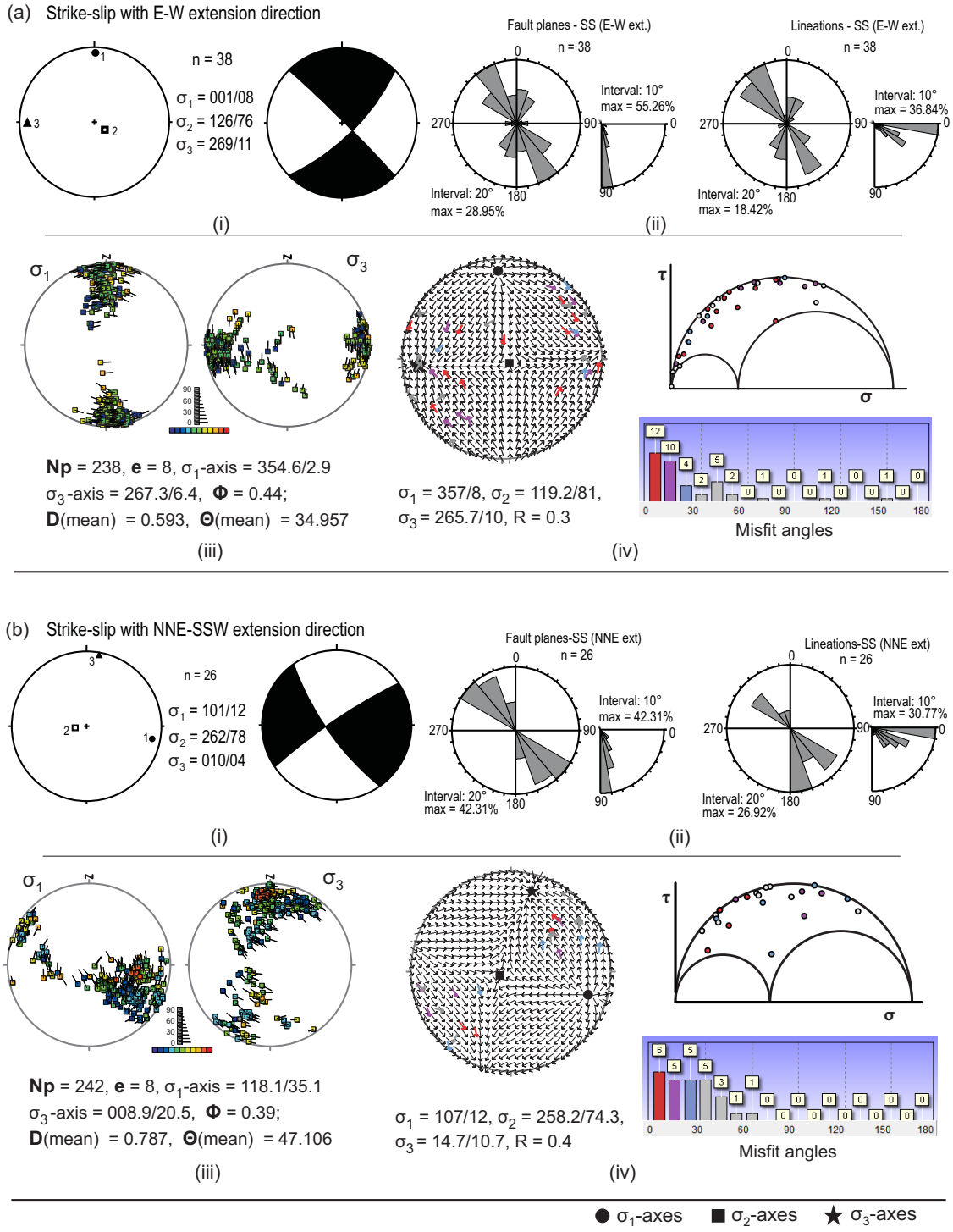

Fig. 5.12 Average stress tensor for summed-up strike-slip stress states. (a) W-E extension, (b) NNE-SSW extension. (i) PBT-generated stress tensor and corresponding dihedra. (ii) left: Rose diagram for fault planes, right: Rose diagram for lineations. (iii) stress-state distribution in MIM-generated paired stereograms, (iv) left: Tangent-lineations plot. upper right: Mohr plot. lower-right: Angular misfits.

Additionally, G2 granites with ages between 1280-1260Ma were reported to have formed under extensional stress (Tack et al. 2010) during the Kibaran event, whereas G3 and G4 granites formed post-Kibaran. The G3 granites showed ages around 1180Ma and were reported to have formed under compressional stress whereas the younger G4 granites with whole-rock Rb-Sr ages of 1125 ± 25Ma were said to have formed under transpression (Tack et al. 2010). This compressional deformation that post-dates the Kibaran event was explained as reflecting far-field effects of global orogenic events.

From microstructural study of the rocks, foliations S1, S3, S4 also suggested W-E to NE-SW directions of extension whereas S2 indicated NNW-SSE extension (Sec. 4.3 on page 53). From inversion of fault-plane solutions data obtained from seismograms of teleseismic events, the fault movements responsible for most of the recent earthquake occurrences in the Rwenzori region reflected extension mainly in the NW-SE direction as summarised in Fig. 5.13. However, extension tending towards directions between WNW-ESE to ENE-SSW are also manifest. Comparing our results from fault-slip analysis with earlier inferences, we think that the oldest observed stress regime consisted of dominantly strike-slip stress-states with horizontal to sub-horizontal ENE-WSW to W-E oriented extension, respectively represented in the northern and Central-Rwenzoris by SK-2^2 and RC^2. This was thought to have resulted from intra-cratonic forces that acted on the Africa plate prior to rifting. The same regime was thought to have been translated into a state of oblique thrust-faulting KK-3^2 exhibited in the east central part. Save for differences in tilt angles, the direction of compression for KK-3^2 varies from those of SK-2^2 and RC^2 by less than 5°, whereas its extension direction varies by about 30° from those of the latter two. These stresses were contemporaneous with or shortly followed by stress-state RB^2, which was responsible for thrust faulting in the central-Rwenzoris. Presence of faults attesting to such reverse movements in three outcrop localities (Elena, Freshfield Pass and John-Matte hut area), could reliably suggest wide influence of the stress field. Since continental interiors are mostly affected by compressional stresses (Zoback 1992a), which would be the case for Africa in the absence of the EARS (Delvaux and Barth 2010), the stress-state RB^2 must have prevailed either before or at the initiation of rifting in this area. Hence stress-states SK-2^2, RB^2 and RC^2 could represent the same stress regime, loosely described here as a 'compressive intra-cratonic regime'.

Alternatively, the Paleoproterozoic Ubendian orogeny (2100–1800Ma) could be responsible for reverse faulting. This orogeny left behind persistent W-E to NE-SW structural trends in Uganda and on the Rwenzori mountains in particular, Ubendian age rocks were thrusted north-ward against a resistant Speak gneiss. The deformation was mainly a product of collisional orogeny along the southwestern margin of the Tanzania and Congo cratons. In this case, the thrusting stress regime occurred earlier than the 'compressive intra-cratonic regime' that caused widespread strike-slip fault kinematics, therefore RC^2 would be the earliest state of stress recorded.

The compressive intra-cratonic regime was proceeded by stress-states RA^2 and KNG-2^2 whose extension axes permutated respectively into NW-SE and NNE-SSW directions in the two areas. Their maximum horizontal principal axes probably rotated from the previous N-S direction under the compressional regime to between NNE-SSW and ESE-WNW directions. The stresses probably prevailed through most of the late rifting and uplift stages and persisted to the present. It has been demonstrated that at shallow crustal levels, slip can occur along cohesionless planes of weakness that dip $> 10^\circ$, enabling reactivation of low angle faults in extensional regimes (Ivins et al. 1990; Huyghe and Mugnier 1992; Nieto-Samaniego and Alaniz-Alvarez 1995). Sibson (1985) suggested that for this

to happen σ_3 should be negative. Hence this regime is thought to have reactivated old thrust faults (of subset RB) with normal movements. Although stress-state RD^2 exhibited NW-SE σ_1-direction, its σ_3-direction corresponded with that of RA^2 and varied by about 13° from that of KNG-2^2. This implied that stress-states RA^2, RD^2 and KNG-2^2 belonged to the same stress regime, here described as an 'extensional rifting regime'.

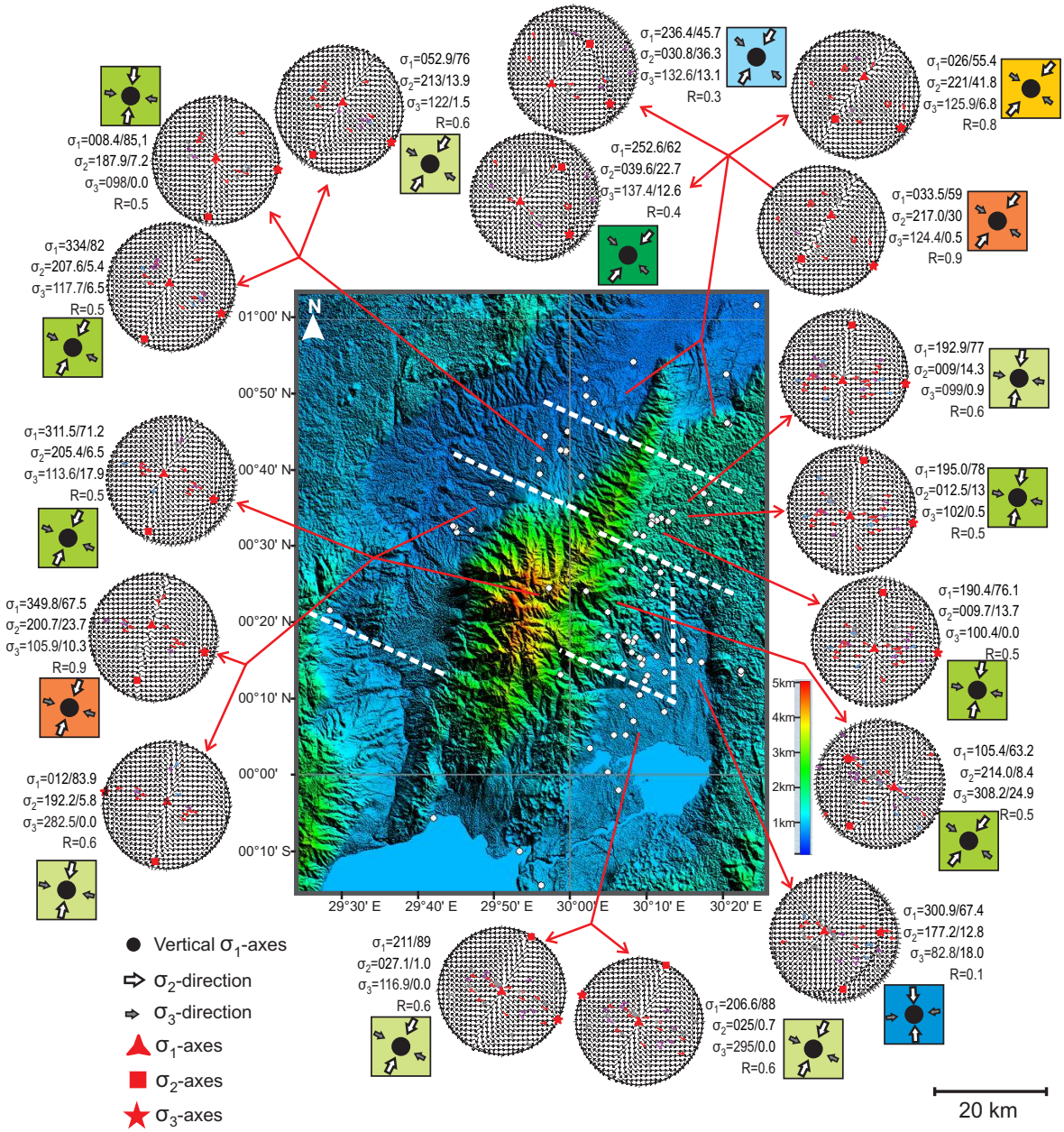

Fig. 5.13 Current directions of extension around the Rwenzoris. Stress states determined by inversion of focal-plane solutions using multiple inversion method. Fault-plane slip directions are denoted by coloured arrows in tangent-lineation plots. Smaller gray-filled arrows in coloured boxes indicate extension direction; background colour denotes stress ratio R of the specified stress state. Focal-mechanisms data adopted from Gummert (2009).

Delvaux and Barth (2010) suggested that the consistent W-E orientation of the maximum horizontal principal stress ($S_{(Hmax)}$) observed in the lowlands of the Nubian plate plus a compressional regime observed in the Congo River Basin, could represent the 1^{st}-order stress pattern of the Africa plate far from effects of the EARS and its elevated regions. RD^2 with its WNW-ESE striking (and ESE-ward tilted) σ-axis, was the only stress-state that closely attested to the far-field effect of horizontal W-E compression in the entire study area. Thus it can be argued that RD^2 was a manifestation of locally superimposed effects on the 1^{st}-order stress pattern of the Africa plate. This would indicate that indeed for most of the part, global stresses have been locally interfered with, resulting in local differences in deformation style. Hence RD^2 is likely to have been active during the initial stages of rifting as a transient stress-state between the older intra-cratonic regime and the younger extensional rifting regime.

Fault kinematics derived from focal mechanisms around the Albertine Rift mainly from Semliki basin and southern Rwenzoris, showed a tensional regime under NW-SE extension with σ_1, σ_2 and σ_3 axes respectively oriented 295/75, 033/02 and 124/15 (Delvaux and Barth 2010). Focal mechanisms data from around the lake Kivu segment immediately south of the Rwenzoris, also revealed a tensional regime with NW-SE extension and σ_1, σ_2, σ_3 axes respectively oriented 259/72, 032/13 and 125/13 (Delvaux and Barth 2010), which are quite similar to the Albert-Rwenzori segment. Inversion also of focal-plane solutions from around the Rwenzori mountains confirmed current extension directions mainly between the NW-SE and W-E directions. Thus, in addition to RA^2, tensional stress-states SK-1^2 and KNG-1^2 with NW-SE to WNW-ESE extension directions can be considered to be most recent, reactivating old faults through post-uplift stages of rift evolution. The three were contemporaneous with the strike-slip stress-state KK-12^2, which also exhibited NNW-SSE extension direction. However, stress-states RD^2, KK-12^2 and KNG-2^2 resulted from local temporal and spatial fluctuation of axes orientations of the regional extensional stress regime superimposed on the respective localities. A counterclockwise rotation of extension axes was therefore deduced as illustrated by arrows in Fig. 5.14, from W-E, through ENE-WSW, then NNE-SSW and at present NW-SE direction.

5.2.4 Sources of stress variation

From the above discussion, it can be argued that most of the faults have been (re-)activated with mainly extensional movement, lesser strike-slip and a few with oblique thrust movement. We thus argue that present kinematics in the study area are controlled by a tensional stress regime under NW-SE directed extension, represented by stress-states SK-1^2, RA^2 and KNG-1^2. Stress fields or stress axes orientations have varried as a result of:

(i) temporal fluctuations causing permutations and reversals of stress axes (Ring et al. 1992),

(ii) interference of regional stresses by stress fields around master faults in the vicinity, since deviations (produced by perturbations in the stress field due to interaction between pre-existing planes) between the maximum shear stress calculated from the far-field stress tensor and that calculated from the local stress tensor can reach 40° when the spatial density of faults is high (Pollard et al. 1993),

(iii) block rotation and uplift causing local changes in stress (Koehn et al. 2010),

(iv) interaction of rift segments (Koehn et al. 2008, 2010) and

(v) differences in local state of gravitational potential energy, since gravitational potential energy per unit area of a column of material U, above a given depth z is given by the integral of the vertical stress σ_{zz} from z to the surface h (Coblentz and Randall 1994) as shown in equation (5.1).

$$U = \int_z^h \sigma_{zz}(\tau)d\tau = g\int_z^h \int_\tau^h \rho(\tau^{'})d\tau^{'}d\tau, \tag{5.1}$$

where $\rho(\tau^{'})$ is the density at depth z, h is the surface elevation, **g** is gravitational acceleration and $\tau^{'}$ and τ are integration variables.

Notice that for a lithospheric column, its potential energy is defined by equation (5.1) when z corresponds to the equipotential surface z_{iso} at which the lithosphere is compensated (Coblentz and Randall 1994). Notice also that results from modelling (Coblentz and Sandiford 1994; Stamps et al. 2010) have demonstrated that the large scale extensional stress field in eastern and southern Africa can be the action of gravitational potential energy within the plates (Delvaux and Barth 2010)

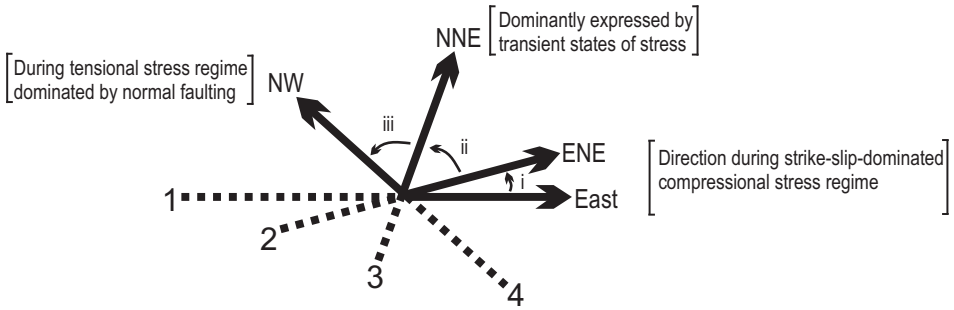

Fig. 5.14 Counter-clockwise rotation of extension directions constrained from relative chronology of stress states responsible for the different fault patterns around the Rwenzoris.

Chapter 6

Results of Analogue Modelling

This chapter contains results and discussion ensuing from the sandbox analogue model experiments. As mentioned in chapter 3, varying the sizes of overstep and extension-orthogonal spacing between VD segments resulted in different rift evolution patterns and geometries. Interacting fault or rift segments from the different experimental series exhibited variable behaviour. Boundary conditions which produced end-members that approximated the target system were reproduced in the final experiments of the R-series. Those whose results varied widely from the observed behaviour of natural counterpart were discarded as indicated at the end of a brief discussion. The resulting fault or rift geometries, structure evolution and age relationships, and fault or rift segment interactions are discussed with regard to their implications for structures found in the Albertine Rift System. In the discussion we scale the model length-scales to natural scales of 1:357000 (model:nature) in order to compare the results better with the natural data from the East African Rift. The results and brief discussion for all preliminary experiments, including series A, B and experiments SbR6, SbR7 of the R-series, are presented in the first section. The second section contains results and discussion for series SbR3, SbR4, SbR5 most of which are published as already indicated in chapter 1.

6.1 Preliminary experimental series

Series A

Generally for lateral VD segment offset (overstep) smaller than 10cm (Fig. 6.1a and b), rift segments nucleated and propagated considerably near-orthogonal to extension vector until they overlapped with the adjacent segment via an oblique transfer zone. For extension greater than 2.0cm propagation direction in the two peripheral segments was controlled by orientation of the basal sheet edges, hence propagation towards the central segment at about 30° to extension vector. Plan-view photographs of the models are presented in figure E.1 on page 143. A closer study of the behaviour of segments where they meet showed that although the segments were offset, only the border faults propagated oblique to extension vector in the region of overlap while other faults continued with trends similar to those in the main segments. An example is shown in figure 6.2a, where only border faults labelled Rs1, Ls1 changed propagation trend depicting local extension directions at high angles to the general extension vector.

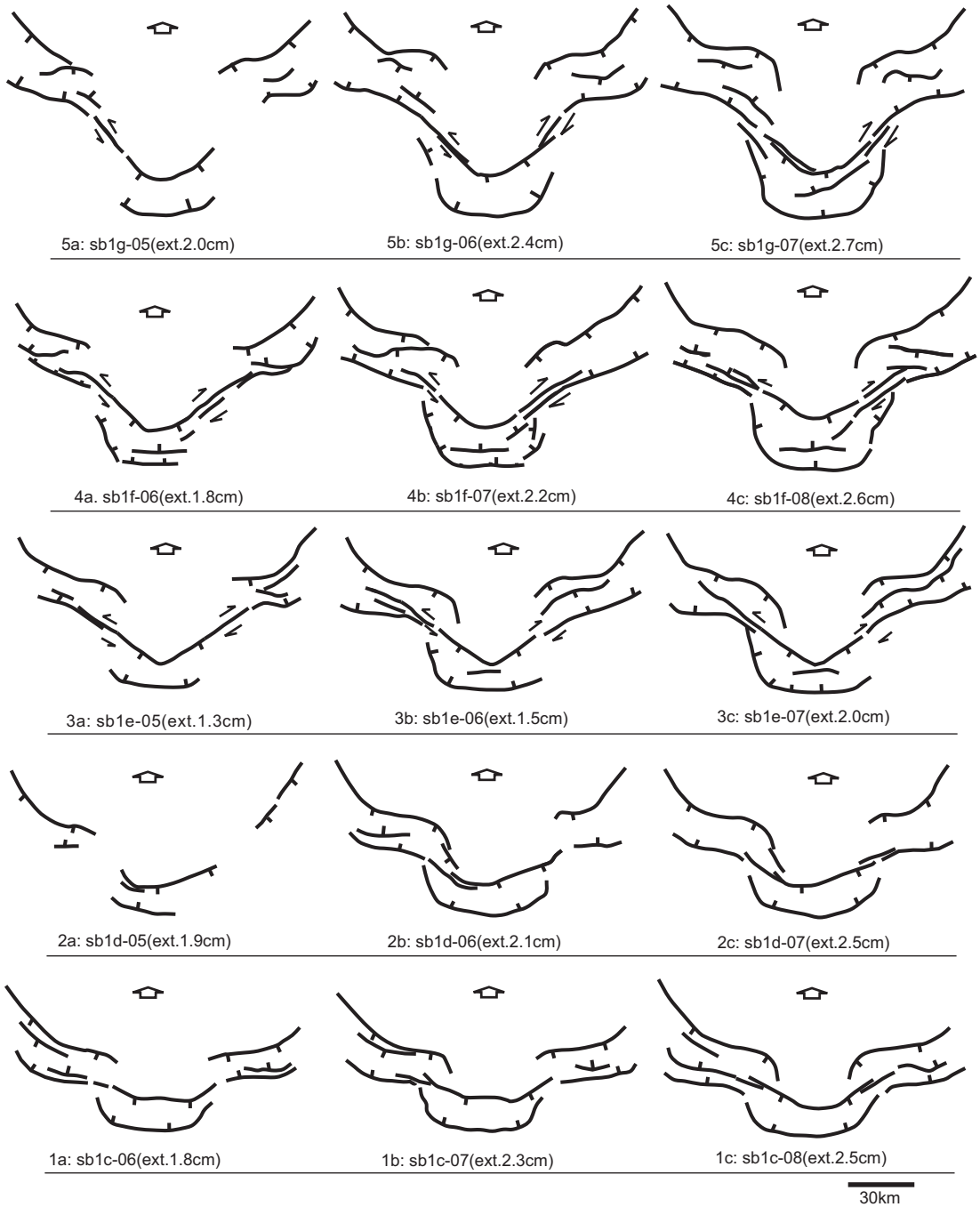

Fig. 6.1 series A:Redrawn plan-view of developing rift segments at different stages of extension indicated below each diagram and for different amounts of lateral offset of two peripheral VD segments from a central one. Respective amounts of offset were, for experiment (1) 6cm, (2) 8cm, (3) 10cm, (4) 12cm, and (5) 15cm. Arrows denote extension vector.

With 10cm lateral VD segment offset (Fig. 6.1c), rift segments nucleated and propagated in both directions at angles greater than 60° to extension vector until they joined up. Further extension caused strike-slip movement along segment connecting faults, resulting in development of an open V-shaped central segment. Basal sheet lateral-edge control on the direction of segment propagation became evident after extension of approximately 2.0cm whereby peripheral segments approached the central segment at about 30° to extension

vector. Unlike the previous example, here all fault segments in the accommodation zone or zone of overlap propagate oblique to extension vector, however, they showed no interaction with one another where they overlapped. An example is presented in Fig. 6.2b, where all border faults Rs1, Rs2, Ls1 and Ls2 change trend.

For VD segment offsets larger than 10cm (Fig. 6.1d and e), rift segments nucleated orthogonal to extension vector. Shortly after, they propagated in directions $45-50^{\circ}$ to extension vector so that the central segment developed an open U-shape. With extension greater than 2.0cm propagation direction in the two peripheral segments was controlled by the orientation of the lateral basal-sheet edges. Thus they propagated toward the central segment near-parallel to extension vector thereby cutting out wedges of blocks into the rift. Further extension caused segments to join and strike-slip movement occurred along the connecting oblique fault segments. In general, the oppositely dipping border faults that are close to each other apparently joined via strike-slip transfer fault segments but but with continued extension they tended to splay out into several short oppositely-dipping oblique fault segments in the accommodation zone. The progression from figure 6.2c to d exemplifies this phenomenon where faults Rs1 and Ls1 developed into the main border faults that delimit the block, whereas Rs2 and Ls2 splayed out into the would-be captured block as shown in figure 6.2d. As such, most deformational strain in the late stage was accommodated by the young faults so that Rs2 and Ls2 exhibited limited or no more activity.

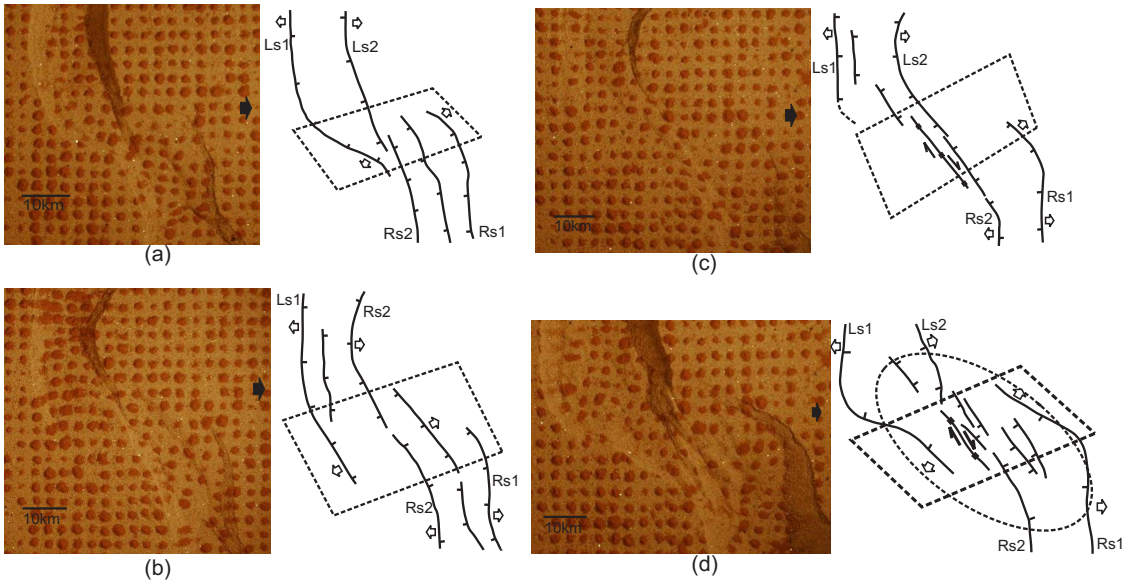

Fig. 6.2 Comparison of transfer zones between left-laterally overstepping segments for (a) 8cm offset after extension of 2.9cm (b) 10cm offset after extension of 2.0cm (c) 12cm offset after extension of 2.2cm (d) 12cm offset after extension of 4.5cm. Note that in d, faults Rs2 and Ls2 splay out into the would-be captured block whereas Rs1 and Ls1 develop into the main border faults that delimit the block . Left: plan-view after deformation. Right: redrawn fault segments. Large black arrows denote general extension vector; small white arrows indicate local extension direction.

On the whole, although offset rift segments developed in all cases, for VD overstep <10cm only border faults propagated oblique to extension vector at the zone of offset. For 10cm VD overstep the segments connected across a slightly oblique accommodation zone in which all faults propagated sub-orthogonal to extension vector. VD overstep >10cm resulted in segments that joined across a strike-slip transfer fault, which accommodated most

of the late deformation. Hence greater overstep between VD segments offered stronger interaction between rift segments through strike-slip movement along adjoining oblique fault segments, although the widths of rifts were similar to those of smaller overstep. Large overstep encouraged development of accommodation zones closely oblique to extension vector. Smaller VD overstep on the other hand developed accommodation zones striking at higher angles to extension vector. Assuming minimum extension on the EARS to be 10km (approximately 2.8cm extension on the model), experiments with VD overstep of 12–15cm (Fig. 6.1- 4c and 5c) provided results that moderately fitted to the natural prototype, suggesting accommodation zone orientation of $30 - 50^{\circ}$ from extension direction. These also suggested approximately 42–53km rift-segment overstep between the Albert-Edward-George rift-segments, which compares well with the 40-50km width of the Rwenzori block that separates the two.

Series B

The first formed faults nucleated above the VD and developed orthogonal or sub-orthogonal to extension vector after 1.0–1.2cm extension. After 1.8cm extension, faults formed between VD segments at 45–50° to extension vector and propagated in both directions toward the rift segments as shown by the progression of figure 6.3. Plan-view photographs of the actual model surfaces in the the sandbox are presented in figure E.2 on page 144. Continued extension produced more orthogonal faults and rift segments were joined by oblique (45–50°) faults at extension of about 2.0cm so that boundary-faults overlapped into accommodation zones. Oblique adjoining faults inhibited further propagation of orthogonal rift segments so that further extension only resulted in widening of the graben. More oblique faults developed while the older ones rotated about a vertical axis gradually increasing obliquity (55–60°) to extension vector (Fig. 6.3c). For extension greater than 2.5cm faults developed above the lateral basal-sheet boundaries, sub-parallel (less than 15°) to extension vector. A simple comparison of the behaviour of interacting segments in the different cases is shown in figure E.2d.

Generally, the larger the extension-orthogonal space between VD segments, the greater the amount of extension required for extension-sub-parallel faults to develop between rift segments. The smaller the spacing, the longer the rift segments propagated orthogonal to extension vector (see Fig. E.2 on page 144). Models with wider VD-segment spacing developed short extension-orthogonal segments implying that most of the extension was accommodated along the connecting oblique faults. The greater the separation between VD segments, the more numerous the fault segments that developed within accommodation zones. These experiments showed that oblique faults in accommodation zones developed in the later stages of extension. This might explain the existence in the Rwenzori mountains, of younger 'abnormal' fault populations reported by Koehn et al. (2008).

Experiment SbR6

During deformation of this model the rift segment on the right nucleated after about 2.0cm extension and propagated considerably before nucleation of the segment on the left at 3.5cm. The two deflected around the central block that separates them (Fig. 6.4). In the region where the rifts approached each other in the foreground and background of

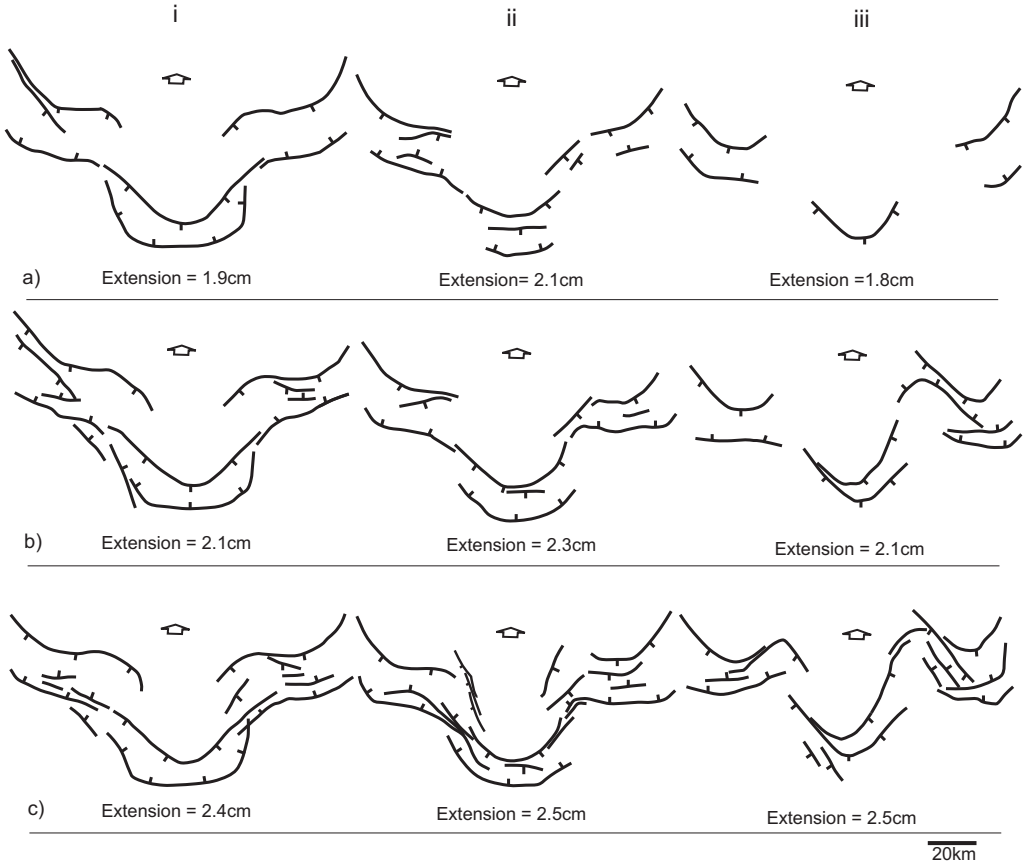

Fig. 6.3 Series B: Redrawn plan-view of rift segments at different stages of extension indicated below each diagram and for different amounts of lateral separation of two peripheral VD segments from a central one. Respective amounts of lateral separation ('spacing') were: (i) experiment sb7: 11cm-wide basal-sheet segments separated from each other by a spacing of 2.5cm (ii) experiment sb8: two peripheral sheets each 9cm-wide and a middle sheet 11cm-wide, separated from each other by a spacing of 4.0cm (iii) experiment sb9: 9cm-wide basal-sheet segments separated from each other by a spacing of 6.0cm. Arrows denote extension vector.

the box, short en echelon left-laterally stepping fault segments developed in a right-to-left progressing front, after approximately 4cm extension - forming transfer zones where the two rifts join. The en echelon fault segments were oriented sub-orthogonal to extension vector, some dipping away and others toward the moving wall. Two asymmetric rifts about 6cm-wide developed, separated by a 20x13cm horst, and segments joined to form one wide rift at the zone of transfer where deformation was diffuse. The horst rotated clockwise as observed from reference lines P_L and P_T (Fig. 6.5) that were used to measure the degree of rotation of the captured block in directions parallel- and transverse to extension vector, respectively. They respectively rotated 2.3° and 1.5° over extension of 3.8cm on the model. Sections in figure 6.4d showed mainly normal faults that propagated from the top downward. A few have a listric component; for example a kind of listric fun developed at the right side of sections $A - A^{'}$ and $B - B^{'}$ (Fig. 6.4d). Valley depths ranged from 2.6-6.8km, the most shallow being in the centre of the model.

The length of the experimental horst, 71km on a scale 1:357000 (model:nature) only approximated 2/3 of the actual length of the Rwenzoris (120km), but its width of about 46km compared well to that of the natural counterpart which is 40–50km. The width

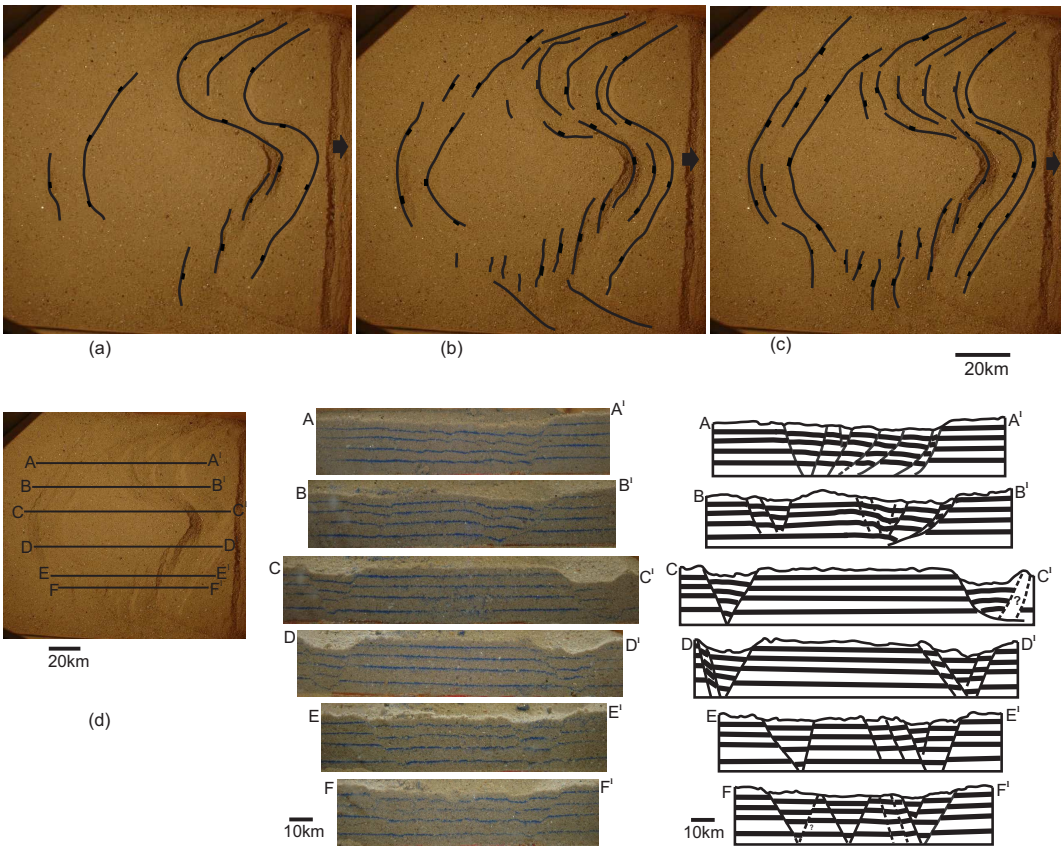

Fig. 6.4 a-c: Redrawn plan-view showing deformational progress of model SbR6 after extension of (a) 4.0cm (14.28km) (b) 4.8cm (17.14km) (c) 5.8cm (20.71km). Black arrows denote extension vector. (d) Sections cut after 5.8cm (20.71km) extension. Distances for respective sections measured from the far end of the wall were: $A-A^{'}$=9.0cm; $B-B^{'}$=13.5cm; $C-C^{'}$=18.0cm; $D-D^{'}$=24.0cm; $E-E^{'}$=29.0cm; and $F-F^{'}$=31.0cm. right: Traced faults.

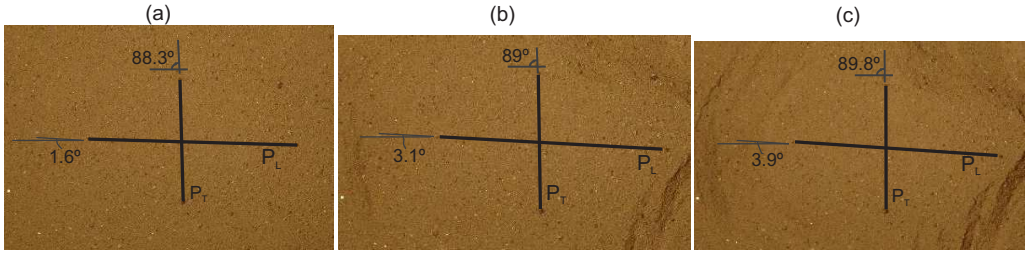

Fig. 6.5 Relative movement of objects on the surface of model SbR6 during extension through (a) 2.0cm (7.14km) (b) 4.4cm (15.71km) (c) 5.8cm (20.71km). Lines P_L and P_T connect marker objects on the model surface, in directions parallel and transverse to extension vector respectively.

21.4km of the natural rift suggested by this model was, however, much smaller than the 40–70km width reported for rift basins in East Africa (Ebinger 1989*b*). Presence of listric normal faults that displayed reverse drag and rollover effect on the hanging wall as observed in sections $A-A^{'}$, $B-B^{'}$ and $C-C^{'}$ (see Fig. 6.4d), suggested ductile shear along layers. This could be explained by the observation that, the graben valleys and basins in the crust comprise a major border fault, linked in depth to a low angle detachment fault inducing asymmetric roll-over pattern (Chorowicz 2005). The range of valley depths between 2.6-6.8km, was in good agreement with valley depths within the Albertine rift for

which a maximum of 6km is reported (Ebinger 1989*b*). Rotation of P_L by 2.3° over 3.8cm extension implied rotation by about 1.7° in nature for total extension of 10km (Ebinger 1989*b*) or $1.0 - 2.7°$ rotation for cumulative extension of 6-16km (Karner et al. 2000). Imposing the same values to line P_T, rotation by 1.5° for P_T yields about 1.1° or between $0.6 - 1.8°$ rotation respectively, under constraints by Ebinger (1989*b*) and Karner et al. (2000). These rotation values suggested that different parts of the horst underwent varying amounts of rotation, however, they were too low compared to 5° rotation estimated for the Rwenzoris. Since the length of the developed horst, rift widths and block rotation angles suggested by this model were much lower than those expressed in nature, this model is not discussed any further than this.

Experiment SbR7

Progress of fault development is shown in figure 6.6, where photographs of the model surface were taken after 3.5cm (12.50km), 4.4cm (15.71km), 4.9cm (17.50km) and 5.5cm (19.64km) of extension. Rift segments to the right nucleated after about 2.5cm extension, propagated toward each other and were connected by offset transfer faults at the centre. After 3.2cm (11.43km) extension faults dipping to the left connected above the oblique-central limit of the rubber strip, whereas the oppositely dipping faults propagated past each other without visible interference. Typical accommodation zones formed where fault segments connect. Border fault segments of the rift to the left nucleated later after 4.0cm (11.28km) extension, meanwhile internal faults developed within the older rift. Right-dipping faults propagated sub-orthogonal to extension vector around the model centre, whereas their left-dipping counterparts formed one main continuous border fault bounding the horst on the right. Two asymmetric 5-6cm (18-21km)-wide rifts formed with normal faults stepping towards the valleys, separated by a narrow (max.1cm-wide at the centre) elongate (17cm [∼60km] -long) horst captured between the two; with rifts joined to form one approximately 12cm (or 43km)-wide diffuse rift towards the limiting walls as seen in sections $A - A^{'}$ and $E - E^{'}$ (Fig. 6.6e). Sections revealed valley depths ranging between 3.0-8.1km, the most shallow being at the periphery of the model.

In summary, the model suggested rift widths 17.9-21.4 km, which were much narrower than the 40-70km-width reported for rift basins across uplifted flanks in East Africa (Ebinger 1989*b*). The length of the model horst suggested more than 60km length of the horst in nature, which is about half of the length of the Rwenzori block. Although the shapes are similar, the model horst (<4km-wide) is too narrow compared to the (40-50km-wide) natural horst. The range of valley depths 3.0–8.1km suggested by this model encompasses the 6km-depth of valleys in the Albertine rift (Ebinger 1989*b*). But since the model resulted in much narrower rifts and horst and a much shorter horst than exists in nature, it is not discussed any further.

6.2 Final R-series

The most part of the results and discussion presented in this section for models SbR3, SbR4, SbR5 were published in the Journal of African Earth Sciences 59 (2011) 168-184, under the title 'Influence of pre-existing fabrics on fault kinematics and rift geometry of interacting segments: Analogue models based on the Albertine Rift (Uganda), Western Branch-East African Rift System' (DOI:10.1016/j.jafrearsci.2010.10.003).

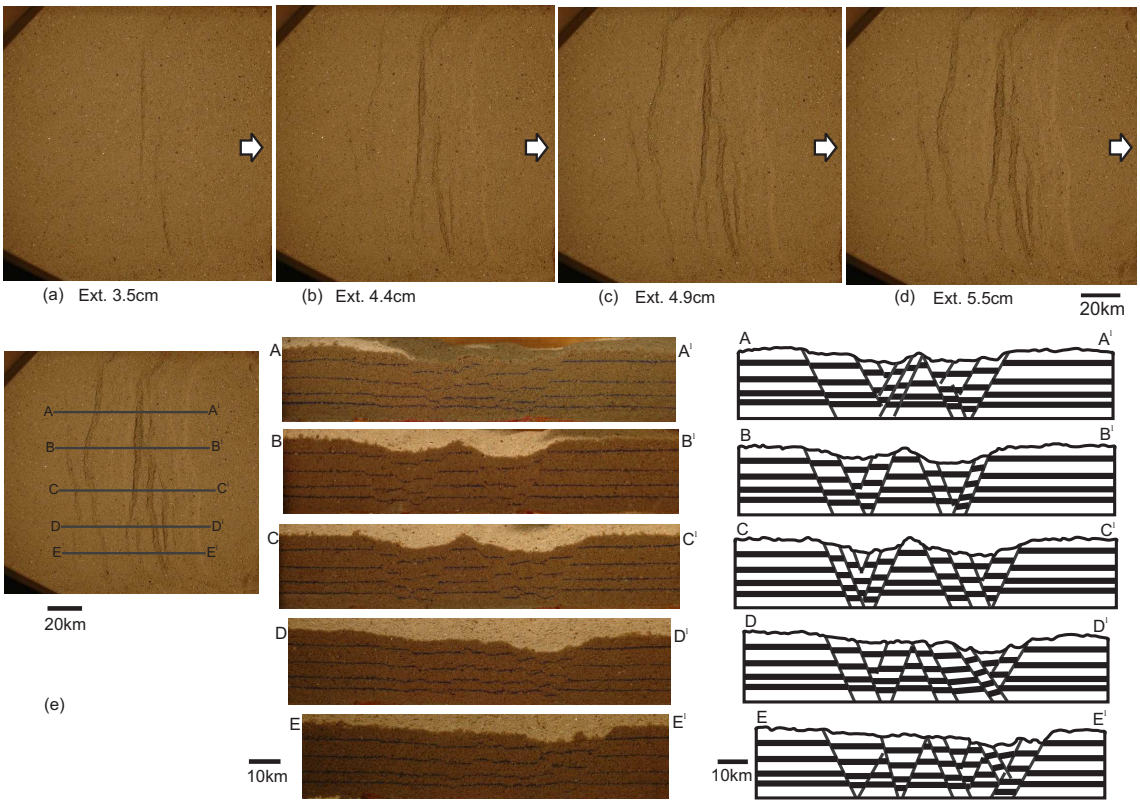

Fig. 6.6 Model SbR7. a-d: Photographs showing plan-view after extension of (a) 3.5cm (12.50km) (b) 4.4cm (15.71km) (c) 4.9cm (17.50km) (d) 5.5cm (19.64km). Ext.=Extension. Arrows denote extension vector. (e) Sections cut after 5.5cm (19.64km) extension. Distances of respective sections measured from the far end of the wall were: $A - A^{'}$=9.5cm, $B - B^{'}$=15.5cm, $C - C^{'}$=22.5cm, $D - D^{'}$=28.5cm and $E - E^{'}$=23.0cm. right: redrawn faults.

(i) Series 1 (SbR3), shear-dominated transfer

Figure 6.7a shows the setup for series 1 and figure 6.7b the plan-view with faults after the final deformation step. The border fault dipping away from the moving wall on the 'northern' segment and the one dipping towards the moving wall on the 'southern' segment formed first, nucleating as short segments that joined along their length. Both rifts nucleated close to the 'limiting walls' of the model, extension being localised above the rubber boundaries so that two offset rift segments formed. They propagated orthogonal to extension vector in the initial stages of extension but were soon followed by oblique en-echelon fault segments in the centre of the box. The en-echelon faults propagated towards each other and joined to form oblique faults that connected the two rift segments, deflecting around the connecting 'rigid-bridge' on its right side.

After this initial deformation, oppositely dipping faults developed to complete the rift structure. Figure 6.8 shows cross-sections through the rifts, whereas figure E.3 on page 145 shows plan-view photographs of the deformed model after varying amounts of extension. The 'northern' rift segment developed one asymmetric depression, while the 'southern' segment developed two asymmetric depressions separated by a small would-be horst block that was later sliced (Fig. 6.8). Valley depressions subsided to maximum depths about 7km lower than the surrounding surface (Fig. 6.8a, x-section G-H). The rifts were bounded by 1–3 faults on each side. Fault dips ranged from $60 - 78°$, the lowest dips having been measured around the centre (average 60°) where segments interacted. Fault throws ranged

from 0.8–6.8km along major border faults making the graben asymmetric and they reduce inward. Fault spacing ranged from 2.5–10km, but particularly within the graben faults were closer with average maximum spacing of 5km (Fig. 6.8a). Although a border fault of the 'northern' rift segment connected with a similarly dipping boundary fault bordering the small horst between the two depressions of the 'southern' segment and vice versa, no block-capture was observed in the transfer zone (Fig. 6.8). Faults did not appear to cross-cut and no fault displacements were observed in section although there was apparent fault-fault interference on the surface. Sections showed some faults that did not reach the base of the model, suggesting downward propagation during growth.

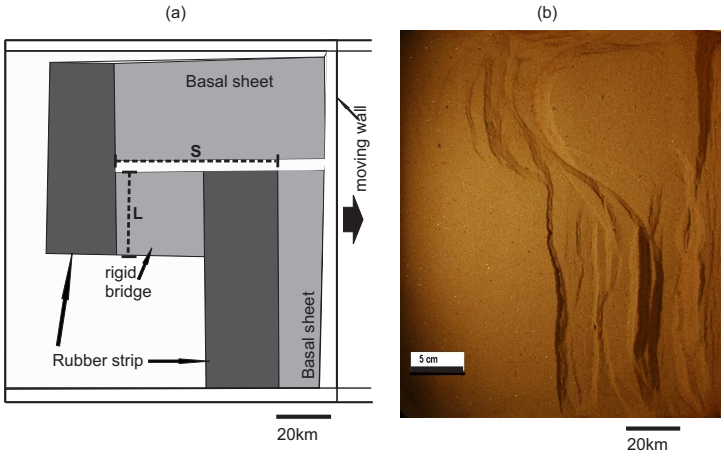

Fig. 6.7 Series 1 (SbR3): (a) Configuration below the sand-pack: two rubber strips (black) 7cm-wide (overlap L=10cm, overstep S=16cm) with boundaries parallel to borders of the connecting 'rigid-bridge' (gray) but orthogonal to extension vector. Large black arrow denotes extension vector. (b) Plan-view of fault and rift geometry after final extensional increment of 10.71km. Extension rate=3.29×10^{-2}mm/sec.

Figure 6.9 and Table 6.1 illustrate clockwise rotation of oblique faults as they evolve through progressive extension. Their obliquity relative to extension vector increased with increment of extension (e.g. F1 vs. F2). F1 and F2 presented rotation rates 1.41°/km and 1.53°/km, respectively. Transfer faults started to nucleate after extension of ≈6.4km and the later the faults nucleated, the smaller their angles relative to extension vector were (Fig. 6.9e). The final appearance of experimental series 1 in plan-view (Fig. 6.8b) was that of two rift segments in the 'north' and 'south' of the box with border- and internal faults mainly orthogonal (few internal fault segments slightly oblique) to extension vector and an oblique transfer zone (37°). Individual fault segments ranged in obliquity from $17 - 55°$ (Fig. 6.9) and faults progressively rotated. The transfer zone was of *"synthetic-approaching"* nature according to the descriptive classification of Morley et al. (1990). Deformation in the transfer zone was shear-dominated, with a transition zone of large overstep and the two rift segments were connected by strongly oblique transfer faults (see Fig. 6.7b). Therefore we termed this experimental series *"shear-dominated transfer"*.

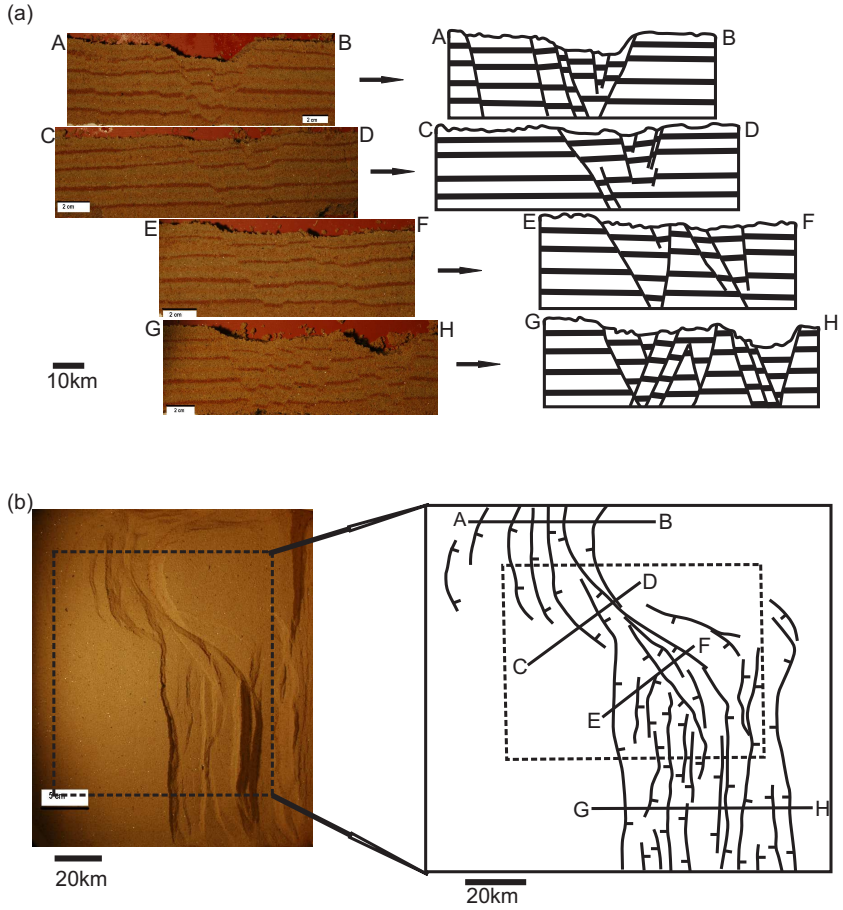

Fig. 6.8 (a) left: sections of model SbR3 after extension of 10.71km (3cm). right: redrawn faults in section. (b) left: plan-view of the deformed model with in-set; right: redrawn fault traces within the in-set and location of sections presented in a. Extension rate=3.29×10^{-2}mm/sec.

Table 6.1 Relative rotation of oblique faults about a vertical axis.

Extension[a](km)	Extension value, β[b]	θ[c](°)			Φ[d](°)	
		F1	F2	F3	F1	F2
6.43	1.05	46.5[n]		-	-	-
8.57	1.07	48.8	26.0[n]	-	2.3	-
10.00	1.08	49.8	27.7	-	1.0	1.7
11.43	1.09	54.4	30.9	17.0[n]	4.6	3.2

[a] Initial length of model was approximately 120km.
[b] Ratio of final to initial length of model.
[c] Horizontal inclination of fault measured relative to extension vector.
[d] Angle of rotation of fault between successive extensional increments, measured relative to extension vector.
[n] Fault inclination at nucleation, measured relative to extension vector.

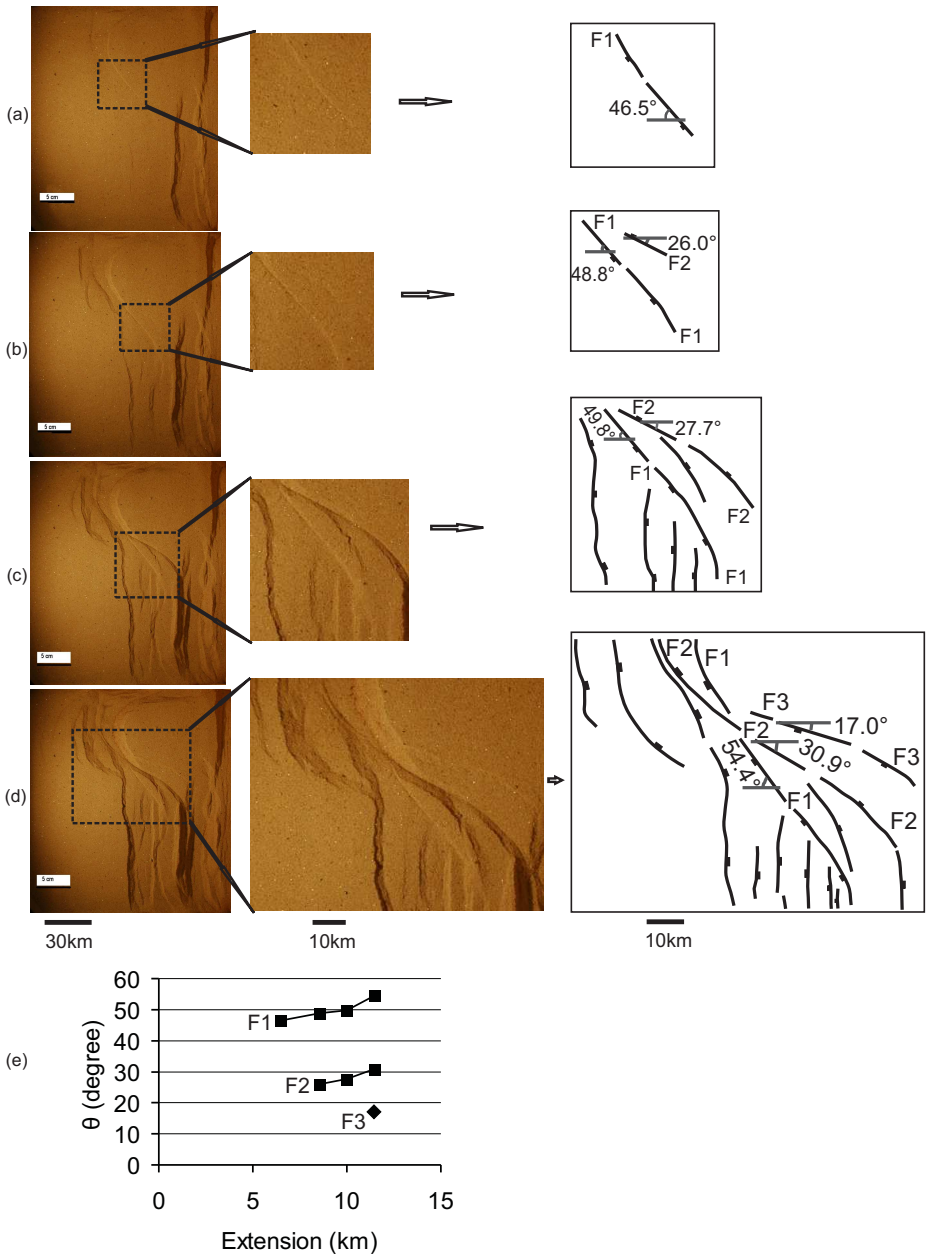

Fig. 6.9 Model SbR3: gradual horizontal deflection of faults with progressive extension. a-d: plan-view of faults F1, F2, F3 in the transfer zone in-set of Fig. 6.8b-right after extension of 6.42, 8.57, 10.0, and 11.42km respectively. left: plan-view of entire model with in-set. centre: plan-view of magnified in-set. right: redrawn faults within in-set. (a) F1 nucleated at 46.5°. (b) F2 nucleated at a lesser angle 26°than F1, angles increase through b and c. (d) F3 (youngest fault) nucleated at the lowest angle of 17°to extension direction. (e) Variation of fault trends, θ, with progressive extension (θ = horizontal inclination of fault measured relative to extension direction). Diamond-shaped spot labelled F3 indicates the point of nucleation of fault F3.

(ii) Series 2 (SbR4), extension-dominated transfer.

Figure 6.10 compares the setup of experimental series 2 and the general plan-view of the faults after the final extension increment. The developed rifts were dominated by normal faulting and graben formation, with small oversteps but no transition zone between rift segments (Fig. 6.10b). Three experiments of this setup were done, varying the amounts

of extension as shown in figures E.4 to E.6. In (a) with 7cm-wide rubber strip, extension reached a maximum of 14.29km (4cm). The respective appearances of the model plan-view at different stages of deformation and sections cut after the final increment of extension are shown in figure E.4 on page 146. (b) maximum extension of 7.86km, with 6cm-wide rubber strip. The model plan-view at different stages of deformation and sections cut after the final extensional increment are shown in figure (E.5 on page 147. (c) maximum extension of 5.71km, with 6cm-wide rubber strip. Plan-view of model at different stages of deformation and sections cut after the final deformation step are shown in figure E.6 on page 148. As shown in figure E.6a-c, only the rift segment on the right side developed while the other only started to nucleate as seen in x-section A-B (Fig. E.6d). This was probably because the amount of extension applied to deform the model was not sufficient to develop both rift segments.

On the whole, two narrow asymmetric rifts formed each bordered by one or two faults. The rift segment closer to the mobile wall was wider, more developed with more pronounced down-throw in the graben. The one to the left of the model was generally narrower and less developed with a shallow depression. The maximum valley depressions reached 4.6km. Generally all faults were normal (Fig. 6.11a) with spacing ranging from 3.7–12km, parallel to sub-parallel, moderately steep and propagated from bottom upward. Fault dips ranged from 62–70° with normal displacements up to 3.8km where a fault was cut and offset by another. Fault throws ranged from <0.5–3km, the greatest having been measured along border faults and they reduced toward the centre of the graben and from the surface downward (Fig. 6.12). Faults also seemed to rotate about horizontal axes so that fault dips reduced with progressive deformation e.g. in Fig. 6.12 the dips of border faults on the right side became gentler, reducing from (a) 70° after 3.57km extension, through (b) 67.3° after 7.14km extension, to (c) 65.5° after 10.71km extension.

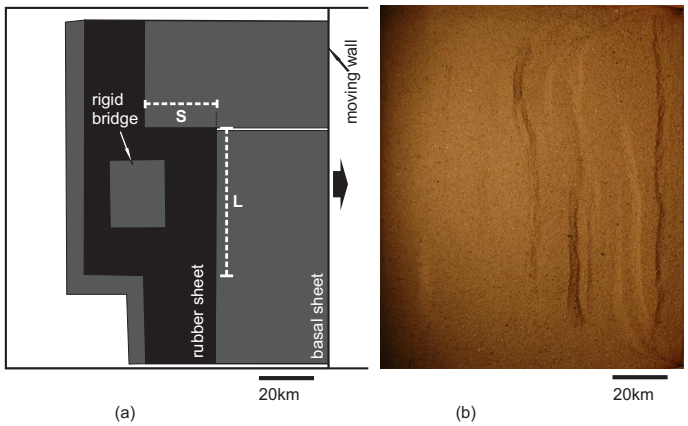

Fig. 6.10 Series 2 (SbR4): (a) Configuration below the sand-pack: two rubber strips (black) 6cm wide, (overlap L=15cm, overstep S=6cm) surround the 'rigid-bridge' (gray). Rubber boundaries parallel to borders of the bridge and orthogonal to extension vector. Large black arrow denotes extension vector. (b) plan-view of fault and rift geometry after final extensional increment of 7.14km. Extension rate=3.35 × 10^{-2}mm/sec.

In figure 6.12a and b, faults bounding the rifts on both sides were of nearly same dip although fault angle relationships in b were affected by cross cutting interaction. In figure 6.12c, angles of the two faults bounding the depression showed a larger difference suggesting that strain was accommodated mainly by horizontal lateral expansion and throw along one fault plane on the right side of the graben. On the left however, strain accommodation

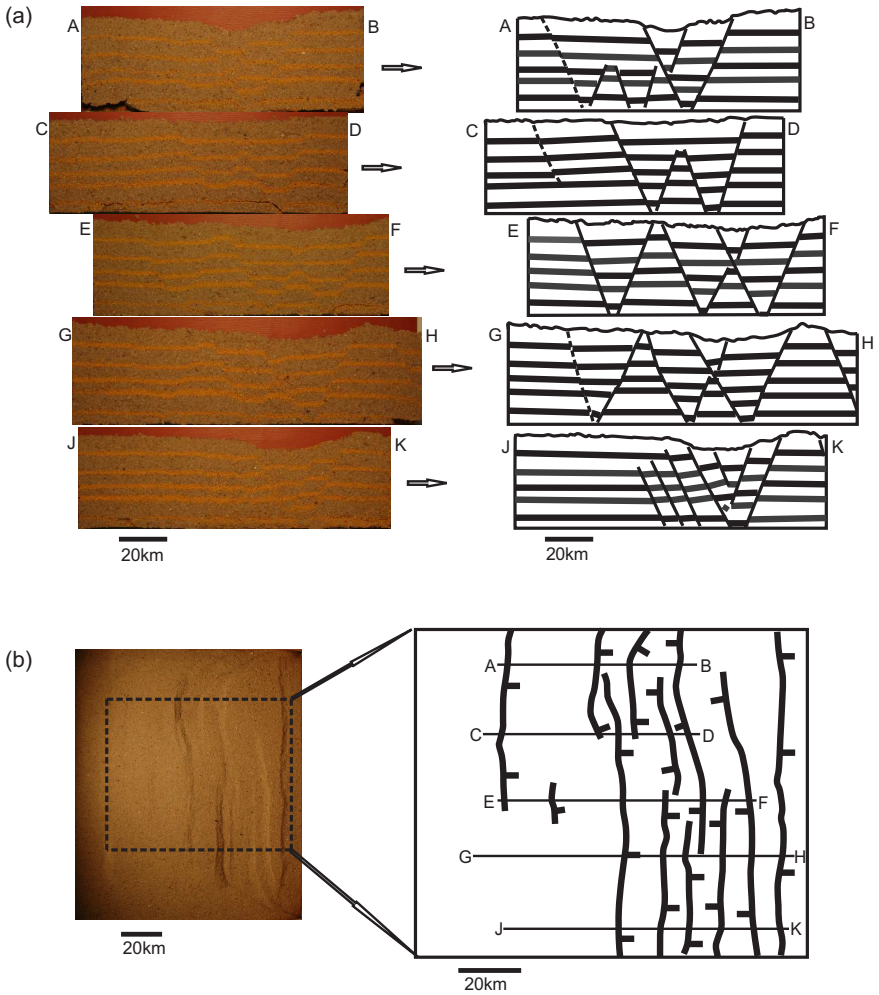

Fig. 6.11 (a) left: sections of model SbR4b after extension of 7.14km (extension rate=3.35×10^{-2}mm/sec.); right: redrawn faults in section. (b) left: plan-view of deformed model with in-set. right: redrawn faults within in-set and location of sections presented in a.

by horizontal lateral expansion was accompanied by development of younger faults synthetic to the border fault, whose cumulative throw was probably great enough to compensate for the lesser relative angular deflection (about horizontal axes) on fault dips resulting from limited expansion. Therefore the graben was asymmetric with greater cumulative throw on the left. Individual border fault relationships between the two slightly offset grabens formed both synthetic and conjugate overlapping transfer zones (Morley et al. 1990) as in figure 6.10b and figure 6.11a, x-section E-F). The developed rifts were dominated by normal faults therefore we termed these *"extension-dominated transfer"* experiments, where blocks did not rotate about vertical axes and no transfer or transsection faults developed.

(iii) Series 3 (SbR5), rotation-dominated transfer.
Figure 6.13a shows the setup of experimental series 3 and figure 6.13b the plan-view of faults after the final extensional increment. Again, three experiments of this setup carried out with varying amounts of extension as shown in figures E.7 to E.9. In (a) the final extensional increment was ∼10.71km. The model plan-view at different stages of deformation and sections cut after the final deformation step are shown in figure E.7.

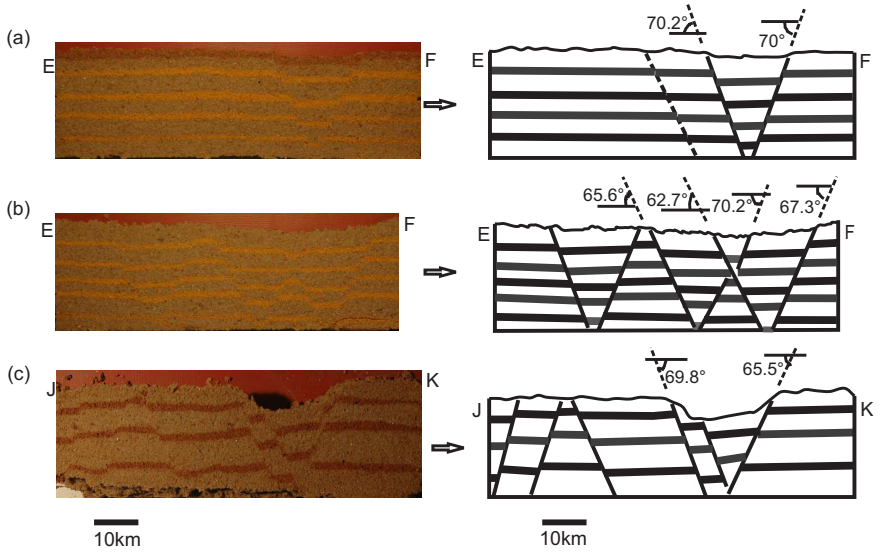

Fig. 6.12 Gradual change of border-fault dips with progressive extension of model SbR4. Left: sections of model SbR4 after extension of (a) 3.57km (b) 7.14km (c) 10.71km. Right: redrawn faults in section showing variation in fault dips.

For (b) the final extensional increment was ∼8.93km. The model plan-view at different stages of deformation and sections cut after the final deformation step are shown in figure E.8 on page 150. (c) Final extension increment at ∼5.71km. The model plan-view at different stages of deformation and sections cut after the final deformation step are shown in figure E.9 on page 151.

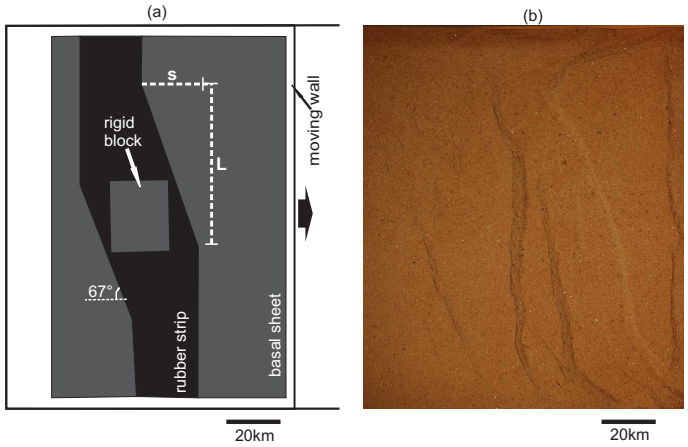

Fig. 6.13 Series 3 (SbR5): (a) Configuration below the sand-pack: a 'rigid-bridge' (gray) surrounded by rubber strips (black) each 7cm wide (overlap L=10cm, overstep S=5cm). Rubber boundaries orthogonal to extension vector near the 'limiting walls' of the model but oblique to borders of the 'rigid-bridge' and to extension vector around the centre. Large black arrow denotes extension vector. 67°=obliquity of rubber to extension vector around the centre. (b) plan-view of fault and rift geometry after extension of 7.14km. Extension rate=3.32×10^{-2}mm/sec.

On the whole, both shear and normal faults develop within a large transfer zone between the two rifts. Fault segments overlapped with no overstep (collinear). Rifts captured a lozenge shaped horst between them, which rotated clockwise as extension continued. Figure 6.14 shows cross-section cuts through the deformed region. Generally, all faults

propagated from the bottom upward although a few seemingly propagated downward. The first formed border fault segments nucleated close to the centre of the model where extension was localised and where the rubber boundary was orthogonal to extension vector. The faults propagated orthogonal to extension vector but as they approached each other they repelled and started to curve. Two slightly offset rift depressions developed, each bounded by a main early forming graben to the right and a minor late forming one to the left. The grabens were slightly asymmetric, each bounded by 1–3 faults. The graben on the right side was wider, more developed with more pronounced down-throw (deepest valley depressions reached about 2.9km) while the minor one to the left of the model was generally narrower and less developed with a shallower depression. For example, border faults on the left of the main graben (Fig. 6.15b, c) dipped at lesser angles than those of border faults to the right of the same graben, causing asymmetry with greater throws on one side.

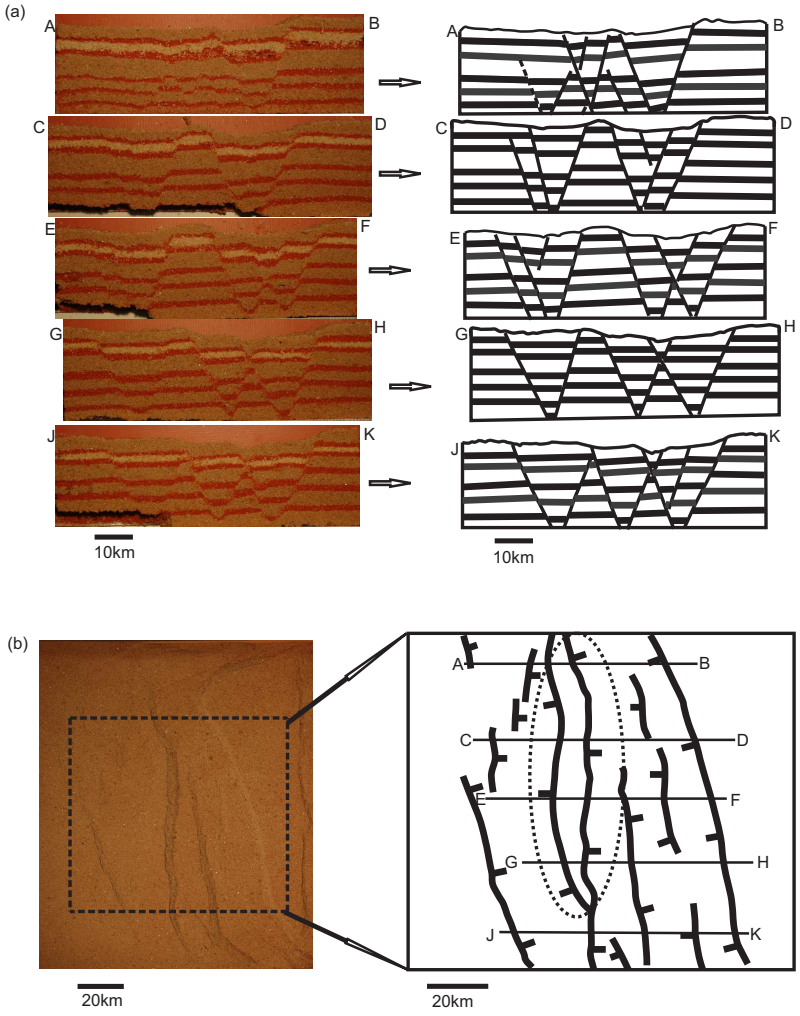

Fig. 6.14 (a) left: Sections of model SbR5b after extension of 7.14km. right: redrawn faults in section. (b) left: plan-view of the deformed model with in-set. right: Traced faults within in-set and location of sections presented in a. dotted oval ring includes the captured block. Extension rate=3.32×10^{-2}mm/sec.

Fault dips ranged from 62–75° but became gradually gentler with progressive deformation. For example, border faults on the left of the graben for all sections in figure 6.15 deflected about a horizontal axis during progressive extension and their dips reduced from 74° at

3.57km extension (in a), through 68° after 7.14km extension (in b), to 62.5° after 10.7km extension (in c). Likewise, dips of the border faults close to point B of the same sections should have reduced from a (70.5°) to c (68.5°). In b, however, most of the deformation is accommodated within a number of interfering, surface-reaching, antithetic faults located left of the graben and less extension is taken up by the border fault to the right. Late formed faults together with earlier faults that were still propagating, were deflected to the left and followed the line of velocity discontinuity. Some late formed faults did not reach the model surface and were steeper than older faults. Fault throws ranged from a few hundred meters to 2.7km, the greater throws having been measured along border faults and diminished toward the centre both parallel and orthogonal to extension vector. Fault spacing was close - ranging from 4–8km and sub-parallel except where conjugate pairs formed. Conjugate pairs offset each other with normal displacements of up to 2.3km (Fig. 6.14a, x-section AB).

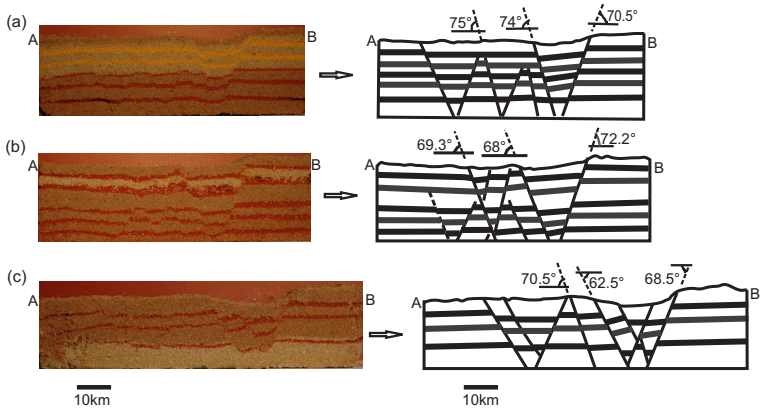

Fig. 6.15 Left: Sections cut from similar spots (30cm from the limiting wall at the foreground) of model SbR5 after extension of (a) 3.57km. (b) 7.14km. (c) 10.71km. Right: redrawn faults showing variation of fault angles relative to the vertical, indicating fault rotation about horizontal axes.

Clockwise rotation occurred above the 'rigid-block' at the centre (Fig. 6.16). From this figure we see that lines P1, P2 that joined positions of pairs of marker objects (located at the ends of the lines) on the model surface,were deflected clockwise during deformation. This implied clockwise shift of objects relative to each other and suggesting clockwise block rotation at the centre of the model. Measured relative to extension vector, the angle of line P1 before extension (70°) was maintained after extension of $3.57km$ in b, but changed through 68° in c (extension $6.78km$), to 65° in d (extension $8.925km$), giving a rotation rate of about 1°/km of extension. That of P2 changed from 60.5° before commencement of deformation in a, through 58° in b and 51° in c, to 48° in d. This gave a rotation rate of about 2°/km of extension. On the left in c and d, are young faults that nucleated in right-stepping en-echelon pattern describing a right-lateral oblique shear zone (indicated by half-arrows) whose obliquity was opposed to that of the rubber strip at the centre.

The rotation of the block should be responsible for the oblique NE-SW ward propagating late faults that cut the would-be horst, and slight NE-ward deflection of older faults. Border faults curved into the transfer zone as the two rift segments approach and propagated toward each other sub-parallel to the oblique line of velocity discontinuity. Range cutting faults dipped in any one of the two directions. Minor block tilting occurred along the centre, within the well-developed graben. Tilting was seen where younger faults interfered with older ones implying that tilting occurs at a later stage in the deformation phase. The

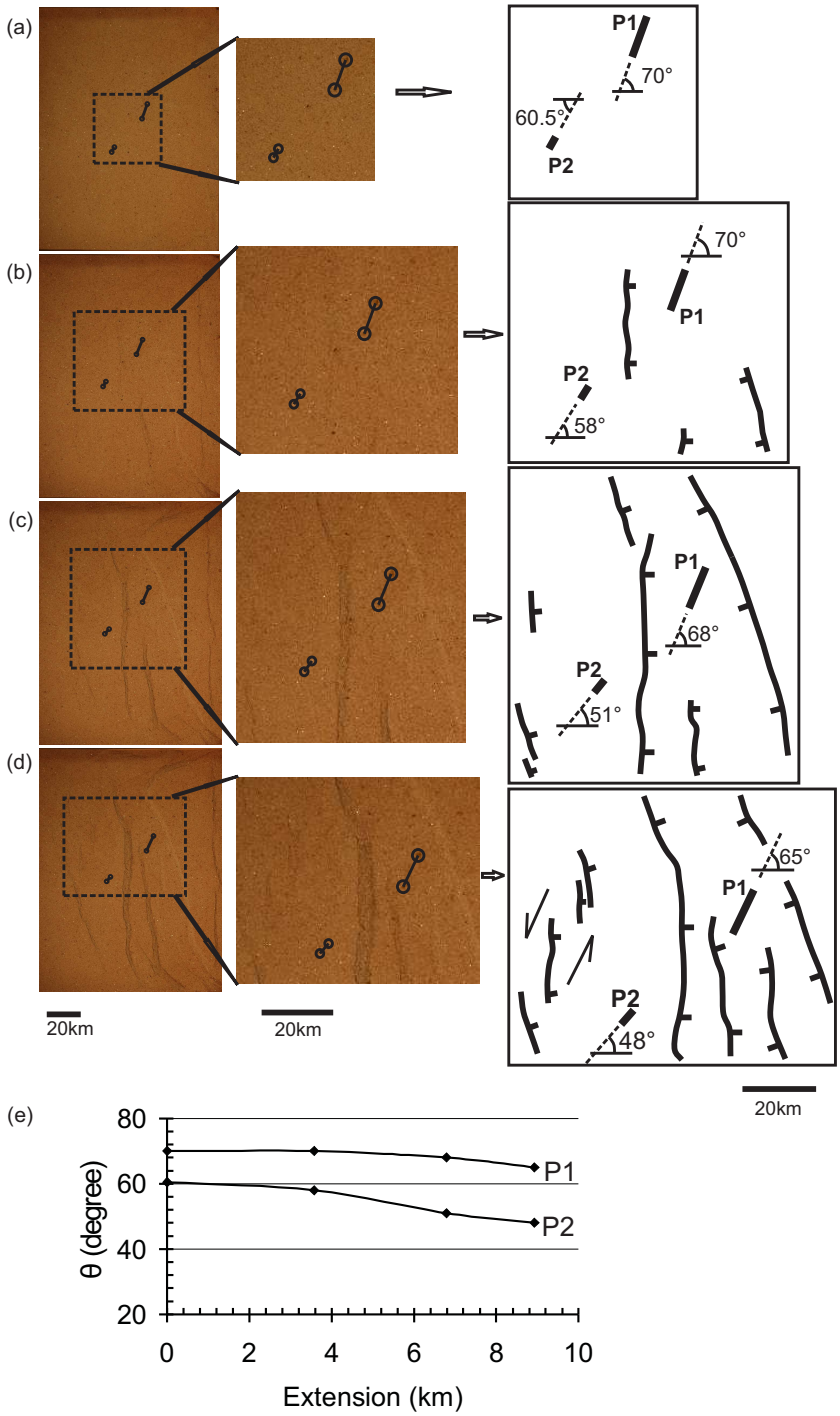

Fig. 6.16 Evidence for block rotation in model SbR5. left: model plan-view at different stages, showing positions of marker objects (in-set). centre: in-set magnified. right: faults redrawn to show relative positions and angles of marker objects after each extensional increment. Straight solid black lines P1, P2 join pairs of marker objects on the model surface (encircled at the ends of the lines). Note clockwise deflection of P1 and P2 from (a) before commencement of extension. (b) after 3.57km extension. (c) after 7.14km extension. (d) after extension of 10.71km. (e) Variation of trend θ of lines P1, P2 with progressive extension. θ = horizontal inclination of line measured relative to extension vector.

horst block was >11km-wide in the centre but tapered out gradually in both directions orthogonal to extension vector, as the two adjacent divergent conjugate border faults intersected. Thus around the centre two distinct rift segments developed but they joined up to form one wider, less discrete rift at both ends.

6.2.1 Comparison with natural scenario

(i) Shear-dominated model (SbR3):
The shear-dominated model is similar to the prototype, since the rift-border faults in the model are normal and orthogonal to extension vector and a larger transfer zone develops. However, no block-capture was observed in the zone of overlap and thus no block rotation occurred. In addition we did not find a strong shear-dominated transfer zone in the Albertine rift system. In the transfer zone of the model, faults were oriented oblique to extension vector. These faults are comparable to the transsection faults found within the Rwenzori massif (Koehn et al. 2008, 2010). The model produced fault throws 0.8–6.5km, which were of similar magnitude to those measured from the EAR faults (1–6km). Graben depths reached a maximum of 7km, which was very close to the 6km maximum graben depth in the Albertine graben.
The effect of pre-existing fabrics is seen where border fault segments nucleated and propagated parallel to the velocity discontinuity presented at the boundaries of the rubber strips. The late-formed oblique fault segments, however, nucleated in the model centre above the zone of overstep of the rubber strips and propagated at an angle to the direction of overstep.

(ii) Extension-dominated model (SbR4):
Similar again to asymmetry of rift basins around the Rwenzoris, two asymmetric rifts formed in the analogue model, each with 1–2 bounding faults on the sides. Graben depths were moderate reaching a maximum of 4.6km, which is close to the 6km maximum graben depth for the Lake Albert basin. Fault throws of this model (<0.5–3.0km) fall within range of throws obtained in the field for faults of the EAR system (1–6km). The geometry of the intersection zone of the rifts is however very different compared to the Rwenzori case. Faults in the extension-dominated analogue model did not rotate or curve, did not transect the transfer zone, no block-capture and no rotation was observed. Instead faults were mainly orthogonal to the extension vector and simply overstepped without much interference.
Although rift segments of this model did not interact via oblique transfer faults, the location of border-fault-segment nuclei above the rubber strips and propagation direction of border-fault-segments parallel to the line of velocity discontinuity indicated that to a large extent pre-fabrics controlled the locus of the developing rift.

(iii) Rotation-dominated model (SbR5):
The rotation-dominated model best reproduced the Rwenzori transfer system in the Albertine rift. The boundary faults of the initial interacting rifts were oriented orthogonal to the extension direction in nature and model and two distinct graben systems developed. In the model transfer zone a horst was captured with a shape similar to that of the Rwenzori mountains. Similar to the horst block in the analogue model whose width gradually reduced from 11km at its centre tapering out towards the limiting walls, width of the Rwenzori block (40–50km-wide) gradually reduces outward from the centre in both directions along its longer dimension giving it a lozenge shape, a shape that was also ob-

served in numerical models (Koehn et al. 2008). The horst in the analogue model rotated clockwise in similar fashion to that predicted by numerical simulations of the natural case. In addition late faults of the analogue model cut through the earlier formed horst faults similar to transsection faults found in the north of the Rwenzoris (Koehn et al. 2010). Same as the other two models, nucleation and initial propagation of border fault segments parallel to the velocity discontinuity that was orthogonal to extension vector, a final geometry in which faults were on the whole sub-parallel to both oblique and orthogonal sections of the line of velocity discontinuity and capture of a block above the 'rigid-block' all attested to control of the rift locus by pre-existing zones of weakness represented by the imposed basal boundary conditions.

6.2.2 Discussion

(a) Fault and graben evolution

Corti (2004) found in his extension model that included a weak lower crust (WLC) that boundary normal faults nucleated as long and straight segments at low extension values of β[1]=1.05, when the WLC was orthogonal to the extension direction. During continued stretching short sigmoidal en-echelon fault segments formed within transfer zones with an oblique strike relative to the extension direction. The fault segments lengthened along strike and linked together giving rise to continuous oblique border faults, in a manner that Clifton and Schlische (2001) and McClay et al. (2002) describe as typical for areas characterised by oblique rifting kinematics. Applying the concept of β-values (Corti 2004) to define extension values in our sandbox models, the segment bounding faults nucleated at low extension values β=1.02–1.04 ($< 5\%$ bulk model stretching). Internal faults formed later during successive extension. The rubber boundaries presented discrete extension-orthogonal, pre-existing fabric below the brittle crust that exerted local influence on the orientation of structures (Corti 2004). Hence border fault segments in our model nucleated parallel to and above the points where the rubber boundaries are orthogonal to extension vector.

The order of fault evolution in our models is similar to that obtained by Corti (2008*b*,*a*) for the Main Ethiopian rift (MER), where NE-SW trending border faults formed first and later N-S to NNE-SSW trending fault segments developed. The change of fault orientation during extension was explained as an effect of both local and far-field stresses and controls fault kinematics, which in turn cause block rotation. Block rotation created a complex local stress field, which again affected fault propagation directions and kinematics so that they reinforced each other. This ensured that a pre-structured crust controlled the locations of fault nucleation and initial propagation direction especially where extension direction was orthogonal to regional orientation of zones of weakness. However, as extension progressed the local stress-state was altered so that faults locally diverted from the inherited trends of weakness particularly where some segments were oblique to extension vector. The tendency of oblique, late-forming faults in the models to cut across and offset earlier faults that are orthogonal to extension vector, is comparable to the NW-SE striking faults that transect the normal NE-SW to N-S striking border faults that delineate the Rwenzori block. Fault throws obtained from the analogue models (max. 6.8km) fitted correctly within range of the 1–6km throws (Ebinger 1989*b*) observed from the natural rift.

[1] β-value = ratio of final to initial length of model measured from the model plan-view

According to Brun (1999), faults that initiate as steep normal faults can rotate (even to form flat-lying detachment faults) either when layer-parallel stretching is partly or totally transformed into rigid body rotation within the brittle layer or when rotation is imposed on the faulted layer at its base by the local rise of a ductile layer. Since the scope of our experiments was confined to the brittle crustal domain, the former mechanism of rotation explains better the gradual reduction of fault-dip as deformation progressed i.e. rotation of faults about a parallel horizontal axis; and the deflection in trend of faults later in the deformation i.e. rotation of faults about a parallel vertical axis. This also agreed with the observation by Hendrie et al. (1994) that the upper and middle crust experience simple shear (homogeneous rotational strain) by planar faults, while the lower crust and upper mantle are extended by pure shear (homogeneous non-rotational strain) and plastic deformation. Conjugate convergent pairs of faults in the analogue models resulted from faults that propagated oblique to older ones. The predominant presence of at least two major faults on each side of the model rifts suggested deformation by pure shear (Brun 1999; Tirel et al. 2006).

Graben structures were bordered by faults that cut through to the bottom in parallel manner to the boundaries of the rubber strips. Some fault blocks showed slight antithetic block tilting (e.g. in Fig.6.10 and Fig.6.14) in agreement with the observation of Baker (1986) that blocks formed by faulting are usually characterised by antithetic tilt sloping away from the rift valley. Nelson et al. (1992) observed that due to rifts being areas of 3-D strain or non-plane strain, the overall structural relief of the floor of the offset segment displays less down-dropping in the dip direction for a given extensional strain than the adjoining segments. In similar accord the grabens that developed in our models were deeper in the two adjoining segments than in the offset segment. This difference makes the offset zones structurally higher at the basement level than in the normal segments generating a regional structural saddle between deeper adjoining segments (Nelson et al. 1992). Characteristic model graben widths of 18–30km were smaller than widths of grabens in numerical models 40-50km (Sachau and Koehn 2010) and fall below the width range for grabens in the EARS 40–70km, taken from that of rift basins across uplifted flanks (Ebinger 1989*b*).

Development of horst and graben structures accompanied by conjugate normal faults around the graben axes is comparable to rift structures formed in brittle-ductile models at low strain rates (weak brittle-ductile coupling). Low strain rates also produce narrow fault zones just as is the case for a thick brittle crust (Brun 1999). The crustal thickness, however, in the rift region around the Rwenzori block is considered normal (average 25km within the rift, 35km under the rift shoulders), except beneath the southern part of the Rwenzori block where it is thickened to 40km (Woelbern et al. 2010) and thus localised rifting is expected.

(b) Fault types and block rotation

In the analogue models nearly all faults were normal, striking parallel to rift axes and were orthogonal to extension vector except within the transfer zone segment where oblique faults occurred and some strike-slip movements were observed during progressive extension. Likewise, Jakovlev et al. (2008) noted that nearly all source mechanisms for the resulting fault plane solutions on the Rwenzoris revealed normal faulting with strike directions more or less parallel to the rift axis (NNE-SSW) and orthogonal to extension vector. However, a few events with strike directions tilted anticlockwise to the NNW-SSE were found around the northeastern corner where the block is said to be still attached to the Victoria plate (Tanzania craton). It has been observed that structural complexity increases where there is a mixture of fault orientations and displacements and significant

block rotation about vertical axes may occur (Nelson et al. 1992). Since faults in the normal segments were predominantly dip-slip and those in the offset segment were oblique with both normal and strike-slip components of motion, this could explain the rotation observed in the models.

Clockwise block rotation evident around the centre of the rotation-dominated model caused oblique NE-SW-ward propagation of late faults and NE-ward deflection of initially orthogonal faults. Given the scale 1:357000 (model:nature), block-rotation rates of 0.93°/km and 1.84°/km of extension were obtained from the relative deflection of objects represented by P1, P2 respectively. Imposing these two results on a cumulative extension of 6-16km (Karner et al. 2000), the Rwenzoris should have rotated $5-15°$ and $11-29°$ respectively. Applying the same predictions to crustal extension of less than 10km (Ebinger 1989*b*), however, we predict that the Rwenzoris have rotated $9-18°$. If during block rotation the sense of shear changes gradually with it, causing change in direction of fault dip as well (Sokoutis et al. 2007), it can also be argued that the direction of fault dip was influenced by the sense of shear at the rubber-sand interface whereby the non-expanding 'rigid-bridge' between the rubber sheets interfered with the would be top-to-the left shear sense during extension resulting in cross-cutting relationships.

Koehn et al. (2008) observed that approaching rift segments captured basement blocks (micro-plates) so that during successive rift opening, the captured block rotated causing complex stress fields within itself and transsection faults developed when the basement block rotated and detached from the surrounding larger plates. In fact they noted that a major transsection, normal ENE-ward dipping (60°) fault in the north of the Rwenzoris showed current seismic activity down to 20km depth, suggesting that the Rwenzori block was indeed rotating and that it is currently detaching from the adjacent Victoria plate. Block rotations observed in the models range on average between $8-20°$ indicating that different parts of the captured block rotate at different rates, thus suggests local kinematic control. Although the extent of extension in the analogue models did not reach detachment of the crust above the 'rigid-bridge' from the surrounding, rotation of this block and development of oblique faults in the centre implied that the process had started. Thus given the appropriate setting and optimum duration it would result in what is currently happening at the northeastern tip of the Lake George rift and finally to complete detachment similar to the southwestern part of the Rwenzoris. Although wrench tectonics and complex fault networks observed in a captured block such as the Rwenzoris can be explained by the complex stress fields developed within the block as it rotates during successive rift opening (Koehn et al. 2008), the direction of rotation is absolutely determined by the sense of overstep (right- or left-lateral) of the interacting rift segments, which to a large extent is dependent on structural weakness zones in the basement. Thus pre-existing fabrics still play an extended role.

(c) Relationship of overstep/overlap ratio to end-member geometry

Greater overstep as in the *shear-dominated model* (SbR3) produced prominent obliquity of the transfer zone and deeper grabens (max. 7.0km). On the other hand, greater overlap as in the *extension-dominated model* (SbR4) nullified the effect of the overstepping segment relationship on the development of oblique transfer zones and produced moderately deep grabens (max. 4.6km). Where the overlap was twice as big as the overstep, as is the case for the *rotation-dominated model* (SbR5), no clear transition zone developed. In this case the effects of orthogonal (near the rims of the box) and oblique (in the centre of the box) rubber boundary orientation relative to extension vector merged and rifts propagated sub-orthogonal to extension vector resulting in shallow depressions (max. 2.9km). Using

the description of Nelson et al. (1992) the large-scale end-member geometries for the three models were respectively, *an offset*, *a jump* and *a pass*. Therefore the relative size of overlap compared to that of the overstep between two rift segments that propagate towards each other determined the extent of interaction hence the final geometry of the end-member. Moreover overstep-overlap relationships are tied to the inherited basement structure.

Chapter 7

Final Discussion and Conclusions

This chapter contains a combined discussion of the results and conclusions drawn from the previous chapters. Some possible sources of error and shortcomings of the study are explored. Remarks are also made on possible additions to improve the models, so as to obtain more realistic results that fit more closely to the natural scenario.

7.1 Discussion

The field activities involved in this study included structural data collection, noting characteristics of observed field structures and rock sampling. Successful accomplishment of these activities laid the foundation for fulfilment of the other objectives namely microtectonic study of rock thin-sections, reconstruction of paleostresses and physical modelling. Three main sources of error may be anticipated from field activities. First, when structural measurements are taken during data collection, measurement errors are practically inevitable. However, in this case the error margin may be negligible since the program software TectonicsFP1.7 performed corrections to bring all lineations to lie directly on the respective fault planes. Inaccessibility of certain parts of the mountains also caused non-uniform distribution of data collection and sampling points. This may have introduced a bias so that ultimately, a state of stress determined for a certain tectonic unit was not adequately representative for a fault population in some part of the unit. Lastly, because of the discontinuous nature and limited exposure of some faults in the field, some of the fault data used in paleostress reconstruction might have been measured from larger-scale faults reflecting 2^{nd}-order stress patterns rather than the intended smaller-scale ones that reflect 3^{rd}-order stress patterns and which are appropriate for this purpose.

Microstructural study of rock thin-sections was aimed at identifying the different deformation phases and metamorphic events represented by the micro-structures. This was done by studying mainly porphyroblast-matrix relationships. The mineral assemblages, textures and micro-structures portrayed in thin-section indicated deformation under low to medium-grade metamorphic conditions and low strain rate, invoking mainly ductile behaviour. Such conditions point to regional metamorphism. Notice that regional metamorphism occurs over large areas during deformational events that take place under non-hydrostatic (also called deviatoric or differential) stress, which results from tectonic forces that produce compressional stresses in the rock (Nelson 2010). Therefore, the rock record portrayed mainly effects of far-field stresses.

Polyphase deformation was reflected by re-orientation of ductile micro-fabrics and was supported by existence of differently orientated brittle fabrics in the field. Moreover foliations S1, S2, S3, S4 respectively indicated extension approximately in the W-E, NNW-SSE, ENE-WSW and NE-SW directions. Assumptions were made that these foliations developed in the same sequential order and that the direction of compression reflected by each of them corresponded to the maximum horizontal compression direction $S_{(Hmax)}$ of the stress field prevalent at the time of its development. As such, it was deduced that extension axes rotated non-uniformly[1] in clockwise manner, similar to the clockwise rotation of extension directions demonstrated for various sections of the East African rift e.g. by Strecker et al. (1990); Strecker and Bosworth (1991) and Ring et al. (1992). This provided good justification for the possibility to change extension direction in the physical models.

Correspondence of ENE-WSW striking S3 and NNW-SSE striking S2 foliation in thin-section respectively with the NE-SW and NW-SE trending crenulation and fold axes observed in the field; coupled with corresponding joint and fault trends, indicated that the faults and shear zones to some extent took advantage of pre-existing cleavage planes. This inference can be explained by the fact that, under deformation the fracture or shear orientation and dip are strongly linked to pre-existing pervasive fabrics that present anisotropic fracture strength. Summed up, these observations indicated temporal rotation or deflection of stress axes hence temporal variation of stress fields. However, not all rock types were used for microstructural study. This might have invented a bias on the inferred deformation history that was used to evaluate schemes of regional deformation phases anticipated to be representative for the entire study area. An integrated microtectonic study in which all possible rock types are studied could produce a more representative deformation history.
Secondly, inferences were made based on the assumptions stated above, however, invalidation of such assumptions leads to inaccurate deductions.

As pertains to fault kinematics and stress regimes, the complex architecture of the East African Rift System with spatial changes in direction and overlapping zones between rift segments makes the assessment of regional variations in the local extension directions critical for evaluation of the rifting process (Acocella and Korme 2002). Thus fault kinematic analysis was intended to show if there were temporal variations in the field or if the stress field varied locally. The assumption made here was that all fault data used to estimate paleostresses were measured from smaller scale faults of spatial wavelength 1-100km, which express 3^{rd}-order stress patterns that result from local density and strength contrasts, basin geometry, basal detachment, topography or active faulting (Heidbach et al. 2010). Fault kinematic analysis revealed that the region in question has been affected by two to three regional stress regimes. The stress regime that possibly prevailed earliest was dominated by thrusting fault kinematics. It resulted from compressional stress fields developed during a paleoproterozoic collisional orogeny along the southwestern margin of the Tanzania and Congo cratons. This stress regime averages a stress tensor orientation σ_1=144/9, σ_2=235/6, σ_3=349/80 and R=0.7, however, locally the compression axes trend N-S. The next one was a strike-slip dominated compressional intra-cratonic stress regime, with orientation of extension axes fluctuating between ENE-WSW and W-E directions. This resulted from the compressional 1^{st}-order stress pattern on Africa plate prior to rift development and it existed prior or up to the time of rift initiation.

The youngest is a tensional rifting regime dominated by normal fault movements, with

[1] Rotation of axes was mainly clockwise but some counterclockwise deflection also occurred.

mainly NW-SE oriented extension axes. However, a local variation in the central and south to southeast showed NNE-SSW extension direction under this regime. Save for variations arising from temporal axes reversals, rotations and fluctuations, the latter has prevailed since rift initiation throughout the various phases of rift evolution, to the present-day. The transition of the two stress regimes was gradual, since some observed states of stress especially of oblique nature, were transient between compression and extension. Among the latter were the reverse stress-states with mainly NNW-SSE compression, oblique-reverse and oblique-normal stress-states that led to localised transpression and transtension in certain areas and contributed to block-uplift (Ring et al. 1992) especially around the high peaks. Hence, it appears that the main stress regime that presently controls fault kinematics in this study area approximates the regional stress field and is a tensional regime with NW-SE to WNW-ESE and NNE-SSW extension as supported also by predictions from seismic data analysis. The corresponding NE-SW to NNE-SSW and ESE-WNW orientations for the maximum horizontal compression direction $S_{(Hmax)}$, average a stress tensor orientation σ_1=069/82, σ_2=225/5, σ_3=317/3 and R=0.1.

The major causes for spatial variations in orientation of stress axes included temporal fluctuation, rotation or reversal of stress axes, interference of regional stresses by stress fields around master faults, interference of local stress fields by interacting rift segments whose greatest stresses are concentrated at their tips, block rotation and uplift. Moreover there are differences in elevation and since higher surface elevation means greater gravitational potential energy on a column, variations of stress axes orientation were also contributed to by the local differences of potential energy. Stress-states SK–1^2, RA^2, RD^2, KK–12^2, KNG–1^2, KNG–2^2 (see Fig. 5.10) are presently active in the respective tectonic units. Although new faults developed more recently, most faults have probably been reactivated with mainly extensional movements, lesser strike-slip and a few with oblique thrust movements. It is apparent that similar stress regimes were imposed on the entire region. However, presence of four distinguishable stress-states within the high peaks region, minor representation of normal faulting in the east central part and the predominance of normal faulting in the south to southeastern part with minor representation of the strike-slip regime, attested to local differences of stress field orientations. It can thus be argued that different parts of the study area were locally deformed in dissimilar fashion, depending on the "effective" local state of stress. Variation of R-values from 0.1 to 0.9 indicated activity of all the three categories of deforming stress - axial tension, plane deviatoric stress and axial compression, although not necessarily at the same time.

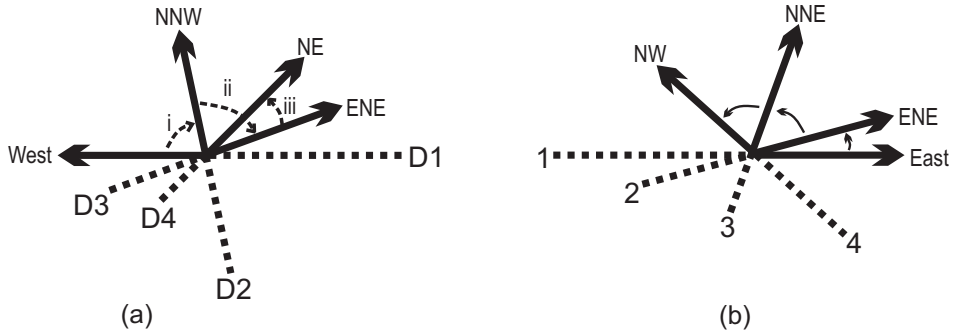

Fig. 7.1 Juxtaposed rotation of extension directions. (a) Non-uniform clockwise rotation i to iii inferred from microtectonics (b) Counterclockwise rotation 1 to 4 obtained from chronology of stress-states deduced from fault kinematics.

In general, applicability and reliability of results obtained using PBT-axes method are dependent on a uniform strain field and on correct grouping of slip information generated during different deformational phases. For the multiple inverse method on the other hand, applicability and reliability of results rely on assumptions underlying the Wallace-Bott hypothesis (Fossen 2010). Hence for fault subsets that consisted of few and/or relatively scattered data sets, their resultant large cones of confidence and large misfits yielded mean vectors and reduced stress tensors that were probably unrealistic for some part of the data, thereby introducing some error in the result. Both methods were however, capable of separating stresses from heterogeneous data, provided that a data set consisted of at least four independent faults of known attitude. The methods were appropriate, given the heterogeneous nature of data and they successfully separated out the different stresses responsible for fault activation and/or re-activation. One shortcoming however, was that both methods are incapable of discriminating newly formed faults from the old re-activated ones. As such, inferences regarding relative chronologic prevalence of stress fields were made by reference to other work e.g. Delvaux and Barth (2010); Koehn et al. (2010) and by incorporating certain assumptions in the interpretation of micro-tectonic deformational structures. Notice however, that the most current extension directions were confirmed by inversion of focal-plane solutions for the target region. A general counterclockwise rotation of extension directions was deduced from fault-slip analysis, contrary to the clockwise rotation demonstrated by results of the microtectonic study (Fig. 7.1). However, some counterclockwise rotation was also suggested by the microstructures.

The main objective for carrying out analogue modelling was to constrain the conditions under which the Rwenzoris developed and to study fault development and growth so as to understand the role of faults in the uplift process. The Rwenzori block lies in a comparatively high strain accommodation zone between two sinistrally overstepping and overlapping basins (Rosendahl 1987; Ebinger 1989*b*) within an extensional rift. Hence we used the model setup where two sinistrally overstepping rift segments were caused to develop under extension. Results showed that changes of fault orientation and kinematics caused block rotation and vice versa in rift transfer zones and that these effects, once in play, reinforced each other. Ability of the velocity discontinuity to determine the locus for nucleation and initial propagation of faults makes it plausible that locations of segments of the EARS were controlled by pre-existing fabrics, the Albertine Rift inheriting its trend from older zones of weakness between the Tanzania and Congo cratons. From the evolution of fault segments through progressive extension, however, we concluded that extending a pre-structured crust only initially centres fault nucleation and propagation parallel to pre-existing weakness structures.

The models showed that at later stages and with progressive extension, such boundaries were locally defied so that faults propagated sub-parallel or oblique to the pre-existent structure and attempted to breach it. Thus the mechanical strength anisotropy of pre-structured crust, for example orientation of pervasive foliations as indicated also by the microstructural study, played an important role in determining orientations and distribution of fault patterns but not throughout a protracted period of extension. The relative sizes of overlap/overstep between two rift segments that propagated towards each other and interacted, also dictated the final geometry of the end-member by determining the kind of transition or accommodation zone that developed. Additionally, the size of overlap/overstep also dictated whether or not a block like the Rwenzoris was captured between the two rift segments thereby dictating involvement or non-involvement of rotation in the kinematic 'equation'.

Three scenarios of rift interaction were presented in the analogue models, one of which was *'shear-dominated'*, one *'extension-dominated'* and the other *'rotation-dominated'*. Only the third model captured a horst block, which then rotated. Considering the different types of transfer zones, the Rwenzoris should lie in what Morley et al. (1990) described as a 'divergent-overlapping-transfer-zone', within which a large horst that separates the rift into two individual basins is characteristically present. This qualified our rotation-dominated model $SbR5$ to be the closest approximation to the situation of the western branch of the EAR around the Rwenzori horst, since *a 'pass'* is required for a block to be captured. Model SbR5 agreed with the idea that the Rwenzoris formed as a captured block in a "pass" between two rift segments that propagated towards each other and interacted via sinistral overlap as they approached. It also produced the proposed clockwise rotation of the Rwenzori mountains and presented late-fault orientations and angles of block rotation approximately 5–20° that agreed with those obtained from other sources.

Normally, transfer faults trend at high angles to the rift axis and tend to parallel and selectively re-activate older faults (Chorowicz 1989) thereby suggesting inheritance from earlier geodynamic periods. Thus successful modelling of similar faults in these experiments coupled with the fact that the seismically active major fault northeast of the Rwenzoris is of transsection type (Koehn et al. 2010), enabled us to conclude that rotation of the Rwenzori block has played an important role in the activation and/or re-activation of such transfer faults. Rotation rates varied for different parts of this horst as observed in the model, each part controlled by the local fault kinematics which varied due to different local fault interactions.

Thus even if far-field stresses played a big role in determining the orientation of faults and although fault trends may have been inherited from trends of older geodynamic periods, interference of the local stress field by block rotation played a significant role on a local scale. Moreover the direction of rotation was also controlled by pre-existing fabrics in that the sense of overstep of interacting rift segments (right- or left-lateral) was determined by locations of weakness zones in the basement, whose approximate trend was inherited by the fault- and ultimately rift-segments. Despite the constant extension vector, faults rotated about a vertical axis and differently oriented faults (than the early-formed extension-orthogonal fault segments) developed in the transfer zone of the model at later stages of extension. This pointed to development of complex stress fields between interacting rift segments especially after initial phases of rifting. The stress fields probably became even more complex when block rotation set in. Thus although temporal fluctuations of the regional stress field and axes reversals on local stress fields played a leading role in determining 'kinematic trends' in the region, internally developed complex fields perturbed them to such extents that strike-slip movements might have led to block up-lift.

Some possible sources of error were noted, arising especially from handling of analogue experiments and from material properties. For instance, porosity and bulk physical properties of sand depend on the size, shape and packing of grains and because less closely packed sand is weaker, errors were bound to arise from involuntary fluctuations in packing (Krantz 1991; Cobbold and Castro 1999) as the sand was introduced into the sandbox. Therefore different sandbox experiments may have experienced variations in packing, making the initial strengths of the models different. Moreover the exact density and grain-sizes may also have varied between experiments since they were not directly measured. Secondly, extension rates may have varied slightly between experiments but possibly also between observation sessions of a specific experiment, since the extensional increments on the model were performed by hand.

Since the Moho-discontinuity in the study region lies at average depth of 25km, we modelled a crustal thickness 25km in the sandbox. However, in reality crustal thickness beneath the eastern rift-flank reaches 30km, whereas beneath the Rwenzori block where the inner crustal structure becomes complex, crustal thickness widely varies in the range 20–28km (Woelbern et al. 2010). Moreover the thickness of the sandpack might have slightly varied due to difference in levelling in a specific experiment. Hence the crustal thickness was probably not adequately modelled. Additionally, rubber is an elastic material so the rate of extension (elasticity rate) of the rubber strips changes with continued extension especially if its elastic limit is exceeded, thereby varying the "effective" amount of extension on the deforming model as the experiment progresses. This possibly posed a non-uniform extension rate during deformation of a specific model. Moreover the rubber strips were attached to the basal sheet beneath the sand-pack but only one side of the box was extended, which might have interfered with the geometry of the growing fault or rift segments. Finally, sand has zero tensile strength, therefore it does not adequately represent the deformational behaviour of the modelled crust.

As in every physical modelling study, certain demerits were observed especially with regard to the scope of the analogue models. First, a physical model should incorporate a number of aspects of the target system but should be kept as simple as possible because a complex model becomes difficult to analyse. However, it is not possible to model several attributes of a natural system at the same time without complicating the model. As such the models employed in this study excluded some processes that might have influenced the formation and evolution of the natural rift. For instance, the western part of the EARS experienced a change in principle extension direction through time (Strecker et al. 1990; Ring et al. 1992; Acocella and Korme 2002) and the changes probably had a bearing on the uplift of the Rwenzori block. However, the scope of analogue models used in the current study did not address change in the external stress field (change in extension direction). Use of a more complex sandbox would address this problem and would provide some insights into the mechanism of uplift of the block and rift-flanks.

Secondly, only the brittle crust was modelled hence the realistic deformational behaviour of the crust under influence of the underlying mantle, was not fully represented. Introduction of mantle material beneath the sand-pack would produce rifts that address combined effects as in the natural lithosphere. Additionally, because the nature of the upper mantle - brittle or ductile - drastically changes the style of crustal thickening (Davy and Cobbold 1991), altering rheology of the upper mantle for different experiments would enable observation of variations in properties of the developing extensional rifts and provide useful inferences to be compared to the prototype. Existence of a magma chamber beneath the Rwenzoris may also be a possible explanation for extreme uplift in a rift setting. Thus by introducing a low-viscosity melt within the crust of the analogue model, it may be possible to observe effects of such heterogeneity on the developing rift and on block- or flank uplift. Once again, the models involved simple extension as the only external parameter, without incorporating any exogenic processes.

Lastly, some faults in the natural realm were re-activated as stress fields changed during rift evolution but the sandbox experiments did not model fault re-activation. If they did, e.g. by using a more complex sandbox, they could probably address all or most of the fault types revealed by data analyses i.e. normal, strike-slip, reverse, oblique strike-slip and oblique reverse faults.

Since the actual properties of the rubber material added to the basal-sheet in sandbox experiments were not explored, inclusion of rubber strips at the base of the sand-pack was done with the assumption that the rubber did not exceed its elastic limit during extension. This introduces some uncertainty. Other uncertainties could arise from ommission in the models, of stratigraphic differences that exist in the natural crust due to 3-D variation in mineral composition and hence rock properties. In addition to that, possible changes of fault orientation and dip from the top of the crust downward were also uncertain and therefore not taken into account at any stage of the study.

7.2 Conclusions

On the whole, the field study indicated variously oriented brittle and ductile fabrics that suggested difference in the causative forces. Micro-structures observed in rock thin-sections provided insights pointing to three or four deformation phases under low to medium-grade metamorphic conditions and low strain-rate. These implied that rocks in the study area were regionally metamorphosed as deformation occurred under differential (non-hydrostatic) stress. The far-field stresses responsible for rock deformation and accompanying metamorphism resulted mainly from tectonic forces. Micro-fabrics indicated non-uniform clockwise rotation of extension axes, as earlier demonstrated for different sections of the East African rift.

Analyses of fault-slip data indicated that the study area lies in a region that was affected by two main regional stress regimes. Paleostress reconstruction expressed change of stress fields from a reverse slip dominated stress regime developed due to collision of Tanzania and Congo cratons at their southwestern margin, through the strike-slip dominated stress regime, through spatially varying transient stress states, to the younger tensional stress regime with varying extension directions. The transition of the two stress regimes was gradual, dominated by (reverse?) and oblique fault kinematics that led to localised transpression and transtension in certain areas; and contributed to block-uplift (Ring et al. 1992). These demonstrated major changes in fault kinematics with time, the kinematics being controlled at present by a tensional stress regime with NW-SE to WNW-ESE and NNE-SSW extension directions. Moreover activation of some faults by more than one state of stress as reflected by data analyses, suggested re-activation with different modes of slip as stress fields changed. The results satisfactorily addressed the target questions, making it clear that stress fields varied not only temporally but also locally or spatially as observed from differences of axes orientations from one locality to another. They also indicated that there were some local differences in deformation pattern under a specific state of stress. The variations in paleostress extension directions justified changing extension direction in the analogue models and using differently oriented VD segments so as to develop differently oriented fault patterns.

Faults were replicated by simulating the rifting process in sandbox analogue experiments, where fault development and growth were studied. From depth-to-detachment estimates of 20-30km in the East African rift, rollover geometry of asymmetric basins and occurrence of seismicity throughout the depth range 0–30km, it was inferred that border faults along one side of basins penetrated the crust (Ebinger 1989*b*). Similarly, border faults in the models cut through the whole thickness of the sand-pack. Although the models did not demonstrate the high uplift, they reasonably addressed certain questions thereby suggesting some of the conditions necessary to produce a scenario like the one existing around

the Rwenzoris. The models demonstrated conditions under which block-capture occurred and how pre-existing fabrics determined rotation direction. However, they also did show that pre-structured crust only controlled orientation of fault patterns during initial stages of extension. They demonstrated that older pervasive structure trends can be defied especially at later stages of a protracted extensional phase. They also demonstrated how block rotation can contribute to change or complication of stress fields locally, thereby influencing local fault orientations and portraying spatial variations of stress fields.

Different amounts of rotation in the range 5–20° implied that different parts of a dissected block like the Rwenzori horst rotated by varying amounts influenced by the local kinematic environment. However, the "net" angle of rotation for the Rwenzori block as a whole was probably less than that. This also implies that the "net" extension rate varied even locally from one part of the rift to the next. The models showed the possibility of developing locally complex stress fields and hence activating variously oriented faults particularly in accommodation zones between interacting rift segments, even with a constant regional extension direction (constant external or regional stress field). Notice however that fault segments in the models showed mainly normal displacements whereas the field data reflected normal, reverse, strike-slip and oblique fault patterns.

Even with a constant extension vector, the models indicated that although changes in the external or regional stress field contributed the most towards change of fault kinematics, other processes also influenced local fault kinematics thereby causing spatial variations of kinematics in the region. Such processes included block capture and rotation, fault rotation especially about vertical axes and interaction of rift segments where stresses concentrated at the tips; coupled with the respective stage of rifting. This is so because in the early stages the regional extension direction strongly controls the kinematics but in the late stages of rift evolution the existent structures and developed geomorphology are imposed on and interfere with the regional stress field. Hence although the models used in this study were very basic, they provided good results.

Results of analogue modelling and fault-slip data analyses both suggested development of complex stress fields locally within the Rwenzori mountains, arising from rift and fault segment interactions. The models also implicated block capture and rotation, rift-segment-interaction and fault rotation to have influenced local fault kinematics. The field scenario, on the other hand, attested to possibility of altering stress fields by imposing regional stresses on areas that differ in local gravitational potential energy. Thus integrating the field observations with results of microstructural study, fault-slip data analyses and physical modelling, our hypothesis was considered to be rightly fitting that *'the high rift-flank uplift around the Rwenzoris was not simply controlled by movements along major boundary faults but rather a result of interplay of several tectonic processes that altered the stress fields to effect kinematic changes'.*

Modelling outlook

In summary, farther work and better constraints on the conditions under which the Rwenzoris formed may be determined using related physical modelling by:

(i) Extension to a more complex sandbox model that would address change in extension direction (change in the external stress field). It would also enable addition of exogenic processes such as erosion and sedimentation to the sandbox, in order to show how the two processes affected uplift and subsidence within the rift. A box that can be extended on two opposite sides at the same time would also prevent deformational asymmetry in the model and in the geometry of the resulting fault and rift segments.

(ii) Using the right mixture of materials to adequately approximate the tensile strength of the crust in the study region. Introduction of some low-viscosity materials to account for the mantle below the sand-pack, would also yield more realistic deformational behaviour mimicking the prototype.

(iii) Employing a mechanised sandbox to prevent variation of extension rates both for different experiments and between observation sessions of a specific experiment. It would also yield uniform thickness of models.

(iv) Ensuring that the specific material properties such as density and grain-size of the sand being used are known and that the grain-size is uniform. Knowledge of the Young's modulus of the rubber used in the experiments should give one an idea how far it can be loaded during extension.

Consideration of the additional improvements outlined in the preceding discussion would help to build much more realistic models and if relatively simple enough to be analysed, the models would produce more realistic relationships to the prototype. Alternatively, simulation using numerical models would incorporate more attributes of the prototype in a single model and avert most sources of errors introduced during handling of sandbox experiments. A comparison of results ensued from the two types of models would be a great addition.

Appendix A

Field Photographs

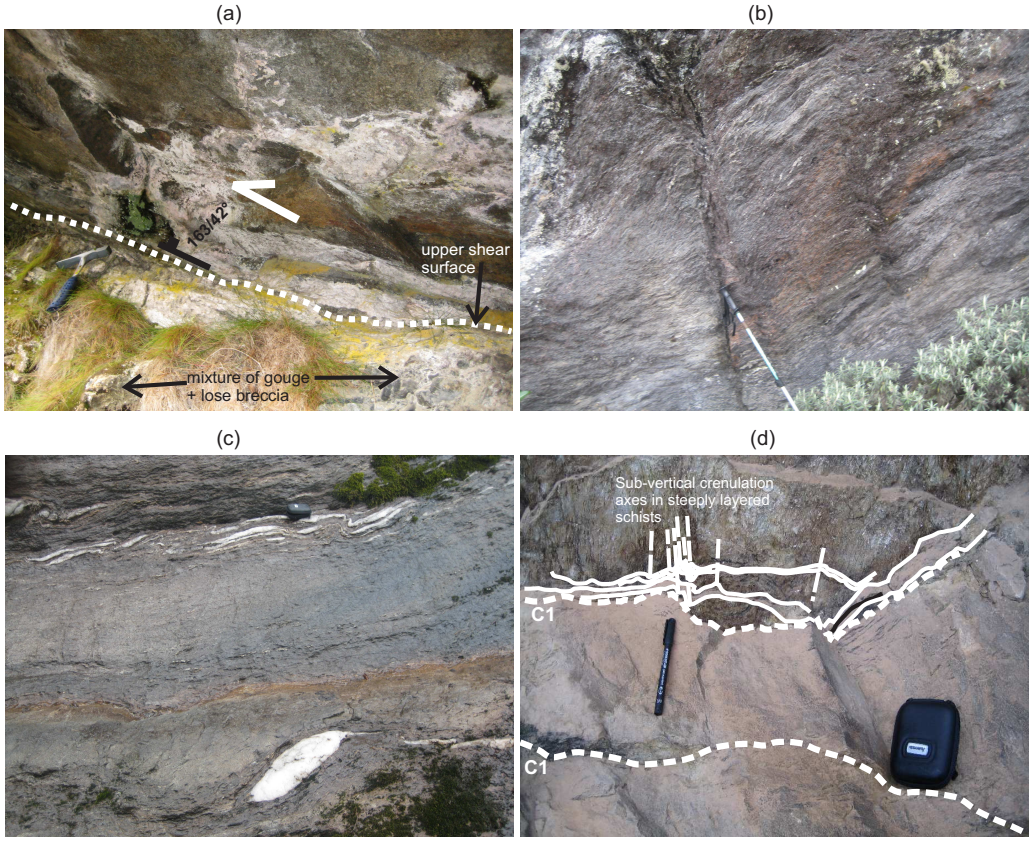

Fig. A.1 (a) Shear zone (dip 163/42°) below white broken line highlighting the upper shear surface; contains about 1m-wide mixture of gouge and breccia within mylonitic gneiss. White calcitic and black needle-like minerals grow in the shear. Lineations pitching 154/40° on the upper shear plane suggest reverse shear. Photograph taken 120m east of Kitandara hut at 3997m a.s.l, face to the west. (b) Sub-vertical shear plane (dip 305/701°) in schists along Freshfield Pass. Schistosity drawn into shear plane in a manner that suggests sinistral shear. Photograph taken at 4121m a.s.l, face to the NE. (c) Folded quartz veins (dip 163/70°) with hinges sub-parallel to the NE-SW striking foliation (approx. left to right trend in photo); axial planes dip 140/70° suggesting NW-SE directed compression. Note the finer-grained texture in the centre compared to the coarser textures beyong quartz veins in the back- and foreground. Photograph taken in plan-view at 3906m a.s.l, along Freshfield Pass. (d) Crenulations with axial planes (dip 122/70°) constituting a second cleavage at high angles to an older one, C1, where the main foliation dips 176/56°. Trend of axial planer cleavage corresponds with that of brittle fractures in the foreground, although fractures are steeper (80°). Photograph taken at 4039m a.s.l, along the trail towards Mt.Baker.

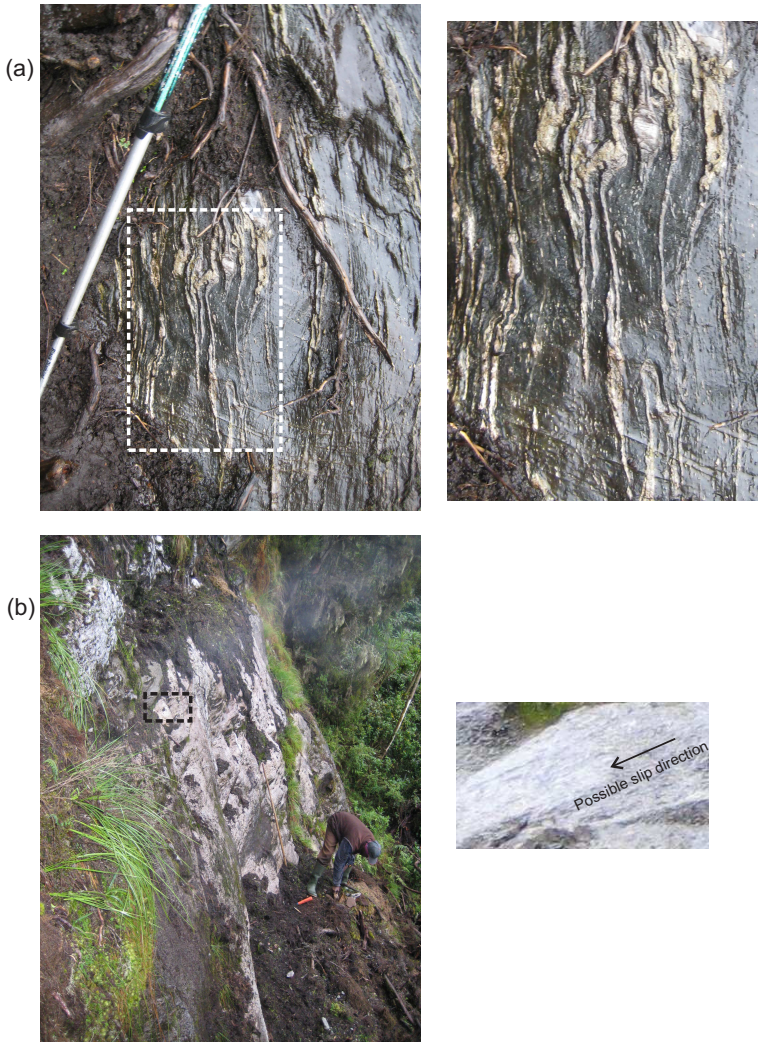

Fig. A.2 (a) Left:Mylonitic gneiss with mantled feldspar porphyroclasts whose trails parallel an E-W striking foliation and exhibit stair-stepping character of δ-, σ- and a few of ϕ-type suggesting dextral shear. Photograph taken in plan-view at elevation $\sim$3900m along Freshfield Pass. Right:magnified version of the portion indicated by the rectangular box on the left. (b) Left:Possible fault face on a gneissic outcrop with brecciated face bearing calcitic growth. A shear zone $\sim$0.5m-wide at a higher level (not visible in the photo) dips $\sim 200/30^{\circ}$ suggesting reverse shear where the hanging wall was thrust NE-ward. Photograph taken about 300m south of Guy-Yeoman hut at elevation of 3512m; face to the NE. Right:magnified portion indicated by the rectangular box on the left, showing possible slip along an oblique strike-slip vector.

Appendix B

Field Structural Measurements

Note: Alt.(m) = Altitude at which the data was taken, Dipdir = Dip direction;
lin-Az = lineation azimuth, Lin-Plg = lineation plunge.

In table B.5: Plgdir. = measured lineation plunge direction, Plg. = measured lineation plunge,
Plgdir.* = corrected lineation plunge direction, Plg.* = corrected lineation plunge, Sns = sense of slip,
Qlty = quality of slip indicator.
.

Table B.1 Measured attitudes of Foliation-Planes representative for the entire study area

GPS Loc.(UTM)	Alt.(m)	Dipdir/Dip	Comment
e821657/n0041557	4149	192/80	Junc.Scott-Ell.Pass-Elena; Amphib.
e821195/n0041347	4372	145/50	main fol.; mica-schist in shear zone
	4372	100/75	minor fol.(axial planar cleavage).
e821486/n0042342	3934	215/45	S of suture; Mica-schists.
	3934	226/61	
e821486/n0042342	3934	211/80	Along suture; N of fault.
e822039/n0038740	4396	109/89	Above FFP, toward Mt.Baker
	4396	097/84	
	4396	227/89	
	4396	097/79	
	4396	280/77	Mylon. greenschist.
e821510/n0038396	4130	210/45	Attitude same as shear zone.
	4130	163/34	
e826576/n0030707	3359	160/85	Kamusonga river
e822839/n0032070	3991	110/17	Earlier foliation
	3991	180/30	Younger foliation
e822674/n0038273	4185	180/53	Foliated gneiss
e824454/n0039317	3939	130/70	Crenulated Muscovite schist
e821385/n0038707	4308	220/43	Mylonitic gneiss
e821047/n0038551	4030	262/68	Mylonitic amphibolite
	4030	220/45	
	4030	188/45	
	4030	262/68	
e821155/n0038154	4039	176/56	-
e821436/n0038670	3997	150/45	Mylonitic gneiss.
e821327/n0041088	4367	198/34	Mylon. shear zone in amphib.;
	4367	224/65	2m-wide.
	4367	110/27	
e821944/n0038392	4275	164/45	Schists with quartz lenses
	4275	188/50	

Table B.2 Measured attitudes of Shear-Planes (zones) representative for the entire study area

GPS Loc.(UTM)	Alt.(m)	Dipdir/Dip	Comment
e821195/n0041347	4372	145/50	towards Elena Hut(RW6); zone-width $\leq 1m$; reverse shear.
e822039/n0038740	4396	171/38	above FFP(RW7);en echelon tension gashes suggest reverse shear
e821510/n0038396	4130	210/45	b'tn Kitand. and FFP; asymm. crenulations-axial plane attitude 210/40
e188427/n0083211	1219	030/20	Complementary shears
	1219	240/40	
e821358/n0038710	3985	195/40	Strongly sheared amphibolite
e821056/n0039793	4003	136/33	Lower Tsavoia-peaks;S and C surfaces suggest reverse-shear.
e821385/n0038707	4308	190/50	N-ward thrust; Mylonitic amphibolite; stretching-lineation 212/60
e821047/n0038551	4030	252/35	-
	4030	190/48	-
e821436/n0038670	3997	163/42	Mylonitic gneiss; Black needle-like mineral (+Carbonate?) growing in shear
e822142/n0038303	4275	196/65	Schists within the Freshfield Pass
	4275	202/43	
e822933/n0038236	4121	205/70	-

Table B.3 Measured attitudes of stretching lineations representative for the entire study area

GPS Loc.(UTM)	Alt.(m)	lin-Az/Lin-Plg	Comment
e821657/n0041557	4149	096/25	Junction Scott-Elliot Pass/Elena; phylonitic amphybolite
	4149	110/25	
	4149	102/21	
e821195/n0041347	4372	140/35	Mica-schists in shear zone; reverse-shear
	4372	120/48	
e821510/n0038396	4110	174/25	b'tn Kitandara and Freshfield Pass;
	4110	197/35	Porphyroclasts step-up parallel to stretching lineation-
	4110	200/48	suggesting normal-shear along dip of shear zone
e168170/n0020460	-	350/75	
e821385/n0038707	4308	212/60	N-ward thrust Mylonitic amphybolite.
	4308	328/79	
e821047/n0038551	4030	188/45	-
e821436/n0038670	3997	154/40	Mylonitic gneiss
	3997	156/44	

Table B.4 Measured attitudes of Fractures/Joints representative for the entire study area

GPS Loc.(UTM)	Alt.(m)	Dipdir/Dip	Comment
e820155/n0007287	1131	070/85	Kajwenge area
	1131	088/80	
	1131	064/81	
e824722/n0009795	1162	050/60	Kyonda sub-county
	1162	298/70	
	1162	350/80	
e824131/n0012725	1295	137/75	Kyonda; adjacent to river valley
	1295	310/75	
e814993/n0001681	1106	182/86	Near Kanyampara river
	1106	352/42	
	1106	178/84	
e827736/n9994024	980	166/70	Lake Katwe area
Bujuku hut	-	205/30	-
Bujuku hut	-	200/40	-
e820010/n0037569	3907	068/70	Near fault(120/70)-greenschist
	3907	074/70	
	3907	150/50	
	3907	125/65	
	3907	077/70	
e821056/n0039793	4003	170/70	Lower Tsavoia Peaks
	4003	230/58	
	4003	350/67	
e822632/n0038702	4235	350/89	-
e821510/n0038396	4110	245/72	-
	4110	272/86	-
	4110	245/82	-
	4110	301/83	-
	4110	251/69	-
	4110	271/84	-
	4110	260/87	-
	4110	118/79	-
	4110	223/70	-
	4110	240/75	-
	4110	276/81	-
	4110	270/85	-
	4110	096/70	-
	4110	118/61	-
	4110	110/80	-
	4110	260/82	-
e821385/n0038707	4308	272/82	-
	4308	300/84	-
	4308	268/85	-
	4308	272/80	-
	4308	258/85	-
	4308	254/62	-
	4308	026/81	-
	4308	304/62	-
	4308	323/62	-
	4308	349/62	-
	4308	121/22	-
	4308	358/70	-
	4308	345/59	-
	4308	270/77	-
e821047/n0038551	4030	002/65	-
e821155/n0038154	4039	115/85	-
	4039	112/84	-
e821436/n0038670	3997	014/48	Mylonitic gneiss
	3997	058/80	
	3997	301/64	
	3997	335/70	
e820841/n0041295	4540	230/84	Taken from walls of basaltic dykes
	4540	095/89	
	4540	260/87	

Table B.5 Measured fault-slip data and corrected lineation attitudes

GPS Loc.(UTM)	Dipdir.	Dip	Plgdir.	Plg.	Plgdir.*	Plg.*	Sns	Qlty
	Sempaya and Kazingo (SK) area							
e852479/n91780	330	70	330	70	329.99	70	2	1
	335	55	340	50	340.61	54.87	2	1
e853579/n93166	180	70	165	70	165.43	69.39	2	2
	100	80	-	-	-	-	-	-
	010	60	-	-	-	-	-	-
	100	80	-	-	-	-	-	-
	240	80	320	05	328.83	06.63	3	2
	310	85	290	80	275.6	83.95	2	2
	290	60	270	50	265.51	57.61	1	3
e860069/n91029	320	80	-	-	-	-	-	-
	080	60	-	-	-	-	-	-
	255	75	-	-	-	-	-	-
	036	70	310	01	306.79	2.17	3	1
	280	82	192	30	194.59	29.66	4	1
	074	60	140	12	152.03	19.76	3	1
	057	50	160	10	327.36	00.43	3	1
	300	85	-	-	-	-	-	-
	180	80	095	20	093.73	20.23	0	0
e858050/n84596	240	62	-	-	-	-	-	-
	140	80	-	-	-	-	-	-
	280	80	045	05	190.16	00.93	3	3
e856290/n83198	300	80	050	10			0	0
	290	75	-	-	-	-	-	-
	130	70	140	70	139.87	69.72	2	3
	320	85	-	-	-	-	-	-
	302	70	010	45	010.5	45.2	2	0
	130	70	100	70	103.07	67.79	0	0
e855468/n81888	270	70	-	-	-	-	-	-
	290	45	290	50	290	45	0	0
	012	60	035	70	027.39	59.09	0	0
	270	30	240	30	240.93	26.78	2	1
	330	65	-	-	-	-	-	-
	200	85	138	60	119.89	63.01	0	0
	078	80	300	62	012.09	66.64	0	0
	300	89	-	-	-	-	-	-
	340	80	-	-	-	-	-	-
	300	56	330	55	328.19	52.57	2	1
	315	80	-	-	-	-	-	-
	205	85	-	-	-	-	-	-
	300	65	315	65	314.6	64.27	2	1
e192178/n90988	040	80	130	01	129.83	00.97	3	1
	115	85	025	01	025.09	00.99	3	2
	158	70	068	45	085.82	40.05	2	1
	140	80	050	50	061.52	48.56	2	1
	114	74	025	84	092.38	72.86	2	1
e188168/n82905	288	80	018	70	352.83	67.48	2	1
Kazingo trail	148	50	-	-	-	-	-	-
	254	70	-	-	-	-	-	-
e852360/n72622	220	88	142	66	134.59	66.44	0	0
	336	80	-	-	-	-	-	-
	125	74	200	55	192.6	53.04	0	0
	330	72	248	50	260.16	46.69	0	0
	Central Rwenzoris (C-RWZ)							
Mt. Baker	275	89	270	80	233.72	88.67	2	1
	150	45	-	-	-	-	-	-
	070	80	-	-	-	-	-	-
	230	60	325	35	304.23	25.21	4	1
	170	55	170	60	170	55	0	0
	130	70	160	63	164.33	66.21	2	1
	250	80	150	75	192.73	71.94	2	1
	170	50	-	-	-	-	-	-
	110	89	300	70	035.34	86.23	1	1
	110	89	030	05	020.09	05.25	4	1

... continued on next page

GPS Loc.(UTM)	Dipdir.	Dip	Plgdir.	Plg.	Plgdir.*	Plg.*	Sns	Qlty
	070	65	160	30	147.53	24.85	4	1
	220	70	130	01	130.32	00.88	4	1
	227	60	137	01	137.43	00.75	4	1
	221	89	136	12	131.21	12.12	3	3
	140	77	214	49	214.53	49.13	2	3
	135	65	065	50	073.84	45.97	1	1
Savoia peaks	220	70	130	01	130.32	00.88	4	1
	227	60	137	01	137.43	00.75	4	1
e821486/n42342	221	89	136	12	131.21	12.12	3	3
	140	77	214	49	214.53	49.13	2	3
	135	65	065	50	073.84	45.97	1	3
Elena	190	15	190	15	189.99	15	1	1
	180	32	180	32	178.99	32	1	1
	235	80	130	50	156.47	48.44	2	1
	255	85	170	25	167.37	25.25	4	2
	230	55	170	30	166.71	32.7	4	2
	220	50	225	45	225.51	49.87	0	0
	225	70	160	10	141.68	17.72	4	1
	170	89	-	-	-	-	-	-
	080	85	165	58	162.02	57.77	4	1
	080	85	170	30	167.13	29.78	4	1
	170	30	190	22	195.41	27.54	1	1
	220	85	145	55	137.43	55.92	2	1
	246	75	164	28	164.17	27.95	4	1
	190	35	200	35	199.95	34.59	1	1
	160	75	070	45	084.04	42.15	2	1
	088	38	042	25	040.43	27.8	1	1
	130	50	125	50	125.01	49.89	1	1
	234	80	138	40	152.03	38.4	4	1
	230	80	310	50	308.02	49.66	2	1
	330	70	242	14	244.82	12.99	4	1
	060	40	340	10	340.85	08.97	2	1
	054	80	330	01	324.35	02	3	1
	224	65	142	30	147.95	27.34	3	1
	230	85	140	01	140.09	00.99	3	1
	225	80	131	01	135.05	00.29	3	1
	190	40	170	40	170.48	38.34	2	1
Way from	250	70	180	60	192.41	55.82	2	1
Nyabitaba	175	60	-	-	-	-	-	-
to John	285	80	350	55	359.17	57.12	2	1
Matte hut	145	60	150	65	149.23	59.93	1	1
	125	55	215	01	214.53	00.67	4	3
	130	75	130	80	130	75	2	1
	130	75	200	25	211.56	28.72	3	1
	160	60	150	45	145.66	59.21	2	1
	124	75	170	55	184.71	61.29	2	1
	000	85	76	65	079.03	65.3	2	1
Around	230	40	-	-	-	-	-	-
Bujuku Hut	220	85	-	-	-	-	-	-
	090	85	-	-	-	-	-	-
	160	88	-	-	-	-	-	-
	225	80	154	30	141.55	32.9	3	1
	165	50	-	-	-	-	-	-
	230	45	285	30	284.91	29.89	0	0
	162	54	-	-	-	-	-	-
	240	88	152	38	151.56	38.02	3	3
	160	85	-	-	-	-	-	-
	050	88	-	-	-	-	-	-
Towards DRC	270	80	340	50	347.16	51.56	4	3
	115	85	025	30	027.87	29.78	0	0
	190	50	170	50	170.67	48.36	2	1
	100	65	-	-	-	-	-	-
	320	85	-	-	-	-	-	-
	120	85	350	45	036.11	50.56	2	3
	190	50	170	50	170.67	48.36	2	1
Bujuku to FFP	090	80	135	62	154.13	68	1	1
	220	60	120	52	157.42	38.57	0	0
	170	55	-	-	-	-	-	-

... continued on next page

GPS Loc.(UTM)	Dipdir.	Dip	Plgdir.	Plg.	Plgdir.*	Plg.*	Sns	Qlty
	240	80	-	-	-	-	-	-
	160	40	160	40	159.99	40	2	2
	190	80	-	-	-	-	-	-
	295	88	-	-	-	-	-	-
	177	40	-	-	-	-	-	-
	100	50	150	45	145.3	39.97	2	1
	160	55	-	-	-	-	-	-
near Kitandara	170	60	-	-	-	-	-	-
	185	40	-	-	-	-	-	-
Kitandara-	050	45	050	40	050	45	2	2
back valley	115	65	070	45	060.76	51.42	0	0
	250	75	318	35	327.82	38.22	2	1
	100	65	026	40	031.08	37.65	2	1
	080	60	-	-	-	-	-	-
	280	80	-	-	-	-	-	-
	285	76	015	50	359.37	47.22	3	1
	210	55	120	15	127.18	10.11	2	1
	157	55	222	22	227.06	25.97	3	1
	157	55	113	45	112.48	45.52	2	1
	215	50	160	50	170.16	40.2	1	1
Freshfield Pass	175	30	165	45	166.57	29.73	1	2
	190	35	-	-	-	-	-	-
	190	50	-	-	-	-	-	-
	220	45	175	45	180.36	37.6	0	0
	250	80	-	-	-	-	-	-
	178	35	-	-	-	-	-	-
	070	85	-	-	-	-	-	-
	260	78	-	-	-	-	-	-
	270	70	-	-	-	-	-	-
	110	80	-	-	-	-	-	-
	270	70	-	-	-	-	-	-
	110	55	100	55	100.1	54.6	2	0
e821056/n39793	220	70	130	01	130.32	00.88	4	3
	227	60	137	01	137.43	00.75	4	3
	160	42	245	10	242.24	06.93	4	1
	160	42	140	42	140.52	40.33	1	1
	100	76	180	30	181.58	30.41	3	1
	066	88	150	30	154.83	30.26	3	1
Kitandara-								
Kilembe trail	116	70	-	-	-	-	-	-
	130	50	-	-	-	-	-	-
Kitandara hut	120	70	170	60	170.48	60.23	1	2
	110	36	-	-	-	-	-	-
	070	56	110	15	130.49	36.14	3	2
	090	80	010	25	004.93	25.99	3	1
	248	75	310	38	323.6	42.87	2	1
	075	75	004	68	019.12	64.47	2	1
	255	88	004	68	335.6	77.93	2	1
	300	66	210	05	211.86	04.17	4	1
	286	82	270	80	266.99	81.55	2	1
	230	45	166	25	166.71	24.21	4	1
	236	48	062	10	252.29	46.83	3	1
	205	40	275	12	277	14.54	3	1
Kitand.Congo	220	78	130	01	130.2	00.96	4	1
	130	90	-	-	-	-	-	-
	054	89	318	72	327.09	72.05	2	1
	74	80	-	-	-	-	-	-
	070	62	158	05	157.48	04.72	4	1
South of	064	85	325	10	334.82	09.28	4	1
Kitandara	290	75	-	-	-	-	-	-
e821657/n40488	234	80	318	35	316.96	34.82	4	1
	170	40	010	25	216.74	29.9	0	0
	284	50	340	35	339.22	34.21	3	1
	266	65	334	30	338.74	32.47	3	1
	280	80	010	06	008.97	05.82	4	1
	250	55	160	05	162.35	03.36	4	1
	275	88	180	10	185.35	09.86	4	1
	080	50	160	05	163.35	07.86	3	1

... continued on next page

GPS Loc.(UTM)	Dipdir.	Dip	Plgdir.	Plg.	Plgdir.*	Plg.*	Sns	Qlty
	078	70	170	35	155.53	30.67	3	1
	062	78	140	45	139.75	44.95	4	1
	110	45	170	30	168.12	27.84	2	1
	188	80	290	20	274.72	17.95	4	1
Kitand.southwest	214	82	302	22	300.77	21.83	4	1
			Kigolo-Kabakoru Hill (KK) area					
Kigolo area								
e846289/n25093	315	55	300	55	300.33	54.1	0	0
	028	70	312	44	317.24	42.16	3	1
	115	35	008	01	193.88	07.69	3	1
	120	60	200	05	205.28	08.11	4	1
	300	72	000	60	357.26	59	1	1
	018	72	-	-	-	-	-	-
	030	89	325	45	301.11	48.01	1	1
	030	70	315	45	320.01	43.23	2	1
	112	30	180	05	183.02	10.63	3	1
	100	40	180	07	180.64	07.77	3	1
	090	60	179	08	176.27	06.43	3	1
first lin.	138	72	126	12	084.86	61.56	0	0
second lin.	138	72	070	42	065.95	43.49	1	3
	115	55	030	10	031.39	09.03	3	1
	042	72	320	10	315.76	11.42	4	1
	120	65	220	15	205.84	08.84	4	1
	040	88	300	32	311.26	32.11	4	1
	215	88	290	50	302.52	51.13	1	3
	130	55	220	20	210.3	13.54	3	1
e178576/n25214	085	80	355	40	003.17	38.85	3	2
	222	20	132	28	141.7	03.51	0	0
	285	42	195	29	210.41	13.46	3	2
	124	50	214	30	198.13	18.05	0	0
	102	40	192	30	176.13	12.92	0	0
	274	34	184	30	198.98	09.89	0	0
	330	75	020	62	026.18	64.29	2	2
	040	82	350	75	344.52	76.07	2	2
	058	70	030	87	053.69	69.95	2	2
	058	72	312	88	051.46	71.89	2	2
e166183/n22602	010	70	040	70	036.93	67.79	2	2
	230	80	000	60	300.13	62.58	2	2
e181044/n26662	207	30	340	26	139.32	12.37	0	0
	207	40	340	20	133.81	13.64	0	0
	185	22	185	20	185.01	22	3	2
	185	22	185	20	185.01	22	3	2
	246	70	336	30	325.49	26.62	2	2
	220	64	310	10	306.03	08.09	4	1
Kabakoru Hill and surroundings								
e849012/n26662	190	60	142	75	167.38	57.98	2	1
	214	80	120	55	137.64	53.22	2	1
	240	15	255	15	254.97	14.51	0	0
	285	72	200	16	200.31	15.9	3	1
	280	60	320	48	323.71	51.39	1	1
			Kilembe-Nyabirongo-George flanks (KNG)					
Kilembe Mines and surroundings								
	100	80	-	-	-	-	-	-
	350	70	020	62	025.32	65.96	2	1
	284	70	340	60	337.12	58.77	2	1
	350	70	020	62	025.32	65.96	0	0
	042	50	000	54	007.81	44.59	2	1
	130	65	090	65	096.15	60.69	2	1
	118	82	034	56	039.72	55.33	0	0
	290	70	358	30	006.1	33.42	0	0
	120	45	-	-	-	-	-	-
	300	70	-	-	-	-	-	-
	150	60	194	35	205.19	44.68	0	0
	180	80	230	70	237.44	71.86	2	1
	310	70	350	65	349.53	64.74	0	0
	280	70	-	-	-	-	-	-

... continued on next page

GPS Loc.(UTM)	Dipdir.	Dip	Plgdir.	Plg.	Plgdir.*	Plg.*	Sns	Qlty
	030	70	-	-	-	-	-	-
	220	40	-	-	-	-	-	-
	190	60	305	56	249.38	41.41	2	1
	030	80	310	60	317.02	58.93	0	0
	075	62	-	-	-	-	-	-
	010	78	300	60	301.33	59.7	2	1
	050	65	-	-	-	-	-	-
	310	85	040	60	031.45	59.53	1	1
	300	75	345	70	343.92	69.59	2	1
	280	52	285	50	285.21	51.88	2	1
	010	70	-	-	-	-	-	-
	260	78	030	55	331.07	56.76	0	0
	300	75	090	85	310.13	74.77	0	0
	315	55	300	55	300.33	54.1	0	0
	330	75	260	10	244.08	14.86	0	0
	320	65	015	40	022.64	44.58	0	0
	120	80	-	-	-	-	-	-
	010	20	030	20	029.86	18.9	0	0
	290	80	-	-	-	-	-	-
	330	89	-	-	-	-	-	-
	260	20	300	10	301.24	15.31	1	1
Nyabirongo area								
e820152/n7289	022	70	310	35	307.36	36.04	0	0
Kasese south,	065	01	290	40	110.61	00.7	2	1
towards DRC.	050	70	350	40	340.75	44.23	2	0
	340	78	062	15	066.5	16.01	3	1
	350	80	090	80	035.59	75.86	0	0
	220	75	310	20	304.8	18.69	4	0
	070	60	028	60	034.43	54.63	2	1
gneiss, at	295	80	-	-	-	-	-	-
e824590/n9736	345	60	-	-	-	-	-	-
	238	80	-	-	-	-	-	-
	245	85	320	45	329.75	46.3	0	0
	160	65	160	60	160	65	0	0
	300	90	-	-	-	-	-	-
	100	70	-	-	-	-	-	-
	220	89	305	30	309.42	30.15	0	0
	165	65	260	28	244.31	21.7	0	0
e823863/n12749	125	60	100	65	104.91	58.42	2	1
	320	80	040	70	024.25	67.91	2	1
e817823/n5406	330	70	340	65	342.18	69.58	2	1
	330	88	260	55	243.06	56.81	2	1
	330	70	-	-	-	-	2	-
e815000/n1682	170	75	220	60	228.14	63.09	0	0
	135	80	-	-	-	-	-	-
	110	80	030	20	023.92	21.19	0	0
	220	60	-	-	-	-	-	-
e820155/n07287	074	60	074	60	073.99	60	2	1
e817712/n05336	150	78	146	70	143.39	77.92	0	0
The Lake George-flanks								
e868333/n291	020	88	280	50	292.4	50.23	2	3
	310	75	-	-	-	-	-	-
	340	60	320	60	320.85	58.57	2	1
e190105/n45248	240	89	330	80	324.35	79.95	2	1
	080	84	350	82	026.49	79.98	2	1
	140	70	-	-	-	-	-	-
	200	80	-	-	-	-	-	-
	245	89	335	01	334.98	01	4	1
	124	80	034	32	040.1	31.07	3	1
George-fl.‘09	195	50	190	60	191.06	49.93	2	0
	210	80	-	-	-	-	-	-
	340	45	010	45	008.19	41.39	2	0
	305	89	-	-	-	-	-	-
	150	75	170	70	174.52	73.59	2	0
	360	60	-	-	-	-	-	-
	045	80	-	-	-	-	-	-
	180	85	090	38	093.88	37.72	0	0
	195	80	-	-	-	-	-	-

... continued on next page

GPS Loc.(UTM)	Dipdir.	Dip	Plgdir.	Plg.	Plgdir.*	Plg.*	Sns	Qlty
	220	75	-	-	-	-	-	-
	270	80	-	-	-	-	-	-
	000	50	-	-	-	-	-	-
	260	75	-	-	-	-	-	-
	270	70	350	05	357.18	07.69	0	0
	310	45	-	-	-	-	-	-
	125	80	030	30	040.51	28.57	4	1
	330	50	340	60	337.85	49.73	2	1
	130	89	045	25	040.47	25.15	4	1
	010	60	090	25	086.01	22.72	3	1
	285	89	270	80	215.98	87.21	0	0
	090	50	090	45	090	50	0	0
	290	89	310	80	003.82	86.42	0	0
	270	60	300	55	300.92	56.06	0	0
	195	80	110	60	121.7	58.46	0	0
	120	80	-	-	-	-	-	-
	280	55	230	40	228.33	41.53	0	0
	160	75	-	-	-	-	-	-
	265	60	-	-	-	-	-	-
	275	60	-	-	-	-	-	-
	310	78	040	68	013.28	64.7	2	2
	288	80	018	70	352.83	67.48	2	1
Basement outcrop on Fort Portal-Kasese Rd								
e858037/n45305	060	70	040	65	036.83	68.4	0	0
	255	80	180	60	182.47	59.57	2	0
	200	75	-	-	-	-	-	-
	140	70	-	-	-	-	-	-
	310	75	018	70	002.48	66.25	2	1
	060	88	295	03	330.08	02.26	0	0
Outcrop along Kasese-QENP Road								
e839241/n12299	120	60	130	60	129.89	59.63	2	1
	080	75	-	-	-	-	-	-
bedding 310/50	300	88	-	-	-	-	-	-
	130	70	070	35	058.13	40.53	0	0
	260	70	-	-	-	-	-	-
	170	75	070	65	108.04	60.32	0	0
	060	80	150	01	149.83	00.97	4	2
QENP volcanics	245	85	-	-	-	-	-	-
e819595/n15215	110	78	-	-	-	-	-	-
	330	70	-	-	-	-	-	-
	350	85	-	-	-	-	-	-

Appendix C

Results of fault-slip data analysis using PBT-axes method

Note: Dipdir = Dip direction, Az = Azimuth, Plg = Plunge, Lin-az = Lineation azimuth, Lin-Plg = Lineation plunge, S = Sense of slip, Q^F = Quality of slip indicator; P-az/P-Plg, T-az/T-Plg, B-az/B-Plg = azimuths/plunges of kinematic axes P, T, and B respectively; . σ_n = value of normal stress, τ = value of shear stress, τ/σ_n = ratio of shear to normal stress.

Table C.1 Fault-slip data and orientations of corresponding kinematic axes calculated by PBT-axes method

Dipdir	Dip	Lin-az	Lin-Plg	S	Q^F	P-az	P-Plg	T-az	T-Plg	B-az	B-Plg.	Pitch	Bew
						Sempaya-Kazingo (SK) area							
e852479/n91780													
330	70	329.99	70	2	1	150.02	80	330	10	060	00	90	2
335	55	340.61	54.87	2	1	004.42	84.31	153.62	05.04	246.85	02.64	-86.78	7
e853579/n93166													
180	70	165.43	69.39	2	2	023.69	79	177.42	09.89	268.26	04.77	84.92	5
240	80	328.83	06.63	3	2	358.9	10.77	089.91	05.32	205.79	77.96	-06.71	7
310	85	275.6	83.95	2	2	136.95	64.79	308.12	24.94	039.7	03.4	86.58	5
290	60	265.51	57.61	1	3	277.33	28.77	122.37	58.78	013.5	11.09	77.17	8
e860069/n91029													
036	70	306.79	2.17	3	1	155.11	07.94	247.76	18.37	042.72	69.87	02.31	8
280	82	194.59	29.66	2	1	159.9	29.88	254.11	07.29	356.44	59.07	29.98	5
074	60	152.03	19.76	2	1	182.32	32.87	282.51	15.31	033.7	52.87	-22.98	7
057	50	327.36	00.43	3	1	171.16	18.35	274.13	34.08	057.87	50	00.56	8
180	80	093.73	20.23	0	0	123.92	12.28	029.65	18.86	245.15	67.23	20.58	0
e858050/n84596													
280	80	190.16	00.93	3	3	039.74	04.17	130.42	09.12	285.42	79.96	00.92	8
e856290/n83198													
300	80	028.79	06.83	0	0	359.29	00.93	089.49	12.11	264.99	77.85	-06.94	0
130	70	139.87	69.72	2	3	293.54	79.54	131.73	09.95	041.17	03.2	-86.59	7
302	70	010.5	45.2	2	0	055.44	51.77	321.17	03.36	228.54	38.03	-49.03	7
130	70	103.07	67.79	0	0	118.99	39.1	317.56	49.39	216.6	09.26	80.14	0
e855468/n81888													
290	45	290	45	0	0	290.01	15	109.99	75	200.01	00.01	-89.99	0
012	60	027.39	59.09	0	0	019.8	29.54	184.27	59.54	285.94	06.78	-82.16	0
270	30	240.93	26.78	2	1	228.58	55.41	075.27	31.66	337.37	12.53	64.29	5
200	85	119.89	63.01	0	0	165.61	46.73	035.18	31.4	287.51	26.45	63.44	0
078	80	012.09	66.64	0	0	651.64	45.09	271.2	37.55	164.14	20.18	68.77	0
300	56	328.19	52.57	2	1	018.76	75.31	128.29	05	219.52	13.77	-73.32	7
300	65	314.6	64.27	2	1	073.3	82.52	303.15	04.84	212.66	05.69	-83.72	7
e192178/n90988													
040	80	129.83	00.97	3	1	159.5	05.82	250.33	08.16	034.35	79.95	-00.98	7
115	85	025.09	00.99	3	2	234.98	01.64	325.11	04.83	126.26	84.9	01.03	8
158	70	085.82	40.05	2	1	045.07	46.74	136.62	01.46	228	43.22	43.22	5
140	80	061.52	48.56	2	1	016.06	47.39	120.56	12.97	221.58	39.69	49.57	5
114	74	092.38	72.86	2	1	315.13	74.88	110.79	13.83	202.28	05.99	83.77	5
288	80	352.83	67.48	2	1	067.49	62.48	298.51	18.15	201.67	19.96	-69.72	7
e852360/n72622													
220	88	134.59	66.44	0	0	186.81	50.93	053.2	29.24	309.13	23.46	66.5	0
125	74	192.6	53.04	0	0	160.33	33.65	283.84	39.66	045.44	32.3	-56.23	0

... continued on next page

Dipdir	Dip	Lin-az	Lin-Plg	S	Q^F	P-az	P-Plg	T-az	T-Plg	B-az	B-Plg.	Pitch	Bew
330	72	260.16	46.69	0	0	290.66	28.4	174.53	39.16	045.42	37.76	49.91	0
						The Central Rwenzoris (C-RWZ) area							
Mt. Baker													
275	89	233.72	88.67	2	1	098.26	59.95	274.5	29	004.98	00.88	89.12	5
230	60	304.23	25.21	1	1	279.41	06.83	015.23	40.24	181.51	48.94	-29.46	6
170	55	170.01	55	0	0	170.01	25	349.99	65	080	00	-89.99	0
130	70	164.33	66.21	2	1	262.63	74.47	136.62	09.28	044.57	12.34	-76.85	7
250	80	192.73	71.94	2	1	103.04	65.53	242.07	18.96	337.31	14.88	74.88	5
110	89	035.34	86.23	2	1	296.46	60.79	107.92	28.93	199.94	03.63	86.36	5
110	89	020.09	05.25	4	1	349.97	05.05	080.12	01.76	189.25	84.66	05.14	5
070	65	147.53	24.85	1	1	120.93	08.78	217.18	35.18	018.92	53.42	-27.62	6
220	70	130.32	00.88	4	1	101.76	10.62	008.52	16.77	222.74	69.98	00.94	5
227	60	137.43	00.75	4	1	110.78	15.15	013.45	25.24	228.73	59.99	00.86	5
221	89	131.21	12.12	3	3	161.71	09.97	070.5	06.9	306.35	77.84	11.86	8
140	77	214.53	49.13	2	3	261.6	50.12	158.71	10.56	060.36	37.91	-50.9	7
135	65	073.84	45.97	1	1	099.66	24.29	341.25	46.51	207.03	33.49	52.49	8
Savoia peaks													
220	70	130.32	00.88	4	1	101.76	10.62	008.52	16.77	222.74	69.98	00.94	5
227	60	137.43	00.75	4	1	110.78	15.15	013.45	25.24	228.73	59.99	00.86	5
e821486/n42342													
221	89	131.21	12.12	3	3	161.71	09.97	070.5	06.9	306.35	77.84	11.86	8
140	77	214.53	49.13	2	3	261.6	50.12	158.71	10.56	060.36	37.91	-50.9	7
135	65	073.84	45.97	1	1	099.66	24.29	341.25	46.51	207.03	33.49	52.49	8
Elena													
190	15	189.99	15	1	1	009.99	15	189.98	75	279.99	00	89.99	1
180	32	178.99	32	1	1	179.99	02	000.12	90	269.99	00	89.99	1
235	80	156.47	48.44	2	1	111.11	47.29	215.52	12.93	316.55	39.81	49.44	5
255	85	167.37	25.25	4	2	134.25	24.39	227.86	07.92	334.58	64.19	25.4	5
230	55	166.71	32.7	2	1	132.82	48.99	027.3	13.1	286.82	38.01	41.26	5
220	50	225.51	49.87	0	0	223.27	19.92	034.84	69.88	132.28	02.72	-86.45	0
225	70	141.68	17.72	4	1	110.47	25.76	016.44	08.28	270.03	62.75	18.9	5
080	85	162.02	57.77	1	1	119.13	43.55	242.27	29.9	353.1	31.75	-58.13	6
080	85	167.13	29.78	1	1	134.49	22.74	232.73	18.89	358.62	59.72	-29.91	6
170	30	195.41	27.54	1	1	009.25	01.87	269.71	78.87	099.61	10.97	-67.64	6
220	85	137.43	55.92	2	1	087.86	49.54	202.83	19.79	306.67	33.61	56.24	5
246	75	164.17	27.95	2	1	129.7	32.36	220.07	00.58	311	57.63	29.02	5
190	35	199.95	34.59	1	1	197.1	04.71	332.09	83.35	106.71	04.68	-81.82	6
160	75	084.04	42.15	2	1	042.29	45.28	138.78	06.4	235	44.01	44.02	5
088	38	040.43	27.8	1	1	053.56	00.57	322.28	66.29	143.81	23.7	49.24	8
130	50	125.01	49.89	1	1	127.04	19.93	314.68	69.9	217.93	02.46	86.79	8
234	80	152.03	38.4	2	1	113.39	38.66	210.85	09.22	311.94	49.84	39.09	5
230	80	308.02	49.66	2	1	354.44	48.32	248.99	13.34	148.09	38.58	-50.7	7
330	70	244.82	12.99	4	1	214.62	21.45	120.4	10.59	005.77	65.84	13.85	5
060	40	340.85	08.97	4	1	319.19	31.2	203.25	35.83	078.08	38.58	14.05	5
054	80	324.35	02	3	1	173.9	03.24	264.46	09.66	065.54	79.8	02.01	8
224	65	147.95	27.34	1	1	174.54	10.74	076.45	36.56	278.28	51.38	30.45	8
230	85	140.09	00.99	3	1	349.98	01.64	080.11	04.83	241.26	84.9	10.03	8
225	80	135.05	00.29	3	1	344.66	04.73	075.39	08.8	226.69	80	00.29	8
190	40	170.48	38.34	2	1	154.550	66.96	001.95	20.69	268.25	09.7	74.81	5
Way between Nyabitaba and John-Matte huts													
250	70	192.41	55.82	2	1	133.02	62.56	236.18	06.74	329.56	26.47	61.69	5
285	80	359.17	57.12	2	1	053.84	54.5	300.73	15.64	201.07	30.95	-58.52	7
145	60	149.23	59.93	1	1	147.12	29.96	322.88	59.97	056.06	01.83	-87.88	6
125	55	214.53	00.67	4	3	009.3	16.06	269.67	30.17	123.57	54.99	-00.82	6
130	75	130	75	2	1	309.99	75	130	15	040	00	-90	7
130	75	211.56	28.72	2	1	246.31	33.06	155.71	00.92	064.29	56.92	-29.83	7
160	60	145.66	59.21	2	1	068.16	83.69	336.37	00.2	246.34	06.3	82.72	5
124	75	184.71	61.29	2	1	251.6	62.74	136.38	12.38	040.81	23.87	-65.23	7
000	85	079.03	65.3	2	1	140.39	56.14	012.86	22.26	272.25	24.12	-65.79	7
Around Bujuku Hut and the way towards Kitandara Hut													
225	80	141.55	32.9	1	1	173.54	22.56	072.39	24.96	300.29	55.23	33.47	8
230	45	284.91	29.89	0	0	268.04	04.47	005.68	59.49	175.44	30.11	-44.81	0
240	88	151.56	38.02	1	3	187.23	31.06	084.73	19.77	327.45	51.91	37.97	8
Towards DRC													
270	80	347.16	51.56	1	3	310.62	36.26	068.92	32.83	187.54	36.65	-52.7	6
115	85	027.87	29.78	0	0	060.51	22.74	322.27	18.89	196.38	59.72	29.91	0
190	50	170.67	48.36	2	1	140.02	75.6	003.58	10.55	271.75	09.7	77.29	5

... continued on next page

Dipdir	Dip	Lin-az	Lin-Plg	S	Q^F	P-az	P-Plg	T-az	T-Plg	B-az	B-Plg.	Pitch	Bew
120	85	036.11	50.56	2	3	351.22	45.43	100.59	18.1	205.94	39	50.85	5
190	50	170.67	48.36	2	1	140.02	75.6	003.58	10.55	271.75	09.7	77.29	5
Bujuku to FFP													
090	80	154.13	68	1	1	114.72	45.74	257.73	37.88	003.56	19.39	-70.3	6
220	60	157.42	38.57	0	0	181.1	16.85	071.33	48.14	284.27	36.94	46.06	0
160	40	159.99	40	2	2	159.98	70	340	20	249.99	00	89.99	2
100	50	145.3	39.97	2	1	179.92	61.37	296.28	13.62	032.36	24.66	-56.99	7
Valley behind Kitandara Hut													
050	45	050	45	2	2	050.02	75	230	15	320.01	00	-89.99	7
115	65	060.76	51.42	0	0	085.31	27.76	317.78	49.19	191.07	27.3	59.59	0
250	75	327.82	38.22	2	1	007.04	41.7	272.67	04.89	177.24	47.88	-39.83	7
100	65	031.08	37.65	2	1	352.11	47.76	258.28	03.47	165.14	42.03	42.37	5
285	76	359.37	47.22	3	1	044.97	49.16	304.34	09.06	206.82	39.39	-49.15	7
210	55	127.18	10.11	4	1	100.29	26.03	357.64	24.14	230.94	53.14	12.39	5
157	55	227.06	25.97	2	1	258.13	41.76	003.1	16.13	109.2	43.81	-32.31	7
157	55	112.48	45.52	2	1	070.1	64.79	322.64	08.05	229.07	23.73	60.58	5
215	50	170.16	40.2	1	1	186.3	13.74	069.45	61.57	282.66	24.37	57.41	8
Fresh-Field Pass (FFP)													
175	30	166.57	29.73	1	2	348.67	00.2	081.83	86.34	258.66	03.65	82.69	8
220	45	180.36	37.6	0	0	193.6	10.07	079.43	66.55	287.5	20.94	59.64	0
110	55	100.1	54.6	2	0	064.45	83.06	287.13	05.12	196.71	04.68	84.28	5
e821056/n39793													
220	70	130.32	00.88	4	3	101.76	10.62	008.52	16.77	222.74	69.98	00.94	5
227	60	137.43	00.75	4	3	110.78	15.15	013.45	25.24	228.73	59.99	00.86	5
160	42	242.24	06.93	4	1	042.12	15.49	296.18	44.74	146.14	41.16	-10.39	6
160	42	140.52	40.33	1	1	147.04	10.89	010	75.27	238.95	09.79	75.27	8
100	76	181.58	30.41	2	1	216.96	34.01	125.28	02.5	031.58	55.87	-31.46	7
066	88	154.83	30.26	2	1	188.93	26.99	092.28	12.81	339.42	59.66	-30.34	7
Kitandara Hut													
120	70	170.48	60.23	1	2	144.04	35.5	283.72	46.9	038.07	21.1	-67.48	6
070	56	130.49	36.14	2	2	166.56	52.22	270.97	10.92	008.92	35.64	-45.35	7
090	80	004.93	25.99	1	1	035.8	17.02	298.86	21.68	160.74	61.88	26.42	8
248	75	323.6	42.87	2	1	005.87	45.94	268.94	06.66	172.62	43.29	-44.77	7
075	75	019.12	64.47	2	1	303.48	65.62	064.44	13.12	159.35	20.16	69.09	5
255	88	335.6	77.93	2	1	054.19	59.81	261.67	27.3	165.42	11.9	-78.1	7
300	66	211.86	04.17	4	1	183.59	15.45	088.31	18.41	311.11	65.59	04.56	5
286	82	266.99	81.55	2	1	112.31	67.85	284.52	21.96	015.62	02.72	87.25	5
230	45	166.71	24.21	2	1	140.12	45.13	023.51	24.04	275.19	35.18	35.44	5
236	48	252.29	46.83	2	1	276.13	75.06	061.64	12.4	153.45	08.2	-78.94	7
205	40	277	14.54	2	1	299.47	36.9	058.09	32.54	176.02	36.28	-22.98	7
Kitandara - Congo side													
220	78	130.2	00.96	4	1	100.69	06.8	009.51	09.89	224.71	77.96	00.96	5
054	89	327.09	72.05	2	1	262.76	56.37	044.02	27.42	143.68	17.92	72.08	5
070	62	157.48	04.72	4	1	310.92	09.41	216.17	26.6	058.72	61.53	-05.36	6
South of Kitandara Hut													
064	85	334.82	09.28	4	1	304.38	10.56	034.43	00.3	126.02	79.44	09.33	5
e821657/n40488													
234	80	316.96	34.82	1	1	284.6	24.06	027.09	25.84	157.71	53.36	-35.42	6
170	40	216.74	29.9	0	0	203.19	02.79	299.44	65.88	111.95	23.94	-50.85	0
284	50	339.22	34.21	2	1	011.52	53.93	124.69	16	224.75	31.35	-47.21	7
266	65	338.74	32.47	2	1	014.71	42.55	109.88	05.6	205.89	46.9	-36.32	7
280	80	008.97	05.82	4	1	339.48	00.06	069.49	11.6	249.2	78.4	-05.91	6
250	55	162.35	03.36	4	1	136.58	19.73	035.66	27.87	257.12	54.79	04.09	5
275	88	185.35	09.86	4	1	154.91	09.54	245.44	03.18	353.65	79.94	09.93	5
080	50	163.35	07.86	3	1	188.41	26.09	294.32	29.23	064.24	48.92	-10.28	7
078	70	155.53	30.67	2	1	191.02	37.79	282.85	02.36	015.88	52.11	-32.89	7
062	78	139.75	44.95	1	1	106.05	30.52	217.87	32.23	343.26	42.57	-46.24	6
110	45	168.12	27.84	2	1	195.52	49.29	313.93	22.26	058.8	32.07	-41.33	7
188	80	274.72	17.95	4	1	244.74	10.37	338.1	17.73	125.79	69.28	-18.26	6
Southwest of Kitandara Hut													
214	82	300.77	21.83	3	1	333.27	23.06	241.67	03.75	142.96	66.61	-22.07	7
						Kigolo-Kabakoru hill (KK) area							
Kigolo area													
e846289/n25093													
315	55	300.33	54.1	0	0	306.88	24.5	144.89	64.39	040.08	06.99	81.46	0
028	70	317.24	42.16	1	1	346.35	24.22	234.88	39.18	099.47	41.12	45.58	8
115	35	193.88	07.69	2	1	213.19	31.7	334.38	39.98	098.67	33.9	-13.49	7
120	60	205.28	08.11	4	1	359.49	07.34	265.18	30.24	101.73	58.7	-09.38	6

... continued on next page

Dipdir	Dip	Lin-az	Lin-Plg	S	Q^F	P-az	P-Plg	T-az	T-Plg	B-az	B-Plg.	Pitch	Bew
300	72	357.26	59	1	1	327.63	36	102.44	44.12	218.45	24.33	-64.33	6
030	89	301.11	48.01	1	1	341.43	39.42	231.26	22.75	119.1	41.97	47.99	8
030	70	320.01	43.23	2	1	276.82	49.83	009.96	02.65	102.19	40.04	46.8	5
112	30	183.02	10.63	3	1	200.09	36.35	330.09	41.13	087.37	27.69	-21.66	7
100	40	180.64	07.77	3	1	202.12	30.01	317.49	36.57	084.31	38.93	-12.14	7
090	60	176.27	06.43	3	1	203.7	20.3	302.41	22.14	075.38	59.18	-07.43	7
138	72	084.86	61.56	0	0	113.46	37.37	333.63	45.01	220.74	21.25	67.6	0
138	72	065.95	43.49	1	3	096.23	26.2	343.86	37.71	211.58	41.03	46.35	8
115	55	031.39	09.03	3	1	235.7	08.68	331.86	35.11	133.8	53.51	11.05	8
042	72	315.76	11.42	4	1	285.63	19.02	192.25	09.71	076.56	68.47	12.01	5
120	65	205.84	08.84	4	1	358.88	04.49	266.66	26.29	097.85	63.28	-09.77	6
040	88	311.26	32.11	2	1	276.6	28.54	014.17	13.62	126.82	57.81	32.22	5
215	88	302.52	51.13	1	3	261.06	41.04	014.8	24.8	126.61	38.8	-51.14	6
130	55	210.3	13.54	3	1	237.88	29.31	341.19	22.32	102.53	51.72	-16.59	7
e178576/n25214													
085	80	003.17	38.85	1	2	036.39	27.15	290.79	27.65	163.13	49.39	39.58	8
222	20	141.7	03.51	0	0	332.39	24.63	108.68	57.61	232.96	19.66	10.31	0
285	42	210.41	13.46	1	2	049.52	09.79	151.16	49.46	311.53	38.86	20.35	8
124	50	198.13	18.05	0	0	356.48	03.04	263.4	45.36	089.47	44.47	-23.86	0
102	40	176.13	12.92	0	0	337.78	10.92	234.09	50.83	076.15	37.06	-20.36	0
274	34	198.98	09.89	0	0	035.25	15.41	147.12	53.5	295.27	32.15	17.89	0
330	75	026.18	64.29	2	2	101.26	65.47	340.66	13.08	245.71	20.37	-68.88	7
040	82	344.52	76.07	2	2	244.5	65.53	033.89	21.39	128.39	11.33	78.56	5
058	72	053.69	69.95	2	2	245.32	71.91	057.25	09.99	147.49	01.39	88.52	5
058	72	051.46	71.89	1	2	055.64	41.96	239.52	47.97	147.37	01.93	87.97	8
e166183/n22602													
010	70	036.93	67.79	2	2	150.2	76.61	014.98	09.6	283.4	09.26	-80.14	7
230	80	300.13	62.58	2	2	003.57	58.82	243.09	17.06	144.77	25.25	-64.34	7
e181044/n26662													
207	30	139.32	12.37	0	0	333.13	14.33	088.28	58.99	235.7	26.86	25.36	0
207	40	133.81	13.64	0	0	332.03	10.3	075.18	51.38	234.24	36.72	21.52	0
185	22	185.01	22	1	2	005.01	08	185.03	82	095.01	00	-89.99	6
185	22	185.01	22	1	2	005.01	08	185.03	82	095.01	00	-89.99	6
246	70	325.49	26.62	2	2	359.35	33.99	092.15	04.14	188.23	55.69	-28.48	7
220	64	306.03	08.09	4	1	099.26	05.58	006.43	26.74	200.12	62.59	-09	6
Kabakoru hill and surroundings													
e849012/n26662													
190	60	167.38	57.98	2	1	097.03	79.81	004.15	00.52	274.05	10.17	78.23	5
214	80	137.64	53.22	2	1	087.7	51.3	196.51	14.48	296.92	34.96	54.41	5
240	15	254.97	14.51	0	0	072.98	15.43	267.18	74.12	164.01	03.71	-75.52	0
285	72	200.31	15.9	3	1	288.68	04.75	136.57	23.87	329.23	65.61	16.74	8
280	60	323.71	51.39	1	1	304.39	25.26	077.65	55.46	203.44	21.93	-64.45	6
Kilembe-Nyabirongo-George flanks (KNG)													
Kilembe Mines and surroundings													
350	70	025.32	65.96	2	1	121.74	74.14	356.85	09.23	264.74	12.79	-76.38	7
284	70	337.12	58.77	2	1	043.16	65.72	296.07	07.55	202.86	22.94	-65.49	7
350	70	025.32	65.96	0	0	005.07	38.31	159.69	48.84	264.74	12.79	-76.38	0
042	50	007.81	44.59	2	1	332.14	68.34	210.2	11.87	116.32	17.85	66.41	5
130	65	096.15	60.69	2	1	016.83	75.12	122.14	04.01	213.17	14.31	74.17	5
118	82	039.72	55.33	0	0	078.98	39.99	317.2	32.12	202.67	33.47	56.14	0
290	70	006.1	33.42	0	0	337.48	17.82	080.42	34.86	225.3	49.58	-35.89	0
150	60	205.19	44.68	0	0	182.8	21.04	301.91	51.68	079.78	30.37	-54.28	0
180	80	237.44	71.86	2	1	326.8	65.48	187.97	18.95	092.7	14.98	-74.79	7
310	70	349.53	64.74	0	0	327.31	37.75	118.19	48.45	225.51	14.79	-74.24	0
190	60	249.38	41.41	2	1	290.36	55.37	028.93	05.87	122.9	33.98	-49.81	7
030	80	317.02	58.93	0	0	355.56	40.92	227.61	35.36	114.37	29.08	60.44	0
010	78	301.33	59.7	2	1	240.95	58.39	355.95	14.57	093.68	27.37	61.97	5
310	85	031.45	59.53	1	1	347.63	44.66	113.1	30.43	222.89	29.97	-59.9	6
300	75	343.92	69.59	2	1	081.71	70.24	307.17	14.15	213.69	13.51	-76	7
280	52	285.21	51.88	2	1	299.33	81.57	101.62	08.04	191.98	02.53	-86.79	7
260	78	331.07	56.76	0	0	294.92	38.34	061.12	36.74	177.19	30.48	-58.77	0
300	75	310.13	74.77	0	0	303.24	44.92	118.13	44.96	210.69	02.56	-87.35	0
315	55	300.33	54.1	0	0	306.88	24.5	144.89	64.39	040.08	06.99	81.46	0
330	75	244.08	14.86	0	0	273.02	05.32	181	20.63	016.78	68.63	15.41	0
320	65	022.64	44.58	0	0	356.64	23.36	113.02	45.8	249.04	34.98	-50.76	0
010	20	029.86	18.9	0	0	206.47	10.91	057.22	77.35	297.69	06.31	-71.25	0
260	20	301.24	15.31	1	1	114.57	13.96	338.19	71.05	207.74	12.56	-50.52	6
Nyabirongo area													

... continued on next page

Dipdir	Dip	Lin-az	Lin-Plg	S	Q^F	P-az	P-Plg	T-az	T-Plg	B-az	B-Plg.	Pitch	Bew
e820152/n7289 (South of Kasese towards DRC)													
022	70	307.36	36.04	0	0	336.14	19.79	230.88	36.18	088.93	47.11	38.77	0
065	01	110.61	00.7	1	0	290.2	29.3	113.27	59.97	020.6	00.71	-44.39	6
050	70	340.75	44.23	2	0	296.69	50.81	030.4	03.01	122.84	39.02	47.93	5
340	78	066.5	16.01	3	1	097.81	20.05	188.69	02.42	285.28	69.79	-16.39	7
350	80	035.59	75.86	0	0	003.28	48.85	163.51	39.44	261.76	09.0	-79.95	0
220	75	304.8	18.69	4	0	275.7	08.52	009.27	22.6	166.35	65.67	-19.37	6
070	60	034.43	54.63	2	1	335.05	72.98	240.3	01.45	149.86	16.95	70.32	5
e824590/n9736													
245	85	329.75	46.3	0	0	292.14	35.63	042.52	25.91	159.72	43.26	-46.51	0
160	65	160.01	65	0	0	160	35	340	55	070	00	-90	0
220	89	309.42	30.15	0	0	275.87	25.23	013.35	15.44	131.72	59.83	-30.12	0
165	65	244.31	21.7	0	0	217.7	06.25	311.84	33.43	118.41	55.84	-24.07	0
e823863/n12749													
125	60	104.91	58.42	2	1	032.4	81.03	299.84	00.4	209.78	08.96	79.64	5
320	80	024.25	67.91	2	1	100.11	62.78	330.27	18.23	233.58	19.49	-70.2	7
e817823/n5406													
330	70	342.18	69.58	2	1	129.93	79.29	332.14	09.93	241.45	03.97	-85.78	7
330	88	243.06	56.81	2	1	194.94	47.92	312.75	22.84	058.69	33.11	56.86	5
330	70	267.97	52.19	2	0	214.78	58.78	314.21	05.67	047.58	30.58	57.22	5
e815000/n1682													
170	75	228.14	63.09	0	0	195.76	40.01	334.99	42.07	086.15	21.8	-67.39	0
110	80	023.92	21.19	0	0	054.21	13.07	319.53	19.34	176.25	66.36	21.53	0
e820155/n07287													
074	60	073.99	60	2	1	343.76	90	074	00	164	00	89.99	0
e817712/n05336													
150	78	143.39	77.92	0	0	148.21	47.98	330.93	41.99	239.71	01.35	88.62	0
The Lake George-flanks													
e868333/n291													
020	88	292.4	50.23	2	3	249.28	43.08	000.02	20.74	108.34	39.7	50.22	5
340	60	320.85	58.57	2	1	247.52	81.47	155.09	00.37	065.04	08.52	80.15	5
e190105/n45248													
240	89	324.35	79.95	2	1	042.77	59.48	245.67	28.5	150.18	10	-80	7
080	84	026.49	79.98	2	1	276.55	64.83	075.62	23.69	169.15	08	81.96	5
245	89	334.98	01	4	1	304.98	00.37	035	01.37	199.99	88.59	-01.15	6
124	80	040.1	31.07	3	1	071.76	21.11	331.81	24.11	198.24	57.01	31.61	8
195	50	191.06	49.93	2	0	182.53	79.78	013.71	10.02	283.37	01.94	87.47	5
340	45	008.19	41.39	2	0	034.48	67.84	170.64	16.37	265	14.51	-69.24	7
150	75	174.52	73.59	2	0	308.7	73.77	153.48	14.8	061.75	06.5	-83.27	7
180	85	093.88	37.72	0	0	128.54	29.1	025.28	22.42	263.61	51.83	37.89	0
270	70	357.18	07.69	0	0	149.15	03.16	057.97	21.3	247.18	68.45	-08.2	0
125	80	040.51	28.57	2	1	006.02	30.07	098.97	05.09	197.64	59.42	29.05	5
330	50	337.85	49.73	2	1	354.02	79.17	152.57	10.09	243.26	03.88	-84.94	7
130	89	040.47	25.15	4	1	007.81	22.13	102.51	11.38	217.87	64.83	25.18	5
010	60	086.01	22.72	2	1	117.2	35.77	217.45	13.88	325.1	50.82	-26.49	7
285	89	215.98	87.21	0	0	280.63	58.9	106.52	30.97	014.95	02.6	87.39	0
090	50	090	50	0	0	090.01	20	270.1	70	000	00	-89.99	0
290	89	003.82	86.42	0	0	295.76	58.83	108	30.94	200.06	03.44	-86.56	0
270	60	300.92	56.06	0	0	286.33	27.94	074.39	57.98	188.52	14.39	-73.33	0
195	80	121.7	58.46	0	0	160.13	40.64	032.85	35.21	279.26	29.57	59.94	0
280	55	228.33	41.53	0	0	247.93	16.7	131.6	55.92	347.41	28.75	54.04	0
310	78	013.28	64.7	2	2	084.31	62.49	321.44	15.78	224.91	21.92	-67.56	7
288	80	352.83	67.48	2	1	067.49	62.48	298.51	18.15	201.67	19.96	-69.72	7
Basement outcrop on Fort Portal-Kasese Rd; e858037/n45305													
060	70	036.83	68.4	0	0	050.66	39.36	246.41	49.56	147.13	07.82	81.67	0
255	80	182.47	59.57	2	1	124.23	56.47	240.42	16.3	339.53	28.41	61.11	5
310	75	002.48	66.25	2	1	084.36	67.24	319.45	13.5	224.99	17.97	-71.37	7
060	88	330.08	02.26	0	0	000.06	00.96	270.02	02.86	108.53	86.98	02.29	0
Outcrop at e839241/n12299													
120	60	129.89	59.63	2	1	211.28	85.69	302.49	00.09	032.5	04.31	-85.02	7
130	70	058.13	40.53	0	0	087.16	23.07	337.44	38.4	200.34	42.75	43.75	0
170	75	108.04	60.32	0	0	141.06	38.54	006.88	41.19	252.83	24.97	64.08	0
060	80	149.83	00.97	4	2	300.25	04.14	209.58	09.14	054.35	79.95	-00.98	6

Appendix D

Results of MIM calculation and parameters specifying the stress states

Note: Az = Azimuth, Plg = Plunge, S = Sense of slip, σ_n = value of normal stress, τ = value of shear stress, τ/σ_n = ratio of shear to normal stress.

Table D.1 Results from MIM calculation

F-az	F-Plg	S-az	S-Plg	S	Misfit(β)	σ_n	τ	τ/σ_n
			Sempaya-Kazingo (SK) area					
Faults activated by stress state $SK-1^2$								
330	70	329.99	70.00	N	3.4	0.114	0.263	2.364
335	55	340.61	54.87	N	0.1	0.292	0.405	1.379
310	85	275.60	83.95	N	8.9	0.012	0.106	11.000
130	70	139.87	69.72	N	17.1	0.097	0.296	3.000
302	70	010.50	45.20	N	26.5	0.147	0.354	2.333
300	56	328.19	52.57	N	0.8	0.354	0.478	1.371
158	70	085.82	40.05	N	21.6	0.208	0.374	1.762
140	80	061.52	48.56	N	15.2	0.042	0.188	4.750
114	74	092.38	72.86	N	9.1	0.048	0.185	3.800
288	80	352.83	67.48	N	3.6	0.090	0.267	3.000
180	70	165.43	69.39	N	19.1	0.328	0.391	1.181
300	65	314.60	64.27	N	9.0	0.218	0.413	1.864
115	85	025.09	00.99	D	16.7	0.009	0.042	4.000
Faults activated by stress state $SK-2^2$								
036	70	306.79	02.17	D	1.3	0.539	0.498	0.926
280	82	194.59	29.66	N	7.4	0.132	0.308	2.385
074	60	152.03	19.76	N	6.7	0.058	0.222	3.667
057	50	327.36	00.43	D	2.7	0.228	0.399	1.739
040	80	129.83	00.97	D	2.3	0.472	0.493	1.042
240	80	328.83	06.63	D	7.0	0.157	0.301	1,875
Subset $SK-LSS^*$ **under stress state** $SK-1^2$ **and R=0.1**								
180	80	093.73	20.23	N	50.2	0.167	0.302	1.765
300	80	028.79	06.83	N	67.5	0.053	0.224	4.400
130	70	103.07	67.79	N	4.4	0.097	0.296	3.000
290	45	290.00	45.00	N	20.0	0.575	0.494	0.845
012	60	027.39	59.09	N	6.7	0.174	0.270	1.588
200	85	119.89	63.01	N	14.3	0.174	0.265	1.529
078	80	012.09	66.64	N	135.0	0.058	0.058	1.000
220	88	134.59	66.44	N	23.5	0.168	0.238	1.412
125	74	192.60	53.04	N	45.7	0.052	0.221	4.400
330	72	260.16	46.69	N	44.2	0.077	0.232	2.875
			The Central Rwenzoris (C-RWZ) area					
Faults activated by stress state RA^2								
130	70	164.33	66.19	N	22.4	0.086	0.280	3.256
285	76	359.37	47.20	N	27.8	0.130	0.321	2.469
285	80	359.17	57.09	N	17.2	0.090	0.267	2.967

... continued on next page

F-az	F-Plg	S-az	S-Plg	S	Misfit(β)	σ_n	τ	τ/σ_n
130	75	130.00	75.00	N	9.3	0.044	0.205	4.659
160	60	145.66	59.21	N	8.1	0.291	0.440	1.512
157	55	112.48	45.52	N	14.3	0.358	0.470	1.313
160	75	084.04	42.15	N	3.7	0.108	0.276	2.556
255	88	335.6	77.93	N	14.3	0.097	0.182	1.876
236	48	252.29	46.83	N	8.9	0.647	0.444	0.686
275	89	233.72	88.67	N	24.4	0.049	0.148	3.020
250	80	192.73	71.94	N	25.9	0.171	0.292	1.708
110	55	100.1	54.60	N	1.2	0.246	0.419	1.703
285	80	359.17	57.12	N	17.2	0.090	0.267	2.967
286	82	266.99	81.55	N	17.9	0.071	0.236	3.324
190	50	170.67	48.40	N	1.3	0.552	0.467	0.846
190	50	170.67	48.40	N	1.3	0.552	0.467	0.846
160	40	159.99	40.00	N	17.3	0.613	0.482	0.786
190	40	170.48	38.34	N	0.7	0.706	0.436	0.618
050	45	050.00	45.00	N	3.7	0.401	0.429	1.070
054	80	324.35	02.00	D	18.3	0.092	0.028	0.315
Subset $RA-LSS^*$ under parameters $\sigma_1 = 58.8/82$, $\sigma_3 = 208/6.9$ and R=0.2								
170	55	170.00	55.00	N	0.9	0.431	0.444	1.030
220	50	225.51	49.87	N	9.8	0.546	0.496	0.908
230	45	284.91	29.89	N	52.0	0.645	0.471	0.730
115	85	027.87	29.78	N	6.2	0.199	0.014	0.070
220	60	157.42	38.57	N	37.5	0.375	0.481	1.283
115	65	060.76	51.42	N	19.1	0.295	0.263	0.892
220	45	180.36	37.60	N	24.0	0.631	0.481	0.762
170	40	216.74	29.90	N	43.3	0.667	0.435	0.652
Faults activated by stress state RB^2								
270	80	347.16	51.59	R	24.6	0.796	0.182	0.229
190	15	189.99	15.00	R	22.8	0.011	0.092	8.364
180	32	179.99	32.00	R	1.0	0.138	0.340	2.464
175	30	166.57	29.73	R	1.0	0.108	0.297	2.750
170	30	195.41	27.54	R	29.7	0.111	0.306	2.757
190	35	199.95	34.59	R	9.2	0.174	0.364	2.092
215	50	170.16	40.20	R	29.6	0.373	0.405	1.086
145	60	149.23	59.93	R	2.8	0.575	0.474	0.824
120	70	170.48	60.23	R	9.1	0.668	0.357	0.534
130	50	125.01	49.89	R	1.8	0.442	0.485	1.097
160	42	140.52	40.29	R	7.1	0.280	0.445	1.589
054	89	327.09	72.09	N	7.5	0.698	0.039	0.056
090	80	154.13	68.00	R	11.2	0.762	0.209	0.274
080	85	162.02	57.79	R	18.2	0.748	0.133	0.178
080	85	167.13	29.79	R	10.0	0.748	0.133	0.178
280	80	009.00	05.80	S	17.4	0.852	0.176	0.206
275	88	185.30	9.899	S	3.6	0.830	0.149	0.179
066	88	154.80	30.29	N	16.4	0.710	0.060	0.084
Faults activated by stress state RC^2								
110	89	020.09	05.25	S	1.3	0.193	0.394	2.041
221	89	131.21	12.12	D	12.7	0.465	0.499	1.073
054	80	324.35	02.00	D	12.7	0.265	0.430	1.623
230	85	140.09	00.99	D	5.0	0.315	0.464	1.473
225	80	135.05	00.29	D	6.5	0.405	0.487	1.202
300	66	211.86	04.17	S	10.9	0.390	0.448	1.149
280	80	008.97	05.82	S	25.4	0.089	0.274	3.079
275	88	185.35	09.86	S	7.4	0.036	0.187	5.194
214	82	300.77	21.83	D	19.8	0.590	0.490	0.830
066	88	154.83	30.26	N	24.9	0.097	0.294	3.031
250	75	327.82	38.22	N	6.3	0.098	0.278	2.837
100	65	031.08	37.65	N	3.2	0.200	0.349	1.163
250	75	327.82	38.22	N	6.3	0.098	0.278	2.837
125	55	214.53	00.67	S	19.0	0.537	0.429	0.799
160	42	242.24	06.93	S	28.4	0.826	0.194	0.235
248	75	323.60	42.87	N	14.9	0.114	0.300	2.631
070	56	130.50	36.09	N	13.1	0.267	0.353	1.322
180	32	180.00	32.00	R	26.2	0.794	0.151	0.190
175	30	166.60	29.70	R	0.8	0.788	0.138	0.175

... continued on next page

F-az	F-Plg	S-az	S-Plg	S	Misfit(β)	σ_n	τ	τ/σ_n
170	30	195.30	27.5	R	11.8	0.788	0.138	0.175
330	70	244.80	13.00	S	23.1	0.806	0.355	0.440
205	40	277.00	14.5	N	26.4	0.721	0.298	0.413
Faults activated by stress state RD^2								
220	70	130.32	00.88	S	1.9	0.113	0.287	2.540
227	60	137.43	00.75	S	3.1	0.197	0.391	1.985
225	70	141.68	17.72	S	15.4	0.164	0.344	2.097
070	62	157.48	04.72	S	29.3	0.320	0.294	0.919
220	70	130.32	00.88	S	1.9	0.113	0.287	2.540
227	60	137.43	00.75	S	3.1	0.197	0.391	1.985
060	40	340.85	08.97	S	9.2	0.150	0.100	0.667
250	55	162.35	03.36	S	4.0	0.507	0.499	0.984
064	85	334.82	09.28	S	24.7	0.369	0.393	1.065
234	80	316.96	34.82	R	22.5	0.220	0.410	1.864
080	85	167.13	29.78	R	2.1	0.584	0.420	0.719
230	55	166.71	32.70	N	26.3	0.270	0.410	1.518
080	85	162.02	57.77	R	30.4	0.584	0.420	0.719
062	78	139.75	44.95	R	29.3	0.320	0.344	1.075
255	85	167.37	25.25	S	10.5	0.568	0.447	0.787
246	75	164.17	27.95	N	23.9	0.454	0.469	1.033
070	65	147.50	24.89	R	2.8	0.260	0.360	1.385
210	55	127.10	10.10	S	0.4	0.050	0.218	4.360
090	80	154.10	68.00	R	25.8	0.657	0.399	0.607
130	50	125.00	49.90	R	22.5	0.307	0.393	1.280
190	40	170.50	38.29	N	12.7	0.021	0.091	4.333
135	65	73.80	46.00	R	7.5	0.482	0.473	0.981
275	88	185.30	9.899	S	25.7	0.810	0.347	0.428
120	70	170.50	60.20	R	27.4	0.670	0.400	0.615
Kigolo-Kabakoru hill (KK) area								
Faults activated by stress state $KK-12^2$								
115	35	193.88	07.69	N	3.7	0.584	0.486	0.832
112	30	183.02	10.63	N	5.7	0.634	0.469	0.740
100	40	180.64	07.77	D	9.8	0.718	0.448	0.624
090	60	176.27	06.43	D	11.8	0.837	0.357	0.426
115	55	031.39	09.03	D	18.2	0.509	0.497	0.976
130	55	210.30	13.54	D	0.5	0.306	0.460	1.503
030	70	320.01	43.23	N	6.3	0.753	0.431	0.572
042	72	315.76	11.42	S	25.4	0.857	0.345	0.402
040	88	311.26	32.11	N	2.4	0.704	0.435	0.618
215	88	302.52	51.13	R	18.4	0.603	0.470	0.779
220	64	306.03	08.09	S	7.0	0.510	0.428	0.839
330	75	026.18	64.29	N	3.5	0.322	0.400	1.242
Subset $KK-LSS^*$ under stress state $KK-12^2$								
315	55	300.33	54.10	N	33.6	0.641	0.331	0.516
138	72	084.86	61.56	N	116.7	0.169	0.357	2.112
222	20	141.70	03.51	N	22.9	0.609	0.366	0.601
124	50	198.13	18.05	N	7.1	0.406	0.491	1.224
102	40	176.13	12.92	N	16.4	0.698	0.457	0.655
274	34	198.98	09.89	N	30.4	0.791	0.105	0.133
207	30	139.32	12.37	N	13.5	0.461	0.403	0.874
207	40	133.81	13.64	N	4.7	0.385	0.400	1.039
240	15	254.97	14.51	N	83.4	0.694	0.318	0.458
Subset $KK-LSS^*$ under assumed flip-configuration of stress state $KK-12^2$								
315	55	300.33	54.10	N	41.8	0.792	0.405	0.511
138	72	084.86	61.56	N	130.4	0.161	0.338	2.099
222	20	141.70	03.51	N	9.7	0.732	0.437	0.597
124	50	198.13	18.05	N	5.5	0.327	0.395	1.208
102	40	176.13	12.92	N	7.3	0.571	0.376	0.658
274	34	198.98	09.89	N	43.3	0.983	0.127	0.129
207	30	139.32	12.37	N	7.2	0.566	0.495	0.874
207	40	133.81	13.64	N	6.2	0.478	0.498	1.042
240	15	254.97	14.51	N	102.8	0.821	0.371	0.452

... continued on next page

F-az	F-Plg	S-az	S-Plg	S	Misfit(β)	σ_n	τ	τ/σ_n
Faults activated by stress state $KK-3^2$								
028	70	317.24	42.16	R	3.9	0.439	0.496	1.130
030	89	301.11	48.01	R	8.6	0.646	0.459	0.711
120	65	205.84	08.84	S	1.6	0.430	0.451	1.049
246	70	325.49	26.62	N	1.0	0.380	0.293	0.771
185	22	185.00	22.00	R	4.3	0.470	0.440	0.936
185	22	185.00	22.00	R	4.3	0.470	0.440	0.936
Kilembe-Nyabirongo-George flanks (KNG)								
Faults activated by stress state $KNG-1^2$								
284	70	337.12	58.77	N	7.2	0.262	0.418	1.595
130	65	096.15	60.69	N	7.2	0.111	0.313	2.820
300	75	343.92	69.59	N	0.5	0.140	0.344	2.457
280	52	285.21	51.88	N	12.8	0.559	0.485	0.868
330	88	243.06	56.81	N	5.6	0.026	0.083	3.192
125	60	104.91	58.42	N	4.3	0.163	0.363	2.227
320	80	024.25	67.91	N	18.1	0.058	0.220	3.793
330	70	342.18	69.58	N	3.6	0.153	0.327	2.137
330	50	337.85	49.73	N	2.7	0.443	0.473	1.068
340	60	320.85	58.57	N	11.4	0.279	0.397	1.423
310	78	013.28	64.70	N	12.6	0.085	0.279	3.282
288	80	352.83	67.48	N	0.1	0.125	0.304	2.432
350	70	025.32	65.96	N	22.5	0.167	0.265	1.587
010	78	301.33	59.70	N	11.1	0.159	0.112	0.704
074	60	073.99	60.00	N	17.0	0.224	0.267	1.192
240	89	324.35	79.95	N	7.4	0.220	0.191	0.868
Subset $KNG-LSS^*$ **under stress state** $KNG-1^2$								
118	82	039.72	55.33	N	90.1	0.005	0.024	4.800
290	70	006.10	33.42	N	41.2	0.232	0.415	1.789
310	70	349.53	64.74	N	4.7	0.176	0.380	2.159
260	78	331.07	56.76	N	20.4	0.210	0.350	1.667
300	75	310.13	74.77	N	9.9	0.138	0.344	2.493
315	55	300.33	54.10	N	21.0	0.388	0.484	1.247
330	75	244.08	14.86	N	79.5	0.088	0.260	2.955
320	65	022.64	44.58	N	29.2	0.220	0.408	1.855
010	20	029.86	18.90	N	1.0	0.793	0.380	0.479
030	80	317.02	58.93	N	49.5	0.097	0.017	0.175
150	60	205.19	44.68	N	52.0	0.227	0.414	1.824
160	65	160.00	65.00	N	18.4	0.197	0.382	1.939
350	80	035.59	75.86	N	22.0	0.057	0.122	2.140
170	75	228.14	63.09	N	44.1	0.124	0.284	2.290
150	78	143.39	77.92	N	19.6	0.042	0.182	4.333
245	85	329.75	46.30	N	35.6	0.162	0.260	1.605
220	89	309.42	30.15	N	65.8	0.138	0.182	1.319
165	65	244.31	21.70	N	84.8	0.217	0.391	1.470
110	80	023.92	21.19	N	116.4	0.014	0.041	2.929
022	70	307.36	36.04	N	50.9	0.125	0.172	1.376
285	89	215.98	87.21	N	22.7	0.049	0.177	3.612
090	50	090.00	50.00	N	0.5	0.269	0.405	1.505
290	89	003.82	86.42	N	16.1	0.039	0.165	4.231
270	60	300.92	56.06	N	5.7	0.448	0.478	1.067
195	80	121.70	58.46	N	11.8	0.162	0.268	1.654
280	55	228.33	41.53	N	48.8	0.502	0.492	0.980
Faults activated by stress state $KNG-2^2$								
130	65	096.15	60.69	N	16.5	0.516	0.451	0.874
280	52	285.21	51.88	N	4.0	0.227	0.319	1.405
125	60	104.91	58.42	N	7.6	0.593	0.448	0.755
330	50	337.85	49.73	N	3.8	0.212	0.331	1.561
340	60	320.85	58.57	N	14.0	0.112	0.222	1.982
350	70	025.32	65.96	N	4.3	0.049	0.102	2.082
042	50	007.81	44.59	N	0.6	0.369	0.482	1.306
180	80	237.44	71.86	N	4.5	0.152	0.342	2.250
190	60	249.38	41.41	N	19.9	0.387	0.486	1.256
070	60	034.43	54.63	N	4.8	0.374	0.467	1.249
074	60	073.99	60.00	N	24.2	0.398	0.469	1.178

... continued on next page

F-az	F-Plg	S-az	S-Plg	S	Misfit(β)	σ_n	τ	τ/σ_n
050	70	340.75	44.23	N	18.6	0.137	0.335	2.445
065	01	110.61	00.70	R	27.4	0.916	0.263	0.287
080	84	026.49	79.98	N	17.3	0.135	0.261	1.933
Subset $KNG - LSS^*$ under stress state $KNG - 2^2$								
118	82	039.72	55.33	N	28.7	0.265	0.348	1.313
290	70	006.10	33.42	N	57.6	0.102	0.053	0.520
310	70	349.53	64.74	N	20.0	0.096	0.039	0.406
260	78	331.07	56.76	N	89.5	0.067	0.049	0.731
300	75	310.13	74.77	N	172.8	0.101	0.041	0.406
315	55	300.33	54.10	N	14.1	0.168	0.256	1.524
330	75	244.08	14.86	N	161.8	0.073	0.058	0.795
320	65	022.64	44.58	N	24.1	0.099	0.118	1.192
010	20	029.86	18.90	N	43.4	0.713	0.439	0.616
030	80	317.02	58.93	N	11.3	0.009	0.096	10.667
150	60	205.19	44.68	N	24.1	0.564	0.469	0.831
160	65	160.00	65.00	N	15.2	0.449	0.474	1.056
350	80	035.59	75.86	N	126.5	0.043	0.089	2.070
170	75	228.14	63.09	N	4.8	0.257	0.414	1.611
150	78	143.39	77.92	N	13.2	0.288	0.399	1.385
245	85	329.75	46.30	N	149.4	0.040	0.058	1.450
220	89	309.42	30.15	N	76.8	0.007	0.040	5.714
165	65	244.31	21.70	N	49.3	0.429	0.477	1.112
110	80	023.92	21.19	N	58.4	0.276	0.360	1.304
022	70	307.36	36.04	N	38.4	0.052	0.216	4.154
285	89	215.98	87.21	N	163.4	0.154	0.225	1.461
090	50	090.00	50.00	N	23.7	0.637	0.460	0.722
290	89	003.82	86.42	N	173.0	0.163	0.233	1.429
270	60	300.92	56.06	N	11.7	0.158	0.248	1.570
195	80	121.70	58.46	N	49.2	0.097	0.293	3.021
280	55	228.33	41.53	N	42.4	0.196	0.285	1.454

Appendix E

Sandbox figures

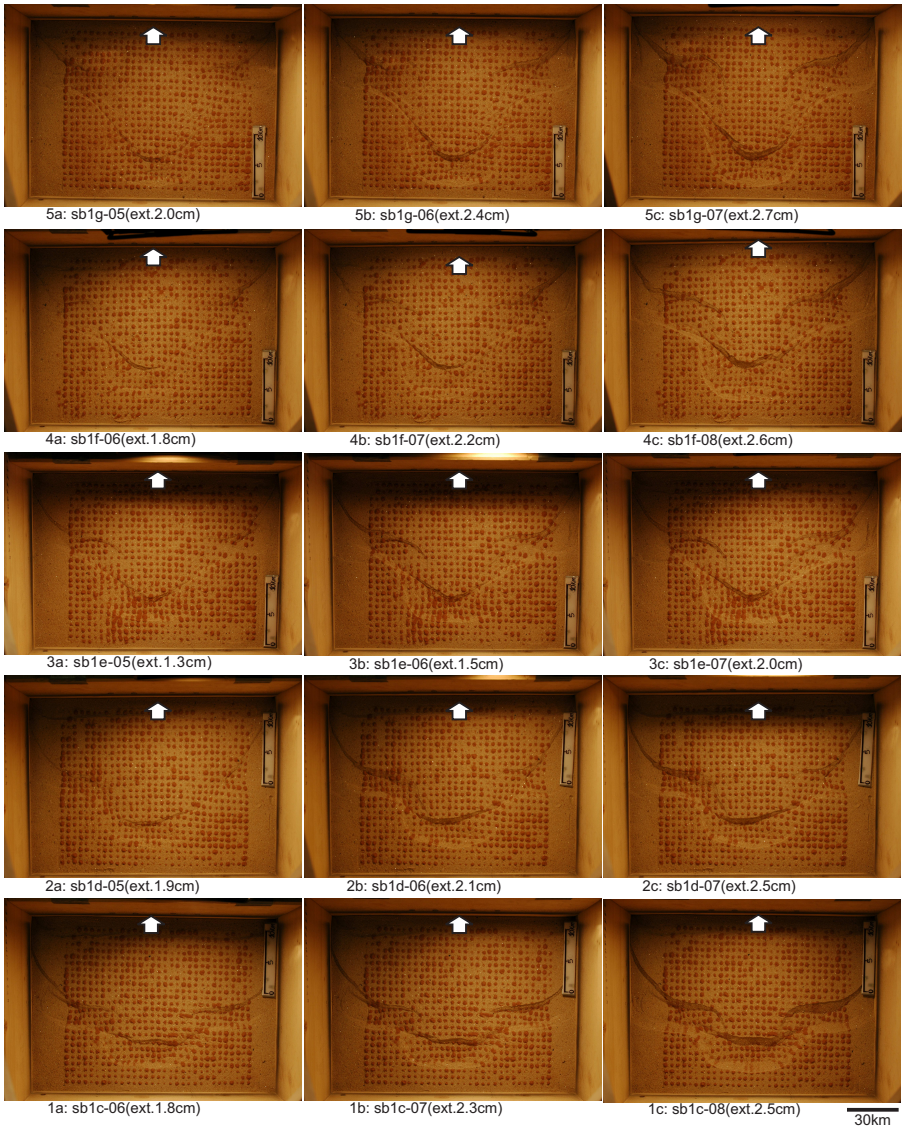

Fig. E.1 Plan-view of rift segments for series A after different amounts of extension indicated below each sub-figure. Respective amounts of lateral offset of peripheral VD segments from the central one were, for experiment (1) 6cm (2) 8cm (3) 10cm (4) 12cm (5) 15cm. Arrows indicate extension vector.

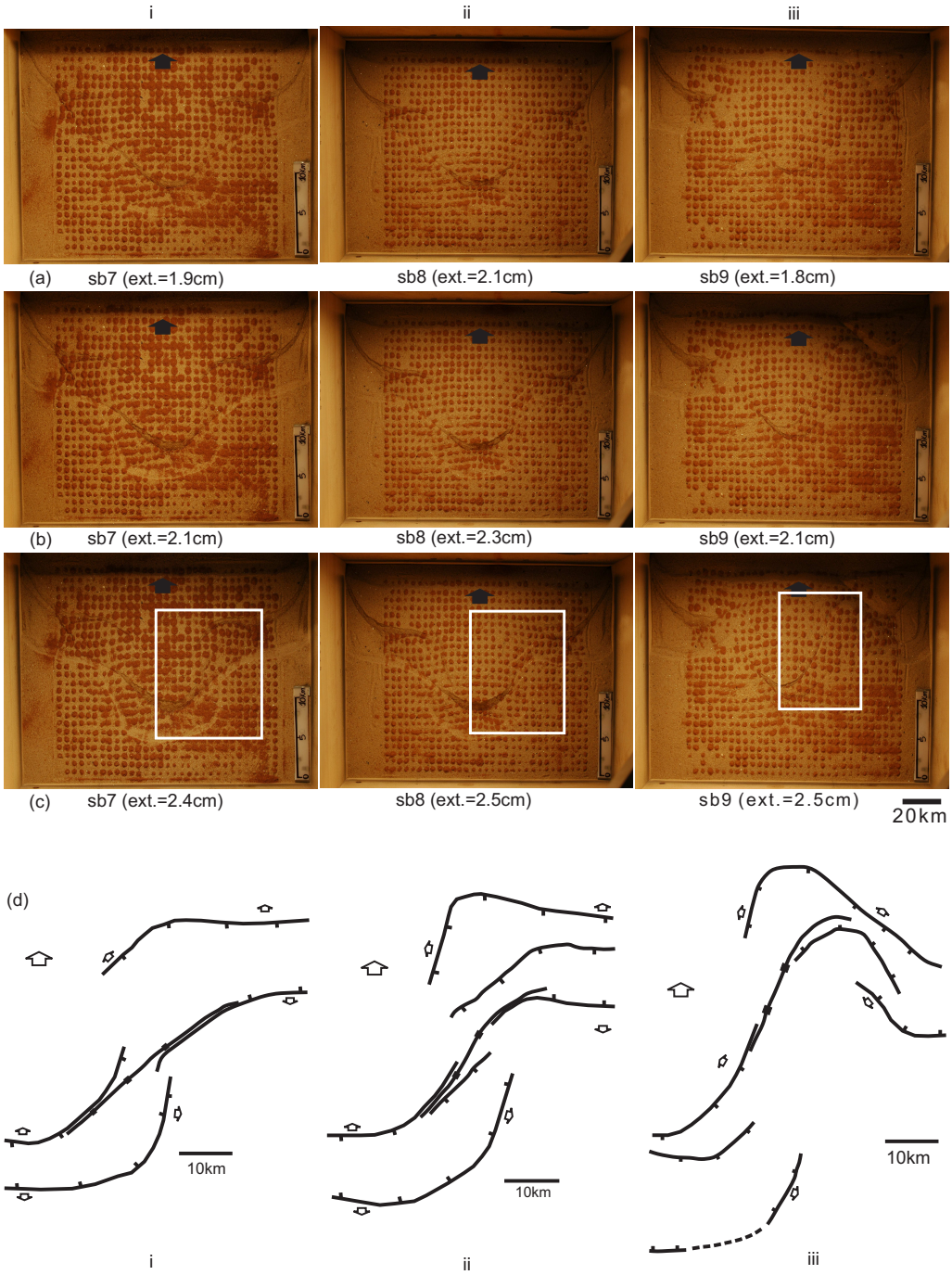

Fig. E.2 a-c: Plan-view of rift segments for series B at different stages of extension indicated below each sub-figure. Respective amounts of lateral separation ('spacing') of peripheral VD segments from the central one were: (i) sandbox sb7: 11cm-wide basal-sheet segments separated from each other by a spacing of 2.5cm (ii) sandbox sb8: two peripheral sheets each 9cm-wide and a middle sheet 11cm-wide, separated from each other by a spacing of 4.0cm (iii) sandbox sb9: 9cm-wide basal-sheet segments separated from each other by a spacing of 6.0cm. Arrows denote extension vector. (d) Comparison of interacting segments in the section indicated by the white rectangle, respectively for experiments (i) sb7 after extension of 2.4cm (ii) sb8 after extension of 2.5cm (iii) sb9 after extension of 2.5cm. Large arrow denotes general extension vector; small arrows indicate local extension direction.

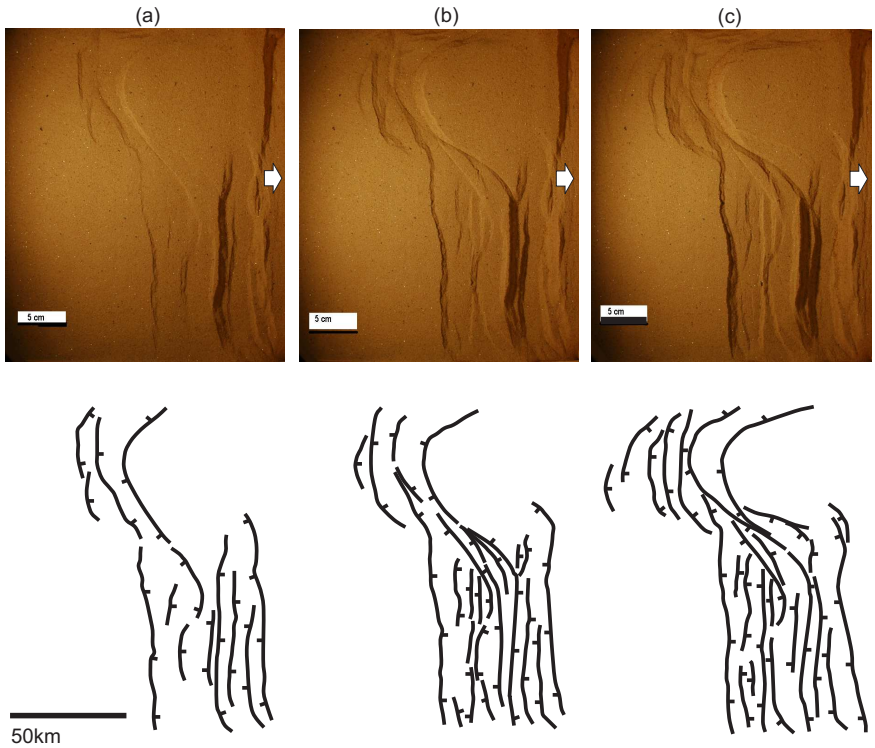

Fig. E.3 Model SbR3. top: Progressive plan-view of developing rift segments after extension by (a) 8.57km, (b) 10.00km and (c) 11.43km. Arrows indicate imposed extension vector. bottom: trace of fault segments.

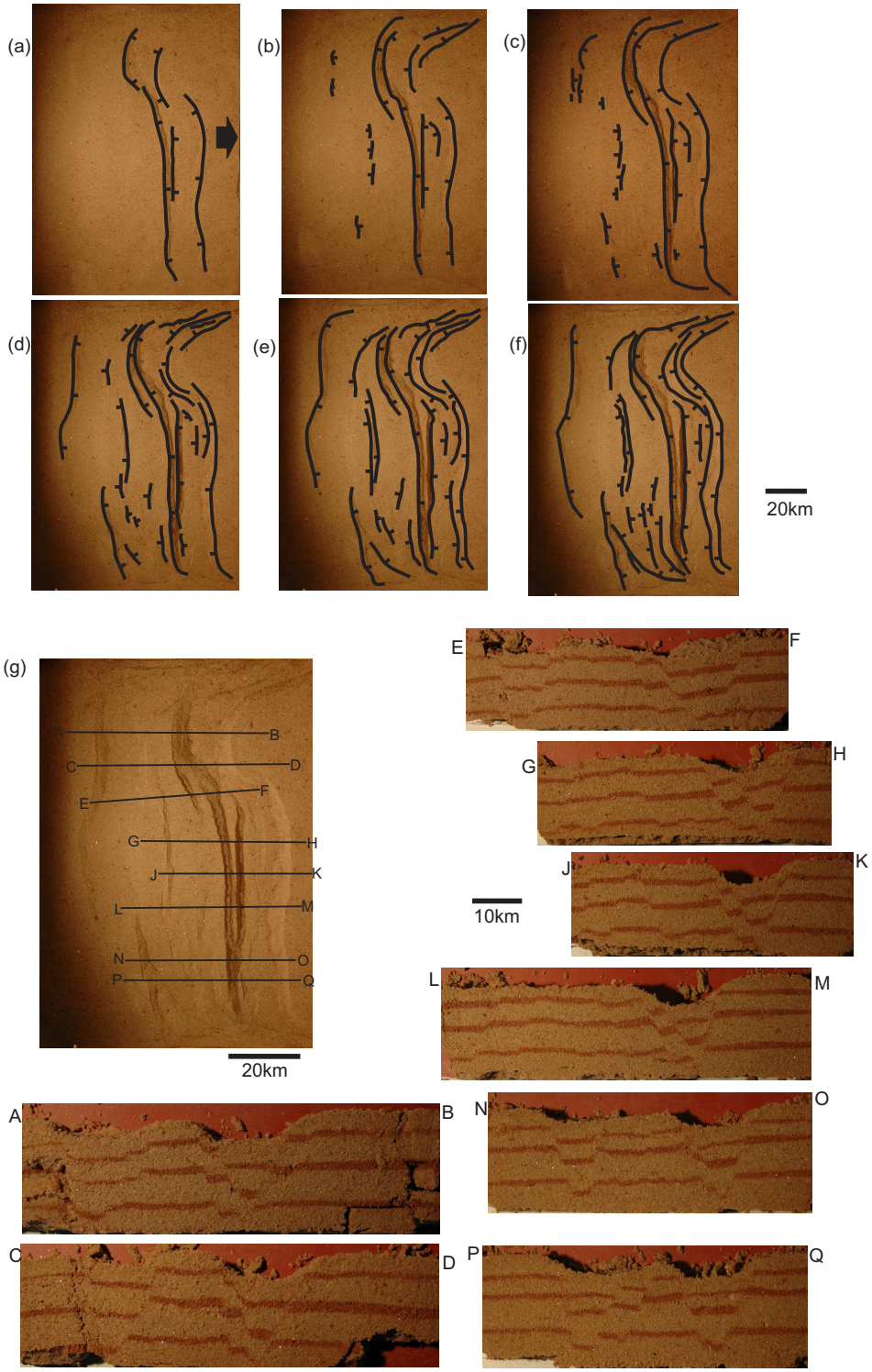

Fig. E.4 Model SbR4-a: a-f=Progressive plan-view of developing fault segments through extension of (a) 8.93km, (b) 10.35km, (c) 11.43km, (d) 12.86km, (e) 13.93km and (f) 14.64km. Black arrow in a indicates general extension vector. (g) Cross-sectional view of faults after $\sim 14.64km$ extension.

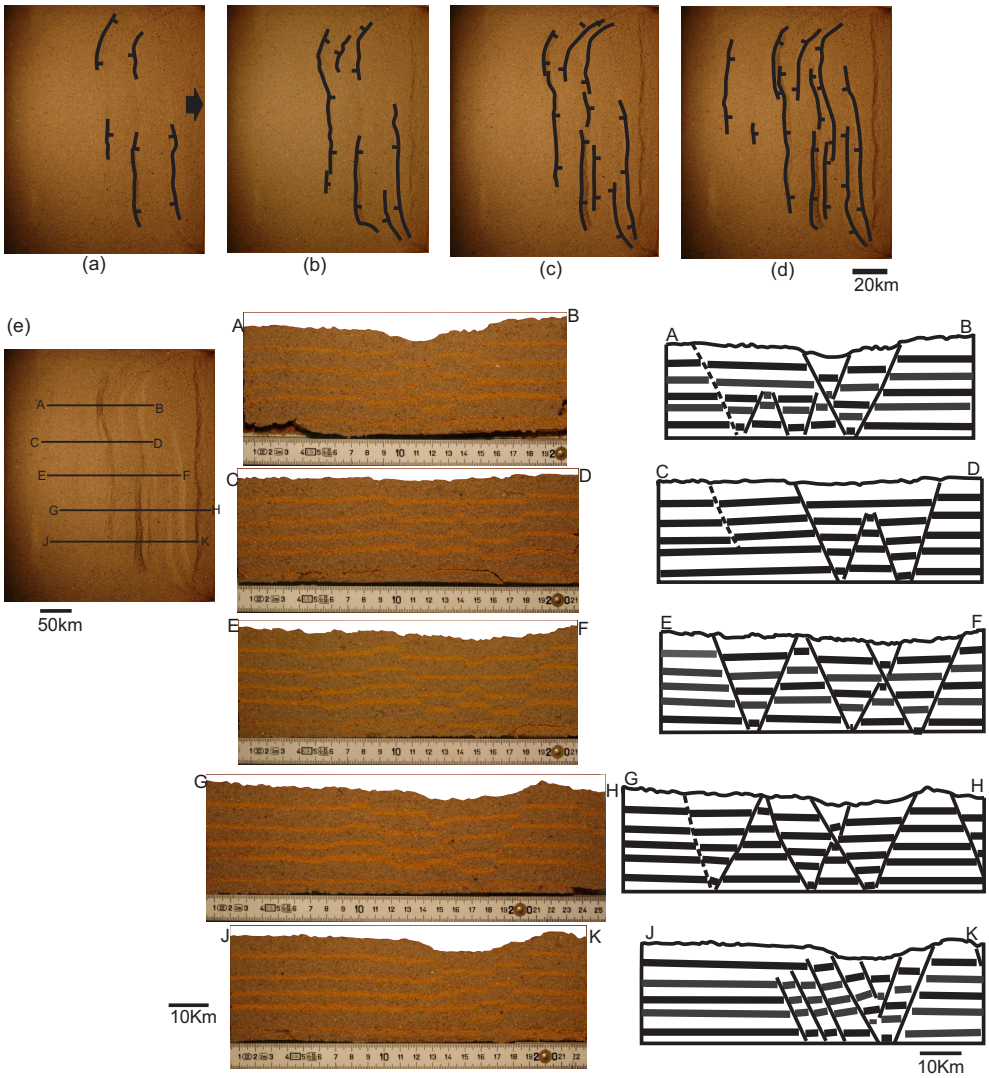

Fig. E.5 SbR4-b: Progressive plan-view of developing fault segments through extension of (a) 5.36km (b) 6.43km (c) 7.14km and (d) 7.86km. (e) Cross-sectional view of faults after 7.86km extension; left: photographs of model, right: faults traced in redrawn section.

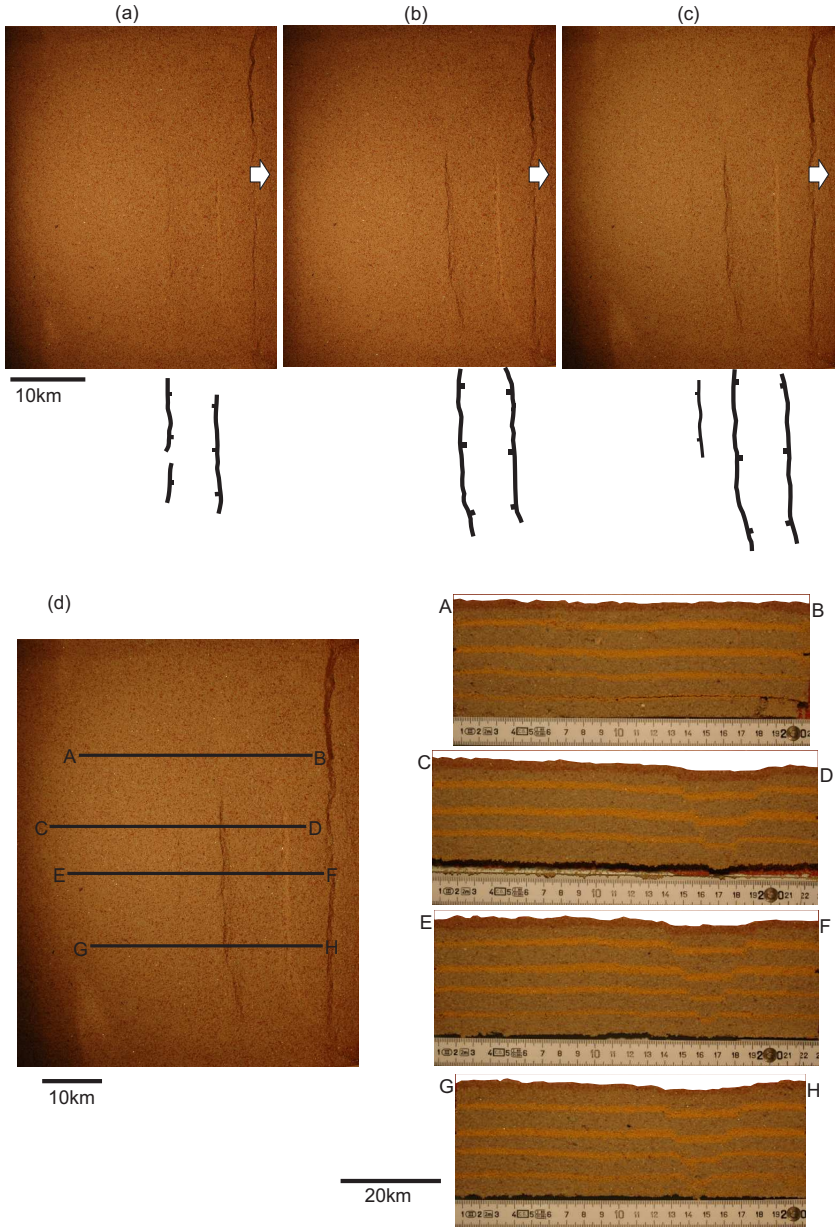

Fig. E.6 SbR4-c: a-c=top: Plan-view of developing fault segments through extension of (a) 3.57km (b) 5.00km and (c) 5.71km. Arrow indicates general extension vector. bottom: Traced rifts. (d) Cross-sectional view of faults after 5.71km extension. Corresponding distances for respective sections measured from the far end of the wall were: A-B=11.0cm; C-D=17.5cm; E-F=22.0cm; and G-H=29.5cm.

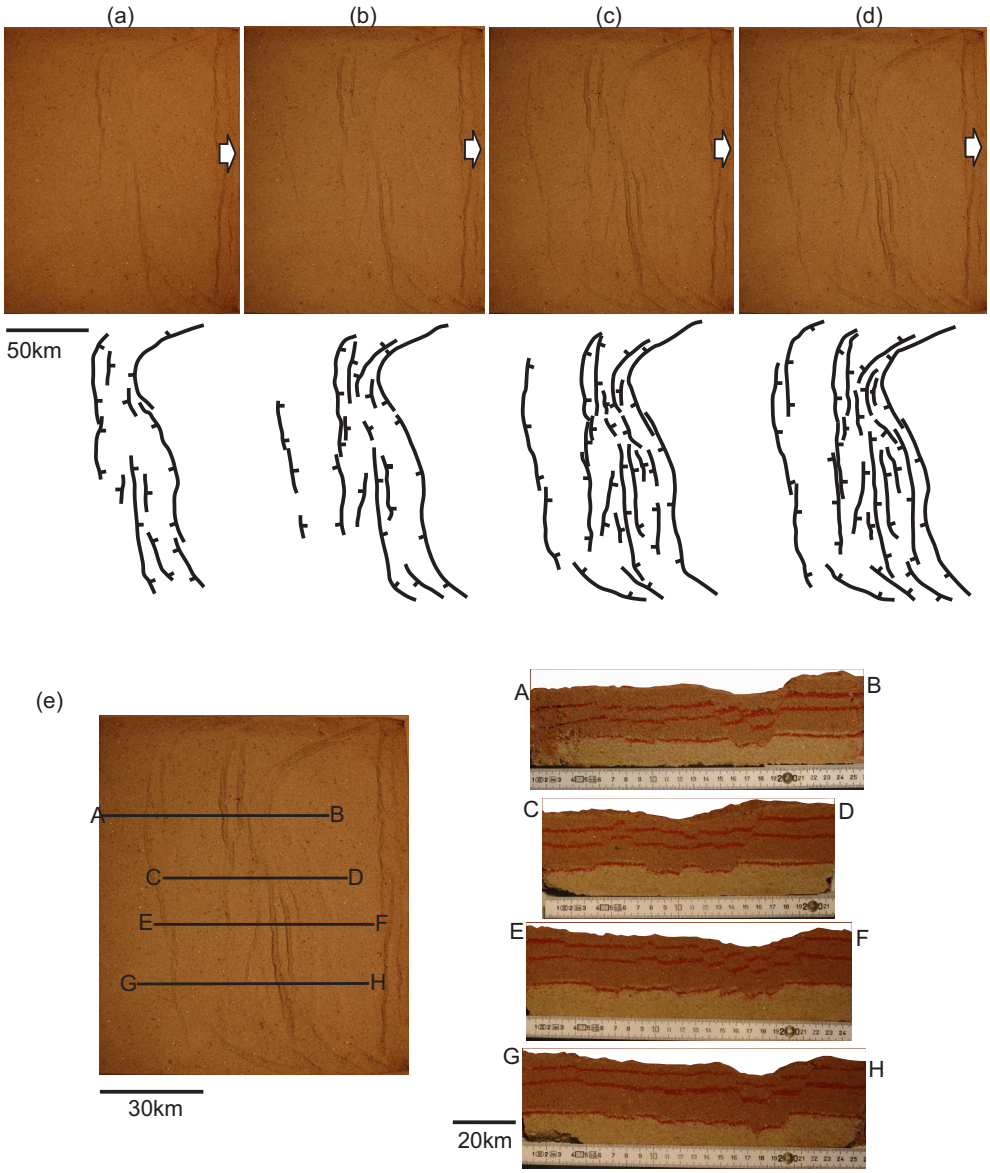

Fig. E.7 Model SbR5-a: [a-d] top: Plan-view of developing rift segments through extension of (a) 6.43km (b) 8.57km (c) 9.64km (d) 10.71km. Arrows indicate general extension direction. bottom: trace of fault segments above. (e) Cross-sectional view of faults after 10.71km extension. Corresponding distances for respective sections measured from the far end of the wall were: A-B=11.0cm; C-D=18.0cm; E-F=23.0cm; and G-H=30.0cm.

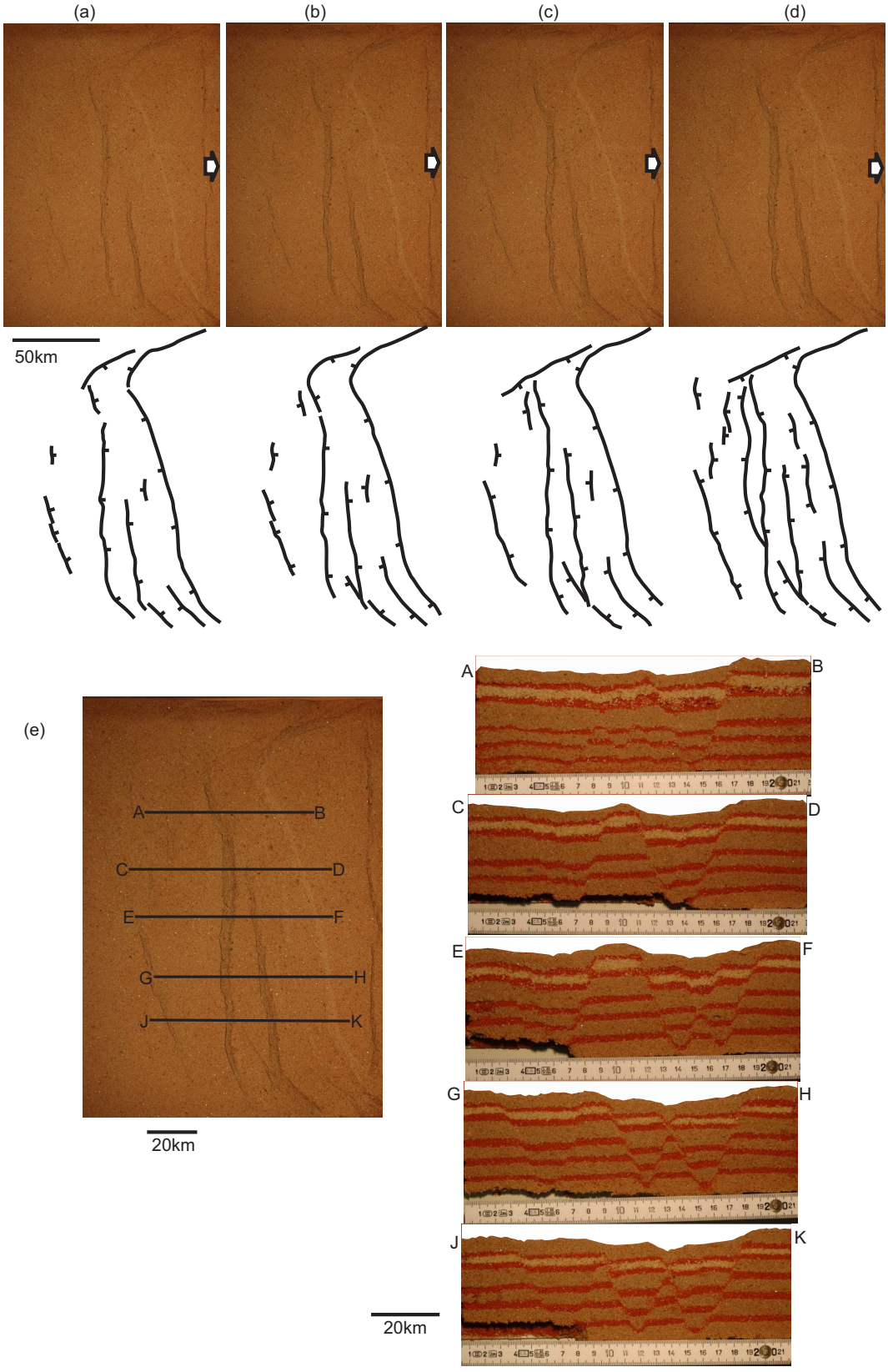

Fig. E.8 Model SbR5-b: a-d=top: Plan-view of developing rifts through extension of (a) 6.79km (b) 7.50km (c) 8.21km and (d) 8.93km. bottom: traced fault segments. (e) Cross-sectional view of faults after 8.93km extension. Corresponding distances for respective sections measured from the far end of the wall were: A-B=11.2cm; C-D=16.5cm; E-F=21.0cm; G-H=26.8cm and J-K=31.0cm. Arrows indicate general extension direction.

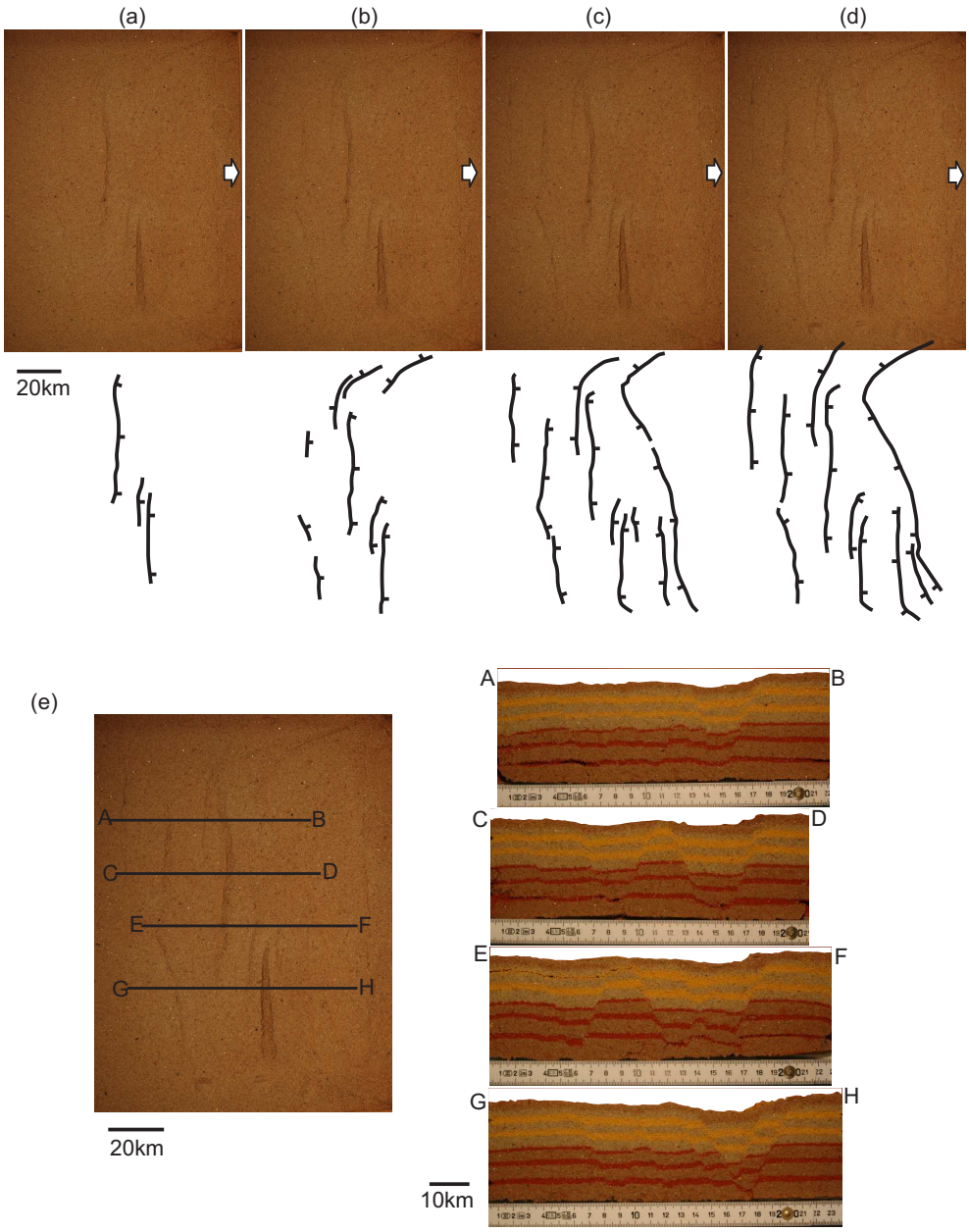

Fig. E.9 Model SbR5-c: a-d=top: Plan-view of developing fault segments through extension of (a) 3.93km (b) 4.64km (c) 5.36km (d) 5.71km. Arrows indicate general extension direction. bottom: trace of fault segments above. (e) Cross-sectional view of faults after 5.71km extension. Corresponding distances for respective sections measured from the far end of the wall were: A-B=10.3cm; C-D=15.5cm; E-F=20.8cm; and G-H=26.7cm.

Bibliography

Aanyu, K. and Koehn, D. (2011), 'Influence of pre-existing fabrics on fault kinematics and rift geometry of interacting segments: Analogue models based on the albertine rift (Uganda), Western Branch-East African Rift System', *Journal of African Earth Sciences* **59**, 168–184. DOI:10.1016/j.jafrearsci.2010.10.003.

Acocella, V. and Korme, T. (2002), 'Holocene extension direction along the Main Ethiopian Rift, East Africa.', *Tera Nova* **14**, 191–197. DOI:10.1046/j.1365-3121.2002.00403.x.

Allen, P. and Allen, J. (1990), *Basin Analysis: Principles and Applications*, Blackwell Science.

Anderson, E. (1951), *The Dynamics of Faulting*, Second edn, Oliver and Boyd, Edinburgh.

Angelier, J. (1979), 'Determination of the mean principle directions of stresses for a given fault population', *Tectonophysics* **56 (3-4)**, T17–T26.

Angelier, J. and Mechler, P. (1977), 'Sur une méthode graphique de recherche des constraintes principales également utilisable en tectonique et en sésmologie: la méthode des diédres droits', *Bulletin de la sociéte Géologique de France* **19 (6)**, 1309–1318.

Angelier, J., Tarantola, A., Valette, B. and Manoussis, S. (1982), 'Inversion of field data in fault tectonics to obtain the regional stress-1. single phase fault populations: a new method of computing the stress tensor', *Geophysical Journal of Research Astr. Soc.* **69**, 607–621.

Aydin, A. (1997), Faulting in Sandstone, Utah, PhD thesis, Stanford, California.

Baker, B. and Wohlenberg, G. (1971), 'Structure and evolution of the Kenya rift valley', *Nature* **229**, 538–542.

Baker, G. (1986), Tectonics and volcanism of the southern Kenya rift valley and its influence on rift sedimentation, *in* 'Sedimentation in the East African Rifts', Vol. 25, Geological Society of London Special Publication, pp. 45–57.

Bassi, G., Keen, C. and Potter, P. (1993), 'Contrasting styles of rifting: Models and examples from the eastern canadian margin', *Tectonics* **12**, 639–655.

Bauer, F., Glasmacher, U., Ring, U., Schumann, A. and Nagudi, B. (2010), 'Thermal and exhumation history of the central Rwenzori Mountains, Western Rift of the East African Rift System, Uganda', *International Journal of Earth Sciences* **99 (7)**, 1575–1597.

Bellieni, G., Justin-Vicentin, E., Zanettin, B., Piccirrillo, E., Radicati, C., Brozolo, F. and Rita, F. (1981), 'Oligocene transitional tholeiitic magmatism in northern Turkana (Kenya): comparison with the coeval Ethiopian volcanism', *Bulletin of Volcanology* **44(3)**, 411–427.

Bellon, H. and Pouclet, A. (1980), 'Datations K-Ar de quelques laves du Rift-Ouest de l'Afrique Centrale; implications sur l'evolution magmatique et structurale', *Geologische Rundschau* **69(1)**, 49–62.

Bingham, C. (1964), Distributions on a sphere and the projective plane., PhD thesis, Yale University, New Haven. 93pp.

Bosworth, W. and Strecker, M. (1997), 'Stress-field changes in the Afro-Arabian rift system during during the Miocene to Recent period', *Tectonophysics* **278**, 47–62.

Bosworth, W., Strecker, M. and Bliniuk, P. (1992), 'Integration of East African paleostress and present-day stress data: implications for continental stress field dynamics', *Journal of Geophysical Research* **97 (B8)**, 11851–11865.

Brandl, G. (1986), 'The Palala shear belt and its relationship to the development of the Southpansberg graben', *Geocongress* **86**, 751–753.

Braun, J. and Beaumont, C. (1987), Styles of continental rifitng: results from dynamic models of lithospheric extension, *in* C. Beaumont and A. Tankard, eds, 'Sedimentary basins and basin forming mechanisms', Vol. 12, Can. Soc. Pet. Mem., pp. 241–258.

Brun, J.-P. (1999), Narrow rifts versus wide rifts: inferences for the mechanics of rifting from laboratory experiments, *in* 'Philosophical Transactions of the Royal Society of London', Vol. 357, Royal Society of London, pp. 695–712.

Brun, J.-P., Sokoutis, D. and Van Den Driessche, J. (1994), 'Analogue modeling of detachmemnt fault systems and core complexes.', *Geology* **22**, 319–322.

Buck, W. (1991), 'Modes of continental lithospheric extension', *Journal of Geophysical Research* **96**, 20161–20178.

Buck, W., Martinez, F., Steckler, M. and Cochran, J. (1988), 'Thermal consequences of lithospheric extension: pure and simple', *Tectonicd* **7**, 213–234.

Burg, J.-P., Sokoutis, D. and Bonini, M. (2002), 'Model-inspired interpretation of seismic structures in the central alps: Crustal wedging and buckling at mature stage of collision', *Geology* **30**, 643–646.

Byerlee, J. (1968), 'Brittle-ductile transition in rocks', *Journal of Geophysical Research* **74 (B14)**, 4741–4750.

Calais, E., Ebinger, C., Hartnady, C. and Nocquet, J. (2006), Kinematics of the east african rift from gps and earthquake slip vector data, *in* G. Yirgu, C. Ebinger and P. Maguire, eds, 'The Afar volcanic province within the East African Rift System', Vol. 259, Geol. Soc. Spec. Publ., pp. 9–22.

Chemenda, A., Burg, J.-P. and Mattauer, M. (2000), 'Evolutionary model of the himalaya-tibet system: geopoem based on new modelling, geological and geophysical data', *Earth and Planetary Science Letters* **174**, 397–409.

Chemenda, A., Mattauer, M. and Bokun, A. (1996), 'Continental subduction and a mechanism for exhumation of high-pressure metamorphic rocks: new modelling and field data from oman', *Earth and Planetary Science Letters* **143**, 173–182.

Chemenda, A., Mattauer, M., Malavieille, J. and Bokun, A. (1995), 'A mechanism for syn-collisional rock exhumation and associated normal faulting: results from physical modelling', *Earth and Planetary Science Letters* **132**, 225–232.

Chorowicz, J. (1989), 'Transfer and transform fault zones: examples in the Afro-Arabian Rift System. implications of crustal breaking', *Journal of African Earth Sciences* **8**, 203–214.

Chorowicz, J. (1992), 'The role of ancient structure in the genesis and evolution of the East African rift', *Bulletin Société geologique de France* **163(3)**, 217–227.

Chorowicz, J. (2005), 'The East African rift system', *Journal of African Earth Sciences* **43**, 379–410.

Chorowicz, J., Collet, B., Bonavia, F., Mohr, P., Parrot, J.-F. and Korme, T. (1998), 'The Tana Basin, Ethiopia: intra-plateau uplift, rifting and subsidence', *Tectonophysics* **295**, 351–367.

Chorowicz, J., Le Fournier, J. and Vidal, G. (1987), A model for rift development in Eastern Africa, *in* P. Bowden and J. Kinnaird, eds, 'African Geology Reviews', Vol. 22, Geological Journal, pp. 495–513.

Clifton, A. and Schlische, R. (2001), 'Nucleation, growth and linkage of faults in oblique rift zones: results from experimental clay models and implications for maximum fault size', *Geology* **29**, 455–458.

Cloetingh, S., Sassi, W. and Horváth, F. E. (1993), *The origin of sedimentary basins: Inferences from quantitative modelling and basin analysis*, Vol. 226, Tectonophysics.

Cloetingh, S., van Vees, J., van der Beek, P. and Spadini, G. (1995), 'Role of pre-rift rheology in kinematics of extesniona; basin formation: constraints from thermomechanical models of mediterranean and intracratonic basins', *Mar. Pet. Geol.* **12**, 793–807.

Cobbold, P. R. and Castro, L. (1999), 'Fluid pressure and effective stress in sandbox models.', *Tectonophysics* **301**, 1–19. DOI:10.1016/S0040-1951(98)00215-7.

Coblentz, D. and Randall, M. (1994), 'On the gravitational potential energy of the Earth's lithosphere', *Tectonics* **13 (4)**, 929–945.

Coblentz, D. and Sandiford, M. (1994), 'Tectonic stresses in the African plate: Constraints on the ambient lithospheric stress state', *Geology* **22**, 831–834.

Cohen, A., Soreghan, M. and Schotz, C. (1993), 'Estimating the age of formation of lakes: an example from Lake Tanganyika, East African Rift', *Geology* **21**, 511–514.

Corti, G. (2004), 'Centrifuge modeling of the influence of crustal fabrics on the development of transfer zones: insights into the mechanics of continental rifting architecture', *Tectonophysics* **384**, 191–208.

Corti, G. (2008*a*), Constant Nubia-Somalia kinematics controls a polyphase volcano-tectonic evolution of the Main Ethiopian Rift, *in* R. G., ed., 'RiftLink Workshop 2008 Presentations and Abstracts, Neustadt/Weinstr.24-28 June 2008', RiftLink Research, pp. 16–17.

Corti, G. (2008*b*), 'Control of rift obliquity on the evolution and segmentation of the Main Ethiopian Rift', *Nature Geoscience* **1 (4)**, 258–262.

Daly, M., Chorowicz, J. and Fairhead, D. (1989), Rift basin evolution in Africa: The influence of reactivated steep basement shear zones., *in* M. Cooper and G. Williams, eds, 'Inversion Tectonics,', Vol. 44, Geological Society London, Special Publications, pp. 309–334.

Davy, P. and Cobbold, P. (1988), 'Indentation tectonics in nature and experiment. 1. experiments scaled for gravity', *Bulletin of the Geological Institutions of the University of Uppsala, New Series* **14**, 129–141.

Davy, P. and Cobbold, P. (1991), 'Experiments on shortening of a 4-layer model of the continental lithosphere', *Tectonophysics* **188**, 1–25.

Delvaux, D. and Barth, A. (2010), 'African stress pattern from formal inversion of focal mechanism data', *Tectonophysics* **482**, 105–128. doi: 10.1016/j.tecto.2009.05.

Dupin, J.-M., Sassi, W. and Angelier, J. (1993), 'Homogeneous stress hypothesis and actual fault slip: A distinct element analysis', *Journal of Structural Geology* **15 (8)**, 1033–1043.

Ebinger, C. (1989*a*), 'Geometric and kinematic development of border faults and accommodation zones, Kivu-Rusizi Rift, Africa', *Tectonics* **8(1)**, 117–133.

Ebinger, C. (1989*b*), 'Tectonic development of the western arm of the East African Rift System', *Geological Society of America Bulletin* **101**, 885–903.

Ebinger, C., Deino, A., Tesha, A., Becker, T. and Ring, U. (1993a), 'Regional control of rift basin morphology: evolution of the Northern Malawi (Nyassa) Rift', *Journal of Geophysical Research* **98(17)**, 821–836.

Elder, J. (1966), 'Penetrative convection: its role in volcanism', *Volcanolgy Bulletin* **29**, 327.

Etchecopar, A., Vasseur, G. and Daignieres, M. (1981), 'An inverse problem in microtectonics for the determination of stress tensors from fault striation analysis', *Journal of Structural Geology* **3**, 51–65.

Faccenna, C., Funiciello, F., Giardini, D. and Lucente, P. (2001), 'Episodic back-arc extension during restricted mantle convection in the central mediterranean', *Earth and Planetary Science Letters* **187**, 105–116.

Fernàndes, M. and Ranalli, G. (1997), 'The role of rheology in xetensional basin formation modelling', *Tectonophysics* **282**, 129–145.

Fisher, R. (1953), Dispersion on a sphere, *in* 'Proceedings of the Royal Society of London', A 217, pp. 295–305.

Fitch, F., Hooker, P., Miller, J., Mitchell, J. and Watkins, R. (1985), 'Reconnaissance Potassium-Argon gochronology of the Suregai-Asille district, northern Kenya', *Geological Magazine* **122**, 609–622.

Flannery, J. and Rosendahl, B. (1990), 'The seismic stratigraphy of Lake Malawi, Africa: implications for interpreting geological processes in lacustrine rifts', *Journal of African Earth Sciences* **10(3)**, 519–548.

Fleuty, M. (1974), 'Slickensides and slickenlines', *Geological Magazine* **112**, 319–322.

Fossen, H. (2010), *Structural Geology*, Cambridge University Press, New York.

Frostick, L. (2005), AfricaRift Valley, *in* 'Encyclopedia of Geology', Elsevier Ltd, chapter AFRICA, pp. 26–34.

Funiciello, F., Faccenna, C., Giardini, D. and Lucente, P. (2000), 'Episodic back-arc extension during restricted mantle convection in the central mediterranean', *Eos, Transactions, American Geophysical Union* **81 (48)**, 1081–1082.

Guatteri, M. and Spudich, R. (1998), 'Coseismic temporal changes of slip direction: the effect of absolute stress on dynamic rupture', *Bulletin of Seismological Society of America* **88**, 777–789.

Gummert, M. (2009), 'Herdflaechen- und magnituden-bestimmung fuer Erdbeben im OstAfrikanischen rift (Rwenzori Gebirge)', Bachelor thesis; 92pp. Johann Wolfgang Goethe Universitaet, Frankfurt am Main.

Harris, R. (1969), 'Basalt type and African rift valley tectonism', *Tectonophsics* **8 (4-6)**, 567–577.

Hayward, N. and Ebinger, C. (1996), 'Variations in the long-axis segmentation of the Afar Rift system', *Tectonics* **15(2)**, 244–257.

Heidbach, O., Tingay, M., Barth, A., Reinecker, J., Kurfeß, D. and Mueller, B. (2008), 'The World Stress Map database release 2008'.

Heidbach, O., Tingay, M., Barth, A., Reinecker, J., Kurfeß, D. and Müller, B. (2010), 'Global crustal stress pattern base on the World Stress Map database release 2008', *Tectonophysics* **482**, 3–15. doi:10.1016/j.tecto.2009.07.023.

Hendrie, D., Kusznir, N., C.K., M. and Ebinger (1994), 'Cenozoic extension in northern Kenya: a quantitative model of rift basin development in the Turkana region', *Tectonophysics* **236**, 409–438.

Hepworth, J. and MacDonald, R. (1966), 'Orogenic belts of the northern Uganda basement', *Nature* **210**, 726–727.

Hoeppener, R. (1955), 'Tektonik im Schiefergebirge: eine Einfuehrung', *Geologische Rundschau, Stuttgart* **44**, 26–58.

Hoffman, C., Courtillot, G., Feraud, G., Rochette, P., Yirgu, G., Ketefo, E. and Pik, R. (1997), 'Timing of the Ethiopian flood basalt event: implications for plume birth and global change', *Nature* **389**, 838–841.

Hubbert, M. (1937), 'Theory of scale models as applied to the study of geologic structures', *Geological Society of America Bulletin* **48**, 1459–1520.

Hughes, G., Varol, O. and Beydoun, Z. (1991), 'Evidence for Middle Oligocene rifting of the Gulf of Aden and for Late Oligocene rifting of the southern Red Sea', *Marine and Petroleum Geology* **8**, 354–358.

Huyghe, P. and Mugnier, J.-L. (1992), 'The influence of depth on reactivation on normal faulting', *Journal of Structural Geology* **14**, 991–998.

Illies, J. and Greiner, G. (1978), 'The Rhinegraben and the Alpine system', *Geological Society of American Bulletin* **89**, 770–782.

Ivins, E., Dixon, T. and Golombek, M. (1990), 'Extensional reactivation of an abandoned thrust: a bound on shallowing in the brittle regime', *Journal of Structural Geology* **12**, 303–314.

Jaeger, J. and Cook, N. (1979), *Fundamentals of Rock Mechanics*, Chapman and Hall.

Jaeger, J., Cook, N. and Zimmerman, R. (2007), *Fundamentals of Rock Mechanics*, Fourth edn, Blackwell Publishing.

Jakovlev, A., Lindenfeld, M., Woelbern, A., Schumann, A., Batte, A., Koulakov, I. and Ruempker, G. (2008), Mantle plumes, earthquakes and rifting: Seismological constraints on the structure of the crust and mantle in the Rwenzori region. in rümpker g. (ed.). RiftLink Workshop 2008, Neustadt. Presentations and Abstracts, 29–32.

Johnson, R. and McConnell, R. (1951), 'Notes on the geology of the northern part of the Rwenzori Mountains', *Geology Magazine* **88 (4)**, 249–256.

Kampunzu, A., Bonhomme, M. and Kanika, M. (1998), 'Geochronolgy of volcanic rocks and evolution of the Cenozoic Western Branch of the East African Rift System', *Journal of African Earth Sciences* **26(3)**, 441–461.

Kampunzu, A. and Mohr, P. (1991), Magmatic evolution and petrogenesis in the East African Rift System, *in* A. Kampunzu and R. Lubala, eds, 'Magmatism in Extensional Structural Settings', Springer-Verlag, Berlin, pp. 85–136.

Karner, G., Byamungu, B., Ebinger, C., A.B., K., Mukasa, R., Nyakaana, J., Rubondo, E. and Upcott, N. (2000), 'Distribution of crustal extension and regional basin architecture of the Albertine Rift System, East Africa.', *Marine and Petroleum Geology* **17**, 1131–1150.

Kebede, F. and Kulhanek, O. (1992), 'Recent seismicity of the East African Rift system and its implications', *Tectonophysics* **209**, 51–54.

Keen, C. (1985), 'The dynamics of rifting: Deformation of the lithosphere by active and passive driving forces', *Philosophical Transactions of the Royal Society of London* **80**, 95–120.

Keen, C., Boutilier, R., de Voogd, Mudford, B. and Enachescu, M. (1987), Coastal geometry and extensional models for the grand banks, eastern canada: Constraints from deep seismic reflection data, *in* C. Beaumont and A. Tankard, eds, 'Sedimentary basins and basin forming mechanisms', Vol. 12, Can. Soc. Pet. Geol. Mem., pp. 101–115.

Klerkx, J., Liégeois, J.-P., Lavreau, J. and Claessens, W. (1987), Crustal evolution of the northern Kibaran belt, eastern and central Africa, *in* A. Kroener, ed., 'Proterozoic Lithospheric Evolution', Vol. 17, American Geophysical Union and the Geological Society of America, pp. 217–233.

Koehn, D., Aanyu, K., Haines, S. and Sachau, T. (2008), 'Rift nucleation, rift propagation and the creation of basement micro-plates within active rifts', *Tectonophysics* **458**, 105–116.

Koehn, D., Lindenfeld, M., Ruempker, G., Aanyu, K., Haines, S., Passchier, C. W. and Sachau, T. (2010), 'Active transsection faults in rift transfer zones: evidence for complex stress fields and implications for crustal fragmentation processes in the western branch of the East African Rift', *International Journal of Earth Sciences* **99 (7)**, 1633–1642. doi: 10.1007/s00531-010-0525-2.

Krantz, R. W. (1991), 'Measurements of friction coefficients and cohesion for faulting and fault reactivation in laboratory models using sand and sand mixtures.', *Tectonophysics* **188 (1-2)**, 203–207. DOI:10.1016/0040-1951(91)90323-K.

Kusznir, N., Karner, G. and Egan, S. (1987), Geometric, thermal and isostatic consquences of detachments in continental lithosphere extension and basin formation., *in* C. Beaumont and A. Tankard, eds, 'Sedimentary basins and basin forming mechanisms', Vol. 12, Can. Soc. Pet. Mem., pp. 185–203.

Kusznir, N. and Park, R. (1987), The extensional strength of continental lithosphere: its dependence of geothermal gradient, and crustal composition and thickness, *in* M. Coward, J. Dewey and P. Hancock, eds, 'Continental extension tectonics', Vol. 28, Gelogical Society Special Publication., pp. 35–52.

Kusznir, N. and Ziegler, P. (1992), 'The mechanics of continental extension and sedimentary basin formation: A simple-shear/pure-shear flexural cantilevermodel', *Tectonophysics* **215**, 117–131.

Le Bas, M. (1971), 'Per-alkaline volcanism, crustal swelling and rifting', *Nature Phys. Sci., London* **229**, 3027–3031.

Leggo, P. (1974), 'A geochronological study of the basement complex of Uganda', *Journal of Geological Society London* **130**, 263–277.

Lenoir, J., Liégeois, J., Theunissen, K. and Klerkx, J. (1994), 'The Paleoproterozoic Ubendian shear belt in Tanzania: geochronology and structure', *American Association of Petroleum Geologists Bulletin* **19**, 169–184.

Link, K., Koehn, D., Barth, M., Tiberindwa, J., Barifaijo, E., Aanyu, K. and Foley, S. (2010), 'Continuous cratonic crust between the Congo and Tanzania blocks in western Uganda', *International Journal of Earth sciences* **99 (7)**, 1559–1573. doi: 10.1007/s00531-010-0548-8.

Maerten, L. (2000), 'Variation in slip on intersecting normal faults:Implications for paleostress inversion', *Journal of Geophysical Research* **105 (B11)**, 25,553–25,565. doi:10.1029/2000JB900264.

Malone, S., Rothe, G. and Smith, H. (1975), 'Details of micro-earthquake swarms in the Columbia basin, Washington', *Seismological Society of America Bulletin* **65**, 855–864.

Marshak, S. and Mitra, S. (1988), *Basic Methods of Structural Geology*, Prentice-Hall, Eaglewood-Cliffs, New Jersey.

McClay, K., Doodley, T., Whitehouse, P. and Mills, M. (2002), '4-D evolution of rift systems: insights from scaled physical models', *American Association of Petroleum Geologists Bulletin* **86**, 935–959.

McConnell, R. (1972), 'Geological development of the rift system of eastern Africa', *Geological Society of America Bulletin* **83**, 2549–2572.

McConnell, R. B. (1959), 'Outline of the geology of the Rwenzori Mountains: A preliminary account of the results of the british rwenzori expedition 1951-52', *Overseas Geology and Mineral Resources Quarterly Bulletin* **7 (3)**, 245–268.

Mckenzie, D. (1978), 'Some remarks on the development of sedimentary basins', *Earth and Planetary Science Letters* **40**, 25–32.

McKenzie, D. and Bickle, M. (1988), 'The volume and composition of melt generated by extension of the lithosphere', *Journal of Petroleum* **21**, 625–679.

Mège, D. and Korme, T. (2004), 'Dyke swarm emplacement in the Ethiopian large igneous province: not only a matter of stress', *Journal of Volcanology and Geothermal Research* **132**, 283–310.

Michon, L. and Sokoutis, D. (2005), 'Interaction between structural inheritance and extension direction during graben and depocentre formation: an experimental approach', *Tectonophysics* **409**, 125–146.

Mondeguer, A., Ravenne, C., Masse, P. and Tiercelin, J. (1989), 'Sedimentary basins in an extension and strike-slip background: the South Tanganyika troughs complex, East African Rift', *Bulletin Société geologique de France* **3**, 501–522.

Morley, C., Cunningham, S., Harper, R., Wigger, S. and Karanja, F. (1992), 'Geology and geophysics of the Rukwa rift, East Africa', *Tectonics* **11**, 68–81.

Morley, C. K. (1995*a*), *Geoscience of Rift Systems-Evolution of East Africa*, Vol. 44, American Association of Petroleum Geologists studies in Geology.

Morley, C. K. (1995*b*), 'How successful are analogue models in addressing the influence of pre-existing fabrics on rift structures', *Journal of Structural Geology* **21**, 1267–1274.

Morley, C. K., Nelson, R., Patton, T. and Munn, S. (1990), 'Transfer zones in the East African Rift System and their relevance to hydrocarbon exploration in rifts', *American Association of Petroleum Geologists Bulletin* **74(8)**, 1234–1169.

Nagudi, B., Bauer, F., Glasmacher, U., Foerster, A., Foerster, H., Schumann, A. and Kontny, J. (in preparation), 'Petrography and geochemistry of Rwenzori mountains lithologies, East African Rift Systen, Uganda', *in preparation* .

Nagudi, B., Koeberl, C. and Kurat, G. (2003), 'Petrography and geochemistry of the Singo Granite, Uganda, and implications for its origin', *Journal of African Earth Sciences* **36**, 73–87.

Negredo, A., Fernàndez, M. and Zeyen, H. (1995), 'Thermo-mechanical constraints on kinematic models of lithospheric extension', *Earth and Planetary Science Letters* **134**, 87–98.

Nelson, A. S. (2010), 'Types of metamorphism and metamorphic textures and structures', Lecture notes. Department of Earth and Environmental Sciences, Tulane University, New Orleans.

Nelson, R., Patton, T. and Morley, C. (1992), 'Rift segment interaction and its relation to hydrocarbon exploration in continental rift systems', *American Association of Petroleum Geologists Bulletin* **76(8)**, 1153–1169.

Nemcok, M. and Lisle, R. (1995), 'A stress inversion procedure for polyphase fault/slip data sets', *Journal of Structural Geology* **17 (10)**, 1445–1453.

Nieto-Samaniego, A. and Alaniz-Alvarez, S. (1995), 'Influence of the structural framework on the origin of multiple fault patterns', *Journal of Structural Geology* **17**, 1571–1577.

Nieto-Samaniego, A. and Alaniz-Alvarez, S. (1997), 'Origin and tectonic interpretation of multiple fault patterns', *Tectonophysics* **270**, 197–206.

Oertel, G. (1965), 'The mechanism of faulting in clay experiments', *Tectonophysics* **2**, 343–393.

Orife, T. and Lisle, R. (2003), 'Numerical processing of paleostress results', *Journal of Structural Geology* **25**, 949–957.

Ortner, H., Reiter, F. and Acs, P. (2002), 'Easy handling of tectonic data: the programs TectonicVB for Mac and TectonicsFP for WindowsTM', *Computers and Geosciences* **28**, 1193–1200.

Otsubo, M., Sato, K. and Yamaji, A. (2006), 'Computerized identification of stress tensors determined from heterogeneous fault-slip data by combining the multiple inverse method and k-means clustering', *New dynamics in paleostress analysis - Journal of Structural Geology* **28 (6)**, 991–997.

Oxburgh, E. and Turcott, D. (1974), 'Membrane tectonics and the East African Rift', *Earth and Planetory Science Letters* **22**, 133–140.

Pascal, C. (2002), 'Interaction of faults and perturbation of slip: influence of anisotropic stress states in the presence of fault friction and comparison between Wallace-Bott and 3D Distinct Element Models', *Tectonophysics* **356**, 307–322.

Passchier, C. and Trouw, R. (2005), *Microtectonics*, Second edn, Springer.

Pickford, M. (1982), 'The tectonics, volcanics and sediments of the Nyanza rift valley', *Zeitschrift fuer Geomorphologie N.F.* **42**, 1–33.

Pickford, M., Senut, B. and Adoto, D. (1993), 'Geology and Palaeobiology of the Albertine rift valley Uganda-Zaire', *CIFEG Orleans, Occasional Publication: Geology* **1**, 179p.

Pollard, D. and Fletcher, R. (2005), *Fundamentals of Structural Geology*, Cambridge University Press, New York.

Pollard, D., Saltzer, S. and Rubin, A. (1993), 'Stress inversion methods: Are they based on faulty assumptions?', *Journal of Structural Geology* **15 (8)**, 1045–1054.

Price, N. and Cosgrove, J. (1990), *Analysis of Geological Structures*, Cambridge University Press, Great Britain.

Ragan, D. (2009), *Structural Geology: an introduction to geometric techniques*, Fourth edn, Cambridge University Press, New York.

Ramberg, H. (1967*a*), *Gravity, deformation and the earth's crust*, London Academic Press.

Ramberg, H. (1967*b*), 'Model experimentation of the effect of gravity on tectonic processes', *The Geophysical Journal of the Royal Astronomical Society* **14**, 307–329.

Ranalli, G. (2000), 'Rheology of the crust and its role in tectonic reactivation', *Journal of Geodynamics* **30**, 3–15.

Ratschbacher, L., Merle, O., Davy, P. and Cobbold, P. (1991), 'Lateral extrusion in the eastern alps: Part 1, boundary conditions and experiments scaled for gravity', *Tectonics* **10**, 245–256.

Reches, Z. (1987), 'Determination of the tectonic stress tensor from slip along faults that obey the Coulomb yield condition', *Tectonics* **6**, 849–861.

Reicherter, K. and Peters, G. (2005), 'Neotectonic evolution of the Central Betic Cordilleras (southern spain)', *Tectonophysics* **405 (1-4)**, 191–212.

Reiter, F. and Acs, P. (1996–2009), 'TectonicsFP 1.7.01. A computer program for structural geology'.

Ring, U. (2008), 'Extreme uplift of the Rwenzori Mountains in the East African Rift, Uganda: structural framework and possible role of glaciations', *Tectonics* **27(TC4018)**.

Ring, U., Betzler, C. and Delvaux, D. (1992), 'Normal vs. strike-slip faulting during rift development in East Africa: the Malawi Rift', *Geology* **20**, 1015–1018.

Ring, U., Kroener, A., Buchwaldt, R., Toulkeridis, T. and Layer, P. (2002), 'Shear zone patterns and eclogite-facies metamorphism in the Mozambique belt of northern Malawi, east-central Africa: implications for the assembly of Gondwana', *Precambrian Research* **116**, 19–56.

Rosendahl, B. (1987), 'Architecture of continental rifts with special reference to East Africa', *Annual Reviews Earth and Planetory Sciences* **15**, 445–503.

Sachau, T. and Koehn, D. (2010), 'Faulting of the lithosphere during extension and related rift-flank uplift: a numerical study', *International Journal of Earth Sciences* **99 (7)**, 1619–1632. doi: 10.1007/s00531-010-0513-6.

Schellart, W. (2002), Analogue modelling of large-scale tectonic processes: An introduction, *in* W. Schellart and C. Passchier, eds, 'Analogue modelling of large-scale tectonic processes', Vol. 7, Journal of the Virtual Explorer, Electronic Edition. doi:10.3809/jvirtex.2002.00045.

Schellart, W., Lister, G. and Jessell, M. (2002), 'Analogue modeling of arc and back-arc deformation in the new hebrides arc and north fiji basin', *Geology* **30**, 311–314.

Schlueter, T. (1997), Structural evolution of the East African Rift System, *in* F. Bender, V. Jacobshagen and G. Luettig, eds, 'Geology of East Africa', Gebrueder Boerntraeger, Berlin, Stuttgart, pp. 265–301.

Schreurs, G., Buiters, S., Boutelier, D., Corti, G., Costa, E., Cruden, A., Daniel, J.-M., Hoth, S., Koyi, H., Kukowski, N., Lohrmann, J., Ravaglia, A., Schlische, R., Withjack, M., Yamada, Y., Cavozzi, C., Delventisette, c., Brady, J., Rothe, A., Mengus, J., Montanari, D. and Nilforoushan, F. (2006), Analogue benchmarks of shortening and extension experiments, *in* S. Buiter and G. Schreurs, eds, 'Analogue and Numerical Modeling of Crustal-Scale Processes', Vol. 253, Geological Society, London, Special Publications, pp. 1–27.

Shackleton, R. (1978), Geological map of the Ologesailie Area, Kenya, *in* 'Geological background to fossil man: recent research in the Gregory Rift valley, East Africa', Buffalo: Toronto University Press, p. p.175.

Shudofsky, G. (1985), 'Source mechanisms and focal depths of East African earthquakes using Raleigh-wave and body-wave modeling', *Geophysical Journal of the Royal Astronomical Society* **83**, 563–614.

Sibson, R. (1985), 'A note on fault reactivation. brevia - short notes', *Journal of Structural Geology* **7 (6)**, 751–754.

Sippel, J., Scheck-Wenderoth, M., Reicherter, K. and Mazur, S. (2009), 'Paleostress states at the south-western margin of the Central European Basin System - application of fault-slip analysis to unravel a polyphase deformation pattern', *Tectonophysics* **470**, 129–146.

Smith, M. and Mosley, P. (1993), 'Crustal heterogeneity and basement influence on the development of the Kenya rift, East African', *Tectonics* **12 (2)**, 591–606.

Sokoutis, D., Corti, G., Bonini, M., Brun, J.-P., Cloetingh, S., Mauduit, T. and Manetti, P. (2007), 'Modeling the extension of heterogeneous hot lithosphere', *Tectonophysics* **444**, 63–79.

Spang, J. (1972), 'Numerical method for dynamic analysis of Calcite twin lamellae', *Geological Society of America Bulletin* **83 (1)**, 467–472.

Sperner, B. (1996), Computer programs for kinematic analysis of brittle deformation structures and the Tertiary tectonic evolution of the Western Caraethians (Slovakia),, PhD thesis, Tubingen University. Ph.D. Thesis.

Sperner, B., Ratschbacher, L. and Ott, R. (1993), 'Fault-striae analysis: a turbo-pascal program package for graphical presentation and reduced stress-tensor calculation', *Computers and Geosciences* **19 (9)**, 1361–1388.

Sperner, B. and Zweigel, P. (2010), 'A plea for more caution in fault-slip analysis', *Tectonophysics* **482**, 29–41.

Stamps, D., Calais, E., Saria, E., Hartnady, C., Nocquet, J.-M., Ebinger, C. and Fernàndes, R. (2008), 'A kinematic model for the East Arican Rift.', *Geophysical Research Letters* **35,L05304**, doi: 10.1029/2007GLO32781.

Stamps, D., Flesch, L. and Calais, E. (2010), 'Lithospheric buoyancy forces in Africa from a thin sheet approach', *International Journal of Earth Sciences* **99 (7)**, 1525–1533. doi: 10.1007/s00531-010-0533-2.

Strecker, M., Blisniuk, P. and Eisbacher, G. (1990), 'Rotation of extension direction in the central Kenya Rift', *Geology* **18**, 299–302.

Strecker, M. and Bosworth, W. (1991), 'Quaternary stress-field change in the Gregory Rift, Kenya', *EOS (Transactions, American Geophysical Union)* **72**, 17–22.

Tack, L., Liégeois, J., Deblond, A. and Duchesne, J. (1994), 'Kibaran A-type granitoids and mafic rocks generated by two mantle sources in a late orogenic setting (Burundi)', *Precambrian Research* **68**, 323–356.

Tack, L., Wingate, M., De Waele, B., Belousova, E., Griffin, B., Tahon, A. and Fernàndez-Alanso, M. (2010), 'The 1375ma Kibaran event', *Precambrian Research* **180**, 63–84.

Tapponnier, R., Peltzer, G., Le Dain, A., Armijo, R. and Cobbold, P. (1982), 'Propagating extrusion tectonics in Asia: new insights from simple experiments with plasticine', *Geology* **10**, 611–616.

Theunissen, K., Klerkx, J., Melnikov, A. and Mruma, A. (1996), 'Mechanisms of inheritance of rift faulting in the western branch of the East African Rift, Tanzania', *Tectonics* **15(4)**, 776–790.

Tiercelin, J., Chorowicz, J., Bellon, H., Richert, J., Mwanbene, J. and Walgenwitz, F. (1988), 'East African Rift System: offset, age and tectonic significance of the Tanganyika-Rukwa-Malawi intracontinental transcurrent fault zone', *Tectonophysics* **148**, 241–252.

Tirel, C., Brun, J.-P. and Sokoutis, D. (2006), 'Extension of thickened and hot lithospheres: inferences from laboratory modeling', *Tectonics* **25**, TC1005. doi: 10.1029/2005TC001804.

Townend, J. (2006), What do faults feel? observational constraints on the stresses acting on seismogenic faults, *in* 'Geophysical Monograph', 170, American Geophysical Union, chapter Earthquakes: Radiated Energy and the Physics of Faulting, pp. 313–327. 10.1029/170GM31.

Turner, F. (1953), 'Nature and dynamic interpretation of deformational lamellae in Calcite of three marbles', *American Journal of Science* **251**, 276–298.

Twiss, R. and Geffel, M. (1990), 'Curved slickenfibres: a new brittle sense indicator with application to a sheared serpentinite', *Journal of Structural Geology* **12**, 471–481.

Twiss, R., Protzman, G. and Hurst, S. (1991), 'Theory of slickenline patterns based on the velocity gradient tensor and microrotation', *Tectonophysics* **186**, 215–239.

Verhoogen, J., Turner, F., Weiss, L., Wahrhaftig, C. and Fyfe, W. (1970), *The Earth*, Holt, Rinehart and Winston, New York.

Wallace, R. (1951), 'Geometry of shearing stress and relation of faulting', *Journal of Geology* **59**, 118–130.

Wallace, R. and Morris, H. (1986), 'Characteristics of faults and shear zones in deep mines', *Pure and Applied Geophysics* **124**, 107–125.

Wallbrecher, E. (1986), *Tektonische und gefuegeanalytische Arbeitsweisen*, Enke-Verlag, Stuttgart.

Wernicke, B. (1985), 'Uniform-sense normal sense simple-shear of the continental lithosphere', *Canadian Journal of Earth Sciences* **22**, 108–125.

White, R. and McKenzie, D. (1989), 'Magmatism at rift zones and the generation of volcanic continental margins and flood basalts', *Journal of Geophysical Research* **94**, 7685–7729.

Woelbern, I., Ruempker, G., Schumann, A. and Muwanga, A. (2010), 'Crustal thinning beneath the Rwenzori region, Albertine rift, Uganda, from receiver function analysis', *International Journal of Earth Sciences* **99 (7)**, 1545–1557. DOI:10.1007/s00531-009-0509-2.

Wojtal, S. and Pershing, J. (1991), 'Paleostress associated with faults of large offset', *Journal of Structural Geology* **13 (1)**, 49–62.

Wolfenden, E., Ebinger, C., Yirgu, G., Deino, A. and Ayalew, D. (2004), 'Evolution of the northern Main Ethiopian Rift: birth of a triple junction', *Earth and Planetory Science Letters* **224**, 213–228.

Xu, P. (2004), 'Determination of regional stress tensors from fault-slip data', *Geophysical Journal International* **157 (3)**, 1316–1330.

Yamaji, A. (2000), 'The multiple inverse method: A new technique to separate stresses from heterogeneous fault-slip data', *Journal of Structural Geology* **22 (4)**, 441–452.

Yamaji, A. and Sato, K. (2006), 'Distances for the solutions of stress tensor inversion in relation to misfit angles that accompany the solutions', *Geophysical Journal International* **167**, 933–942.

Yamaji, A., Sato, K. and Otsubo, M. (2010), 'Multiple Inverse Method software package - User's guide'.

Yin, Z.-M. and Ranalli, G. (1992), 'Critical stress diference, fault orientation and slip direction in anisotropic rocks under non-Andersonian stress systems', *Journal of Structural Geology* **14 (2)**, 237–244.

Zoback, M. (1992a), 'First- and second-order patterns of stress in the Lithosphere: The World Stress Map Project', *Journal of Geophysical Research* **B97**, 11703–11728.